

**Deep anisotropic dry etching of  
silicon microstructures by  
high-density plasmas**



# **Deep anisotropic dry etching of silicon microstructures by high-density plasmas**

## **Proefschrift**

ter verkrijging van de graad van doctor  
aan de Technische Universiteit Delft,  
op gezag van Rector Magnificus prof. dr. ir. J.T. Fokkema,  
voorzitter van het College voor Promoties,  
in het openbaar te verdedigen op maandag 19 januari 2004 om 13:00 uur  
door Michiel Alexander BLAUW  
natuurkundig ingenieur  
geboren te Alkmaar.

Dit proefschrift is goedgekeurd door de promotoren:

Prof. dr. ir. S. Radelaar  
Prof. dr. P.J. French

Toegevoegd promotor:

Dr. E.W.J.M. van der Drift

Samenstelling promotiecommissie:

Rector Magnificus,	voorzitter
Prof. dr. ir. S. Radelaar,	Technische Universiteit Delft, promotor
Prof. dr. P.J. French,	Technische Universiteit Delft, promotor
Dr. E.W.J.M. van der Drift,	Technische Universiteit Delft, toegevoegd promotor
Prof. dr. P.M. Sarro,	Technische Universiteit Delft
Prof. dr. H.H. Brongersma,	Technische Universiteit Eindhoven
Prof. dr. ir. M.C.M. van de Sanden,	Technische Universiteit Eindhoven
Dr. M. Puech,	Alcatel Vacuum Technology France

The work described in this thesis was made possible by financial support of the Technology Foundation STW.

The work was performed at the Delft Institute of Microelectronics and Submicron Technology DIMES.

M.A. Blauw, *Deep anisotropic dry etching of silicon microstructures by high-density plasmas*, PhD Thesis, Delft University of Technology (Delft NL, 2004)

ISBN 90-9017644-6

Copyright © 2004 M.A. Blauw

All rights reserved. No part of this thesis may be reproduced or utilised in any form or by any means, electronic or mechanical, including photocopying, recording or by any information storage and retrieval system, without the written permission from the author.







---

# Contents

<b>1</b>	<b>Introduction</b>	<b>1</b>
1.1	Anisotropic dry etching	1
1.2	Profile control in silicon etching	3
1.3	High-density plasma etching	5
1.4	Applications of microfabrication	6
1.5	The scope of this thesis	8
	References	9
<b>2</b>	<b>Experimental methods</b>	<b>11</b>
2.1	Generation of high-density plasmas	11
2.1.1	Inductively coupled plasma reactor	11
2.1.2	Electron cyclotron resonance reactor	14
2.2	Plasma diagnostics	16
2.2.1	Optical emission spectroscopy and actinometry	16
2.2.2	Electrical characterisation with a Langmuir probe	22
2.3	Quantification of the plasma-material interactions	26
2.4	Surface analysis and sample inspection	27
2.4.1	X-ray photoelectron spectroscopy	27
2.4.2	Ellipsometry	30
2.4.3	Transmission electron microscopy and atomic force microscopy	31
2.4.4	Sample inspection and profile analysis	31
2.5	Sample preparation	32
2.5.1	Optical and electron beam lithography	32
2.5.2	Pattern transfer	32
	References	33

---

<b>3</b>	<b>Anisotropic silicon etching with oxide sidewall passivation at low temperatures</b>	<b>35</b>
3.1	Oxygen as an etch inhibitor	35
3.1.1	Suppression of the spontaneous etching of silicon by oxygen	36
3.1.2	Oxygen sidewall passivation	38
3.1.3	Crystal orientation dependent etching	38
3.2	Etching with an extremely low ion-to-radical flux ratio	40
3.2.1	The effects of flow and pressure on the etching mechanism	41
3.2.2	Etching with an extremely high etch yield as a function of bias voltage	44
3.2.3	Further discussion: surface analysis	48
3.3	The transport of radical and ion fluxes in high aspect ratio trenches	56
3.3.1	Introduction to the reaction kinetics of fluorine and silicon	57
3.3.2	The transport of fluorine radicals in high aspect ratio structures	59
3.3.3	Switching between ARDE and ARIE by tuning the ion flux with a variable reactor geometry	60
3.3.4	Switching between ARDE and ARIE by tuning the ion-to-radical flux ratio with a fixed reactor geometry	63
3.3.5	Aspect ratio dependent etching in the ICP reactor	66
3.3.6	Further discussion: plasma diagnostics	68
3.4	Monte Carlo simulation of anisotropic trench etching with oxygen passivation	71
3.4.1	The Monte Carlo simulation model	71
3.4.2	Profile evolution as a function of the oxygen flux	73
3.4.3	Simulation of deep trench etching and comparison with experiment	74
3.5	Conclusions	77
	References	77

---

<b>4</b>	<b>Balancing the etching and passivation in time-multiplexed deep anisotropic dry etching of silicon</b>	<b>81</b>
4.1	Profile control by balancing the etching and passivation pulse	81
4.1.1	Optimising anisotropy with passivation pressure and passivation pulse time	82
4.1.2	Optimising anisotropy by balancing the ion and radical flux	88
4.2	The impact of the ion-to-radical flux ratio on the maximal obtainable aspect ratio	89
4.2.1	Aspect ratio dependent etching	90
4.2.2	Optimising the maximal obtainable aspect ratio by tuning the ion-to-radical flux ratio	91
4.3	Quantification of the ion transport in high aspect ratio trenches with the ion angular distribution	95
4.3.1	The influence of the average absolute ion angle on the ion transport	95
4.3.2	Measurement of the average absolute ion angle	98
4.3.3	The impact of the ion angular distribution on the maximal obtainable aspect ratio	102
4.4	Conclusions	103
	References	104
<b>5</b>	<b>Time-multiplexed directional depassivation with the triple pulse process</b>	<b>105</b>
5.1	Optimisation of the depassivation pulse with a low-pressure, high-density, oxygen-based plasma	105
5.1.1	Physical versus chemical depassivation	106
5.1.2	Depassivation in SF <sub>6</sub> and O <sub>2</sub> plasmas monitored by <i>in situ</i> ellipsometry	107
5.1.3	Sidewall taper control	109
5.1.4	Sidewall corrugation and the transport of fluorine radicals	111
5.1.5	Directional depassivation with CO <sub>2</sub> and SO <sub>2</sub> plasmas	113
5.2	Comparison of the triple pulse process and the Bosch process	114
5.3	Conclusions	119
	References	119

<b>6</b>	<b>Trench profile optimisation by adjusting the surface passivation</b>	<b>121</b>
6.1	The polymer passivation layer deposition mechanism	121
6.1.1	The polymer deposition mechanism	121
6.1.2	Radical-induced and ion-enhanced polymer deposition	127
6.2	The polymer deposition mechanism in trenches	130
6.3	Trench profile optimisation by controlling the ion energy	136
6.4	Bias voltage ramping	141
6.5	Conclusions	142
	References	142
<b>7</b>	<b>Plasma-material interactions in ion-induced etching of silicon carbide and silicon</b>	<b>143</b>
7.1	Fluorine-based high-density plasma etching of high aspect ratio silicon carbide structures	143
7.1.1	SiC etching kinetics: etch rate investigation and plasma characterisation	145
7.1.2	Profile evolution for ion-induced SiC etching	149
7.1.3	High aspect ratio structures and aspect ratio dependent etching	151
7.2	Anisotropic silicon etching in Cl <sub>2</sub> plasmas	154
7.2.1	Ion-neutral synergy	155
7.2.2	Profile evolution: tapering, bowing and microtrenching	157
7.2.3	Aspect ratio independent etching	159
7.3	Conclusions	161
	References	161
<b>8</b>	<b>Conclusions and recommendations</b>	<b>165</b>
8.1	Conclusions	165
8.2	Recommendations	167

---

<b>A</b>	<b>Modelling of the surface kinetics and evaluation of the etch rate in deep structures</b>	<b>169</b>
A.1	The ion-neutral synergy model	169
A.2	Knudsen transport of radicals	170
A.3	The chemically enhanced ion-neutral synergy model	171
	References	175
<b>B</b>	<b>Plasma conditions of the etching experiments</b>	<b>177</b>
B.1	The cryogenic etching process	177
B.2	The Bosch process	181
B.3	The triple pulse process	182
B.4	The silicon carbide etching process	183
<b>C</b>	<b>Modelling of the polymer passivation layer deposition mechanism</b>	<b>185</b>
	References	187
	<b>Summary</b>	<b>189</b>
	<b>Samenvatting</b>	<b>191</b>
	<b>List of abbreviations</b>	<b>193</b>
	<b>List of symbols</b>	<b>195</b>
	<b>List of publications</b>	<b>199</b>
	<b>Curriculum Vitae</b>	<b>201</b>
	<b>Acknowledgements</b>	<b>203</b>





# Chapter 1

## Introduction

### 1.1 Anisotropic dry etching

The ongoing miniaturisation in the semiconductor industry has led to an exceptional increase of the functionality of integrated circuits. For over 30 years the number of electronic components on a chip has increased with a factor of 2 every 2 years. The necessary reduction of the dimensions is achieved by extensive research efforts in both lithography and pattern transfer. Whereas optical lithography is still able to meet the demand for smaller structures, pattern transfer by wet chemical etching struggled with problems in a much earlier stage. Until the 1970's the smallest structures were larger than 6  $\mu\text{m}$  and isotropic wet etching provided a reliable process with a high etch selectivity. However, irreproducible results precluded the use of wet etching for smaller features [1].

Dry etching in plasmas has originally been developed to replace the inadequate wet etching techniques. Plasma etching in barrel reactors offered better process control, but the process was still isotropic in this first stage. In the 1980's the smallest structure sizes decreased down to 1  $\mu\text{m}$ . At the approach of the submicron period the isotropic nature of etching in barrel reactors turned out to be a fundamental limitation to further miniaturisation. Reactive ion etching (RIE) in low-pressure plasmas resolved this problem by using the directionality of the positive ions towards the substrate on the powered electrode. A high degree of anisotropy is obtained due to ion-induced etching perpendicular to the substrate. The precise control of the lateral dimensions for anisotropic etching is compared to isotropic etching in figure 1.1.

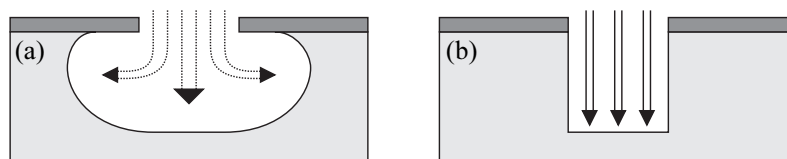


Figure 1.1 Profiles for isotropic and anisotropic etching. (a) Thermally activated etching leads to isotropic profiles. (b) Ion-induced etching results in anisotropic profiles.

Anisotropic dry etching processes have been developed for a wide range of materials mostly using fluorinated and chlorinated gases [2]. Typical materials in very large scale integration (VLSI) technology are silicon, aluminium, tungsten, molybdenum, silicon nitride, silicon oxide and disilicides of tungsten, molybdenum, titanium and tantalum. The boiling point of their fluorides and chlorides is relatively low, so that the reaction products can easily be pumped away. Initially the processes have been implemented on RIE systems and more recently on high-density plasma (HDP) etching systems. A schematic overview of a parallel plate RIE system is depicted in figure 1.2.

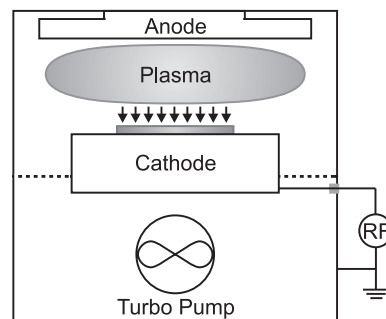


Figure 1.2 Schematic overview of a parallel plate RIE system. The substrate is placed on the powered cathode attracting the positive ions.

The degree of anisotropy of a dry etching process depends on the specific plasma-material interactions. The surface chemistry mainly consists of the three steps: adsorption of radicals, chemical reaction and desorption of reaction products. This is depicted in figure 1.3. If the three steps are all thermally activated the etching is spontaneous and the profiles are isotropic. Each step can also be assisted by ion impact. If at least one of the steps is not thermally activated the ions are necessary for etching and anisotropic profiles are obtained. Due to the synergy of ions and radicals, the etch rate is sufficiently high to make RIE suitable for etch depths up to a few microns [3]. For example, the volatile reaction product silicon tetrafluoride is spontaneously formed in fluorine-based plasma etching of silicon resulting in isotropic profiles. Special techniques that suppress the lateral etch rate are necessary to obtain anisotropic profiles, which are described in section 1.2. In contrast, no volatile reaction products are formed in chlorine-based plasma etching of silicon and anisotropic profiles are obtained due to ion-induced desorption.

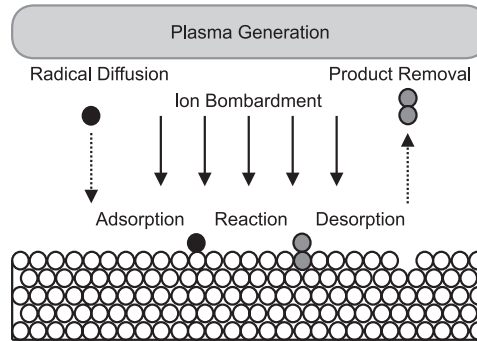


Figure 1.3 The three main steps of the surface chemistry in a plasma etching process. The sequence of adsorption, reaction and desorption leads to etching. Each step can also be assisted by ion impact.

In this thesis fluorine-based HDP etching of deep anisotropic silicon structures is investigated. Special attention is aimed at the transport of plasma particles in deep cavities, which obviously influences the etch rate [4-6]. Detailed investigation of the particle fluxes and their interactions with the substrate results in a comprehensive understanding of the etching mechanism and profile control. The advantages of HDP etching and the profile control techniques are explained in section 1.3. Both high etch rates and anisotropic profiles are required by advanced applications such as microelectromechanical systems (MEMS) for which the etch depths are often more than 100  $\mu\text{m}$ . The process requirements for typical applications are clarified in section 1.4. The scope of this thesis is described in section 1.5.

## 1.2 Profile control in silicon etching

The spontaneous chemical component in fluorine-based plasma etching of silicon has to be suppressed to obtain anisotropic profiles. The directional ion flux results in a high degree of anisotropy if the etching is strongly ion-induced. This is achieved by adjusting the process. The four different methods that are described are subdivided in two categories. The first category includes two methods that diminish the spontaneous chemical reaction of the fluorine radicals relative to the ion-induced component. The second category includes two methods that passivate the silicon surface. The two underlying principles are depicted in figure 1.4.

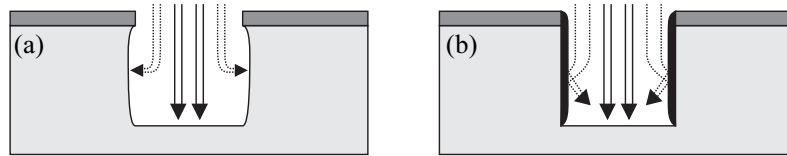


Figure 1.4 Methods to achieve anisotropic etching are categorised by two principles. (a) Suppression of the spontaneous chemical component relative to the ion-induced component. (b) Surface passivation by the addition of an etch inhibitor or the deposition of a protective layer.

### Reduction of the spontaneous chemical reaction of fluorine radicals

1. Below a certain threshold of the fluorine radical partial pressure the lateral etch rate becomes zero and perfect anisotropy is achieved [7,8]. The radical-to-ion flux ratio can be decreased by either reducing the plasma pressure or diluting the fluorine plasma with an inert gas.
2. The lateral etch rate is suppressed by the cooling of the substrate, because the thermally activated chemical reactions are frozen out and the vapour pressure of reaction products becomes very low. The reactions on the horizontal surface still continue under ion bombardment leading to the desired anisotropy. This approach has been applied to several materials such as silicon and tungsten in fluorine plasmas and cobalt in a chlorine plasma [9-12]. The optimal temperature for silicon is about  $-100\text{ }^{\circ}\text{C}$ , but for tungsten and cobalt it is  $-20\text{ }^{\circ}\text{C}$  and  $+200\text{ }^{\circ}\text{C}$  respectively. Because of the very low temperatures needed for silicon etching it is usually called the cryogenic etching process or the cryo-process for short.

### Passivation of the silicon surface

1. The etch rate decreases if oxygen is added to a fluorine-based plasma due to competitive fluorination and oxidation of the surface. Oxygen is an etch inhibitor, because the oxidised surface sites are not available for spontaneous reaction with fluorine radicals. The anisotropy of the process is improved, because the directional ion bombardment removes the oxides [13,14].
2. The addition of a fluorocarbon gas instead of oxygen results in the deposition of a thin polymer layer that blocks the spontaneous chemical reaction of fluorine radicals with silicon. Sputtering removes the polymer layer, so that the etching only proceeds in the direction of the ions. Mixtures of  $\text{SF}_6$  and fluorocarbon gases such as  $\text{CHF}_3$  have been used for etching. With this chemistry there is a compromise between anisotropy and etch rate [15-19]. Anisotropic silicon etching is also possible with several pure fluorocarbon gases such as  $\text{CF}_4$  [20-24].

### 1.3 High-density plasma etching

Silicon etching has gone through a large evolution due to the everlasting demands for higher etch rates, higher selectivity and higher anisotropy. These targets can be obtained almost without compromise in HDP etching systems such as inductively coupled plasma (ICP) and electron cyclotron resonance (ECR) reactors. A schematic overview of an ICP reactor is given in figure 1.5.

Due to the high density of radicals and ions the etch rate is orders of magnitude higher than in RIE systems. The gas flow, the source power and the pumping speed are also higher with the aim to keep the supply of radicals in proportion to the consumption. Besides the concentration of reaction products is low due to the low residence time.

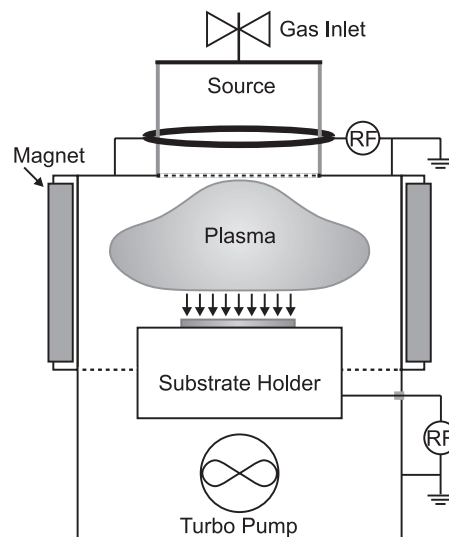


Figure 1.5 Schematic overview of an ICP reactor with independent control of the plasma generation and substrate biasing.

Mask erosion and plasma-induced damage of the etched materials are strongly reduced if the ion energy is lowered. In RIE systems a higher plasma density is always coupled to a higher bias voltage. However, in HDP etching systems the plasma density and the ion energy are independently controlled by separate power sources for plasma generation and substrate biasing. An advantage of HDP etching systems is thus that both a high plasma density and a low ion energy can be obtained simultaneously.

Due to the high fluorine radical partial pressure in high-density  $\text{SF}_6$  plasmas it is impossible to prevent lateral etching by lowering the substrate temperature alone, even near the point where the plasma condenses [25,26]. In this case the addition of oxygen at very low temperatures is necessary to obtain anisotropic profiles. The surface passivation at very

low temperatures is very effective and the cryo-process with oxygen passivation has proven to be highly versatile [27-30].

The addition of a fluorocarbon gas to high-density SF<sub>6</sub> plasmas for sidewall passivation does not give optimal results. The optimal plasma conditions for a high etch rate and a high degree of anisotropy are contradictory. For high etch rates the fraction of fluorocarbon radicals should be as low as possible, but for the deposition of a qualitatively good passivation layer it should be much higher. Moreover, a high concentration of fluorocarbon radicals results in excessive polymer growth on the reactor walls. The invention of a new method of anisotropic silicon etching at room temperature by Robert Bosch GmbH resolved these problems [31]. It is a time-multiplexed process, so that the etching and passivation can be optimised separately in two consecutive plasma pulses. A high etch rate and anisotropic profiles are obtained in combination with a high selectivity and relatively smooth sidewall surfaces. Accurate control of the lateral dimensions is of utmost importance for many applications, which requires a delicate balance between the etching and passivation pulse. The etching pulse is as short as possible, so that lateral etching is minimised. Octafluorocyclobutane (C<sub>4</sub>F<sub>8</sub>) is often used for passivation because this cyclic molecule is efficiently dissociated into precursors for polymer deposition. In a short period of time many improvements have been developed for the Bosch process because of its broad range of applications [32-38].

## 1.4 Applications of microfabrication

Microfabrication by dry etching is increasingly used for applications in fields other than microelectronics such as microelectromechanical systems, microfluidics, micromechanics, optoelectronics and photonics. Integrated passive radio frequency components and trench isolation in integrated circuits are two other applications. The devices are often made in silicon, because many processes have been developed for this material. Besides, it is possible to integrate the devices and electronics on a single chip. Moreover, monocrystalline silicon has excellent material properties. For example the mechanical properties of monocrystalline silicon are perfect for MEMS devices. HDP etching is often necessary to fabricate the devices because of the highly demanding requirements with respect to etch rate, anisotropy and process compatibility.

As a matter of fact HDP etching combines the distinct advantages of the two common approaches in microfabrication, i.e., bulk micromachining and surface micromachining. With bulk micromachining, deep structures are made in monocrystalline silicon wafers by wet chemical etching. However, the lateral resolution is low and some chemicals are incompatible due to contamination of the wafer. With surface micromachining, structures are made in thin deposited layers by using dry etching with a high anisotropy and a high lateral resolution. However, the mechanical properties of the deposited layers are inferior to monocrystalline silicon, and the mass of the fabricated structures is much lower.

A typical example is the MEMS sensor, which transforms signals from the mechanical domain to the electrical domain. Sensors that detect linear acceleration, rotation and vibration are specified with the generic name inertial sensor. Large-scale application is foreseen in automobiles (airbags, electronic stability control and active suspension), three dimensional computer interfaces (virtual reality), automatic navigation systems and precisely controlled automated manufacturing equipment. The measurement of hydrostatic pressure, flow of fluids and strain in a stressed beam are applications of MEMS sensors too.

Capacitive coupling is an important detection mechanism for inertial sensors. An example of a differential accelerometer is given in figure 1.6. It is based on the change of the capacitance between the moving and fixed conducting plates during acceleration of the elastically suspended mass.

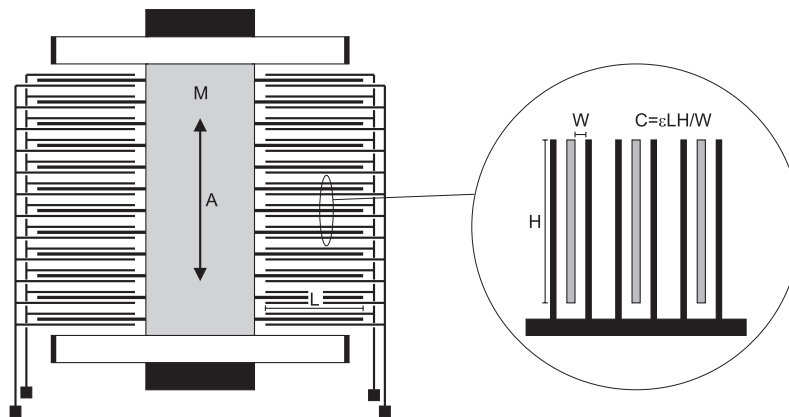


Figure 1.6 The layout and the partial cross-section of a differential accelerometer. The mass  $M$  suspended by four springs moves if an acceleration  $A$  is applied. The measured capacitance  $C$  is proportional the aspect ratio  $H/W$ .

A high sensitivity and a low mechanical noise are prerequisites for future devices with a high performance. Mechanical noise is primarily due to Brownian motion, which is reduced with a larger mass. The signal-to-noise ratio is thus increased with a larger height of the structure. The electrical noise in the measurement circuit is reduced by a larger capacitance, which is directly proportional to the height and inversely proportional to the width of the capacitor. In other words it is determined by the aspect ratio. The number of capacitors in the array is also inversely proportional to the width of the capacitor. Therefore, a high aspect ratio and a high resolution are necessary for highly sensitive inertial sensors. Especially HDP etching fulfils these requirements because of the high etch rate and the precise control of the anisotropy.

## 1.5 The scope of this thesis

High-density plasma etching has resulted in new opportunities to fabricate advanced devices. For many applications it is necessary to obtain high aspect ratios, that is, aspect ratios higher than 10. A high degree of anisotropy is obtained for both the cryogenic etching process and the Bosch process leading to aspect ratios higher than 30. These processes have many common properties, although each process has its own limitations. Yet many aspects of the fundamental etching, passivation and depassivation kinetics are still unexplained. In this thesis a quantitative study that correlates the plasma species fluxes and the etch results is presented to clarify these aspects. Furthermore, a major question in this thesis is how the transport of radicals and ions in high aspect ratio trenches is governed. The transport of plasma species in deep cavities can lead to aspect ratio dependent etching. A closely related question is for which conditions the maximal aspect ratio is obtained while properties like etch rate, selectivity and anisotropy are within acceptable boundaries. In chapter 2 a detailed description of the HDP etching equipment, plasma diagnostics, surface analytics and sample preparation is given.

The quantitative investigation of the so-called cryo-process is described in chapter 3. Anisotropic silicon etching is the result of the interactions between fluorine radicals, oxygen radicals and ions. The oxygen radicals and ions play a crucial role in the passivation and depassivation mechanism. The transport of these species in deep trenches influences the etch rate. The Knudsen transport of fluorine radicals in deep structures was investigated with special structures that block the directional ion flux. A macroscopic model and detailed Monte Carlo simulations explain the experimental results.

In chapter 4 the Bosch process is described. Anisotropy is the result of a delicate balance between passivation and depassivation. Insufficient depassivation by ions is an important limiting factor for the etching of high aspect ratio trenches. Therefore, the transport of ions in deep structures is quantified with the ion angular distribution. Modifications to the *depassivation* and the *passivation* conditions were investigated. In chapter 5 an advanced time-multiplexed plasma etching process is introduced for improved *depassivation*. An additional depassivation pulse consisting of a high-density, low-pressure, oxygen-based plasma removes the polymer layer efficiently from the bottom of the trench directly after the passivation pulse. In chapter 6 the optimisation of the *passivation* pulse is discussed. Predominant sidewall deposition was obtained for certain settings of the pressure, ion flux and ion energy. The ion energy of the etching and passivation pulse were optimised independently to investigate the influence of predominant sidewall deposition on the trench profile.

Chapter 7 aims at a more fundamental understanding of the characteristic role of the ions in the etching process. Ion-induced etching of SiC in an SF<sub>6</sub>-O<sub>2</sub> plasma and ion-induced etching of Si in a Cl<sub>2</sub> plasma were investigated. The plasma-material interactions that influence both profile evolution and aspect ratio dependent etching were quantitatively



investigated. Especially SiC is an interesting material because the removal of a fluorocarbon layer is the rate limiting step comparable to the Bosch process [39].

## References

- [1] A.J. van Roosmalen, J.A.G. Baggerman and S.J.H. Brader, *Dry Etching for VLSI*, (Plenum Press, New York US, 1991)
- [2] R.A. Powell, *Dry Etching for Microelectronics*, (North-Holland Physics Publishing, Amsterdam NL, 1984)
- [3] J.W. Coburn and H.F. Winters, *J. Appl. Phys.* **50**, 3189 (1979)
- [4] R.A. Gottscho, C.W. Jurgensen and D.J. Vitkavage, *J. Vac. Sci. Technol. B* **10**, 2133 (1992)
- [5] A.D. Bailey III, M.C.M. van de Sanden, J.A. Gregus and R.A. Gottscho, *J. Vac. Sci. Technol. B* **13**, 92 (1995)
- [6] J.W. Coburn and H.F. Winters, *Appl. Phys. Lett.* **55**, 2730 (1989)
- [7] B. Mahi, Y. Arnal and C. Pomot, *J. Vac. Sci. Technol. B* **5**, 657 (1987)
- [8] B. Petit and J. Pelletier, *Jpn. J. Appl. Phys.* **26**, 825 (1987)
- [9] S. Tachi, K. Tsujimoto and S. Okudaira, *Appl. Phys. Lett.* **52**, 616 (1988)
- [10] S. Tachi, K. Tsujimoto, S. Arai, H. Kawakami and S. Okudaira, *Extended Abstracts of the 20<sup>th</sup> International Conference on Solid State Devices and Materials*, 553 (Tokyo JP, 1988)
- [11] K. Tsujimoto, S. Okudaira and S. Tachi, *Jpn. J. Appl. Phys.* **30**, 3319 (1991)
- [12] M.S.P. Andriessse, T. Zijlstra, and E. van der Drift, *J. Vac. Sci. Technol. B* **18**, 3462 (2000)
- [13] C.P. D'Emic, K.K. Chan and J. Blum, *J. Vac. Sci. Technol. B* **10**, 1105 (1992)
- [14] J.N. Randall and J.C. Wolfe, *Appl. Phys. Lett.* **39**, 742 (1981)
- [15] R. Legtenberg, H. Jansen, M. de Boer and M. Elwenspoek, *J. Electrochem. Soc.* **142**, 2020 (1995)
- [16] H. Jansen, M. de Boer, R. Legtenberg and M. Elwenspoek, *J. Micromech. Microeng.* **5**, 115 (1995)
- [17] H. Jansen, M. de Boer, J. Burger, R. Legtenberg and M. Elwenspoek, *Microelectronic Engineering* **27**, 475 (1995)
- [18] E. Gogolides, S. Grigoropoulos and A.G. Nassiopoulou, *Microelectronic Engineering* **27**, 449 (1995)
- [19] S. Grigoropoulos, E. Gogolides, A.D. Tserepi and A.G. Nassiopoulou, *J. Vac. Sci. Technol. B* **15**, 640 (1997)

- [20] Y.H. Lee and M.M. Chen, *J. Appl. Phys.* **54**, 5966 (1983)
- [21] G.S. Oehrlein and H.L. Williams, *J. Appl. Phys.* **62**, 662 (1987)
- [22] M. Engelhardt and S. Schwarzl, *J. Electrochem. Soc.* **134**, 1985 (1987)
- [23] G.S. Oehrlein, *J. Vac. Sci. Technol. A* **11**, 34 (1993)
- [24] T.E.F.M. Standaert, M. Schaepkens, N.R. Rueger, P.G.M. Sebel, G.S. Oehrlein and J.M. Cook, *J. Vac. Sci. Technol. A* **16**, 239 (1998)
- [25] M. Puech and P. Maquin, *Appl. Surf. Sci.* **100-101**, 579 (1995)
- [26] J.W. Bartha, J. Greschner, M. Puech and P. Maquin, *Microelectronic Engineering* **27**, 453 (1995)
- [27] T. Pandhumsoporn, M. Feldbaum, P. Gadgil, M. Puech and P. Maquin, *Proceedings of the SPIE* **2879**, 94 (Austin US, 1996)
- [28] M. Esashi, M. Takinami, Y. Wakabayashi and K. Minami, *J. Micromech. Microeng.* **5**, 5 (1995)
- [29] M. Francou, J.S. Danel and L. Peccoud, *Sensors and Actuators A* **46-47**, 17 (1995)
- [30] D.C. Hays, K.B. Jung, Y.B. Hahn, E.S. Lambers, S.J. Pearton, J. Donahue, D. Johnson and R.J. Shul, *J. Electrochem. Soc.* **146**, 3812 (1999)
- [31] F. Lärmer and A. Schilp of Robert Bosch GmbH, German Patent N° DE4241045 (1994)
- [32] F. Lärmer, A. Schilp, K. Funk and M. Offenbergl, *Proceedings of the 12<sup>th</sup> IEEE International Conference on Microelectromechanical Systems*, 211 (Orlando US, 1999)
- [33] J.K. Bhardwaj and H. Ashraf, *Proceedings of the SPIE* **2639**, 224 (Austin US, 1995)
- [34] A.A. Ayón, R. Braff, C.C. Lin, H.H. Sawin and M.A. Schmidt, *J. Electrochem. Soc.* **146**, 339 (1999)
- [35] J. Kiihamäki, *J. Vac. Sci. Technol. A* **18**, 1385 (2000)
- [36] J. Hopins, H. Ashraf, J.K. Bhardwaj, A.M. Hynes, I. Johnston and J.N. Shepherd, *Proceedings of the MRS Fall Meeting*, (Boston US, 1998)
- [37] B. Volland, F. Shi, P. Hudek, H. Heerlein and I.W. Rangelow, *J. Vac. Sci. Technol. B* **17**, 2768 (1999)
- [38] J. Ohara, K. Kano, Y. Takeuchi, N. Ohya, Y. Otsuka and S. Akita, *Proceedings of the 13<sup>th</sup> IEEE International Conference on Microelectromechanical Systems*, 277 (Miyazaki JP, 2000)
- [39] P. Chabert, *J. Vac. Sci. Technol. B* **19**, 1339 (2001)

---

## Chapter 2

### Experimental methods

A fundamental approach of the silicon etching mechanism in high-density fluorine-based plasmas has been pursued. To that aim a quantitative investigation of the plasma composition and the etching results has been performed. This chapter describes the experimental methods that have been used to unravel the surface processes. A description of the plasma generation with the HDP etching equipment that has been used in this research is given in section 2.1. Plasma diagnostic techniques such as the measurement of the radical fluxes with optical emission spectroscopy (OES) and the measurement of the ion flux with a Langmuir probe system are described in section 2.2. The dimensionless numbers that characterise the plasma-material interactions are defined in section 2.3. The most important surface analytic techniques that are used in this research are treated in section 2.4. The surface composition is investigated with X-ray photoelectron spectroscopy (XPS) and ellipsometry. Generally the etched structures are inspected with electron scanning microscopy (SEM). A short overview of the substrate characteristics and the pattern definition is presented in section 2.5.

#### 2.1 Generation of high-density plasmas

Low-pressure gases submitted to an electric field are easily ionised and radiate characteristic light [1]. The electrons that are accelerated in the electric field collide with molecules, which are dissociated or ionised if the electrons have sufficient energy. Plasma densities in DC discharges and planar AC powered RIE systems are relatively low. Plasma densities can be improved by one to two orders of magnitude with radio frequency (RF) electromagnetic fields that accelerate the electrons by means of induction or electron cyclotron resonance.

##### 2.1.1 Inductively coupled plasma reactor

Inductive coupling is obtained with a coil antenna around a ceramic tube or dome in which the plasma is generated. The power is coupled to the coil through an impedance matching network. In inductively coupled plasma (ICP) etching systems a strong rise of the plasma density is observed above a certain threshold of the RF source power as is shown in figure 2.1. The positive-ion density is in the order of  $10^{10} \text{ cm}^{-3}$ . Below the threshold of about 500 W the plasma density is comparable to RIE systems due to capacitive coupling. The name transformer coupled plasma (TCP) is used for a spiral coil antenna on top of a flat window. In a helicon wave reactor another strong increase of the plasma density is observed due to

excitation of helicon waves by the special antenna geometry in combination with a constant external magnetic field.

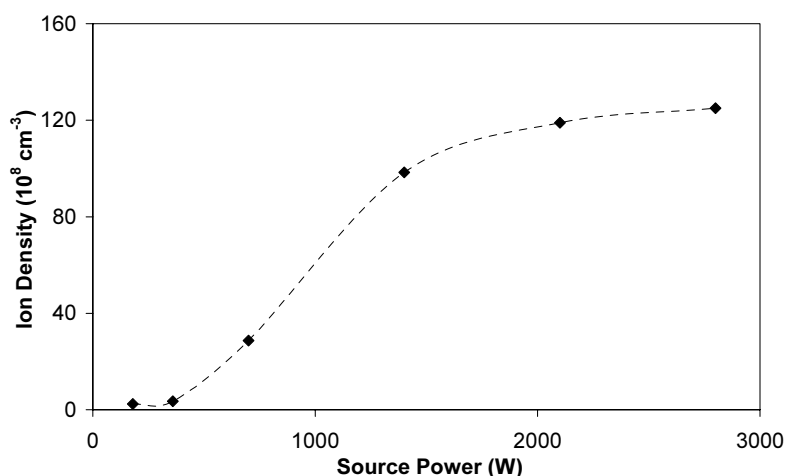


Figure 2.1 Increase of the positive-ion density as a function of ICP source power. A strong increase is observed going from the capacitively coupled to the inductively coupled regime, i.e. from a dim mode to a bright mode.

The equipment that has been used in this research is an Alcatel MET reactor. The coil antenna consists of two semicircular loops around a ceramic tube. Erosion of a quartz liner in the plasma source leads to an oxygen atom density that is comparable to the addition of 30 sccm  $\text{O}_2$ . This inductively coupled plasma (ICP) etching system has two 13.56 MHz RF power sources of 3000 W and 600 W for independently adjustable plasma generation and substrate biasing respectively.

Vacuum is obtained with a  $1000 \text{ l}\cdot\text{s}^{-1}$  magnetically levitated turbomolecular pump and the reactor chamber is accessible through a load lock system. With full pumping speed the residence time is about 0.2 s. The available gases are  $\text{SF}_6$ ,  $\text{C}_4\text{F}_8$ ,  $\text{O}_2$  and Ar. Gas pressure is measured with a Baratron capacitance manometer and can be regulated with an adjustable butterfly valve. Normally the total gas flow is in the range of 50 sccm to 500 sccm and the pressure is in the range of 0.5 Pa to 5 Pa. In the cryo-process a small change of about 10% of the  $\text{O}_2$  flow already leads to a significant degradation of the anisotropy. This is only about 1% of the total gas flow for the current process settings. Deviating etch results due to a shift of the reactor condition can therefore be counteracted by small changes of the  $\text{O}_2$  flow. For the pulsing of gases in the Bosch process the reactor is equipped with fast mass flow controllers and short gas lines, so that the gas in the reactor can be changed within 1 s. The pulsing settings are electronically regulated. Additional electronics have been made for the pulsing of the bias voltage along with the gases.

### Low residence times for high fluorine radical densities

A high density of fluorine radicals is necessary for high-speed silicon etching, because the spontaneous chemical etch rate is proportional to the fluorine radical flux towards the substrate. A higher density of fluorine radicals can be attained by a higher reactor pressure. However, the reactor pressure is the combined result of the gas flow and the pumping speed at the wafer level, which can be controlled with the butterfly valve in front of the turbomolecular pump. The increase of the etch rate is most pronounced if the reactor pressure increases due to an increase of the gas flow with a fixed vacuum conductance. At a given reactor pressure the highest etch rate is obtained for the minimum residence time on the condition that the source power is high enough to dissociate the entire gas flow because of the following three reasons.

1. Reaction of the fluorine radicals with the silicon substrate leads to a fluorine radical density gradient within the plasma. The depletion of the fluorine radical density is minimum if the replenishment of fluorine radicals is the highest.
2. The gas flow speed through the reactor is the highest, so that the fluorine radical losses by sidewall recombination are minimum.
3. The density of the reaction products is minimum due to the highest pumping speed at the wafer level.

An example of the etch rate as a function of reactor pressure and gas flow is given in table 2.1. The increase of the pressure at a constant flow and increase of the flow at a constant pressure give a much smaller increase of the etch rate than the simultaneous increase of the pressure and flow. Because of this the residence time must play a role.

Table 2.1 The etch rate in the ICP reactor depends on the gas flow and reactor pressure.

Flow Rate (sccm)	Pressure (Pa)	Etch Rate ( $\mu\text{m}\cdot\text{min}^{-1}$ )
100	2.21	7.4
100	4.08	9.9
200	2.19	9.6
200	4.11	12.6

### Mixing of gases in the Bosch process

In the Bosch process the mixing of the etching and passivation gas has adverse effects on the polymer deposition process and is particularly noticeable for short passivation pulse times. Both a fundamental and a technical reason cause the mixing of the etching and

passivation gas. The fundamental problem is the residence time. A substantial fraction of the passivation pulse time is needed to reduce the residual gas of the SF<sub>6</sub> pulse to a level where it does not influence the C<sub>4</sub>F<sub>8</sub> pulse. The technical problem is the non-optimal configuration of the gas lines. Beside the short main gas line, which carries the pulsed gases, a secondary gas line, which carries the non-pulsed gases, is connected to the gas inlet. The secondary gas line is filled with SF<sub>6</sub> during etching and releases SF<sub>6</sub> during passivation, because the SF<sub>6</sub> pressure is usually higher than the C<sub>4</sub>F<sub>8</sub> pressure. For that reason the secondary gas line effectively serves as a buffer for SF<sub>6</sub> that mixes with C<sub>4</sub>F<sub>8</sub>. It is the fluid mechanics analogy of a capacitor. As soon as this was recognised the adverse SF<sub>6</sub> buffer was closed with a valve.

### **Substrate temperature control**

The substrate holder temperature can be regulated in the range of  $-150\text{ }^{\circ}\text{C}$  to  $+25\text{ }^{\circ}\text{C}$  with fluctuations smaller than  $\pm 1\text{ }^{\circ}\text{C}$  by liquid nitrogen cooling in combination with resistive heating. The low substrate temperature regime is necessary, because the optimal substrate temperature is approximately  $-125\text{ }^{\circ}\text{C}$  for the cryogenic etching process. The accurate control of the substrate temperature is important, because a change of  $\pm 5\text{ }^{\circ}\text{C}$  already leads to a significant degradation of the anisotropy of the cryogenic etching process. Good thermal contact with the substrate is ensured by a helium flow at the backside of the substrate. Nevertheless some heating of the substrate surface has been observed. The substrate holder temperature and the substrate surface temperature have been independently measured as a function of the source power. These measurements show that the substrate surface temperature is higher and that the difference increases more than  $30\text{ }^{\circ}\text{C}$  at  $2000\text{ W}$  source power. This difference can well explain the difference of the optimal substrate temperature in the ICP reactor ( $-125\text{ }^{\circ}\text{C}$ ) and the electron cyclotron resonance (ECR) reactor ( $-95\text{ }^{\circ}\text{C}$ ), which is described next. The position of the substrate holder can be adjusted. The ion density at the substrate level decreases due to electron-ion recombination in the downstream region if the substrate-to-source distance increases.

### **2.1.2 Electron cyclotron resonance reactor**

Another type of generation is based on the interaction of microwave radiation with a plasma. For efficient power transfer the electrons should be exposed long to the oscillating electromagnetic field. This is achieved by confining the electrons with a magnetic field near the antennas. In a magnetic field the electrons will follow a circular track with the electron cyclotron frequency. In a magnetic field of  $87.5\text{ mT}$  this frequency is exactly equal to the microwave frequency of  $2.45\text{ GHz}$ . The movement of the electrons is in phase with the electromagnetic field leading to a sustained acceleration. This is depicted schematically in figure 2.2. Plasma generation by electron cyclotron resonance only occurs if the mean free path of electrons is large enough to gain sufficient energy for dissociation and ionisation of molecules. In practice the pressure is in the range of  $0.1\text{ Pa}$  to  $0.5\text{ Pa}$ . In the ICP reactor the

radical fluxes are one order of magnitude higher due to the higher pressure making the ICP reactor more suitable for high etch rate applications.

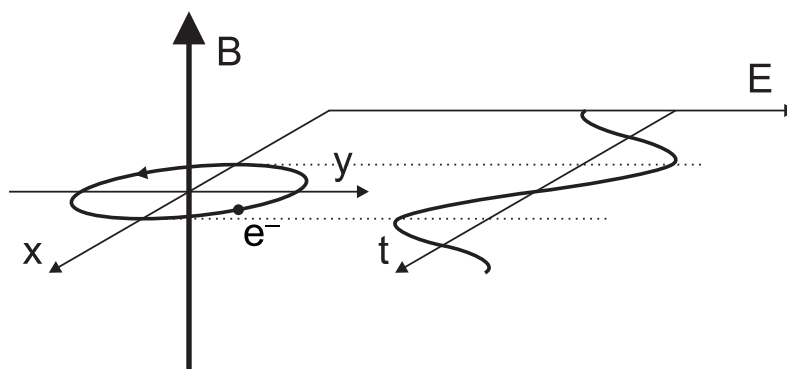


Figure 2.2 Electron cyclotron resonance. In a static magnetic field an electron follows a circular orbit with a certain frequency. Resonant motion of the electrons is obtained, if an electric field is applied with the same frequency.

In this work an Alcatel RCE 200 reactor has been used. It is a distributed electron cyclotron resonance (DECR) reactor with 14 antennas to obtain a better uniformity. The microwave power from a 2000 W, 2.45 GHz magnetron tube is coupled into a distributor and reflected power is reduced to nearly zero with a manual stub tuner. The  $900 \text{ l}\cdot\text{s}^{-1}$  chamber pumping, the wafer handling capabilities, the gas flow control, the substrate temperature regulation and substrate biasing are equally versatile as for the ICP reactor. But the optimal substrate temperature for the cryogenic etching process in the ECR reactor is approximately  $-95 \text{ }^\circ\text{C}$ . An important modification to this system consists of a 15 cm high quartz cylinder that has been placed on the clamping ring around the wafer. Originally it intended to eliminate contamination from the antennas and the reactor wall. However, it effectively results in a downstream reactor geometry because the direct path between the source region and the wafer is blocked. In this way an extremely low ion-to-radical flux ratio is obtained at the wafer level, because electron-ion recombination is much faster than radical-radical recombination. The ion flux is reduced by 2 orders of magnitude due to the quartz cylinder. The ECR reactor geometry is shown in figure 2.3. Without the quartz cylinder the ion flux in the ECR reactor is comparable to the ion flux in the ICP reactor.

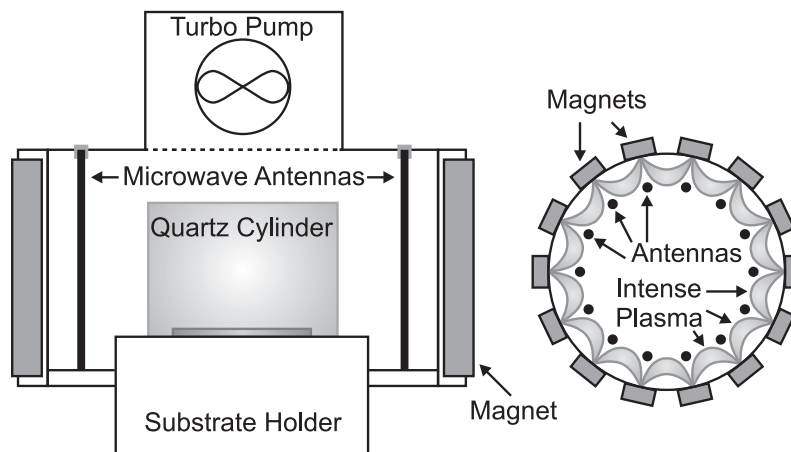


Figure 2.3 Schematic outline of the ECR reactor. The side view shows the quartz cylinder, which blocks the direct path between the source region and the substrate. The top view shows the magnet and antenna positions along with the most intense plasma regions.

## 2.2 Plasma diagnostics

The quantification of the plasma species fluxes to the substrate is an important step towards the understanding of an etching mechanism. The plasma is a complex medium and the density of the plasma species is difficult to predict with analytical and numerical models. Plasma diagnostics make it possible to measure the density of the plasma species that are relevant to the process. Radicals such as fluorine and oxygen are measured with optical emission spectroscopy (OES) and ions with a Langmuir probe system.

### 2.2.1 Optical emission spectroscopy and actinometry

#### Optical emission by electron impact excitation

The characteristic colour of the emitted light is one of the most striking properties of a plasma. Each plasma has a distinct colour spectrum, which is a fingerprint of the plasma composition. With optical emission spectroscopy the intensity distribution is measured as a function of the wavelength. The electron temperature in a plasma is several eV, so that a significant fraction of electrons in the high-energy tail of the electron distribution is capable of exciting the plasma species. The excitation energy depends on the type of plasma species, but normally it is in the range of 6 eV to 15 eV. After electron impact excitation of a plasma species X the excited plasma species  $X^*$  emits a photon with a well-defined



wavelength. The energy of the photon is  $h \cdot \nu$  (Planck constant times frequency). This process is given by formula 2.1.



The line intensity  $I_X$  given in equation 2.2a is the product of the effective plasma diameter  $D$ , the branching ratio  $B_X$ , the radiative lifetime  $\varepsilon_X$  and the density of the excited species  $n_{X^*}$ . In a stationary state the emission rate  $\varepsilon_X \cdot n_{X^*}$  is equal to the excitation rate [2]. The excitation rate given in equation 2.2b is calculated by integrating the product of the electron energy distribution  $f(\varepsilon)$ , the electron velocity  $v(\varepsilon)$  and the excitation cross-section of the involved optical transition  $\sigma_X(\varepsilon)$  over the electron energy  $\varepsilon$ . The excitation rate is proportional to the density of the plasma species  $n_X$  and the density of electrons  $n_e$ . For most plasmas  $n_{X^*} \ll n_X$ .

$$I_X = \frac{D}{2} \cdot B_X \cdot \varepsilon_X \cdot n_{X^*} \quad 2.2a$$

where

$$\varepsilon_X \cdot n_{X^*} = n_X \cdot n_e \cdot \int_0^{\infty} \sigma_X(\varepsilon) \cdot v(\varepsilon) \cdot f(\varepsilon) \cdot d\varepsilon \quad 2.2b$$

### Actinometry of atomic fluorine and oxygen

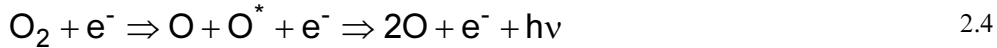
The intensity is not only proportional to the species density, but it also depends on the electron density and temperature, i.e., the electron energy distribution function. For a quantitative measurement of the species density a technique named actinometry has to be deployed. A small amount of an inert gas, e.g., argon, is added to the plasma, so that it does not influence the plasma chemistry and the density of the actinometer gas  $n_A$  is known. The intensity ratio of the actinometer gas and the plasma species is measured. If the excitation cross-sections show similar behaviour as a function of electron energy the density is given by equation 2.3.

$$n_X = \alpha \cdot \frac{I_X}{I_A} \cdot n_A \quad 2.3$$

The proportionality constant  $\alpha$  can be obtained from independent measurements such as chemoluminescent titration and laser induced fluorescence (LIF). Determination of the atomic fluorine density is the classical example of actinometry [3]. The excitation threshold

for fluorine (703.7 nm, 14.75 eV) and argon (750.4 nm, 13.48 eV) are very close. In CF<sub>4</sub> and NF<sub>3</sub> plasmas the fluorine radical density has been measured by titration [4]. With these data a proportionality constant of 0.81 has been calculated, which has been used in this research. It is close to the value of 0.68 derived with a theoretical method [5,6]. The experimental inaccuracy in the fluorine radical partial pressure is about 10% because of the inaccuracy of the argon pressure measurement, noise in the optical emission spectrum, dilution of the plasma by argon and plasma fluctuations. In particular, the inaccuracy of the argon pressure measurement dominates for pressures well below 1 Pa, because the argon pressure is only 5% of the total pressure and the resolution of the manometer is limited.

Actinometry of atomic oxygen is complicated by the dissociative excitation of the oxygen molecule given by formula 2.4.



After dissociation one of the atoms remains in an excited state, which is identical to the state that is occupied after direct electron impact excitation of an oxygen atom. The line intensity at 844.6 nm contains thus two contributions. However, in O<sub>2</sub> plasmas diluted with CF<sub>4</sub> and SF<sub>6</sub> the atomic oxygen concentration measured with LIF increases rapidly due to changes in the plasma chemistry. Moreover the cross-section of atomic excitation is an order of magnitude larger than of dissociative excitation [7]. So especially in diluted high density O<sub>2</sub> plasmas the main excitation path is atomic, so that oxygen actinometry remains valid. A proportionality constant of 0.47 has been derived from literature data [2]. It may be underestimated by 20% due to dissociative excitation. The experimental inaccuracy in the oxygen actinometry is larger than in the fluorine actinometry because the atomic oxygen peaks are much lower than the atomic fluorine peaks.

The particle density can be converted to a thermal flux  $\phi_x$  using equation 2.5a where  $k$  is the Boltzmann constant,  $T$  the plasma temperature and  $m_x$  the mass of the plasma species. It is assumed, that  $T$  is 400 K near the source region. However, in high-density Cl<sub>2</sub> plasmas temperatures above 1000 K have been measured because of plasma heating by hyper-thermal radicals produced in dissociation [8]. It is difficult to predict whether this mechanism plays an important role in SF<sub>6</sub> plasmas. In the cryogenic etching process the temperature gradient within the reactor is large due to the low substrate temperature. The heat transfer by thermal conduction to the substrate is comparable to the heat that is needed to cool down the gas flow to the substrate temperature. Therefore a temperature gradient develops through the reactor, so that  $T$  is nearly equal to the substrate temperature within a few mean free paths above the substrate. However, in low-pressure plasmas a temperature jump from the substrate to the plasma just above the substrate may occur, so that the plasma temperature is not well-defined by the continuum approximation. For example, if the mean free path is ten times smaller than the height of the reactor, the temperature jump can

amount to 15 % of the total temperature difference [9]. The particle density can be converted to a partial pressure with the ideal gas law given in equation 2.5b.

$$\varphi_X = n_X \cdot \sqrt{\frac{k \cdot T}{2 \cdot \pi \cdot m_X}} = p_X \cdot \sqrt{\frac{1}{2 \cdot \pi \cdot m_X \cdot k \cdot T}} \quad 2.5a$$

$$p_X = n_X \cdot k \cdot T \quad 2.5b$$

An ISA/Jobin Yvon-Sofie Digitwin 550 spectrometer system with a range from 200 nm to 900 nm was used for actinometry. It also includes integrated laser interferometry for *in situ* etch rate measurement. The emission spectrum of an SF<sub>6</sub>-O<sub>2</sub>-Ar ICP plasma showing both atomic and molecular peaks is given in figure 2.4a. The optical emission of molecules is complicated by the existence of vibrational and rotational states. During a transition between two electronic states, a change of the vibrational and rotational mode is also possible leading to a progression of peaks. The band at 255 nm is ascribed to the emission of SO molecules showing that chemical reactions do take place in the plasma [10]. A broad band extending from 280 nm to 460 nm due to S<sub>2</sub> and SF<sub>X</sub> fragments also visible is [11].

The sharp atomic lines of fluorine, oxygen and argon are clearly visible between 600 nm and 900 nm. The atomic lines of fluorine, oxygen and argon that have been used for actinometry are indicated by arrows in the high-resolution scan that is shown in figure 2.4b.

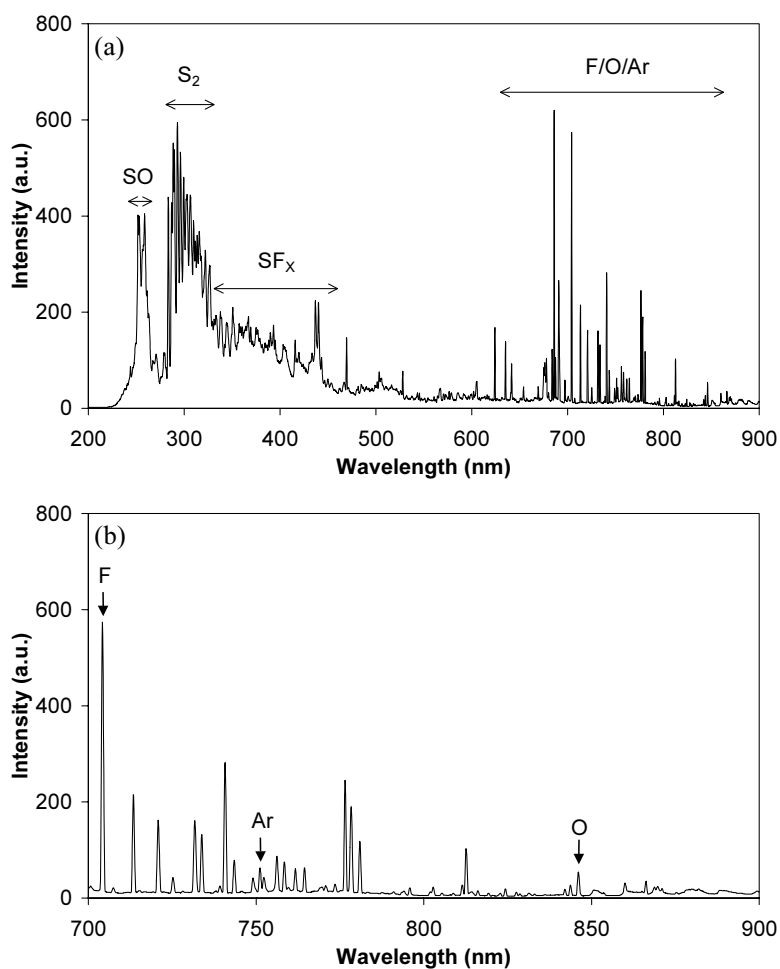


Figure 2.4 Optical emission spectrum of a  $\text{SF}_6\text{-O}_2\text{-Ar}$  ICP plasma. (a) Molecular bands and atomic peaks are clearly visible in the scan from 200 nm to 900 nm. (b) The atomic peaks that have been used for actinometry are indicated by arrows in the high-resolution spectrum.

### Chlorine molecule and radical actinometry

Actinometry of chlorine radicals is more complicated than of fluorine radicals, because the dissociative excitation of  $\text{Cl}_2$  forms an alternative excitation path just as for  $\text{O}_2$  [12]. In the optical emission spectrum of a  $\text{Cl}_2$  plasma both the  $\text{Cl}_2$  molecule peak at 306.0 nm and the Cl radical peak at 837.6 nm are visible. Techniques have been developed, that use the  $\text{Cl}_2$

molecule peak to correct the Cl radical peak for the dissociative excitation [13-15]. In this research the appropriate calibration parameters were not derived, but the Cl<sub>2</sub> molecule partial pressure and the uncorrected Cl radical partial pressure in arbitrary units were measured by actinometry using the Ar peak at 750.4 nm.

#### **Actinometry of CF and CF<sub>2</sub> radicals**

Actinometry has been performed to measure the density of CF and CF<sub>2</sub> radicals that play an important role in the passivation mechanism of the Bosch process [16]. The monitored lines are 202.4 nm and 251.9 nm for CF and CF<sub>2</sub> respectively and 750.4 nm for the actinometer gas Ar. However the proportionality constant has not been determined for these radicals. The OES spectrum of a C<sub>4</sub>F<sub>8</sub> plasma has been plotted in figure 2.5. The strong CF<sub>2</sub> band is clearly visible, but no CF peaks are observed probably due to the low transmittance of the optical fiber at these wavelengths. The optical fiber that guides the light from the reactor to the spectrometer is namely made of quartz. It has been reported that the CF<sub>2</sub> density is about one order of magnitude higher than the CF density [17-19]. The CF<sub>2</sub> partial pressure decreases for a higher source power, which indicates that CF<sub>2</sub> is an intermediate product [19]. Other strong peaks are attributed to C<sub>2</sub> and C<sub>3</sub> molecules which are formed on the reactor walls [20,21]. In this research the 262.9 nm CF<sub>2</sub> peak was chosen for CF<sub>2</sub> actinometry instead of the 251.9 nm CF<sub>2</sub> peak because of interference by the 251.6 nm emission of atomic Si [22]. No calibration of the proportionality constant is available, so that only a relative comparison is possible. Attempts were also made to measure the CF<sub>2</sub> radical density with UV light absorption, but no results were obtained because the radical density was below the detection limit in this research [23].

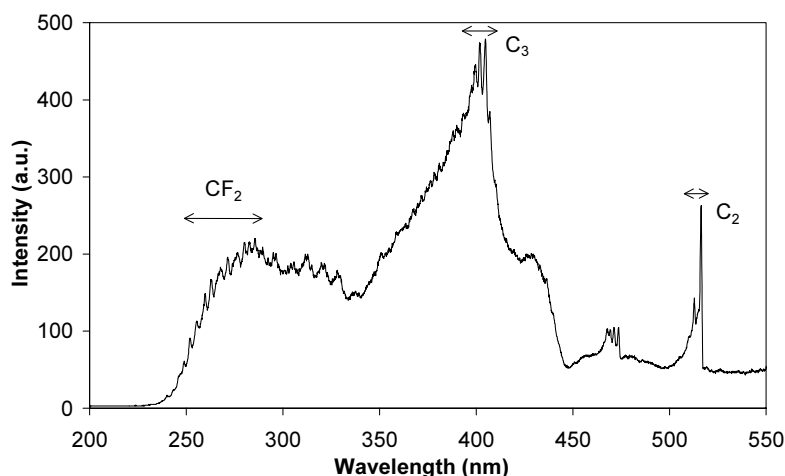


Figure 2.5 The optical emission spectrum of a  $C_4F_8$ -Ar ICP plasma. Strong bands of  $CF_2$ ,  $C_2$  and  $C_3$  radicals are visible.

### 2.2.2 Electrical characterisation with a Langmuir probe

Electrical methods, such as Langmuir probe measurement, retarding field ion energy analysis and mass spectrometry, can measure the charged particle densities. A Langmuir probe can give detailed local information about several electrical plasma parameters. A Scientific Systems Smart Probe system has been used in this research. Six parameters are measured, i.e., the floating potential  $V_f$ , plasma potential  $V_p$ , electron temperature  $T_e$ , electron density  $n_e$ , positive ion density  $n_i$  and the ion current density  $J_i$ . The plasma potential and ion current density are most important, because the ion energy and ion flux depend on these data. The scan-to-scan accuracy of these quantities is about 2%. Ion-neutral collisions in the plasma sheath can alter the ion energy and ion angle distribution. If the plasma sheath thickness is smaller than the mean free path, collisions do not play an important role. These two quantities can be calculated with the equations that are given in this subsection using some basic plasma properties.

#### Langmuir probe measurement of the electrical characteristics

The Langmuir probe basically consists of a cylindrical Pt-Ir tip with a length of 10 mm and a diameter of 0.50 mm, which is submersed in the plasma. The spatial distribution is obtained by moving the tip. A voltage is applied to the tip and the drawn current is measured. The parameters are calculated from different regions in the I-V characteristic, that is, the ion saturation, electron retardation and electron saturation region, which are depicted in figure 2.6. With a software routine the parameters are calculated from the

measured curve. At the floating potential the measured current is exactly zero, whereas the transition from electron retardation to electron saturation is found at the plasma potential. The electron retardation between the floating and plasma potential follows exponential behaviour and the electron temperature is derived from the exponential constant. The ion and electron saturation region are modelled with Laframboise theory and the thermal ion and electron current density at the plasma potential are calculated. The ion and electron density are calculated with the thermal current densities and the electron temperature [24].

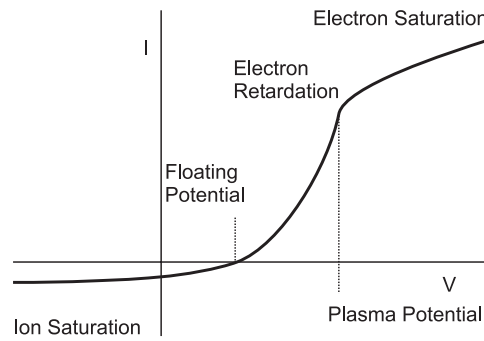


Figure 2.6 The typical form of an  $I$ - $V$  curve obtained with a Langmuir probe. The ion current and the electron current saturate for negative and positive probe potential respectively. The electron retardation region is found between the two saturation regions.

### Acceleration of positive ions in the plasma sheath

The extraction of positive ions from the plasma influences the charge distribution leading to an ambipolar diffusion field in the plasma presheath [25]. The voltage drop in this field (the Bohm criterion) is about  $\frac{1}{2}k \cdot T_e / e$  where  $e$  is the elementary charge, because up to this value electron density rearrangements are able to keep the plasma nearly charge neutral. The ion current density is determined by the acceleration of the ions in the plasma presheath and is calculated by the Bohm ion current density given by

$$J_i = e \cdot n_e \cdot \sqrt{\frac{k \cdot T_e}{e \cdot m_i}} \quad 2.6$$

where  $m_i$  is the ion mass and  $e$  the natural exponential base. Note that the ion current density is related to the electron density and temperature. Beyond the plasma presheath the electrons are retarded, so that the plasma sheath is formed by a positive space charge region is formed. The acceleration of positive ions in the plasma sheath can be described with the space charge limited Child-Langmuir ion current density given by

$$J_i = \frac{4 \cdot \sqrt{2}}{9} \cdot \sqrt{\frac{\varepsilon_0^2 \cdot e}{m_i}} \cdot \frac{(-V)^{\frac{3}{2}}}{d_s^2} \quad 2.7$$

where  $\varepsilon_0$  is the permittivity of vacuum,  $V$  the potential difference between the plasma and the substrate and  $d_s$  the plasma sheath thickness. Thus  $V = V_b - V_p$  where  $V_b$  is the bias voltage. The ion energy  $E_i$  is equal to  $-e \cdot V$ . The ion current density is constant throughout the plasma sheath. If the Bohm ion current density is substituted in the Child-Langmuir law, the plasma sheath thickness  $d_s$  can be calculated as a function of the potential difference. The plasma sheath thickness given in equation 2.8 is proportional to the Debye length  $\lambda_D$ .

$$d_s \cong \lambda_D \cdot \left( \frac{V_p - V_b}{k \cdot T_e} \right)^{\frac{3}{4}} \quad 2.8a$$

where

$$\lambda_D = \sqrt{\frac{\varepsilon_0 \cdot k \cdot T_e}{e^2 \cdot n_e}} \quad 2.8b$$

### Ion-neutral collisions

In theory it is assumed that the ion transport in the plasma sheath is collisionless. However, elastic, charge exchange and dissociative ion-neutral collisions play a role, if the mean free path  $\lambda_c$  is smaller than the plasma sheath thickness. The mean free path of particles in a gas can be calculated with equation 2.9 where  $\sigma_c$  is the collision cross-section and  $d_x$  the diameter of the particle.

$$\lambda_c = \frac{1}{\sigma_c \cdot n_x} \quad 2.9a$$

where

$$\sigma_c = \pi \cdot d_x^2 \quad 2.9b$$



The elastic collision cross-section can be calculated with reasonable accuracy using the Van der Waals radius for atoms and the chemical bonding length for molecules. The Van der Waals diameter and typical values of the elastic mean free path at 1 Pa are given in table 2.2 [26]. The elastic mean free path of an SF<sub>6</sub> molecule is 5.12 mm at 1 Pa, if the diameter along the F-S-F axis is used. However, in a HDP the SF<sub>6</sub> molecules are largely dissociated, so that the calculated elastic collision cross-section of SF<sub>6</sub> is an upper limit for elastic ion-neutral collisions. The elastic ion mean free path is thus underestimated. For ion-neutral collisions charge exchange and dissociation also play an important role [27,28]. These collision cross-sections are of the same order of magnitude and decrease the ion mean free path, but it is difficult to calculate the corresponding mean free paths due to the complexity of the SF<sub>6</sub> plasma. The calculated elastic ion mean free path is underestimated and therefore a part of the charge exchange and dissociative collisions have already been taken into account.

Table 2.2 The Van der Waals diameter and the elastic mean free path at 1 Pa for several plasma particles.

Particle	Diameter (nm)	Mean Free Path (mm)
F	0.270	24.1
S	0.370	12.8
Ar	0.384	11.9
SF	0.478	7.70
SF <sub>6</sub>	0.586	5.12

### Negative ions

It is important to measure the negative ion density, because negative ions can alter the etching process appreciably [29]. Negative ions are likely to exist in plasmas with electronegative particles such as fluorine and chlorine atoms. However, their contribution to the current is negligible compared to the electron current due to their large mass and low temperature leading to an asymmetric I-V characteristic. On the other hand a symmetric I-V curve is observed if the plasma only contains positive and negative ions. The I-V characteristics of a Langmuir probe measurement in the centre and at the edge of a SF<sub>6</sub> plasma are shown in figure 2.7a and 2.7b respectively. At the edge of the plasma the Langmuir probe is retracted in a flange with a diameter of 25 mm connecting the Langmuir probe system to the reactor chamber. A typical I-V curve is measured in the centre of the plasma, whereas a symmetric I-V curve is measured at the edge of the plasma. This indicates that negative ions exist, but the density of the negative ions in the centre of the plasma remains unclear. An explanation of the symmetric I-V curve is that the electrons

attach to the neutrals forming negative ions in the flange or that the electrons are repelled by the permanent magnet field at the edge of the plasma.

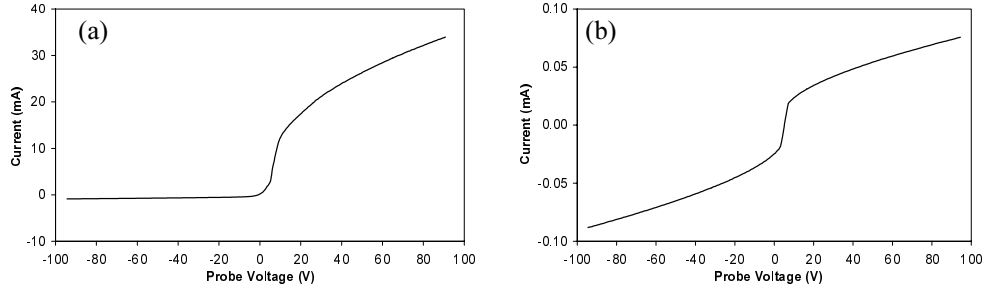


Figure 2.7 Langmuir probe measurement in a typical  $SF_6$  plasma. (a) Typical  $I$ - $V$  characteristic measured in the centre of the plasma. (b) Symmetric  $I$ - $V$  curve at the edge of the plasma.

### 2.3 Quantification of the plasma-material interactions

Eventually the plasma particles interact with the substrate, which in a favourable situation leads to etching. The main surface interactions in the etching mechanism are adsorption of radicals, chemical reaction and desorption of the reaction products. The ions influence the surface interactions and can enhance the rate, which can be modelled with the ion-neutral synergy formalism described in appendix A. Other surface interactions are also likely to occur, such as recombination of radicals and physical sputtering.

The etching mechanism can be quantified with dimensionless numbers such as the etch yield  $Y$  and the fluorine reaction probability  $S_F$  for the ion-induced and chemical plasma-material interactions respectively. These numbers are defined by equation 2.10. The quantities in this equation are the etch rate  $R_E$ , the ion flux  $\phi_i = J_i/e$ , the fluorine radical flux  $\phi_F$ , the substrate density  $\rho_S$ , the molar mass of the substrate atoms  $M_S$ , the stoichiometric ratio of the fluorine and substrate atoms in the reaction product  $r_F$  and the Avogadro number  $N_A$ .  $Y$  and  $S_F$  are related through the fluorine radical-to-ion flux ratio  $\phi_F/\phi_i$ .

$$Y = \frac{R_E \cdot \rho_S \cdot N_A}{\phi_i \cdot M_S} \quad 2.10a$$

$$S_F = \frac{r_F \cdot R_E \cdot \rho_S \cdot N_A}{\phi_F \cdot M_S} \quad 2.10b$$

For example, in spontaneous chemical silicon etching it is assumed that the reaction product is  $\text{SiF}_4$ , so that  $r_F$  is 4, because in literature it has been shown that  $\text{SiF}_4$  is the major reaction product below 300 °C [30]. However, above this temperature  $\text{SiF}_2$  is also an important reaction product. In that case the reaction probability decreases for a given fluorine flux and etch rate, because  $2 \leq r_F < 4$ . Besides, it has been shown that  $\text{Si}_2\text{F}_6$  and  $\text{Si}_3\text{F}_8$  are minor reaction products. Although much larger than  $\text{SiF}_4$ , these molecules are saturated with fluorine and slightly volatile reducing  $r_F$  [31].

## 2.4 Surface analysis and sample inspection

In order to get a good understanding of the surface interactions it is thus of utmost importance to know the particle fluxes towards the substrate. These fluxes can be measured with the techniques outlined in section 2.2. Knowledge of the particle fluxes alone is not enough, because often several mechanisms are still possible within these constraints, i.e., it is difficult to distinguish whether adsorption, reaction or desorption is the rate limiting step. Quantifying the chemical composition of the surface gives essential further information about the surface chemistry. Surface analysis techniques, which have been used in this research, are discussed in this section.

### 2.4.1 X-ray photoelectron spectroscopy

X-ray photoelectron spectroscopy (XPS) is a technique for quantitative analysis of the chemical composition of a substrate surface. The sample is irradiated with X-rays and emitted core electrons are detected. The characteristic photoelectron energy spectrum is a fingerprint of the elemental composition. The area under a peak of a certain element is proportional to its concentration and photoionisation cross-section. In a high-resolution mode the chemical bonding state can also be observed due to a small shift of the photoelectron energy. The probing depth defined by the inelastic mean free path of photoelectrons in a solid is only of the order of a nanometer, making XPS a true surface analysis technique. For example, an inelastic mean free path of 3.3 nm can be deduced for  $\text{Si}_{2p}$  photoelectrons in silicon dioxide.

The XPS analysis has been made with an angle resolved PHI 5400 system using unmonochromated Al or Mg  $K_\alpha$  radiation at 1486.6 eV or 1253.6 eV respectively. Samples were transferred in a hermetically sealed vessel under nitrogen atmosphere to avoid contamination by oxygen, water and hydrocarbons. Figure 2.8 shows the principle of a XPS measurement with the relevant angles for the X-rays and photoelectrons both for measurement on a plain silicon surface and on the sidewalls of a trench. A low take off angle assures a surface sensitive measurement, because the photoelectrons have to travel a longer distance through the upper atomic layers. For sidewall analysis the mask also contributes to the spectrum. Using a Cr mask this component is easily identified, so that the spectrum can be corrected by subtracting the known Cr spectrum.

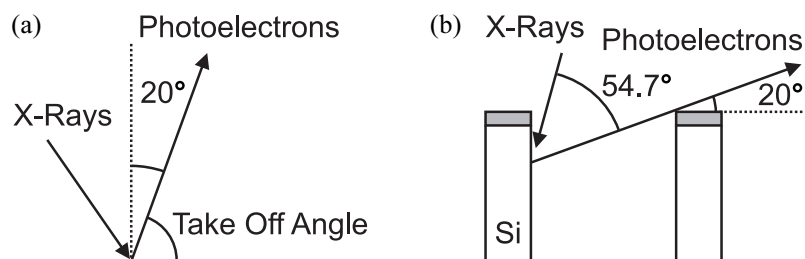


Figure 2.8 Overview of X-ray and photoelectron angles in XPS analysis of (a) the surface and (b) the sidewalls. The angle between X-rays and photoelectrons is fixed, but the take off angle can be adjusted. With sidewall analysis the electrons can escape from the trench only above a certain depth.

Figure 2.9 shows a low-resolution and a high-resolution XPS spectrum of silicon after etching in a  $\text{SF}_6\text{-O}_2$  plasma. Both the monocrystalline silicon peak at 99.5 eV and the chemically shifted peak at 104.0 eV are visible in the high resolution photoelectron spectrum. The chemical shift is due to oxidation and fluorination of silicon. Silicon dioxide is an important component of the silicon reaction layer, because silicon tetrafluoride is a volatile reaction product. The thickness of the silicon reaction layer can be deduced from the intensity ratio of the chemically shifted peak and the monocrystalline silicon peak. The area under each photoelectron peak is obtained by fitting with Gaussian curves after subtraction of the X-ray satellites and the Shirley background.

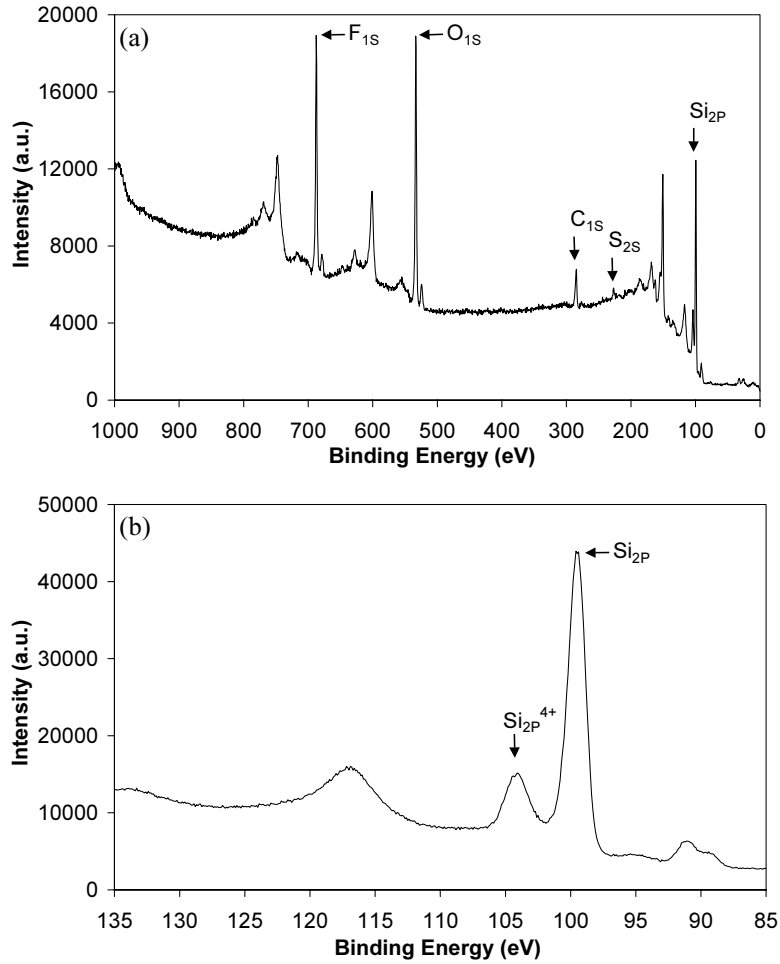


Figure 2.9 XPS spectra measured on a silicon sample after etching in a  $SF_6-O_2$  plasma. (a) Survey scan showing the different chemical components. (b) High resolution scan of the  $Si_{2p}$  peak also reveals the chemically shifted peak indicated by  $Si_{2p}^{4+}$  due to oxidation and fluorination of silicon.

In the following analysis it is assumed that the silicon reaction layer consists of silicon dioxide only, that the layer is uniform and that the intensity of the Si peak decreases exponentially as a function of thickness. The silicon dioxide layer thickness  $d_{SiO_2}$  is given by

$$\frac{d_{SiO_2}}{\lambda_e \cdot \cos \theta} = \ln \left( \frac{I_{SiO_2}}{I_{Si}} \cdot \frac{I_{Si}^\infty}{I_{SiO_2}^\infty} + 1 \right) \quad 2.11$$

where  $I_{\text{SiO}_2}$  is the intensity of the  $\text{SiO}_2$  peak,  $I_{\text{Si}}$  the intensity of the Si peak,  $I_{\text{Si}}^\infty$  the intensity of the Si peak on a clean substrate,  $I_{\text{SiO}_2}^\infty$  the intensity of the  $\text{SiO}_2$  peak of an infinitely thick silicon dioxide layer,  $\theta$  the angle between the surface normal and the direction of the detected photoelectrons and  $\lambda_e$  the inelastic mean free path of the photoelectrons in  $\text{SiO}_2$  [32]. A value of 0.67 has been taken from literature for the ratio of  $I_{\text{SiO}_2}^\infty$  and  $I_{\text{Si}}^\infty$  using the silicon atom density and the inelastic mean free path in both silicon dioxide and silicon. In this research the thickness is often in the submonolayer regime and should be interpreted as the effective thickness. It has been estimated that the sensitivity based on the noise level in the XPS spectra is about 0.1 ML, which corresponds to an effective layer thickness of 0.03 nm.

### 2.4.2 Ellipsometry

For the investigation of the reaction mechanism it is useful to measure the reaction layer thickness during processing. Contamination and evaporation of volatile reaction products are avoided. The thickness of thin dielectric layers on plane silicon substrates was measured with *in situ* ellipsometry. The Digisel system from Sofie Instruments was used with a 632.8 nm wavelength laser and a rotating compensator to eliminate background light. The angle of incidence was  $65^\circ$ . The resolution of the instrument is approximately 0.05 nm. For a thin transparent layer on top of a semi-infinite medium the analysis is straightforward if the optical constants are known. A complex refractive index of  $3.866 + 0.028i$  for silicon and a refractive index of 1.465 for silicon dioxide were used in the cryogenic etching process. In the Bosch process a refractive index of 1.355 was measured for the fluorocarbon layer that was deposited in a  $\text{C}_4\text{F}_8$  plasma.

The measurement of the reaction layer thickness during cryogenic etching is highly complicated because of surface roughness, which is easily formed. Surface roughness shows up as an increase of the measured layer thickness, which obscures the thickness of the thin reaction layer. Silicon oxidation in an  $\text{O}_2$  plasma and formation of an amorphous silicon layer in an Ar plasma have also been observed showing the potential of this technique. An example of plasma oxidation in an  $\text{O}_2$  plasma at  $-30^\circ\text{C}$  and  $-25\text{ V}$  is shown in figure 2.10. An oxide layer of approximately 4 nm is grown after 300 s. The layer is etched back in a  $\text{SF}_6$  plasma after 360 s. Severe roughness indicated by the large peak is observed at the moment, that the layer is almost etched through. At that moment some parts of the silicon are still covered with oxide while other parts that are exposed to the fluorine plasma etch very fast. In this case the ellipsometric signal decays to a steady value due to some residual roughness after 600 s. Plasma oxidation can be used for the dry release of micromechanical structures like in the SCREAM process.

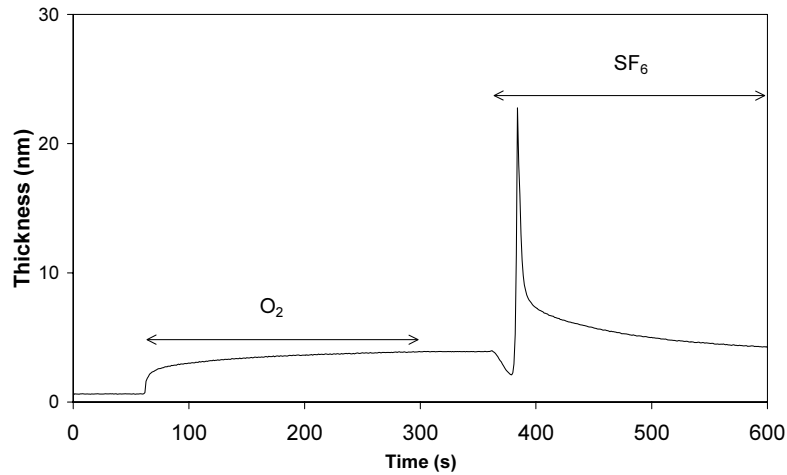


Figure 2.10 *In situ* ellipsometry on a plane silicon wafer. Plasma oxidation in an O<sub>2</sub> plasma followed by etching in a SF<sub>6</sub> plasma. In this case the measured thickness due to surface roughness is just as large as the oxide layer.

### 2.4.3 Transmission electron microscopy and atomic force microscopy

Incidentally transmission electron microscopy (TEM) and atomic force microscopy (AFM) have been used for further surface analysis. With TEM cross-sectional analysis the topography and crystal structure of a sample is observed. With AFM (Park Autoprobe M5) the surface topography of a plain surface is measured in order to investigate the surface roughness.

### 2.4.4 Sample inspection and profile analysis

Scanning electron microscopy (SEM) is normally used for sample inspection. For profile investigation the sample is cleaved along a crystal plane perpendicular to the surface to obtain the cross-section of the structure. Both a Hitachi S-900 and a Philips XL30S are available. For a quick measurement of the etch depth on wide structures also a surface profiler (Tencor Alpha-step 500) is available. Obviously an optical inspection microscope (Olympus DP10 with optional phase contrast and digital imaging) is used during sample preparation.

## 2.5 Sample preparation

### 2.5.1 Optical and electron beam lithography

Boron doped 20  $\Omega\cdot\text{cm}$  Si(100) wafers were used and line patterns were defined perpendicular to the wafer flat. Occasionally, other wafer and line pattern orientations were used. Both optical and electron beam lithography were used to fabricate samples for the etching experiments. Structures with lateral dimensions in the range from 0.4  $\mu\text{m}$  to 20  $\mu\text{m}$  were defined with electron beam lithography. Shipley S1813 photoresist with a thickness of 700nm was spin coated for optical lithography. A single layer 350k or 950k PMMA resist with a thickness in the range from 1000 nm to 1800 nm was employed for electron beam lithography. Also a double layer resist scheme was utilised. In this case a hard baked photoresist (1300 nm Shipley S1813 or 1560 nm HPR 504) was used as the first layer. The second layer consisted of 80 nm SNR M2, which is a silicon-containing negative electron beam resist. After exposure and development of the e-beam resist a low-pressure (0.4 Pa)  $\text{O}_2$  RIE plasma was used to transfer the pattern to the photoresist layer.

### 2.5.2 Pattern transfer

A silicon dioxide mask was used, because it does not introduce contamination in the reaction chamber, which could arise due the mask redeposition. Patterns were transferred to 220 nm thick thermal silicon dioxide layer by  $\text{CHF}_3\text{-O}_2$  RIE. Layers with a thickness of 1000 nm were etched with a continuous  $\text{C}_4\text{F}_8$  HDP and the 1800 nm thick PMMA resist. The  $\text{SiO}_2$  etch rate is 273  $\text{nm}\cdot\text{min}^{-1}$  for 33 sccm  $\text{C}_4\text{F}_8$ , 2000 W source power,  $-150$  V bias voltage and the highest ion flux, but the  $\text{SiO}_2$  etch rate is zero for  $\text{C}_4\text{F}_8$  plasma conditions that were used by the Bosch process.

Metal masks were used if higher etch selectivities were needed in the Bosch process. The silicon etching selectivity is a factor of 52 higher for Cr, because the  $\text{SiO}_2$  etch rate is 91  $\text{nm}\cdot\text{min}^{-1}$  and the Cr etch rate is 1.7  $\text{nm}\cdot\text{min}^{-1}$  for 150 sccm  $\text{SF}_6$ , 2000 W source power,  $-90$  V bias voltage and the highest ion flux. The single layer PMMA resist and the double layer SNR-photoresist scheme were used, because the patterns were transferred with metal evaporation and lift-off. In both cases the sample was exposed for 1 minute to a high-pressure (20.0 Pa)  $\text{O}_2$  RIE plasma prior to evaporation to clean the surface and to obtain a lateral etch which facilitates lift-off. Evaporation of a chromium layer with a nominal thickness of 250 nm was done by either resistive or electron gun heating. Chromium sticks well to the silicon surface. Lift-off was performed in either boiling acetone or in fuming nitric acid. If necessary some ultrasonic vibration assisted the release of metal. For silicon carbide etching a nickel mask with a thickness in the range from 200 to 500 nm was also used. In this case a 20 nm thick titanium layer was used to improve the sticking of nickel.



## References

- [1] The first glow discharge tube was made by M. Faraday in 1838.
- [2] J.P. Booth, O. Joubert, J. Pelletier and N. Sadeghi, *J. Appl. Phys.* **69**, 618 (1991)
- [3] J.W. Coburn and M. Chen, *J. Appl. Phys.* **51**, 3134 (1980)
- [4] V.M. Donnelly, D.L. Flamm, W.C. Dautremont-Smith and D.J. Werder, *J. Appl. Phys.* **55**, 242 (1984)
- [5] A. Manenschijn, PhD Thesis *Ion Bombardment and Ion-Assisted Etching in RF Discharges*, (Delft NL, 1991)
- [6] Y.H. Lee and M.M. Chen, *J. Appl. Phys.* **54**, 5966 (1983)
- [7] R.E. Walkup, K.L. Saenger and G.S. Selwyn, *J. Chem. Phys.* **84**, 2668 (1986)
- [8] V.M. Donnelly and M.V. Malyshev, *Appl. Phys. Lett.* **77**, 2467 (2000)
- [9] R. Dorsman and C.R. Kleijn, *Proceedings of the International Chemical Vapor Deposition XVI and EUROCVI 14 Conference*, 171 (Paris FR, 2003)
- [10] K. Miller and K. Becker, *Can. J. Phys.* **85**, 530 (1986)
- [11] K.E. Greenberg and P.J. Hargis, *Appl. Phys. Lett.* **54**, 1374 (1989)
- [12] A.D. Richards, B.E. Thompson, K.D. Allen and H.H. Sawin, *J. Appl. Phys.* **62**, 792 (1987)
- [13] V.M. Donnelly, *J. Vac. Sci. Technol. A* **14**, 1076 (1996)
- [14] M.V. Malyshev, V.M. Donnelly and S. Samukawa, *J. Appl. Phys.* **84**, 1222 (1998)
- [15] M.V. Malyshev and V.M. Donnelly, *J. Appl. Phys.* **88**, 6207 (2000)
- [16] L.D.B. Kiss, J.P. Nicolai, W.T. Conner and H.H. Sawin, *J. Appl. Phys.* **71**, 3186 (1992)
- [17] S. Samukawa, T. Mukai and K. Tsuda, *J. Vac. Sci. Technol. A* **17**, 2551 (1999)
- [18] H.H. Doh, J.H. Kim, K.W. Whang and S.H. Lee, *J. Vac. Sci. Technol. A* **14**, 1088 (1996)
- [19] K. Miyata, M. Hori and T. Goto, *J. Vac. Sci. Technol. A* **14**, 2343 (1996)
- [20] X. Duten, A. Rousseau, A. Gicquel and P. Leprince, *J. Appl. Phys.* **86**, 5299 (1999)
- [21] T. Takizawa, K. Sasaki and K. Kadota, *J. Appl. Phys.* **88**, 6201 (2000)
- [22] L.D.B. Kiss, J.P. Nicolai, W.T. Conner and H.H. Sawin, *J. Appl. Phys.* **71**, 3186 (1992)
- [23] B.A. Cruden, K.K. Gleason and H.H. Sawin, *J. Appl. Phys.* **89**, 915 (2001)
- [24] M.B. Hopkins and W.G. Graham, *Rev. Sci. Instrum.* **57**, 2210 (1986)

- 
- [25] J. Zheng, R.P. Brinkmann and J.P. McVittie, *J. Vac. Sci. Technol. A* **13**, 859 (1995)
  - [26] A.M. James and M.P. Lord, *Macmillan's Chemical and Physical Data* (The Macmillan Press Ltd., London UK, 1992)
  - [27] M.V.V.S. Rao, R.J. van Brunt and J.K. Olthoff, *Phys. Rev. E* **54**, 5642 (1996)
  - [28] B.L. Peko, R.L. Champion, M.V.V.S. Rao and J.K. Olthoff, *J. Appl. Phys.* **92**, 1657 (2002)
  - [29] H. Shindo, Y. Sawa and Y. Horiike, *Jap. J. Appl. Phys.* **34**, L925 (1995)
  - [30] H.F. Winters and J.W. Coburn, *Surface Science Reports* **14**, 161 (1992)
  - [31] C.B. Mullins and J.W. Coburn, *J. Appl. Phys.* **76**, 7562 (1994)
  - [32] L.P.H. Jeurgens, PhD Thesis *On the Initial Oxidation of Aluminium in Oxygen Gas*, 63 (Delft NL, 2001)

---

## Chapter 3

# Anisotropic silicon etching with oxide sidewall passivation at low temperatures

The cryogenic etching process is extensively used for the fabrication of deep anisotropic silicon microstructures. The etching mechanism is based on the spontaneous chemical reaction of fluorine radicals. Anisotropy is obtained by the passivation by oxygen radicals and the depassivation by ions. However, many aspects of the etching mechanism that determine the profile evolution and the etch rate are still unresolved. In particular, the passivation and depassivation mechanism and the transport of radicals in narrow structures are relatively underexposed. In this chapter the complex interplay of the fluorine radicals, the oxygen radicals and the ions is unravelled in more detail. Both the ECR reactor and the ICP reactor have been used in the etching experiments. In the ECR reactor the ion-to-radical flux ratio can be reduced to an extremely low value. In the ICP reactor the radical and ion densities are at least one order of magnitude higher.

In section 3.1 the effectiveness of oxygen for sidewall passivation at low temperatures is discussed. Moreover, it is shown that the addition of oxygen to the plasma can lead to crystal orientation dependent etching. Section 3.2 describes the etching mechanism, which is investigated with an extremely low ion-to-radical flux ratio in the ECR reactor. The etching is strongly determined by the impact of the ions, so that the passivation and depassivation mechanism can be investigated in detail. Controllable switching between ion-limited and fluorine-limited etching is possible by variation of the plasma conditions. The observations are supported by the investigation of the reaction layer by surface analysis such as XPS. In section 3.3 the influence of the radical transport on the etching of high aspect ratio trenches is treated. The surface kinetics strongly influences the radical transport through the reaction probability. In a fluorine-limited regime the fluorine flux is strongly reduced leading to aspect ratio *dependent* etching (ARDE). On the other hand, in an ion-limited regime the etching mechanism leads aspect ratio *independent* etching (ARIE). Section 3.4 deals with the essential role of the oxygen radicals in the etching mechanism, which is investigated by a Monte Carlo simulation model. The etching of deep anisotropic trenches is accurately simulated.

### 3.1 Oxygen as an etch inhibitor

In high-density fluorine-based plasmas the lateral etch component cannot be suppressed by lowering the temperature alone. The addition of oxygen is necessary for sidewall passivation [1]. The oxygen passivation is removed by the ion bombardment, so that

etching proceeds in the direction of the ion flux and anisotropic profiles are obtained. The combined effect of a low temperature and oxygen addition leads to a highly effective sidewall passivation while high etch rate and a high selectivity are possible [2]. In this section the influence of oxygen on the passivation mechanism and the trench profile is discussed. The etch rate is investigated as a function of  $O_2$  flow and temperature. Besides, it is shown that the passivation mechanism depends on the crystal orientation.

### 3.1.1 Suppression of the spontaneous etching of silicon by oxygen

In this subsection the etch rate investigation of p-type Si(100) and Si(111) in the ECR reactor with an  $SF_6-O_2$  plasma are presented. The plasma conditions were the Cryo 1 process conditions given in appendix B and the variables were the substrate temperature and the oxygen flow. Figure 3.1 shows the etch rate as a function of temperature for both 1.1 sccm and 3.3 sccm  $O_2$  added to the plasma. The samples were etched shortly after each other, so that fluctuations of the plasma conditions were negligible. The inaccuracy of the etch rate is determined by the depth measurement with the surface profiler and is small on this scale. The etch rate decreases quickly below a temperature of  $-80$  °C for both Si(100) and Si(111). Besides, the suppression of the etch rate is stronger for a higher oxygen flow. The etch rate is thus mainly reduced due to the interaction of oxygen with the substrate and not due to the decrease of the reactivity of fluorine.

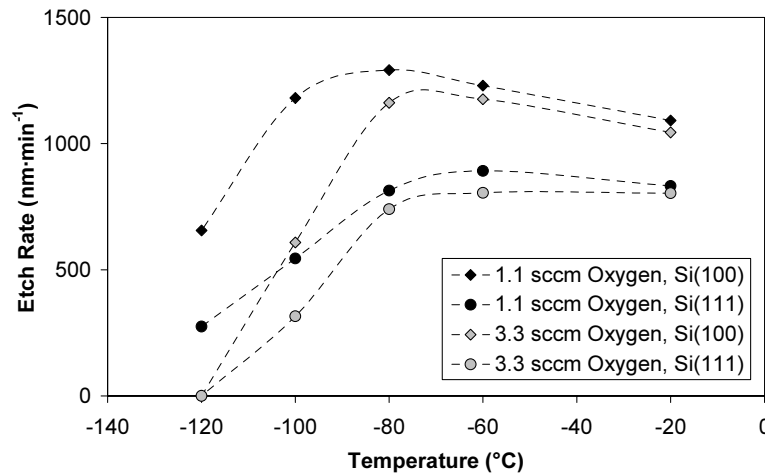


Figure 3.1 The etch rate in the ECR reactor as a function of temperature. Results are given for two different oxygen flows both for Si(100) and Si(111) samples.

The results also show that Si(100) and Si(111) react differently. The ratio of the Si(100) and Si(111) etch rate approached a value of 1.26 at room temperature and increased quickly for

a decreasing temperature due to the more effective oxidation of Si(111) [3]. This is consistent with literature on thermal oxidation showing that the oxidation rate is often higher for Si(111) [4]. Patterns consisting of 6  $\mu\text{m}$  wide lines on a 12  $\mu\text{m}$  pitch that were etched as function of temperature with the Cryo 2 process conditions are shown in figure 3.2. Crystal orientation dependent etching results in the formation of facets near the footprint of structures on Si(100) wafers, because the etch front tends to be limited by the Si(111) crystal planes. The most pronounced crystallographic facets are obtained for  $-95\text{ }^\circ\text{C}$  where the etch rate ratio is the largest. For the  $-65\text{ }^\circ\text{C}$  the sidewall passivation is weak, but the main etching direction is still perpendicular to the substrate.

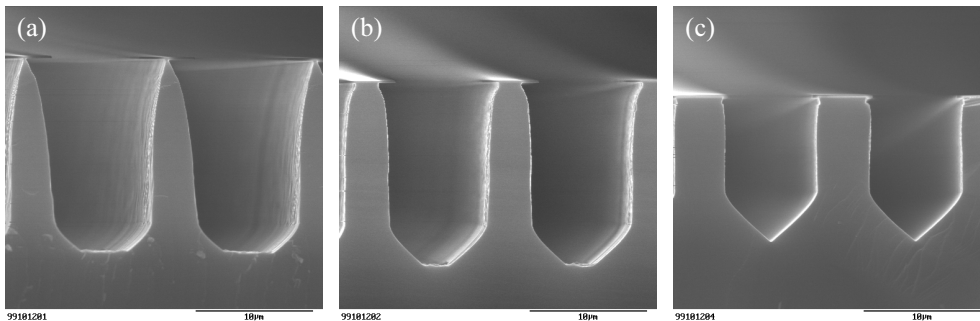


Figure 3.2 The formation of crystallographic facets. The profiles were etched at a substrate temperature of (a)  $-65\text{ }^\circ\text{C}$ , (b)  $-80\text{ }^\circ\text{C}$  and (c)  $-95\text{ }^\circ\text{C}$ .

Successive fluorination is a likely mechanism for the reaction of fluorine radicals with silicon. The results of McFeely show, that the initial reaction step consists of a quick adsorption of a monolayer of fluorine forming SiF. Subsequent adsorption of fluorine involves the breaking of bulk silicon bonds and reconstruction of the surface. The forming of SiF<sub>2</sub> and SiF<sub>3</sub> is thus characterised by a higher activation energy [5]. For prolonged etching the reaction of SiF<sub>3</sub> to volatile SiF<sub>4</sub> becomes rate limiting presumably because the reactivity of SiF<sub>3</sub> is the lowest. As a result SiF<sub>3</sub> accumulates on the surface [6]. It has also been argued that disproportionation reactions play a role in the forming of SiF<sub>4</sub>, for example  $\text{SiF}_3 + \text{SiF}_3 \rightarrow \text{SiF}_2 + \text{SiF}_4$  [7].

Especially, the initial fluorination steps in this chain of reactions are crystal orientation dependent. The difference of the Si(100) and Si(111) etch rates can be explained by the different structure of the crystal planes. All atoms in Si(100) planes have two dangling bonds, but atoms in Si(111) planes only have one dangling bond. The etch rate for Si(100) is slightly higher because no chemical bonds have to be broken for the forming of SiF<sub>2</sub> and steric hindrance is less due to the factor of 1.15 lower surface density.

### 3.1.2 Oxygen sidewall passivation

In the previous subsection it is shown that the silicon etch rate is suppressed at low temperatures by the interaction of oxygen radicals with silicon. In HDP etching the ions are accelerated perpendicular to the substrate. As a result the ion flux to the sidewalls is much smaller than the ion flux to the substrate. The suppression of the lateral etch rate is thus much stronger than the suppression of the etch rate perpendicular to the substrate. For anisotropic etching a certain amount of oxygen is necessary for the complete suppression of the lateral etch rate. A few tenths of an sccm  $O_2$  already influenced the profile substantially and the optimal anisotropy was found by tuning the  $O_2$  flow. Profiles etched with the Cryo 3 process conditions are shown for increasing oxygen flow in figure 3.3. A low oxygen flow leads to a lateral etch and a high oxygen flow leads to a positive sidewall taper.

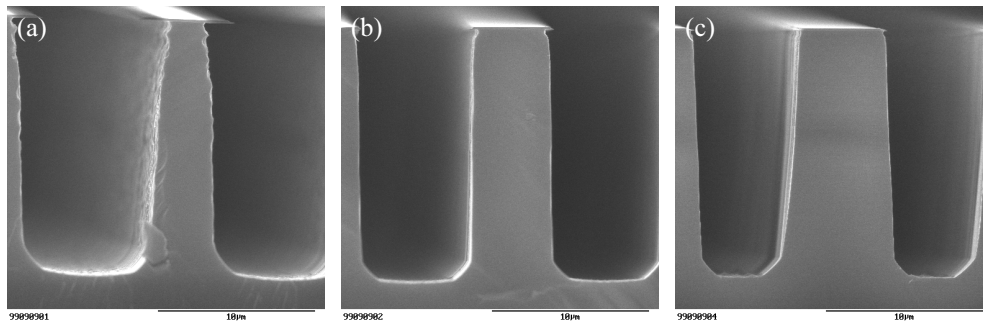


Figure 3.3 Profiles for an increasing oxygen flux. The oxygen flux is (a) 1.6 sccm, (b) 2.4 sccm and (c) 3.2 sccm. If the oxygen flux is too low it leads to a lateral etch and if it is too high the profile becomes positively tapered.

### 3.1.3 Crystal orientation dependent etching

Crystal orientation dependent etching as a result of the passivation behaviour is responsible for the facets of the bottom of the trench. To demonstrate the crystallographic origin of the facets the effect of the pattern orientation and the wafer orientation on the profile were investigated.

#### Pattern orientation

During lithography the 6  $\mu\text{m}$  wide lines on a 12  $\mu\text{m}$  pitch were aligned under an angle of  $45^\circ$  with the flat of a Si(100) wafer. This was in contrast to standard samples where the lines were perpendicular to the flat. The pattern and the crystal plane orientations are shown in figure 3.4.

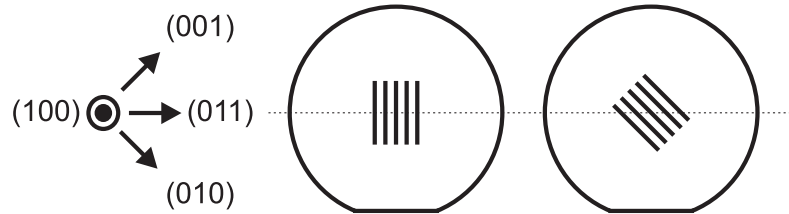


Figure 3.4 The pattern and crystal plane orientations on Si(100). The samples are cut along the dashed line.

The patterns were etched simultaneously with the Cryo 4 process conditions. The profile cross-sections for the two different pattern orientations are shown in figure 3.5. Crystal facets are observed for trenches perpendicular to the flat because there is a (111) crystal plane in the profile cross-section limiting the etch rate. For the 45° rotated pattern the interpretation of the SEM picture is more complicated because the silicon lines are viewed under an angle of 45° sideways. The silicon ridges slope backward due to a slanting cut. It seems that the sidewalls are inclined, but the sidewalls are perfectly perpendicular to the flat bottom of the trench. No crystal facets are observed for the 45° rotated trenches because there is no (111) crystal plane in the profile cross-section but a (101) crystal plane.

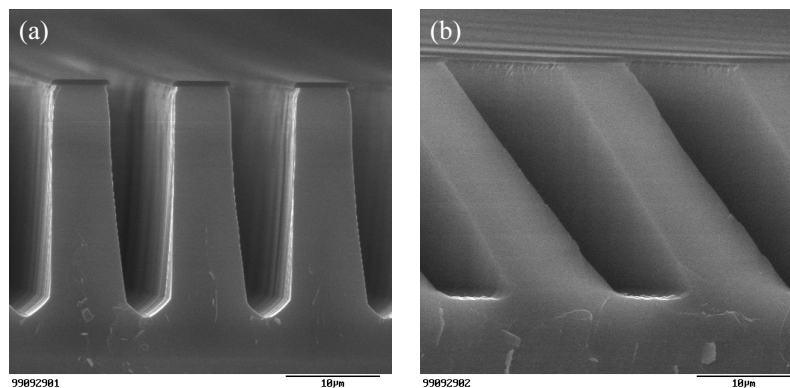


Figure 3.5 Trenches that are obtained for two different pattern orientations. (a) Perpendicular to the flat. (b) Under an angle of 45° with the flat. Due to a slanting cut the silicon ridges slope backward. No crystal facets are observed.

### Wafer orientation

Trenches were etched simultaneously in Si(100) and Si(111) to investigate the impact of the wafer orientation on the profile. The profiles that were obtained in the ICP reactor with the Cryo 12 process conditions are shown in figure 3.6. On Si(100) the formation of

crystallographic facets is clearly visible. On Si(111) the bottom of the trench is only slightly rounded and the etch rate is lower. These effects show once more that the etching of the Si(111) crystal planes is slower. Besides, the sidewall taper changes from positive to negative because the sidewalls on Si(100) consist of Si(111), but the sidewalls on Si(111) consist of Si(1 $\bar{1}$ 0) with the inherent weaker passivation.

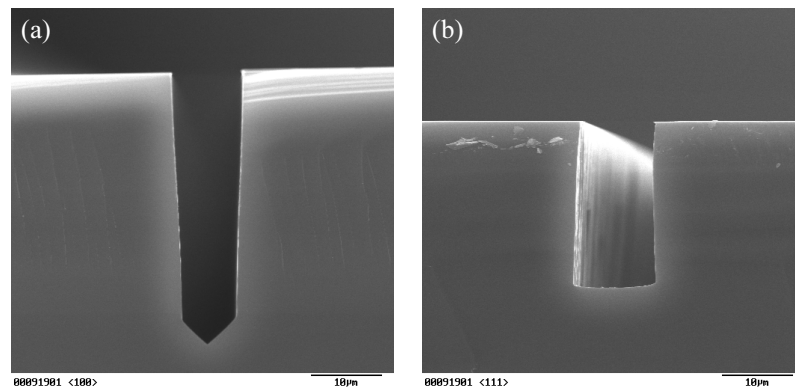


Figure 3.6 ICP etching of Si(100) and Si(111). (a) The crystallographic facets are clearly visible on Si(100). (b) No facets are visible on Si(111).

### 3.2 Etching with an extremely low ion-to-radical flux ratio

Etching experiments have been performed in the ECR reactor to investigate the surface kinetics of the cryo-process. Due to an extremely low ion-to-radical flux ratio it is possible to tune the process from a surface kinetics controlled regime to an ion-dominated regime. In the surface kinetics controlled regime the passivation by oxygen radicals plays a major role because the ion bombardment is weak. The reaction of the fluorine radicals with silicon is rate limiting. Crystal facets are formed at the bottom of the trench due to the stronger passivation of Si(111) compared to Si(100). In the ion-dominated regime the silicon surface is exposed to a strong ion bombardment, so that the passivation by oxygen radicals plays a minor role. The transport of fluorine radicals is rate limiting and the profiles are fully anisotropic. In other words the etching is ion-limited in the surface kinetics controlled regime and fluorine-limited in the ion-dominated regime. The complex interplay between fluorine radicals, oxygen radicals and ions is investigated by changing the relative magnitude of these species with the flow, pressure, source power, bias voltage and substrate temperature. The influence on the etch rate and the trench profile is described. The experimental results reveal details of the passivation and de-passivation mechanism, which are confirmed by surface analysis.



### 3.2.1 The effects of flow and pressure on the etching mechanism

The effects of the flow and the pressure on the etch rate and profile evolution are discussed. The pumping speed at the wafer was constant, so that the pressure was proportional to the injected flow. The etch rate measured by *in situ* laser interferometry and the fluorine radical partial pressure are plotted in figure 3.7. The plasma conditions were the Cryo 5 process conditions given in appendix B. The SF<sub>6</sub> flow was increased from 10.0 sccm to 40.0 sccm in 10.0 sccm steps and the pressure was increased from 0.10 Pa to 0.40 Pa in 0.10 Pa steps. The oxygen flow was proportional to the SF<sub>6</sub> flow. The fluorine radical partial pressure continues to increase up to the largest flow, but in spite of this there is a severe drop of the etch rate for the highest flow/pressure.

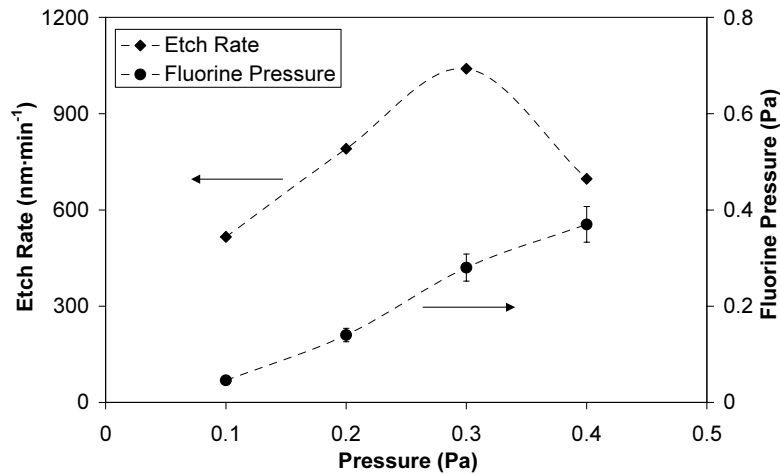
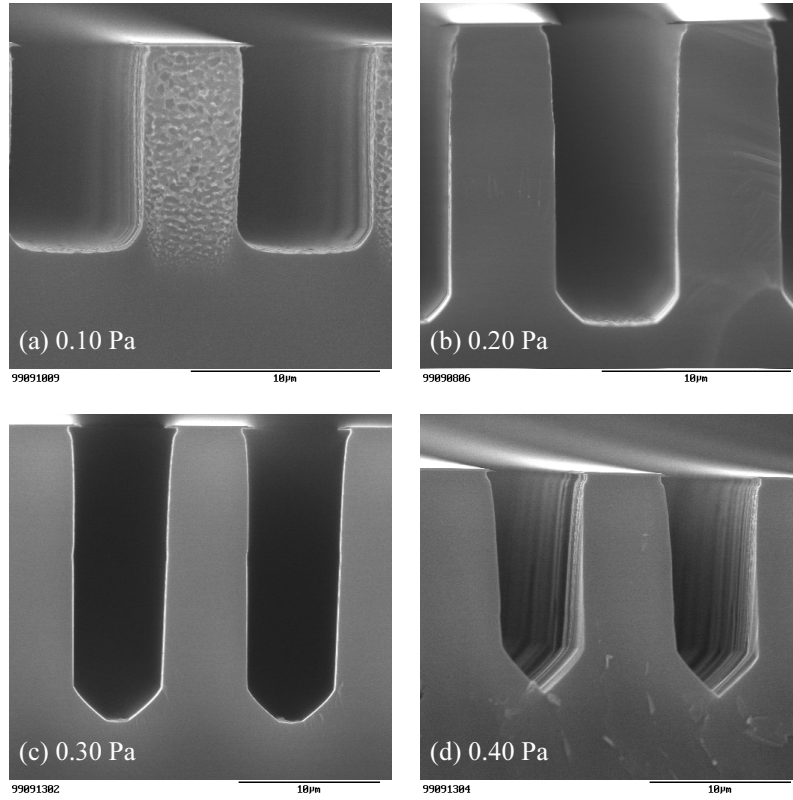


Figure 3.7 The silicon etch rate and the fluorine radical partial pressure as a function of pressure. The pressure increase is due to the flow increase.

The profiles for the four different plasma conditions are shown in figure 3.8. The transition from purely anisotropic to crystal orientation dependent etching is clearly visible. The trenches show pronounced facets for the highest flow/pressure.



*Figure 3.8 Trenches etched with an increasing flow/pressure. The trench profiles are given for a pressure of (a) 0.10 Pa, (b) 0.20 Pa, (c) 0.30 Pa and (d) 0.40 Pa.*

The role of the ions in the transition between the two regimes is investigated. The plasma sheath thickness and the ion mean free path and the fluorine radical-to-ion flux ratio were calculated and are given in table 3.1.

Table 3.1 The sheath thickness, the mean free path and the fluorine radical-to-ion flux ratio for a simultaneous increase of the SF<sub>6</sub> flow and the pressure.

Flow (sccm)	Pressure (Pa)	Sheath Thickness (mm)	Mean Free Path (mm)	Radical To Ion Flux Ratio
10.0	0.10	15	51	6.4·10 <sup>3</sup>
20.0	0.20	10	26	8.8·10 <sup>3</sup>
30.0	0.30	12	17	21·10 <sup>3</sup>
40.0	0.40	11	13	24·10 <sup>3</sup>

The plasma sheath thickness is nearly independent of pressure because the ion flux changes only slightly, but the ion mean free path is inversely proportional to pressure. Below 0.20 Pa the plasma sheath thickness is more than a factor of 2 smaller than the ion mean free path and ion-neutral collisions are not probable. However, for 0.40 Pa the mean free path is almost equal to the sheath thickness, so that ion-neutral collisions occur frequently. The ion bombardment is weaker due to loss of energy and directionality. As a result the surface passivation is less effectively removed and the etching is controlled by the surface kinetics. Moreover, the measured fluorine and oxygen radical-to-ion flux ratio increases with pressure, which is also favourable for surface kinetics controlled etching.

#### Pressure increase by throttling of the gas flow

The pressure also increases by throttling the gas flow instead of increasing the gas flow, but this can lead to different ion and radical densities. Trenches were etched with the Cryo 6 process conditions to investigate the influence of a pressure increase with a fixed gas flow. The pressure was increased from 0.20 Pa to 0.40 Pa with a fixed SF<sub>6</sub> flow of 20.0 sccm. The trench profiles are shown in figure 3.9. At 0.40 Pa the formation of the facets is more pronounced than at 0.20 Pa. The trench profiles are almost similar to the trench profiles shown in 3.8, which were obtained for a simultaneous increase of gas flow and pressure. Apparently, throttling of the gas flow does not influence the ion and radical densities noticeably for a given pressure. A controllable transition between purely anisotropic etching and crystal orientation dependent etching is thus possible with pressure.

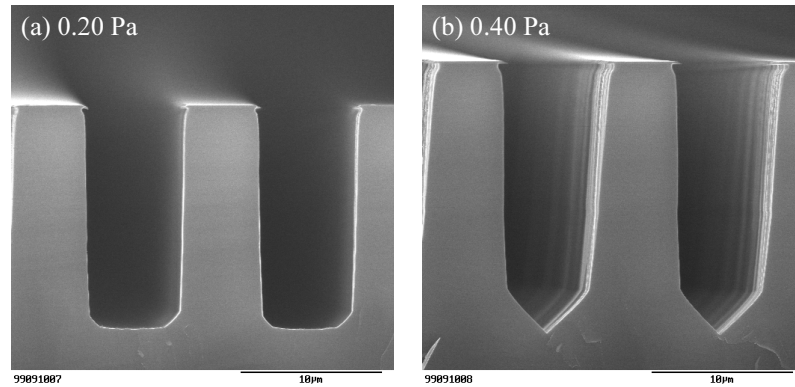


Figure 3.9 Trenches etched with an increasing pressure due to throttling of the gas flow. The trench profiles are given for a pressure of (a) 0.20 Pa and (b) 0.40 Pa. The transition from purely anisotropic to crystal orientation dependent etching is clearly visible.

### 3.2.2 Etching with an extremely high etch yield as a function of bias voltage

The passivation and depassivation mechanism of the cryo-process is based on the interactions of the fluorine radicals, the oxygen radicals and the ions with the silicon surface. The exact nature of the interactions is largely unknown. A better understanding can be obtained by a quantitative comparison of the etch rate and the plasma species fluxes. Etching experiments were performed as a function of bias voltage to investigate the role of the ions. The etch rate for the Cryo 7 process conditions is plotted as a function of the ion energy in figure 3.10. The ion energy is equal to the plasma potential minus the bias voltage. The plasma potential was approximately +15 V and independent on the bias voltage. For 0 V and -2 V the etching resulted in severe roughness (silicon grass), however the etch rate could be measured by the *in situ* laser interferometry before the roughness started to play a role. The corresponding trench profiles are shown in figure 3.11. The crystal orientation dependent etching is observed for a reduced ion energy because the surface passivation plays a major role if the ions energy is reduced, which is in accordance with the variable pressure measurements. The sidewall taper is more negative for higher ion energies due to the increased sidewall erosion.

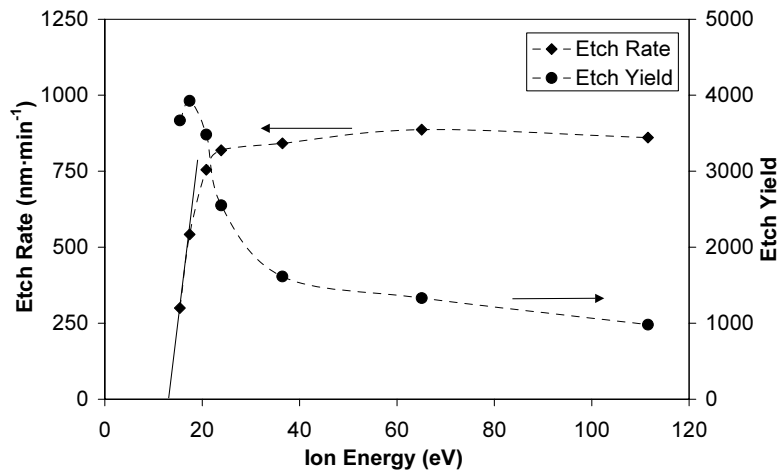


Figure 3.10 The etch rate and the etch yield as a function of the ion energy. The dashed line extrapolates the etch rate and crosses the ion energy axis at 13 eV. The sputter energy threshold of depassivation is thus approximately 13 eV.

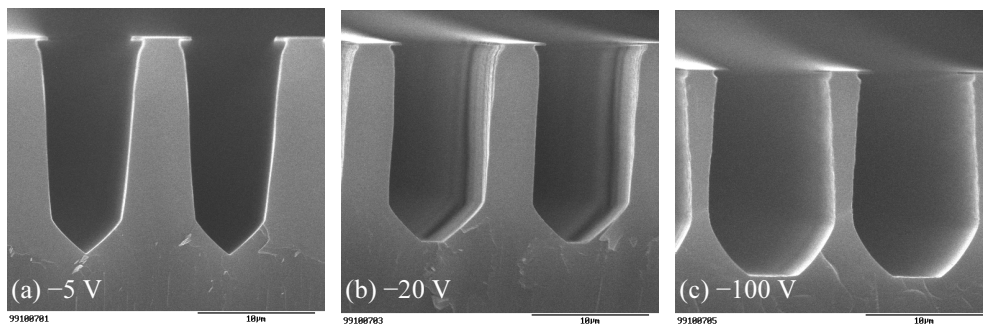


Figure 3.11 Trenches etched with an increasing bias voltage. The trench profiles are given for a bias voltage of (a) -5 V, (b) -20 V and (c) -100 V. The crystal facets and the sidewall taper are strongly influenced by the ion energy.

Notwithstanding the consistent result a further critical evaluation has been pursued. Due to the downstream geometry of the ECR system the plasma is a radical gas with a low ion density. The bias power can therefore easily ionise the gas additionally, so that the measured ion density increases with the bias voltage. It is assumed that the ion density gradient between the probe tip and the substrate surface is negligible because the distance is only about 2 cm, which is comparable to the mean free path. The etch yield is calculated to correct the etch rate for the increasing ion flux and is also plotted in figure 3.10. Three

observations can be made. First, the etch yield in the order of  $10^3$  is extremely large compared to the etch yield for common RIE processes, which is two orders of magnitude smaller [8]. Second, the etch yield decreases quickly for higher ion energies while the etch rate goes up, which illustrates the transition from ion-limited etching for lower ion energies to fluorine-limited etching for higher ion energies. Third, a sputter energy threshold of depassivation of approximately 13 eV is obtained by extrapolating the etch rate data to zero.

The plasma sheath thickness, the ion mean free path and the fluorine radical-to-ion flux ratio are presented for different the bias voltages in table 3.2. The large and decreasing fluorine radical-to-ion flux ratio is consistent with the first and second observation. The plasma sheath thickness shows a remarkable minimum because the plasma sheath thickness increases with both increasing bias voltage and decreasing ion flux. Both for the lowest and highest bias voltage the plasma sheath thickness is larger than the ion mean free path, so that ion-neutral collisions play a role and the ion energy is reduced by ion-neutral collisions. For the highest energy this has a negligible influence on the etch rate and etch yield, but it is important for the lowest ion energy and could lead to an overestimation of the sputter energy threshold that is obtained with the third observation.

*Table 3.2 The plasma sheath thickness, the ion mean free path and the fluorine radical-to-ion flux ratio for different bias voltages.*

Bias Voltage (V)	Pressure (Pa)	Sheath Thickness (mm)	Mean Free Path (mm)	Radical To Ion Flux Ratio
2	0.30	18	17	$76 \cdot 10^3$
5	0.30	13	17	$47 \cdot 10^3$
10	0.30	12	17	$33 \cdot 10^3$
20	0.30	11	17	$23 \cdot 10^3$
50	0.30	14	17	$17 \cdot 10^3$
100	0.30	18	17	$12 \cdot 10^3$

The ion energy available per removed silicon atom is about 20 meV at a bias voltage of  $-20$  V taking into account the extremely high etch yield. This energy is too small to break chemical bonds, but it is enough to stimulate thermal processes. In this view, a nanometres thick layer of loosely bound reaction products only needs to overcome a small energy barrier. However, the transfer of the ion energy to thousands of molecules is physically impossible. In the next subsection surface analysis is used to investigate the reaction layer in more detail. Anticipating these results it is more realistic to suppose that the ions only need to remove the oxygen passivation. The fluorine radicals are able to react with silicon depending on the oxygen coverage. The measured fluorine-to-oxygen flux ratio is constant with a value of 230. Approximately, the ions have to remove a factor of 230 less surface

species with the supposition that only oxidised species have to be sputtered. It results in a sputter yield of oxidised species in the order of 10, which is much more realistic.

The interaction between the ions and the oxygen passivation depends strongly on the ion flux. It may seem contradictory that the etch yield decreases if the ion flux increases. However, the ions are only necessary to remove the passivation layer and do not assist surface reactions or desorption of other reaction products. For a low ion flux the surface is totally covered with oxidised species and the fluorine reaction probability is low. The etch yield is high because the sputtering of the passivation layer is effective. For a high ion flux the passivation layer thickness is nearly zero and the fluorine reaction probability has reached its maximum. The etch yield decreases with ion flux because the ion flux does not influence the etch rate appreciably.

The etch yield is plotted as a function of the ion current density in figure 3.12. An etch yield model is deduced from the chemically enhanced ion-neutral synergy model derived in appendix A to fit the data. The etch yield model is given by

$$Y = \frac{\left( \frac{\kappa_F \cdot \varphi_F}{4 \cdot \kappa_O \cdot \varphi_O} \right) \cdot \gamma_O}{1 + \frac{\gamma_O \cdot \varphi_i}{\kappa_O \cdot \varphi_O}} \quad 3.1$$

where  $Y$  is the etch yield,  $\varphi_F$  the fluorine radical flux,  $\varphi_O$  the oxygen radical flux,  $\varphi_i$  the ion flux,  $\kappa_F$  the adsorption probability of fluorine,  $\kappa_O$  the adsorption probability of oxygen and  $\gamma_O$  the ion-induced desorption coefficient of oxygen. The ion-induced desorption coefficient of oxygen follows the square root dependence given by

$$\gamma_O = \alpha_O \cdot (\sqrt{E_i} - \sqrt{E_T}) \quad 3.2$$

where  $\alpha_O$  is the square root of energy normalised ion-induced desorption coefficient of oxygen,  $E_i$  the ion energy and  $E_T$  the sputter energy threshold. The sputter energy threshold is set to 13 eV, so that the two fit parameters are  $\kappa_F \cdot \varphi_F \cdot \alpha_O / \kappa_O \cdot \varphi_O$  and  $\alpha_O / \kappa_O \cdot \varphi_O$ .

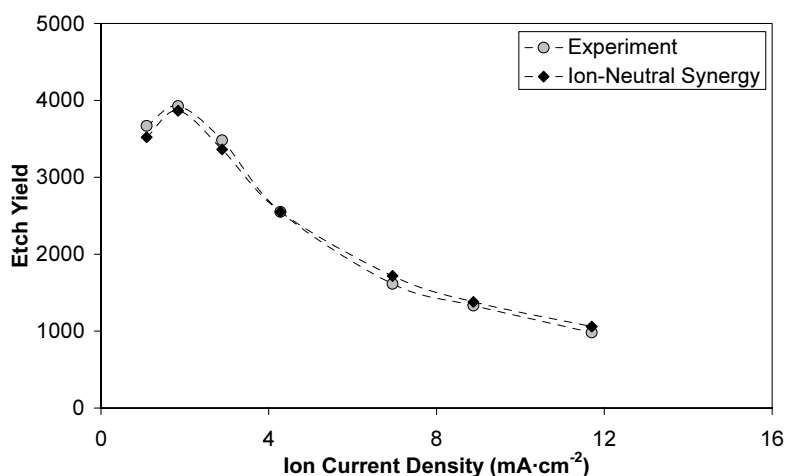


Figure 3.12 The etch yield as a function of the ion current density. It is fitted by the chemically enhanced ion-neutral synergy model.

The model fits the data very well. The points obtained for bias voltages higher than  $-5$  V are approximately inversely proportional to the ion flux. The points at  $0$  V and  $-2$  V deviate from this relation because the ion energy approaches the sputter energy threshold for the oxidised species. The fit parameters can be used to calculate  $\gamma_0$  because the other quantities are either measured or obtained from literature. The sputter yield of oxidised species is a factor of 4 smaller than  $\gamma_0$ . A sputter yield of oxidised species of 340 is obtained for a bias voltage of  $-20$  V. This is more reasonable than a number in the order of  $10^3$ , but it is still quite large. Presumably, there are separate paths along which oxidised species can escape from the surface.

### 3.2.3 Further discussion: surface analysis

Surface processes play a major role in the etching mechanism. In the previous subsection it has been argued that the reaction layer mainly consists of oxidised species and that sputtering of this reaction layer reduces the thickness. However, the composition of the reaction layer is still hypothetical. The actual surface coverage needs to be known before a more definite conclusion about the passivation and depassivation mechanism can be drawn. With surface analysis it is possible to reveal the reaction products that are present on the surface, so that the rate limiting reaction step can be identified.

### XPS

Analysis of the silicon surface after etching by XPS gives an image of the composition of the reaction layer. The peaks of the elements C, O, F, Si, and S are observed in the



photoelectron energy spectrum. The surface densities of these elements are measured, and besides, the effective reaction layer thickness is determined with the method outlined in chapter 2. Physisorbed contamination that may be collected during sample transfer does not influence the result because only chemically bound atoms are used in this method. The XPS measurements are made after all reactions have ceased, so that primarily the rate limiting reaction products are observed. This effect is enhanced by the unavoidable evaporation of volatile reaction products during heating of the sample from cryogenic temperatures to room temperature for analysis. The density of the silicon oxides is increased compared to the silicon fluorides. The competition between oxygen and fluorine in the formation of a reaction layer has been clarified by Oehrlein *et al.* [9].

Table 3.3 gives the effective reaction layer thickness for several ECR etching experiments based on the Cryo 8 process conditions. Three trends are observed. First, the reaction layer thickness is much smaller than 1 nm. With a bias voltage of  $-20$  V the reaction layer is even thinner than one monolayer of silicon dioxide. Second, for a higher bias voltage the reaction layer thickness is strongly reduced. Third, the reaction layer thickness is smaller for Si(111). Implications of these three observations are given in the next three paragraphs. A complication is the shift of the layer thickness, when the take off angle is increased, but the observed trends remain unaltered. The XPS measurement is inaccurate for small take off angles because of surface roughness consisting of silicon dioxide agglomerates. Surface roughness is investigated with AFM and described elsewhere in this subsection. The oxygen-to-fluorine ratio shows that oxygen is the main component of the reaction layer larger and is nearly constant for 0 V bias voltage. For an increase to  $-20$  V bias voltage the oxygen-to-fluorine ratio increases on Si(100), but it decreases on Si(110) and Si(111). It shows that the crystal orientation plays a role in the passivation mechanism.

Table 3.3 The effective reaction layer thickness and the oxygen-to-fluorine ratio depending on the bias voltage and the substrate orientation. For 61° take off angle and -20 V bias voltage no reacted silicon has been observed leading to a thickness of zero.

Bias Voltage (V)	Substrate Orientation	Take Off Angle	Thickness (nm)	Oxygen To Fluorine Ratio
0	(100)	20°	0.40±0.03	3.4
	(110)	20°	0.42±0.03	3.1
	(111)	20°	0.23±0.03	3.2
-20	(100)	25°	0.18±0.03	5.4
	(110)	25°	0.21±0.03	2.5
	(111)	25°	0.07±0.03	3.2
0	(100)	61°	0.19±0.03	3.7
	(110)	61°	0.21±0.03	3.3
	(111)	61°	0.13±0.03	3.1
-20	(100)	61°	0.00±0.03	4.4
	(110)	61°	0.00±0.03	2.5
	(111)	61°	0.00±0.03	2.8

The first observation shows that the reaction layer thickness is in the monolayer regime. Combining this to the extremely high etch yield of the order of 1000 that was observed in the previous subsection it is highly unlikely that etching proceeds by sputtering of a loosely bound reaction layer. In this view, a reaction layer with a thickness of more than 3 nm has to be present on the silicon surface because sputtering is a localised process. For comparison, a cube with 3 nm edges contains 1350 silicon atoms. This is much larger than the observed reaction layer thickness. On the other hand it cannot be excluded that the measured reaction layer thickness is underestimated, because the loosely bound compounds could evaporate during the heating to room temperature before XPS analysis. However, it seems impossible that an ion can distribute its energy over so many molecules, since silicon is a good heat conductor and the energy will be removed quickly from the surface.

The second observation is the reduced reaction layer thickness for a larger substrate bias voltage. This is in contrast to Oehrlein, who observed an increase of the reaction layer thickness for experiments in a RIE reactor with bias voltages larger than -100 V [10]. It is concluded that the mixing and amorphisation of the top silicon layer does not play an important role in our work. On the contrary the surface chemistry is dominant and a reduced reaction layer thickness results in a higher etch rate. Together with the first observation, it leads to the conclusion that the ion bombardment is only needed to remove the oxygen passivation, so that the fluorine reaction probability increases. The extremely high etch yield can be understood better with this concept. When the passivation layer is locally

damaged by ion impact, hundreds of fluorine radicals are available to react with silicon before an oxygen radical arrives to repair the passivation layer.

The third observation is more difficult to understand. The reaction layer on Si(111) is thinner than on Si(100), but the Si(111) etch rate is lower at cryogenic temperatures. The ratio of the Si(100) etch rate and the Si(111) etch rate is only 1.26 at room temperature, but it is 2.07 at  $-80\text{ }^{\circ}\text{C}$  [3]. The effectiveness of oxygen passivation on Si(111) is thus higher, which could be due to the different bonding configuration of the surface atoms. Apparently, less oxygen is needed to passivate the Si(111) surface atoms that are attached to the bulk with 3 strong silicon bonds in line with the lower oxygen-to-fluorine ratio.

Table 3.4 gives the results for XPS measurements on plane Si(100) and on trench sidewalls that were etched with the Cryo 9 process conditions. The trenches have good anisotropy and are shown in figure 3.13. The trenches are sufficiently deep, so that photoelectrons generated on the bottom of the trench are effectively shadowed. A clear difference is observed between plane silicon, which is exposed to the ion bombardment, and the trench sidewalls. The reaction layer thickness of about 3 monolayers on trench sidewalls is much larger than on plane silicon. It is comparable to a native oxide layer and demonstrates the effectiveness of oxygen for sidewall passivation.

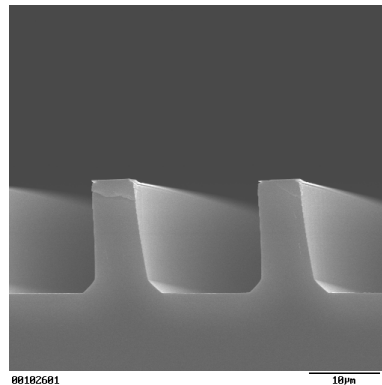


Figure 3.13 The trenches that are made for XPS analysis of the sidewall passivation layer. The observed passivation layer is sufficiently thick because the etching is anisotropic.

Table 3.4 The effective reaction layer thickness on plane silicon and on the trench sidewalls. A thick reaction layer is formed on the sidewalls providing the surface passivation.

Bias Voltage (V)	Silicon Area	Take Off Angle	Thickness (nm)	Oxygen to Fluorine Ratio
-13	Plane Silicon	70°	0.03±0.03	1.97
-13	Sidewall	70°	0.89±0.03	2.01

Table 3.5 gives XPS results for samples etched in the ICP reactor with the Cryo 13 process conditions. Despite the much higher ion flux the thickness of the reaction layer is comparable to ECR etching. The results are consistent with a lower reaction layer thickness for higher bias voltages. It also shows that the reaction layer thickness remains in the same range if the etching temperature is increased to room temperature. The oxygen-to-fluorine ratio increases, but oxygen cannot effectively suppress the etch rate due to the higher temperature.

Table 3.5 The effective reaction layer thickness depending on the bias voltage and the substrate temperature for ICP etching.

Bias Voltage (V)	Temperature (°C)	Take off angle	Thickness (nm)	Oxygen To Fluorine Ratio
0	-115	15°	0.27±0.03	1.6
-25	-115	15°	0.17±0.03	1.5
-25	+25	15°	0.27±0.03	2.7
0	-115	60°	0.45±0.03	1.6
-25	-115	60°	0.13±0.03	1.6
-25	+25	60°	0.14±0.03	2.4

Table 3.6 shows the influence of the ion flux on the reaction layer thickness for the Cryo 14 process conditions. Decreasing the substrate-to-source distance in the ICP reactor increases the ion flux, while the fluorine radical partial pressure remains approximately the same. The high ion flux is approximately a factor of 6 larger than the low ion flux. However, the results do not show a significant difference in the reaction layer thickness probably because in both cases the ion flux is high enough to remove most of the reaction layer. The decrease of the oxygen-to-fluorine ratio for a high ion flux is attributed to an increase of the sputter rate of oxidised species.

Table 3.6 The effective reaction layer thickness depending on the ion flux for ICP etching.

Bias Voltage (V)	Ion Flux	Take Off Angle	Thickness (nm)	Oxygen To Fluorine Ratio
-50	High	15°	0.19±0.03	1.8
-50	Low	15°	0.18±0.03	2.2
-50	High	60°	0.03±0.03	1.6
-50	Low	60°	0.07±0.03	2.6

### Ellipsometry

To exclude any modification of the reaction layer by heating of the sample to room temperature, *in situ* ellipsometry was used on the ICP reactor. The measurement of a silicon sample exposed to an SF<sub>6</sub> plasma with the Cryo 15 process conditions is shown in figure 3.14. The peak immediately after ignition of the plasma is presumably due to some residual native oxide or some contamination from the reactor walls because it diminishes after repeated ignition. This is visible in the inset of figure 3.14. The reaction layer thickness decreases quickly to about 0.4 nm, which is comparable to the thickness estimated by XPS measurements, but then it increases due to surface roughness. The inaccuracy of the thickness of the thin reaction layer is unclear because an adequate silicon reference sample is not available to determine accurately the optical constants of an uncovered substrate. Chemical cleaning leaves residues and physical cleaning has problems like sputtering of source material and amorphisation of the substrate. The inset of figure 3.14 shows the measurement of the thickness and the ellipsometric angle  $\Delta$  during alternated exposure of an Ar plasma with -150 V bias voltage and an SF<sub>6</sub> plasma with -50 V bias voltage. The thickness only depends on the ellipsometric angle  $\Delta$  in this range. When the Ar plasma is on, the reaction layer is totally removed and amorphisation of the top layer is observed by the increase of the ellipsometric angle  $\Delta$ .

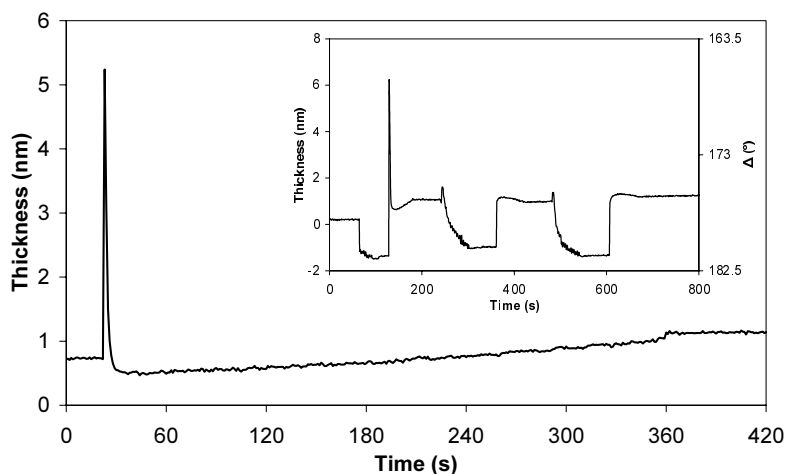


Figure 3.14 Increasing thickness due to the forming of surface roughness in an  $SF_6$  plasma. A strong peak is visible immediately after ignition of the plasma. The inset shows the thickness and the ellipsometric angle  $\Delta$  during alternated exposure of an Ar plasma and an  $SF_6$  plasma.

### AFM

Surface roughness plays an important role when thin reaction layers are investigated with XPS or *in situ* ellipsometry. The surface roughness precludes the absolute measurement of the reaction layer thickness often leading to an overestimation. In particular, at substrate bias voltages below  $-20$  V a large increase in the thickness was observed with ellipsometry. When the bias voltage was above  $-20$  V the thickness decreased, which shows that it is a reversible effect. With AFM the surface roughness can be quantified. Topographic images of  $4 \mu\text{m}$  by  $4 \mu\text{m}$  were made of samples etched with the Cryo 16 process conditions. The images are shown in figure 3.15. The RMS value of the surface roughness for  $0$  V and  $-50$  V bias voltage was  $16$  and  $21$  nm respectively. A clear correlation between the surface roughness and the increase of the ellipsometric thickness was verified [11]. Under the optical microscope the surface roughness often shows up as pyramid shapes revealing the crystallographic origin. The roughness is probably due to micromasking, which appears when the oxide passivation is not sufficiently removed by the ion bombardment. This is supported by measurements at room temperature where surface roughness is absent.

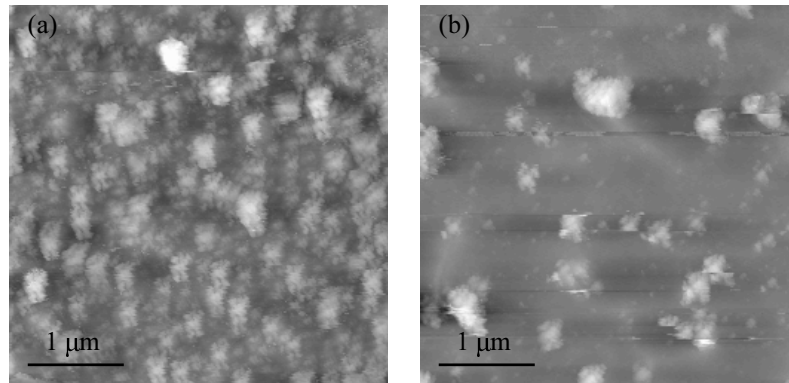


Figure 3.15 AFM images of the topography of  $4\ \mu\text{m}$  by  $4\ \mu\text{m}$  samples. The vertical scale is  $200\ \text{nm}$  going continuously from black to white. The samples are etched in the ICP reactor with a bias voltage of (a)  $0\ \text{V}$ , and (b)  $-50\ \text{V}$ .

### TEM

In order to investigate the silicon surface on an atomic scale, TEM analysis was made of a cross-section of a sample etched in the ICP reactor without bias power. The Cryo 18 process conditions were used. A close-up of the silicon surface and the reaction layer is shown in figure 3.16. Between the crystalline silicon and the aluminium protection layer an amorphous layer of approximately  $1.2\ \text{nm}$  thick is visible, which is larger than the values obtained by XPS measurements. It is attributed to the reaction layer plus some contamination because of exposure to the ambient for  $2\ \text{min}$  while loading the aluminium evaporator.

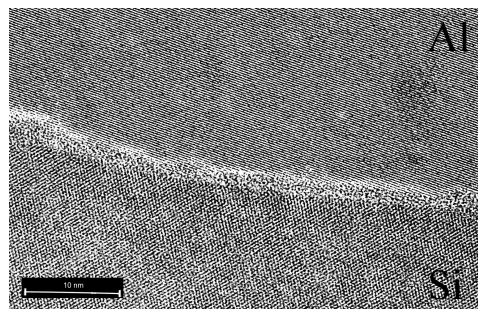


Figure 3.16 TEM image of the interface between the silicon substrate (bottom) and the aluminium protection layer (top). The amorphous layer thickness is approximately  $1.2\ \text{nm}$ .

### 3.3 The transport of radical and ion fluxes in high aspect ratio trenches

The etching of deep trenches with a high-density fluorine-based plasma is mostly characterised by a decrease of the etch rate with depth, which is disadvantageous for processes where a high etch rate is important to obtain the desired throughput. Moreover, the etch rate of silicon depends on the aspect ratio, so that narrower trenches have lower etch rates. Overetching of the wider trenches is inevitable for applications that require trenches with different dimensions, but overetching can lead to sidewall erosion and to notching of silicon on isolator. A better understanding of the etching mechanism and the transport of the fluorine radicals in deep trenches can contribute to a better-controlled process.

In this section the etching mechanism of high aspect ratio trenches with a diameter  $D$  is described. Due to the low pressure the Knudsen number  $Kn$  is much larger than unity,  $Kn = \lambda_c/D \gg 1$ , so that the transport of fluorine radicals is dominated by sidewall collisions. The radical transport in the molecular flow regime is described with the Knudsen transport model derived in appendix A. It is shown that the reaction probability of fluorine radicals is about 0.5 at room temperature, so that the process is largely diffusion-limited. The radical transport from the bulk plasma to the silicon surface is thus an important issue for high aspect ratio trench etching.

The etching mechanism of shallow trenches at cryogenic temperatures was discussed in the previous section. In the transition from a surface kinetics controlled regime to an ion-dominated regime the oxygen passivation layer thickness is gradually reduced, so that the reaction probability increases. The etching mechanism of deep trenches is discussed in this section. The surface kinetics and the transport of fluorine and oxygen radicals are the main factors that explain the observed etch rate as a function of aspect ratio. The chemically enhanced ion-neutral synergy model derived in appendix A is used to model the etch rate as a function of aspect ratio. In the surface kinetics controlled regime the reaction probability is low and ARIE is observed. In the ion-dominated regime the reaction probability is high and ARDE is observed. The characteristics of the two regimes in the most extreme case are given in table 3.7.



Table 3.7 Characteristics of the surface kinetics controlled and the ion-dominated etching regime in the most extreme case.

	Surface Kinetics Controlled	Ion-Dominated
Profile Evolution	Crystal Orientation Dependent	Purely Anisotropic
Etching Mechanism	Ion-Limited	Fluorine-Limited
Reaction Probability	$\ll 1$	$\approx 0.5$
Etching Process	Reaction-Limited	Diffusion-Limited
Transport Mechanism	ARIE	ARDE

### 3.3.1 Introduction to the reaction kinetics of fluorine and silicon

The etching process can be reaction-limited or diffusion-limited. In a reaction-limited regime the reaction probability is much smaller than 1, whereas in a diffusion-limited regime the reaction probability is close to 1. In literature, it has been shown that the reaction is thermally activated with a reaction probability up to 0.004 for a fluorine plasma at high pressures (54 Pa), which indicates that the process is reaction-limited [12]. It has also been shown, that the silicon etch rate is proportional to the fluorine radical partial pressure up to 0.55 Pa with a reaction probability of 0.1. Above this pressure the silicon etch rate slightly saturates, which is ascribed to surface oxidation [13].

In this work high-density low-pressure plasmas were used and as a result it can be expected that surface oxidation did not play a role at room temperature. The results presented in figure 3.1 support this view. The silicon etch rate was measured for ICP etching with the Cryo 18 process conditions given in appendix B. The silicon etch rate at room temperature was proportional to the fluorine radical partial pressure up to 0.82 Pa, which is shown in figure 3.17. A reaction probability of 0.69 was deduced from the regression line. Silicon etching at room temperature is largely diffusion-limited.

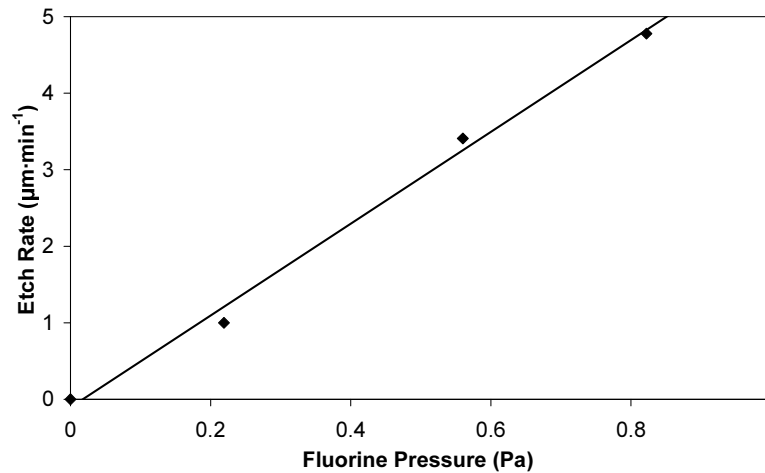


Figure 3.17 The etch rate as a function of the fluorine radical partial pressure for ICP etching. The spontaneous etch rate of silicon at room temperature is proportional to the fluorine radical partial pressure.

The transport of fluorine radicals has important implications for deep trench etching because silicon etching is proportional to the fluorine radical flux. The following experiment consisting of 2 etching steps with the Cryo 19 process conditions was performed to investigate the effects that occur when a flux of fluorine radicals enters a trench. During the first step, silicon etching for 5 min at a substrate temperature of  $-115\text{ }^{\circ}\text{C}$  resulted in the anisotropic trenches that are shown in figure 3.18a. At  $-115\text{ }^{\circ}\text{C}$  the fluorine reaction probability on the sidewalls is nearly zero, so that there is no lateral etch and the trench profiles are anisotropic. During the second step, the anisotropic trenches were exposed for 1 min to the same plasma at a substrate temperature of  $+25\text{ }^{\circ}\text{C}$ . A large lateral etch was superimposed on the anisotropic profiles, while the bottom of the trench was not etched at all. This is shown in figure 3.18b. The transport of fluorine radicals was dominated by sidewall collisions because the mean free path ( $\lambda_c = 1.34\text{ mm}$ ) was much larger than the line width ( $D = 6\text{ }\mu\text{m}$ ). The almost exponential decay of the lateral etch indicates the strong depletion of the fluorine radical flux due to the high fluorine reaction probability. The ions were accelerated perpendicular to the substrate in the thin plasma sheath ( $d_s = 0.79\text{ mm}$ ), so that ion-neutral collisions played a minor role. The ions did not influence the lateral etch due to the narrow ion angular distribution.

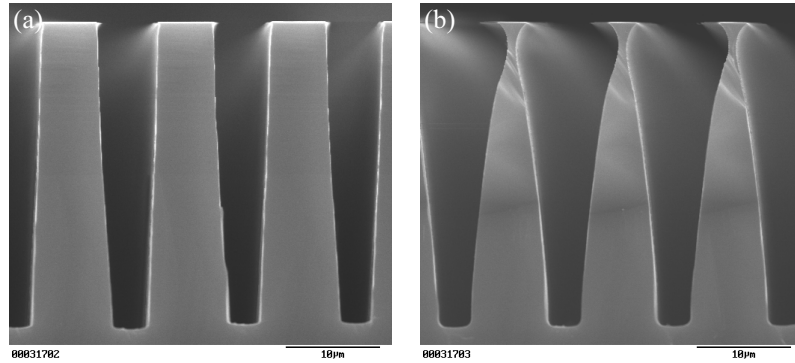


Figure 3.18 Depletion of radicals in a trench. (a) Anisotropic trenches etched at  $-115\text{ }^{\circ}\text{C}$ . (b) The trenches after exposure to the same plasma at  $+25\text{ }^{\circ}\text{C}$ .

### 3.3.2 The transport of fluorine radicals in high aspect ratio structures

The aim of this experiment is to clarify the etching mechanism of fluorine radicals in deep trenches. The vertical ion flux was excluded in the structure consisting of horizontal silicon lines in  $1.5\text{ }\mu\text{m}$  thick silicon on insulator (SOI) covered by thermal silicon dioxide. The fluorine radical flux reached the silicon core through a window at one of the sides. A good comparison with the vertical trench etch experiments was ensured because monocrystalline silicon was used. A tube of silicon dioxide remained after etching at a substrate temperature of  $+25\text{ }^{\circ}\text{C}$  with the Cryo 20 process conditions. No lateral etch was observed if the horizontal lines were etched with plasma conditions that yield anisotropic profiles for the regular vertical trenches.

The average etch rate in a tube with a height and a width of approximately  $1.5\text{ }\mu\text{m}$  is plotted as a function of the aspect ratio together with a view of the structure after etching in figure 3.19. The average etch rate is defined by the total etch depth divided by the total etch time. The aspect ratio is the total etch depth divided by the effective diameter of the tube. The effective diameter is the diameter of a circle that has the same area as the cross-section of the trapezoidal tube. The etch rate  $R_E$  is fitted with the Knudsen transport model derived in appendix A. The Knudsen transport model describes the transport of fluorine radicals and is given by

$$R_E = \frac{S_F \cdot \varphi_F^0}{4 \cdot \rho} \cdot \frac{K^{AR}}{K^{AR} + S_F - K^{AR} \cdot S_F} \quad 3.3$$

where  $S_F$  is the fluorine reaction probability,  $\varphi_F^0$  the fluorine radical flux entering the cavity,  $\rho$  the atomic density of the substrate and  $K^{AR}$  the Clausing factor at a certain aspect

ratio. The fit parameters are the fluorine reaction probability  $S_F$  and the initial etch rate  $S_F \cdot \phi_F^0 / 4 \cdot \rho$ . A least squares fit of the Knudsen transport model to the experimental data resulted in a reaction probability of 0.47 and an initial etch rate of  $10.6 \mu\text{m} \cdot \text{min}^{-1}$ .

With actinometry these results were independently tested. A fluorine radical partial pressure of 2.5 Pa was measured for identical plasma conditions. An initial etch rate of  $10.2 \mu\text{m} \cdot \text{min}^{-1}$  was calculated with the measured fluorine radical flux  $\phi_F^0$  and the fitted reaction probability of 0.47, which agrees well with the fitted initial etch rate. The measured fluorine radical flux is thus consistent with the fitted results. However, these results are in contrast with the aspect ratio independent etching for horizontal polysilicon lines that has been reported in literature [14]. In that case a RIE reactor was used with a low fluorine radical flux. The depletion of the fluorine radical flux was low because oxygen contamination could reduce the fluorine reaction probability.

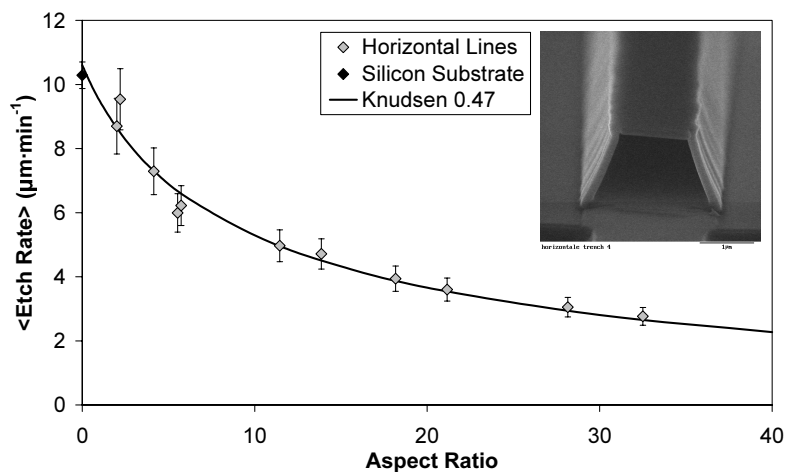


Figure 3.19 The average etch rate as a function of the aspect ratio for horizontal lines (see inset). The solid curve is a least squares fit of the Knudsen transport model with a reaction probability of 0.47 for fluorine. The point at zero aspect ratio is independently measured on a plane silicon sample.

### 3.3.3 Switching between ARDE and ARIE by tuning the ion flux with a variable reactor geometry

In the previous subsection the etching mechanism of the fluorine radicals was characterised with special horizontal structures. The etching of deep vertical trenches under influence of the ions is used to investigate the interplay between ions and radicals. Plasma etching with a low and a high ion flux was performed in the ECR reactor, that is with and without the

quartz cylinder respectively. Plasma conditions were equal to the Cryo 10 process conditions. The average etch rate of Si(100) for trenches with a width in the range of 0.4  $\mu\text{m}$  to 10.0  $\mu\text{m}$  is plotted as a function of aspect ratio in figure 3.20. The aspect ratio is defined by the ratio of the depth and width in the middle of the trench. This can result in a fluctuating aspect ratio because the measurement of the width of high aspect ratio trenches can be inaccurate. With a high ion flux the etch rate is high and decreases relatively fast, whereas with a low ion flux the etch rate is nearly constant. The corresponding SEM pictures of 1.5  $\mu\text{m}$  wide trenches are shown in figure 3.21. The lateral etch directly below the mask for etching with a high ion flux is explained by the increased sidewall erosion. The inset shows a magnification of the bottom of the trench. The transition from purely anisotropic etching to a crystal orientation dependent etching is clearly observed.

The two data sets were fitted with the least squares method using the Knudsen transport model and the chemically enhanced ion-neutral synergy model. The Knudsen transport model does not take into account the oxygen radical flux and as a result the fluorine adsorption probability is equal to the fluorine reaction probability. A separate fluorine reaction probability was taken for each data set, but the fluorine flux at zero aspect ratio was the same in both situations. The best fit for the high ion flux and the low ion flux was obtained for a fluorine reaction probability of 0.42 and 0.17 and an initial etch rate of 1.92  $\mu\text{m}\cdot\text{min}^{-1}$  and 0.78  $\mu\text{m}\cdot\text{min}^{-1}$ , respectively. The fitted Knudsen curves are plotted in figure 3.20a. The strong decrease of the etch rate for the high ion flux is modelled well. However, the Knudsen model for the low ion flux still shows a decrease for high aspect ratios in contrast with the experimental observations.

The best fit of the chemically enhanced ion-neutral synergy model is plotted in figure 3.20b. In this model the fluorine reaction probability is defined by  $\kappa_{\text{F}}\cdot(1-\theta_{\text{O}})$ . The fluorine reaction probability at zero aspect ratio is 0.39 and 0.14 and the initial etch rate is 1.79  $\mu\text{m}\cdot\text{min}^{-1}$  and 0.62  $\mu\text{m}\cdot\text{min}^{-1}$  for the high ion flux and the low ion flux respectively. The aspect ratio independent etch rate was modelled very well because the decreasing fluorine radical flux is compensated by a decreasing oxygen surface coverage. In a deep trench the oxygen flux decreases but the ion flux is constant, so that a larger fraction of empty surface sites is available for the reaction with fluorine.

The fit results of the chemically enhanced ion-neutral synergy model were independently tested with plasma diagnostics. The fit parameter  $b$  is 3.55 and 0.39 for the high and the low ion flux, respectively. The measured ion current density is 0.083  $\text{mA}\cdot\text{cm}^{-2}$  and 0.005  $\text{mA}\cdot\text{cm}^{-2}$  for the high and the low ion flux, respectively. The difference found by the model correlates well with the change of the ion current density. A fluorine radical partial pressure of 0.31 Pa was determined with actinometry. Using the measured fluorine radical flux and the fitted reaction probability, etch rates of 1.05  $\mu\text{m}\cdot\text{min}^{-1}$  and 0.38  $\mu\text{m}\cdot\text{min}^{-1}$  were calculated for the high ion flux case and low ion flux case, respectively. These values are 40% lower than the fitted initial etch rates. Either the actinometry or the fitted reaction probabilities are inaccurate, which is treated in more detail in subsection 3.3.6.

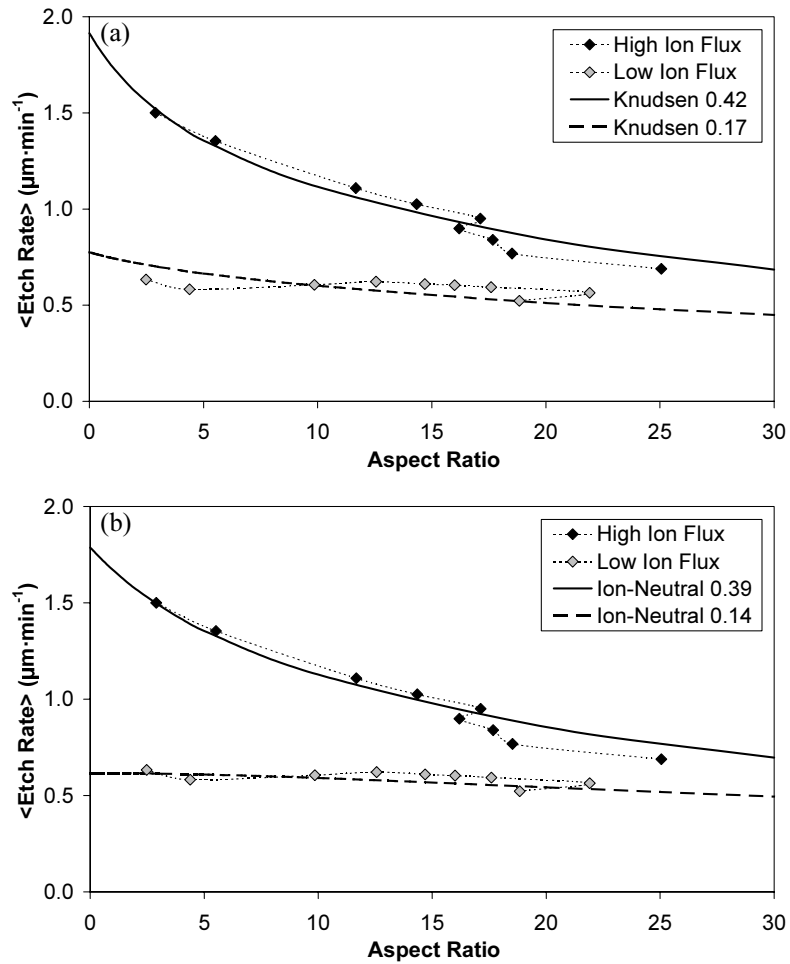


Figure 3.20 Aspect ratio dependent and independent etching by tuning the ion flux. The results have been fitted by (a) the Knudsen transport model and (b) the chemically enhanced ion-neutral synergy model.

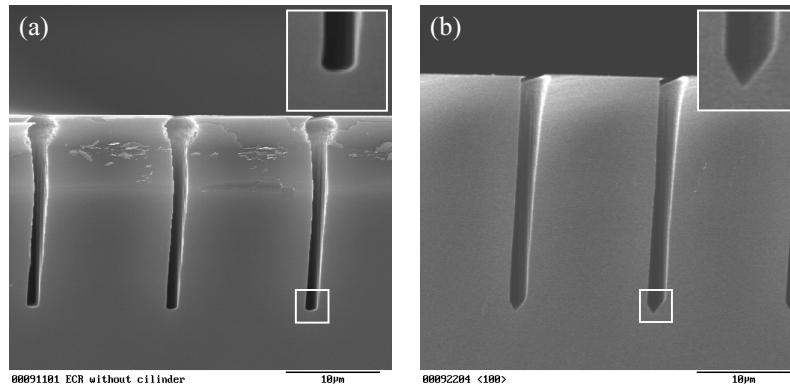


Figure 3.21 SEM pictures of  $1.5\ \mu\text{m}$  wide trenches etched with (a) a high ion flux, and (b) a low ion flux. The lateral etch directly below the mask for etching with a high ion flux is explained by the increased sidewall erosion. The inset shows a magnification of the trench bottom.

### 3.3.4 Switching between ARDE and ARIE by tuning the ion-to-radical flux ratio with a fixed reactor geometry

In the previous subsection switching between ARDE and ARIE has been obtained by decreasing the ion flux. In this subsection switching between ARDE and ARIE is effectuated by a variation of the plasma conditions with a fixed reactor geometry, that is with the quartz cylinder in place. In section 3.2 it was explained that the transition from the ion-dominated to the surface kinetics controlled regime can be obtained by a variation of the plasma conditions in the ECR reactor. It was also explained that the transition is ascribed to an increased oxygen surface passivation. It can be expected that the transition leads to switching between ARDE and ARIE for both Si(100) and Si(111) because the transition is accompanied by a decrease of the reaction probability. Two extreme plasma conditions were selected to investigate the switching between ARDE and ARIE. A higher bias voltage, a lower  $\text{SF}_6$  flow, a lower pressure and a higher substrate temperature favour ARDE and the inverse plasma conditions favour ARIE.

The average etch rate of Si(100) and Si(111) has been plotted as a function of aspect ratio in figure 3.22. Aspect ratio dependent etching was obtained for the Cryo 11 process conditions. For these plasma conditions the stronger ion bombardment can easily sputter away the oxygen passivation layer leading to a higher reaction probability. Crystal orientation dependent etching was less prominent for aspect ratio dependent etching because the ratio of the Si(100) and Si(111) etch rate was higher due to the higher substrate temperature similar to figure 3.1. Aspect ratio independent etching was obtained for the Cryo 10 process conditions. These plasma conditions were the same as in the previous

subsection and the average etch rate of Si(100) was already shown in figure 3.20. The average etch rate of Si(111) is slightly inverse aspect ratio dependent, that is a higher etch rate for a higher aspect ratio. Inverse aspect ratio dependent etching is caused by a strong depletion of oxygen radicals in high aspect ratio trenches [15-17]. The lateral etch for trenches in Si(111) is larger than for trenches in Si(100), which indicates a poor sidewall passivation layer for trenches in Si(111). This could lead to an increased oxygen reaction probability on the sidewalls, which results in a strong depletion of oxygen radicals explaining the inverse aspect ratio dependent etching.

The average etch rate data were fitted with the chemically enhanced ion-neutral synergy model. The fit agrees well for the aspect ratio dependent etching of both Si(100) and Si(111). The fit for aspect ratio independent etching of Si(100) is the same as in figure 3.20. The fit for aspect ratio independent etching of Si(111) is even more constant because reaction probability is lower.

The fit parameters were independently tested with plasma diagnostics. The fluorine reaction probability at zero aspect ratio is 0.46 and 0.28 and the initial etch rate is  $1.04 \mu\text{m}\cdot\text{min}^{-1}$  and  $0.62 \mu\text{m}\cdot\text{min}^{-1}$  for aspect ratio dependent etching of Si(100) and Si(111), respectively. A fluorine radical partial pressure of 0.15 Pa was measured with actinometry. Using the measured fluorine radical flux and the fitted reaction probabilities, initial etch rates of  $0.60 \mu\text{m}\cdot\text{min}^{-1}$  and  $0.37 \mu\text{m}\cdot\text{min}^{-1}$  were calculated for Si(100) and Si(111), respectively. The fluorine reaction probability at zero aspect ratio is 0.14 and 0.08 and the initial etch rate is  $0.62 \mu\text{m}\cdot\text{min}^{-1}$  and  $0.36 \mu\text{m}\cdot\text{min}^{-1}$  for aspect ratio independent etching of Si(100) and Si(111), respectively. A fluorine radical partial pressure of 0.31 Pa was measured with actinometry. Using the measured fluorine flux and the fitted reaction probabilities, etch rates of  $0.38 \mu\text{m}\cdot\text{min}^{-1}$  and  $0.22 \mu\text{m}\cdot\text{min}^{-1}$  were calculated for Si(100) and Si(111), respectively. The calculated initial etch rates are discussed in subsection 3.3.6.



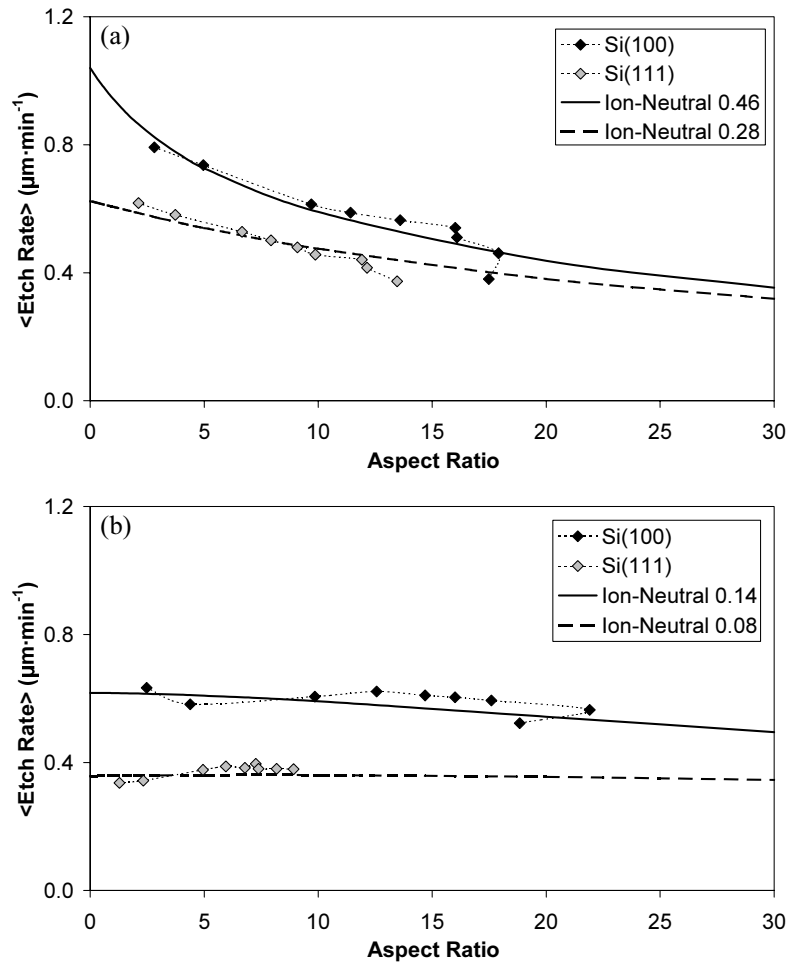


Figure 3.22 The average etch rate as a function of aspect ratio for Si(100) and Si(111). (a) Aspect ratio dependent etching. (b) Aspect ratio independent etching. The Si(111) data show slightly inverse aspect ratio dependent etching. The data are fitted by the chemically enhanced ion-neutral synergy model.

SEM pictures of trenches with a 1.5  $\mu\text{m}$  wide mask aperture are shown in figure 3.23a and 3.23b for aspect ratio dependent etching of Si(100) and Si(111) respectively. The trenches have a lateral etch below the mask and a positive sidewall taper, so that the aspect ratio is not well-defined. A SEM picture is shown in figure 3.23c for aspect ratio independent etching of Si(111). The SEM picture of Si(100) was already shown in figure 3.21b.

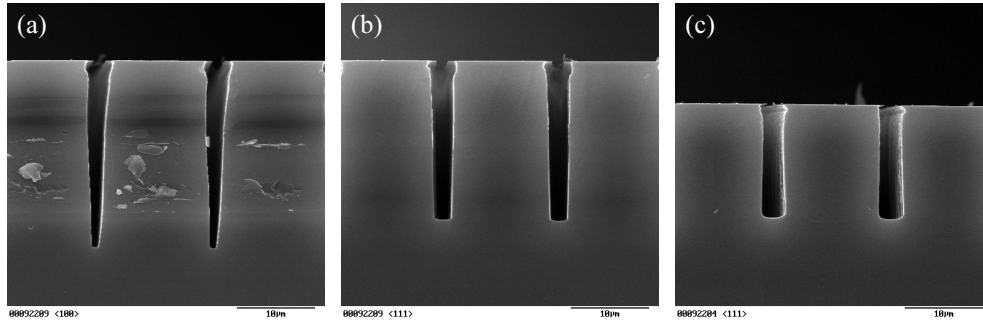


Figure 3.23 SEM pictures of trenches with a  $1.5 \mu\text{m}$  wide mask aperture. Aspect ratio dependent etching of (a) Si(100) and (b) Si(111). (c) Aspect ratio independent etching of Si(111).

### 3.3.5 Aspect ratio dependent etching in the ICP reactor

In the ICP reactor the oxygen surface passivation is intensively removed from the bottom of the trench due to the high ion flux, so that the fluorine reaction probability is high. The ion flux is two orders of magnitude higher than in the ECR reactor. The average etch rate as a function of aspect ratio for the Cryo 12 process conditions is plotted in figure 3.24. The quick drop of the average etch rate above an aspect ratio of 15 is ascribed to the sidewall reactions of the fluorine radicals. In particular for narrow trenches, the lateral etch is relatively large compared to the trench width. The sidewall taper is often more negative leading to an underestimation of the aspect ratio [18]. The corresponding trenches were already shown in figure 3.6. Crystal facets appeared for Si(100) in contrast to aspect ratio dependent etching in the ECR reactor. The surface kinetics play a more important role in the ICP reactor due to the lower substrate temperature. It leads to a marked difference of the Si(100) and the Si(111) etch rate even if the ion flux is high enough to ensure a high fluorine reaction probability. The higher pressure in the ICP reactor could also favour surface kinetics controlled etching.

The average etch rate of both Si(100) and Si(111) is fitted with the Knudsen transport model and the chemically enhanced ion-neutral synergy model. The best fit of the Si(111) etch rate is obtained for the Knudsen transport model. Apparently, the Si(111) reaction mechanism is more determined by the crystal structure than by the oxygen passivation layer. The fit parameters were independently tested with actinometry and are discussed in subsection 3.3.6.

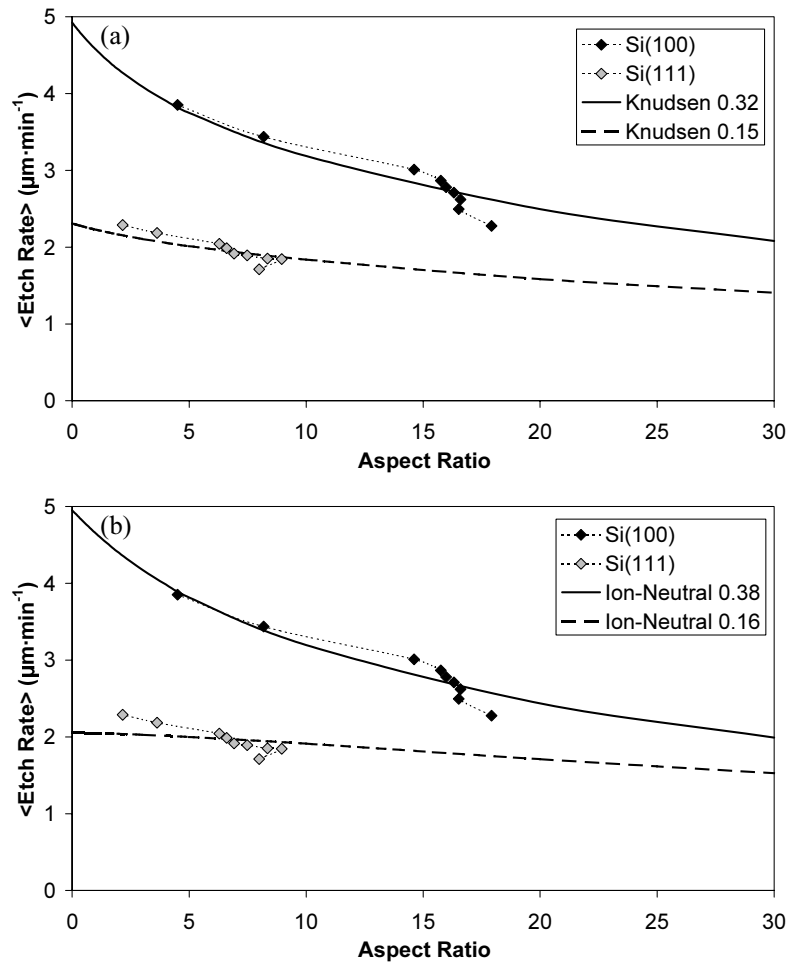


Figure 3.24 Aspect ratio dependent etching of Si(100) and Si(111) in the ICP reactor. The results have been fitted with (a) the Knudsen transport model and (b) the chemically enhanced ion-neutral synergy model.

#### Etch rate measurement by *in situ* laser interferometry

Deep anisotropic trenches in Si(100) were made with ICP etching. The etch rate was measured by *in situ* laser interferometry during two ICP etching experiments with plasma conditions that were equal to the Cryo 21 process conditions. The etch rate as a function of aspect ratio and a SEM image of the  $6\ \mu\text{m}$  wide trenches on a  $12\ \mu\text{m}$  pitch are shown in figure 3.25. The ICP etching experiments were fitted with the Knudsen transport model and

the chemically enhanced ion-neutral synergy model. Except for small differences the models fit equally well due to measurement inaccuracies. The fitted fluorine reaction probability at zero aspect ratio is 0.26 and 0.32 for the Knudsen transport model and the chemically enhanced ion-neutral synergy model, respectively. The fitted initial etch rate is  $5.24 \mu\text{m}\cdot\text{min}^{-1}$  and  $5.14 \mu\text{m}\cdot\text{min}^{-1}$ , respectively. A fluorine radical partial pressure of 1.27 Pa was measured for plasma conditions that were nearly identical to the plasma conditions of the deep anisotropic trench etching experiments. The independent test based on the measured fluorine radical flux and the fitted reaction probability of 0.26 and 0.32 leads to a calculated initial etch rate of  $2.88 \mu\text{m}\cdot\text{min}^{-1}$  and  $3.54 \mu\text{m}\cdot\text{min}^{-1}$ , respectively. It seems that the initial etch rate of the cryo-process is systematically underestimated with this method.

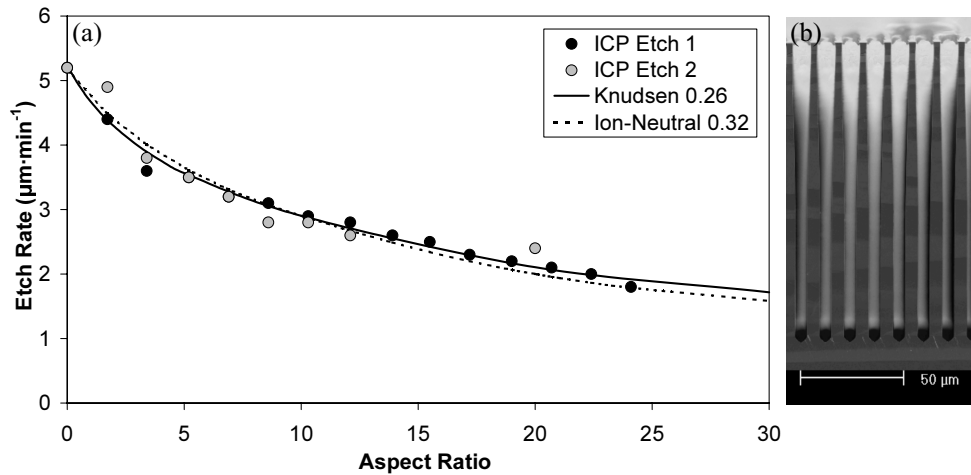


Figure 3.25 Aspect ratio dependent etching. (a) The etch rate is measured by *in situ* laser interferometry during ICP etching. The data points are fitted with the Knudsen transport model (solid curve) and the chemically enhanced ion-neutral synergy model (dotted curve). (b) SEM image of the trenches.

### 3.3.6 Further discussion: plasma diagnostics

All deep anisotropic trench etching experiments that are described in this section are compared to evaluate the models that were used to fit the experimental results. To this aim the fitted initial etch rate, the calculated initial etch rate and the thermal initial etch rate are compared in table 3.8. The calculated initial etch rate is based on the measured fluorine radical partial pressure and the fitted fluorine reaction probability at zero aspect ratio. The thermal initial etch rate is also based the measured fluorine radical partial pressure and the fitted fluorine reaction probability at zero aspect ratio. However, the fluorine flux is

calculated using the substrate temperature instead of the assumed plasma temperature of 400 K. Table 3.8 also contains the fit parameters of the chemically enhanced ion-neutral synergy model except for the etching of the horizontal trenches for which it contains the fit parameters of the Knudsen transport model. However, the differences between the fitted parameters of the chemically enhanced ion-neutral synergy model and the Knudsen transport model are generally small. The calculated initial etch rate deviates from the fitted initial etch rate. Except for the horizontal lines etched at room temperature the calculated initial etch rate is between 26% and 42% lower than the fitted initial etch rate.

*Table 3.8 Comparison of the fitted initial etch rate, the calculated initial etch rate and the thermal initial etch rate. The calculated initial etch rate is based on the measured fluorine radical partial pressure and the fitted fluorine reaction probability at zero aspect ratio. It is assumed that the plasma temperature is 400 K. Better agreement is obtained if it is assumed that the plasma temperature is equal to the substrate temperature.*

Experiment	Fluorine Partial Pressure (Pa)	Fitted Reaction Probability	Fitted Initial Etch Rate ( $\mu\text{m}\cdot\text{min}^{-1}$ )	Calculated Initial Etch Rate ( $\mu\text{m}\cdot\text{min}^{-1}$ )	Thermal Initial Etch Rate ( $\mu\text{m}\cdot\text{min}^{-1}$ )
Horizontal	2.5	0.47	10.6	10.2	11.9
ARIE High	0.31	0.39	1.79	1.05	1.60
ARIE (100)	0.31	0.14	0.62	0.38	0.58
ARIE (111)	0.31	0.08	0.36	0.22	0.33
ARDE (100)	0.15	0.46	1.04	0.60	0.87
ARDE (111)	0.15	0.28	0.62	0.37	0.53
ICP (100)	1.09	0.38	4.95	3.61	5.93
ICP (111)	1.09	0.16	2.06	1.52	2.50
Interferometry	1.27	0.32	5.14	3.54	5.73

The cause of this discrepancy has to be found in either the actinometry technique or the fitting model. The actinometry technique gives an average value of the fluorine radical partial pressure through the whole reactor diameter. The partial pressure in the centre of the reactor above the sample could be higher than the average value due to recombination on the reactor walls. However, it is interesting to see that there is no discrepancy for etching at room temperature. The fluorine radical flux is inversely proportional to the square root of the plasma temperature. In the calculation it has been assumed that the plasma temperature is 400 K, but the fluorine radical flux increases if the plasma above the cold substrate is quickly thermalised. For example, the fluorine radical flux at 400 K is 34 % lower than at 173 K ( $-100\text{ }^{\circ}\text{C}$ ). The temperature effect can largely explain the observed discrepancy because the thermal initial etch rate deviates generally less from the fitted initial etch rate. It

is concluded that the cooling of the plasma is relevant in the cryo-process. Besides, the thermal initial etch rate is larger than the fitted initial etch rate for the ICP reactor but it is smaller for the ECR reactor. A difference in the reactor geometry could thus also play a role in the determination of the fluorine radical flux. The fitting model only incorporates the reaction of radicals at the bottom of the trench. If oxygen radical losses at the trench sidewalls play role, the chemically enhanced ion-neutral synergy model underestimates the fluorine reaction probability. The fluorine reaction probability is also underestimated if the fluorine adsorption probability has been set too low.

The ion-induced desorption coefficient of oxygen in the chemically enhanced ion-neutral synergy model was calculated using the fit parameter  $b$  and the measured oxygen-to-ion flux ratio. It showed that many tens to hundreds of oxygen atoms are removed per ion impact. The binary system of silicon tetrafluoride and silicon dioxide is considered, but such a high number is difficult to explain by sputtering of silicon dioxide. However, in reality the reaction mechanism is more complex with a continuum of surface states from completely fluorinated to completely oxidised. The reaction probability decreases with the oxygen fraction in the reaction layer, which is determined by the oxygen-to-ion flux ratio. The influence of silicon oxyfluorides is included in this representation. The boiling point of  $\text{Si}_2\text{OF}_6$  is  $-23.3\text{ }^\circ\text{C}$  compared to  $-86.0\text{ }^\circ\text{C}$  for  $\text{SiF}_4$  and it cannot be excluded that  $\text{Si}_2\text{OF}_6$  is slightly volatile in the cryo-process [19]. In literature it has actually been shown that  $\text{SiOF}_2$  and  $\text{Si}_2\text{OF}_6$  have a vapour pressure comparable to  $\text{SiF}_4$ , so that these molecules can desorb without the interference of an ion [20]. Only if multiple silicon atoms are linked by oxygen atoms the etch rate is reduced. In this view the oxygen radicals form a sort of network with the silicon atoms and the fluorine radicals terminate the molecules. The function of the ions is to sputter the oxidised species and to break-up the network into smaller molecules that are volatile.

Ideally, the trench profile and etch rate are controlled independently, but the plasma conditions often influence both simultaneously. The fluorine radical flux determines the oxygen radical flux that is needed to prevent lateral etching. A fluorine-to-oxygen flux ratio of 199 and a fluorine-to-oxygen flux ratio of 44 were observed for ECR and ICP etching, respectively. Apparently, the fluorine-to-oxygen flux ratio has to be lower in anisotropic ICP etching due to the different plasma conditions such as pressure and bias voltage. Tuning of the oxygen radical-to-ion flux ratio causes the switching between ARDE and ARIE. However, the ion flux and the ion energy are also factors that are important for profile control and cannot be chosen arbitrarily. Higher ion flux and ion energy lead to a more negative taper due to sidewall erosion deeper in the trench. ARIE has only been observed for lower ion energies. The average absolute angle of incidence is larger for lower ion energies, so that erosion of the sidewall passivation is relatively stronger. In that case the oxygen radical-to-ion flux ratio has to be increased to prevent lateral etching, which favours ARIE. Ion-neutral collisions in the plasma sheath also increase the angle of incidence. In ICP etching it has not been possible to make anisotropic profiles with lower bias voltages due to the forming of surface roughness.

Tuning of the etching process is also possible with the substrate temperature. At a lower temperature the oxidised species are less volatile and a lower oxygen flux is sufficient for sidewall passivation. However, the oxidised species are also more difficult to remove by ion bombardment and it is hard to estimate whether the sidewall taper becomes more positive or negative. A more negative taper has been observed for decreased temperatures while the oxygen flux is kept constant [21]. This is explained by the depletion of oxygen radicals, which is stronger than the depletion of fluorine radicals, so that the sidewall passivation becomes weaker in deep trenches. For increased temperatures the roles are interchanged. The adsorption of fluorine is larger than the adsorption of oxygen leading to a lateral etch below the mask and a positive sidewall taper deeper down the trench. For example, this is visible in figure 3.23a.

### **3.4 Monte Carlo simulation of anisotropic trench etching with oxygen passivation**

In the previous sections the experimental results are analysed with physical models, which only consider a limited number of interactions between the fluorine radicals, the oxygen radicals and the ions. For that reason numerical models based on the Monte Carlo method are useful to investigate the etching process because all relevant interactions can be considered. In this section the etching mechanism and the profile evolution are investigated by comparing the results of a Monte Carlo simulation model with the experimental results.

#### **3.4.1 The Monte Carlo simulation model**

An etching simulator based on the Monte Carlo method that has been developed at the University of Orléans was used to model the cryo-process [22]. Details of the model have already been described in literature and they are only briefly summarised [23]. A 2-dimensional structure is considered, which is composed of a mask and a silicon substrate as shown in figure 3.26. It is defined by a cellular discretisation, which describes both the geometry and the surface composition. In this research the slope of the mask is set to  $0^\circ$  with the substrate normal. The size of each cell is one cubic nanometre and in accordance with the silicon density this corresponds to fifty atoms per cell. The etching process is treated by interactions between the incident plasma species and the substrate atoms. The Monte Carlo approach allows the introduction of chemical and physical mechanisms with a probability distribution. Typical examples are neutral adsorption and desorption, spontaneous chemical etching, isotropic and specular reflection of ions, preferential sputtering, passivation layer formation and redeposition of etched species. All these mechanisms play a role in the profile evolution [24-26].

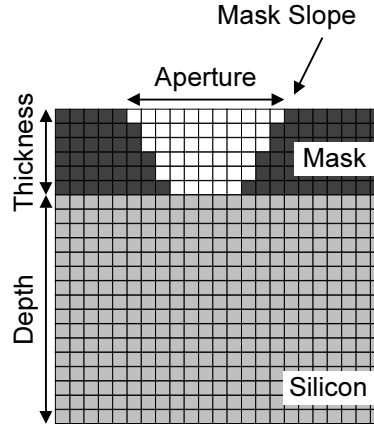


Figure 3.26 The 2-dimensional cellular discretisation in the Monte Carlo simulation model. The structure is composed of a mask with an aperture and a silicon substrate.

In an  $\text{SF}_6\text{-O}_2$  plasma the two main radicals are fluorine and oxygen atoms. For these radicals isotropic fluxes are considered above the mask and chemical reactions are realised in proportion to their adsorption probability. In the model physisorption is thus automatically followed by chemisorption creating a series of  $\text{SiO}_x\text{F}_y$  ( $0 \leq x \leq 2$ ,  $0 \leq y \leq 3$ ,  $x+y \leq 4$ ) cells on the surface. Only if a silicon cell is completely saturated with fluorine, the  $\text{SiF}_4$  cell is immediately desorbed thus modelling the spontaneous chemical etching. In all other cases ion-assistance is needed to remove the cell, which is described in the next paragraph

To include ion-assisted effects, a model of the ion transport through the plasma sheath, which is connected to the surface module, calculates the angular and energetic distribution function of the incident ions. When an ion strikes the surface the preferential sputter yield is determined. The latter depends on the ion energy, angle of incidence and the nature of the impacted surface site. The  $\text{SiO}_x\text{F}_y$  sputter yield  $Y_{x,y}$  is calculated according to

$$Y_{x,y} = \alpha_{x,y} \cdot A \cdot (\sqrt{E_i} - \sqrt{E_T}) \quad 3.4$$

as a function of the ion energy  $E_i$  where  $E_T$  is sputter energy threshold,  $A$  the square root of energy normalised sputter yield and  $\alpha_{x,y}$  the modulation factor. For the Si sputter yield  $Y_{0,0}$ , the results of  $\text{SF}_x^+$  ion beam etching of silicon are used where the sputter energy threshold  $E_T$  is 6 eV and the prefactor  $A$  is 0.15 [27]. This value incorporates the effect that the Si sputter yield increases if the surface is covered with fluorine. The silicon sputter yield for argon ions is approximately 1 order of magnitude smaller [28]. For Si cells the factor  $\alpha_{0,0}$  is equal to one and  $Y_{0,0}$  is 0.79 for a typical ion energy of 60 eV. The factor  $\alpha_{x,y}$  is modulated



for other  $\text{SiO}_x\text{F}_y$  cells. The most extreme values are the factor  $\alpha_{2,0}$  of 0.4 for  $\text{SiO}_2$  cells and the factor  $\alpha_{0,3}$  of 1.3 for  $\text{SiF}_3$  cells.

Redeposition of sputtered species is studied by considering their adsorption on the trench sidewalls. Local surface displacement is thus modelled by disappearance or appearance of a  $\text{SiO}_x\text{F}_y$  cells for etching or redeposition respectively.

The simulation results are compared to the deep anisotropic silicon etching investigated by *in situ* interferometry. This was described in subsection 3.3.5. The fluorine radical, oxygen radical and ion flux in the Monte Carlo simulation model are comparable to the fluxes in the etching experiment for a realistic comparison. In the ICP reactor a fluorine radical partial pressure of 1.27 Pa and an oxygen radical partial pressure of 0.032 Pa were determined for comparable plasma conditions. The fluorine radical flux to the substrate was thus approximately a factor of 40 higher than the oxygen radical flux. In other words the oxygen percentage was 2.5%. In a particular experiment the flow of oxygen was slightly adjusted to obtain perfect anisotropy. The measured ion current density was  $0.39 \text{ mA}\cdot\text{cm}^{-2}$  on the substrate holder position directly below the source and it was  $0.07 \text{ mA}\cdot\text{cm}^{-2}$  on the position 8.0 cm downstream. The fluorine and oxygen radical fluxes did not vary. This gives fluorine radical-to-ion flux ratios from  $1.48\cdot 10^3$  to  $8.26\cdot 10^3$  depending on the position.

### 3.4.2 Profile evolution as a function of the oxygen flux

For the profile simulations a radical-to-ion flux ratio of  $0.950\cdot 10^3$  was chosen. It is of the same order of magnitude as for the experiments and it is already high in comparison with previous simulations and higher flux ratios have not yet been attempted [23]. The pressure was 2.8 Pa. The adsorption probability of fluorine and oxygen was set to 0.5 and 0.7 respectively. The adsorption probability for sputtered species was initially set to 0.5. The value for fluorine is based on the Knudsen transport results of horizontal lines described in subsection 3.3.2. It has been shown that the oxygen adsorption probability is near unity on bare silicon, but it is reduced on a covered silicon surface [29]. In the simulation model two sites per silicon atom are available for oxygen adsorption. Correspondingly, an average value of 0.7 takes into account the reduction of the oxygen adsorption probability in the simulation model.

The simulated trench profiles for an increasing oxygen percentage of 0%, 5% and 7.5% of the total radical flux are given in figure 3.27a, 3.27b and 3.27c, respectively. The mask width and thickness are  $0.50 \mu\text{m}$  and  $0.25 \mu\text{m}$ , respectively. Intermediate profiles are shown for each  $0.50 \mu\text{m}$  etch step. The depth of the profiles is  $2.00 \mu\text{m}$  except for the trench in figure 3.27a because the limits of the simulation grid are reached in the lateral direction. The simulations show that oxygen is necessary for anisotropy. Without oxygen there is a high lateral etch rate corresponding to purely isotropic etching [23]. The best anisotropy is obtained for an oxygen percentage of 5%, because most lateral etching is suppressed. This percentage is rather high compared to the 2.5% observed in the experiments. However, in the simulation the ion flux is higher leading to more sidewall erosion, and moreover, in the

experiment molecular oxygen plays a role in the surface passivation. Sharp silicon spikes appear on the bottom of the trench for 7.5% oxygen. This is similar to the forming of silicon grass due to micromasking, which is experimentally observed as a result of overpassivation. Reducing the adsorption probability for sputtered species to 0.0 improves the trench profile, which is shown in figure 3.27d for 5% oxygen.

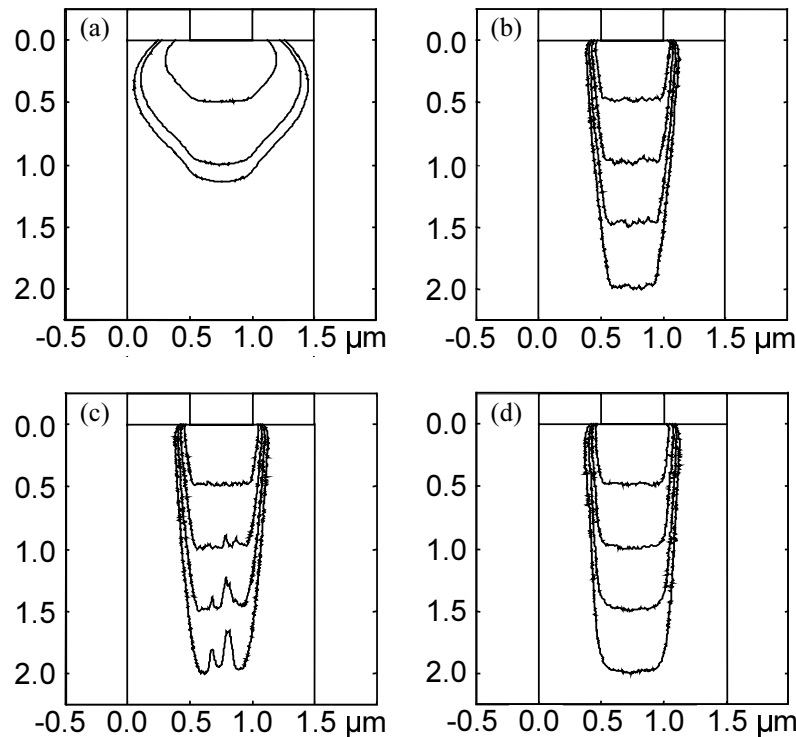


Figure 3.27 Simulation results for a  $0.5 \mu\text{m}$  wide trench with different oxygen percentages. (a) When no oxygen is added the profile is strongly isotropic. (b) The passivation is optimal for 5% oxygen and the profile is anisotropic. (c) Micromasking appears for an increase to 7.5% oxygen. (d) If the adsorption probability of the sputtered species is reduced from 0.5 to 0.0 for 5% oxygen the sidewalls change from positively tapered to vertical.

### 3.4.3 Simulation of deep trench etching and comparison with experiment

The etching of a deep trench was simulated with an adsorption probability for sputtered species of 0.0. The final aspect ratio of the  $0.50 \mu\text{m}$  wide trench was 10. In figure 3.28 this trench is compared to the deep anisotropic trenches etched in the ICP reactor. The trench profiles are very similar regarding anisotropy and lateral etch rate emphasising the accuracy

of the Monte Carlo simulation. The quantitative agreement of the simulated and experimental initial etch rate is very good with  $4.8 \mu\text{m}\cdot\text{min}^{-1}$  and  $5.2 \mu\text{m}\cdot\text{min}^{-1}$  respectively. Although the lateral etch rate of  $0.14 \mu\text{m}\cdot\text{min}^{-1}$  for the simulation is larger than the  $0.03 \mu\text{m}\cdot\text{min}^{-1}$  for the experiment. The investigation of the etch rate as a function of the aspect ratio is presented in the next paragraph. In the simulation the bottom of the trench becomes gradually faceted. A decreasing ion flux in the corners of a trench due to the angular distribution of the ions could be the cause. Angle dependent sputter yield and crystal orientation dependent etching are not included in the simulation. However, these effects could play a role in the plasma etching experiments.

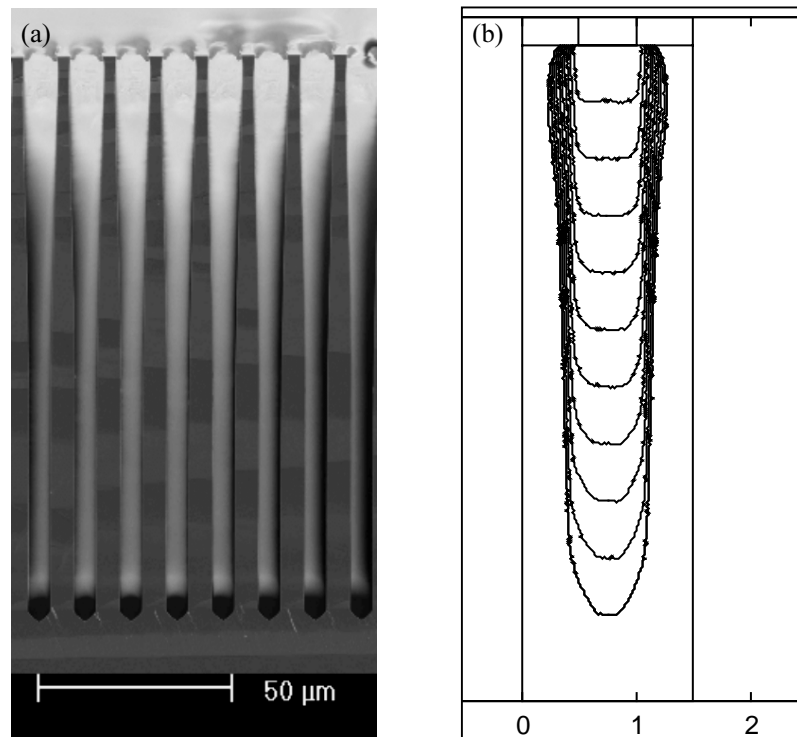


Figure 3.28 Comparison of deep trenches obtained for comparable conditions with (a) ICP etching and (b) Monte Carlo simulation. Both results show a lateral etch in the top part directly below the mask, a straight anisotropic profile in the middle part and an apex at the bottom of the trench.

The simulated etch rate is plotted as a function of aspect ratio in figure 3.29. Corresponding results for the measured etch rate of deep anisotropic trenches are given in figure 3.25. The etch rate is fitted with the Knudsen transport model and the chemically enhanced ion-neutral synergy model. The fluorine reaction probability at zero aspect ratio is 0.41 and

0.44, respectively. There are no visible differences between the two models. This is due to the low oxygen surface coverage of 0.12 in the chemically enhanced ion-neutral synergy model. In this case the etch rate behaviour is mainly governed by Knudsen transport of fluorine radicals.

In the simulations the input is known, so that the fluorine reaction probability can be calculated exactly from the initial etch rate of  $4.8 \mu\text{m}\cdot\text{min}^{-1}$  and the fluorine radical flux. In this case it is 0.33. This value is lower than in the models, which shows that some effects are not incorporated in the models. For example, sidewall reactions that are responsible for the small lateral etch reduce the fluorine flux. The etch rate decreases more quickly as a function of aspect ratio, which effectively results in a higher reaction probability in the fitted models.

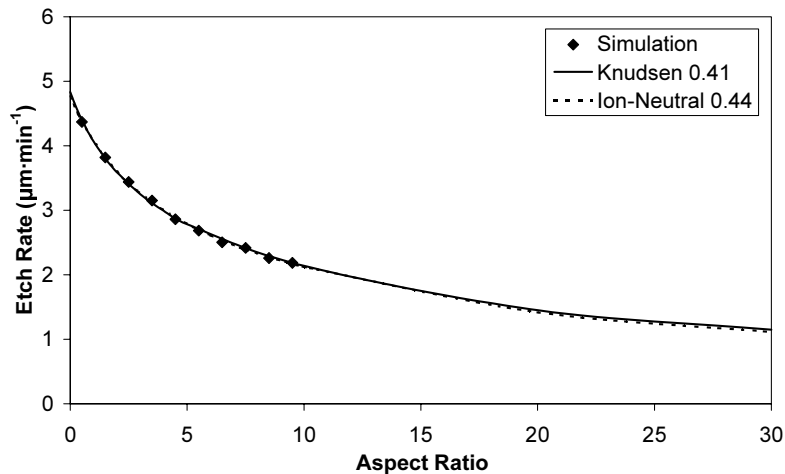


Figure 3.29 Aspect ratio dependent etching for the Monte Carlo simulation of a deep trench. The data points are fitted with the Knudsen transport model (solid curve) and the chemically enhanced ion-neutral synergy model (dotted curve).

Another remark concerns the fit parameter  $b$  in the chemically enhanced ion-neutral synergy model, which is 7.3 for the simulation. The oxygen-to-ion flux ratio is 47.5. In this case the ion-induced desorption coefficient of oxygen has to be 243 to obtain the right value of  $b$ . However, this coefficient is only about 2.22 considering the sputter yield of  $\text{SiO}_2\text{F}_2$  cells. Many oxygen atoms have to be removed in other ways. For example, an oxidised cell can be removed without the interference of an ion if the cell under it is etched away. The chance of this is high because of the low oxygen percentage and the low oxygen surface coverage.

### 3.5 Conclusions

Deep anisotropic silicon etching in fluorine-based high-density plasmas at low temperatures is characterised by a complex interplay between fluorine radicals, oxygen radicals and ions. The spontaneous reaction of fluorine radicals results in isotropic etching because the reaction products are volatile. The oxygen radicals form a surface passivation layer at low temperatures, so that the etch rate is ultimately reduced to zero. The ions are essential in the etching mechanism because the oxidised species have to be sputtered, which leads to anisotropy due to the directionality of the ions. The extremely high etch yield observed for anisotropic silicon etching can be explained better with this etching mechanism. The fraction of reaction products that has to be removed by sputtering is much smaller than one because the oxygen radical flux is much lower than the fluorine radical flux. If the ion flux is low, a thick reaction layer is formed and the etching is ion-limited. As a result the fluorine reaction probability is low. If the ion flux is high, the reaction layer is largely removed and the etching is fluorine-limited. In this case the fluorine reaction probability is approximately 0.5. The etching mechanism has important consequences for the etching of high aspect ratio trenches. The transport of fluorine and oxygen radicals is dominated by sidewall collisions and has been described by the Knudsen transport model. The depletion of the radical fluxes with aspect ratio depends on the reaction probability. Aspect ratio controlled etching has been obtained by tuning the ion flux because the reaction probability depends on the ion flux. For a low reaction probability there is little depletion, which leads to ARIE. Conversely, for a high reaction probability the depletion is large, which results in ARDE. The etch rate has been modelled on the basis of a surface site balance of the fluorine radicals and the oxygen radicals where the fluorine radicals react spontaneously and the oxides are sputtered. ARIE and ARDE have been explained well with this chemically enhanced ion-neutral synergy model. Moreover, the etching process has been investigated by a Monte Carlo simulation model. It shows that oxygen is necessary to obtain anisotropic trench profiles and that ARDE is inherent to etching with a high ion flux.

### References

- [1] M. Puech and P. Maquin, *Applied Surface Science* **100-101**, 579 (1996)
- [2] M. Francou, J.S. Danel and L. Peccoud, *Sensors and Actuators A* **46-47**, 17 (1995)
- [3] T. Zijlstra, E. van der Drift, M.J.A. de Dood, E. Snoeks and A. Polman, *J. Vac. Sci. Technol. B* **17**, 2734 (1999)
- [4] P. Balk (Editor), *Materials Science Monographs* **32** *The Si-SiO<sub>2</sub> System*, 21 (Elsevier Science Publishers B.V., Amsterdam NL, 1988)
- [5] F.R. McFeely, J.F. Morar, N.D. Shinn, G. Landgren and F.J. Himpsel, *Phys. Rev. B* **30**, 764 (1984)
- [6] F.R. McFeely, J.F. Morar and F.J. Himpsel, *Surface Science* **165**, 277 (1986)

- 
- [7] J. Pelletier, *J. Phys. D.* **20**, 858 (1987)
- [8] A. Manenschijn, PhD Thesis *Ion Bombardment and Ion-Assisted Etching in RF Discharges*, (Delft NL, 1991)
- [9] G.S. Oehrlein, S.W. Robey and J.L. Lindström, *Appl. Phys. Lett.* **52**, 1170 (1988)
- [10] G.S. Oehrlein, *J. Vac. Sci. Technol. A* **11**, 34 (1993)
- [11] I. Ohlídal, F. Lukeš and K. Navrátil, *Surface Science* **45**, 91 (1974)
- [12] D.L. Flamm, V.M. Donnelly and J.A. Mucha, *J. Appl. Phys.* **52**, 3633 (1981)
- [13] K. Ninomiya, K. Suzuki, S. Nishimatsu and O. Okada, *J. Appl. Phys.* **58**, 1177 (1985)
- [14] H. Jansen, M. de Boer, R. Wiegink, N. Tas, E. Smulders, C. Neagu and M. Elwenspoek, *Microelectronic Engineering*, **35**, 45 (1997)
- [15] A.D. Bailey III and R.A. Gottscho, *Jpn. J. Appl. Phys.* **34**, 2083 (1995)
- [16] V.F. Lukichev, *Microelectronic Engineering* **41-42**, 423 (1998)
- [17] M.F. Doemling, N.R. Rueger and G.S. Oehrlein, *Appl. Phys. Lett.* **68**, 10 (1996)
- [18] G. Craciun, M.A. Blauw, E. van der Drift and P.J. French, *Proceedings of the 11<sup>th</sup> Conference on Solid-State Sensors and Actuators*, 612, (München DE, 2001)
- [19] R.C. Weast, D.R. Lide, M.J. Astle and W.H. Beyer, *Handbook of Chemistry and Physics* 70<sup>th</sup> Edition, (CRC Press, Boca Raton US, (1989)
- [20] G.G. Devyatykh, D.A. Pryakhin and A.D. Bulanov, *Inorganic Materials* **37**, 413 (2001)
- [21] S. Aachboun, P. Ranson, C. Hilbert and M. Boufnichel, *J. Vac. Sci. Technol. A* **18**, 1848 (2000)
- [22] G. Marcos, PhD Thesis *Simulation Numérique par Méthode Monte Carlo de la Gravure du Silicium en Plasma Fluoré. Etude du Rôle de l'Oxygène dans la Passivation. Comparaison avec des Résultats Expérimentaux*, (Orléans FR, 2002)
- [23] G. Marcos, A. Rhallabi and P. Ranson, *J. Vac. Sci. Technol. A* **21**, 1 (2003)
- [24] R.J. Hoekstra, M.J. Grapperhaus and M.J. Kushner, *J. Vac. Sci. Technol. A* **15**, 1913 (1997)
- [25] J.A. Levinson, E.S.G. Shaqfeh, M. Balooch and A.V. Hamza, *J. Vac. Sci. Technol. A* **15**, 1902 (1997)
- [26] V.K. Singh, E.S.G. Shaqfeh and J.P. McVittie, *J. Vac. Sci. Technol. B* **10**, 1091 (1992)
- [27] T. Chevolleau, P.Y. Tessier, C. Cardinaud and G. Turban, *J. Vac. Sci. Technol. A* **15**, 2661 (1997)
- [28] D.C. Gray, I. Tepermeister and H.H. Sawin, *J. Vac. Sci. Technol. B* **11**, 1243 (1993)

- [29] T. Engel, *Surface Science Reports* **18**, 91 (1993)





---

## Chapter 4

# Balancing the etching and passivation in time-multiplexed deep anisotropic dry etching of silicon

The Bosch process is very suitable for the fabrication of anisotropic silicon structures, but apparent limitations exist for the etching of high aspect ratio trenches. The essential plasma-material interactions and the transport of radicals and ions have been investigated quantitatively to improve the understanding of these limitations. These investigations make clear that insufficient removal of the polymer passivation layer from the bottom of the trench is a major limitation for high aspect ratio trench etching. Obviously, an increase of the ion flux, energy and directionality improve the removal of the polymer passivation layer and therefore the anisotropy of the Bosch process. This approach is further refined with the so-called triple pulse process described in chapter 5. The opposite of this approach is the reduction of the polymer deposition rate on the bottom of the trench to zero ideally, which is discussed in chapter 6.

The structure of chapter 4 is as follows. The influence of the  $\text{SF}_6$  and  $\text{C}_4\text{F}_8$  plasma conditions on the delicate balance of etching and passivation is clarified in section 4.1. In high aspect ratio trenches the balance, which determines the trench profile, shifts towards passivation, so that a positive sidewall taper develops narrowing the trench and eventually preventing the etching. Aspect ratio dependent etching (ARDE) and the impact of the ion-to-radical flux ratio on the trench profile are explained in section 4.2. It is shown that plasma etching with higher ion flux, higher ion energy and lower pressure leads to higher aspect ratios. The reduction of the ion flux in high aspect ratio trenches due to the ion angular distribution (IAD) is treated in section 4.3. The average absolute ion angle has been measured to quantify the adverse effect of the IAD on the profile of high aspect ratio trenches.

### 4.1 Profile control by balancing the etching and passivation pulse

In this section it is shown how the etching and passivation pulse can be tuned to obtain anisotropic profiles. In particular, the polymer passivation layer deposition can be used to effectively control the profile of the microstructures.

#### 4.1.1 Optimising anisotropy with passivation pressure and passivation pulse time

Several passivation pulse settings were investigated to optimise the anisotropy while keeping a high etch rate. The etching pulse settings were a  $\text{SF}_6$  flow of 300 sccm and an etching pulse time of 5 s. The pressure was proportional to the gas flow, because the butterfly valve was fixed in the completely open position. The ICP source power, the bias voltage and the substrate temperature were 2000 W,  $-50$  V and  $25$  °C respectively. The etch rate is plotted as a function of  $\text{C}_4\text{F}_8$  flow for three passivation pulse times in figure 4.1a. The points where the profile is anisotropic are encircled and coincide almost with the  $\text{C}_4\text{F}_8$  flow above which the etch rate decreases abruptly. The decrease of the etch rate is more gradual for a passivation pulse time of 2 s, which is an indication for the mixing of the etching and passivation gas.

Subsequently, the encircled points are plotted in the two-dimensional parameter space of the inverse effective passivation pulse time and the  $\text{C}_4\text{F}_8$  flow given by figure 4.1b. The additional point at a passivation pulse time of 3 s was measured in another experimental run leading to anisotropic etching. Besides, the curve is forced to go through the origin. The curve through the anisotropic etching points forms the boundary between polymer deposition and isotropic etching. In this case the adverse  $\text{SF}_6$  buffer formed by the secondary gas line is open, so that there is considerable mixing of the etching and passivation gas. The effective passivation pulse time is thus shorter than the nominal passivation pulse, and a certain mixing time is subtracted from the nominal passivation pulse to take this into account. The polymer deposition is thus less efficient for smaller passivation pulse times. The points are almost on a straight line through the origin for a mixing time of 0.6 s. The continuous line through the origin represents a constant  $\text{C}_4\text{F}_8$  dose (product of  $\text{C}_4\text{F}_8$  flow and pulse time) and thus a constant passivation layer growth.

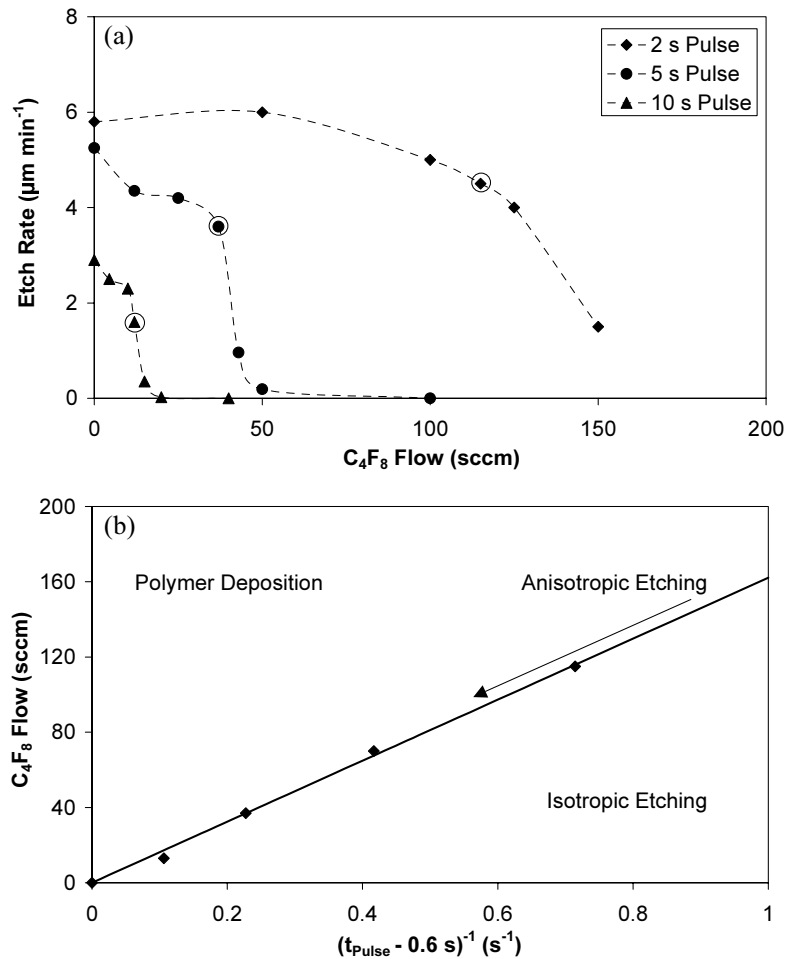


Figure 4.1 (a) The etch rate as a function of the  $\text{C}_4\text{F}_8$  flow for several passivation pulse times with a given etching pulse. At the encircled points the profile is anisotropic and the etch rate decreases abruptly. (b) The  $\text{C}_4\text{F}_8$  flow is plotted versus the inverse effective passivation pulse time for the encircled anisotropic etching points. The effective passivation pulse time is obtained by subtracting a mixing time of 0.6 s from the nominal passivation pulse time. For this mixing time the points are almost on a straight line through the origin, which separates regimes of polymer deposition and isotropic etching.

### Observing the balance of etching and passivation by ellipsometry

During time-multiplexed etching *in situ* ellipsometry was performed to follow the surface passivation and depassivation process. A transition from net passivation to net etching was observed for an increasingly weaker passivation pulse, while the etching pulse was constant with a SF<sub>6</sub> flow of 300 sccm and an etching pulse time of 6 s. The ICP source power, the bias voltage and the substrate temperature were 2000 W, -50 V and 20 °C respectively. Net passivation with a C<sub>4</sub>F<sub>8</sub> flow of 111 sccm and a passivation pulse time of 10 s is visible in figure 4.2a because of the strong increase of the polymer passivation layer thickness. Almost balanced etching and passivation with a C<sub>4</sub>F<sub>8</sub> flow of 74 sccm and a passivation pulse time of 5 s is visible in figure 4.2b. Net etching with a C<sub>4</sub>F<sub>8</sub> flow of 37 sccm and a passivation pulse time of 5 s is visible in figure 4.2c. The sharp peaks are due to surface roughness that is formed when the polymer passivation layer is partially etched through.

The net etching process is considered in more detail in figure 4.2d showing *in situ* ellipsometry which was performed as a function of the C<sub>4</sub>F<sub>8</sub> flow/pressure. In this experiment the plasma conditions were equal to the Bosch 1 process conditions given in appendix B, but the C<sub>4</sub>F<sub>8</sub> flow was 75 sccm, 115 sccm and 155 sccm successively. A higher C<sub>4</sub>F<sub>8</sub> flow/pressure leads to a thicker polymer passivation layer due to a quicker initiation of the deposition (shorter mixing time) and a higher deposition rate, and it leads also to a larger surface roughness. This is consistent with the trench profiles that are shown in figure 4.3 where an increase of the C<sub>4</sub>F<sub>8</sub> flow/pressure leads to stronger sidewall passivation resulting in a more positive sidewall taper.

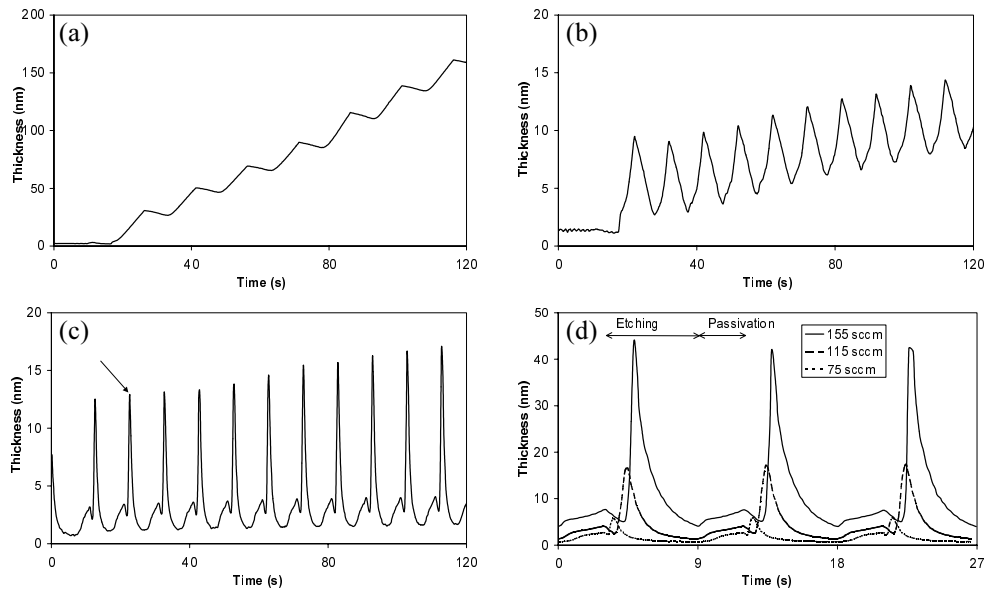


Figure 4.2 In situ ellipsometry during time-multiplexed plasma etching. (a) Net passivation. (b) Almost balanced etching and passivation. (c) Net etching. One of the sharp peaks that are due to surface roughness is indicated by the arrow. (d) In situ ellipsometry for a net etching process as a function of the  $C_4F_8$  flow.

### Trench profiles as a function of the $C_4F_8$ flow

In the transition range between isotropic etching and polymer deposition the sidewall taper changes from slightly negative to positive with increasing  $C_4F_8$  flow, which is shown in figure 4.3. Anisotropic profiles are obtained for a  $C_4F_8$  flow of 115 sccm, i.e., for the Bosch 1 process conditions given in appendix B. The passivation pulse time of 3 s is sufficiently long to stabilise the gas flow because the mass flow controllers have a response time of about 1 s. The etching pulse time is set to 6 s to obtain a reasonable duty cycle of 67 % and an acceptable lateral etch. Both the passivation and etching pulse time should be as short as possible to maximise the duty cycle and to minimise the lateral etch simultaneously. The  $SF_6$  flow of 300 sccm is near the maximum that can be pumped with high speed and the source power of 2000 W is the maximum for continuous operation of ICP reactor resulting in the maximal density of fluorine radicals and the maximal etch rate. The pressure is continuously changing between 6.4 Pa during etching and 2.6 Pa during passivation. For a bias voltage of  $-90$  V, the passivation layer is more quickly removed compared to a bias voltage of  $-50$  V, so that surface roughness due to inhomogeneity of the polymer layer is reduced.

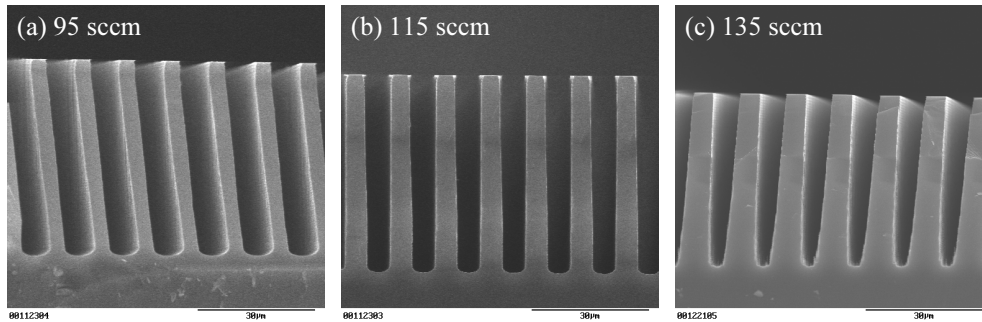


Figure 4.3 The sidewall taper of the trench profile changes from slightly negative to positive for an increasing  $C_4F_8$  flow. (a) 95 sccm, (b) 115 sccm and (c) 135 sccm.

#### Trench profiles with minimised gas mixing

The mixing of the etching and passivation gas is minimised by closing the adverse  $SF_6$  buffer formed by the secondary gas line and setting the  $SF_6$  flow to 150 sccm, which is close to the  $C_4F_8$  flow. Trenches etched with a  $C_4F_8$  flow of 105 sccm, 150 sccm and 195 sccm are shown in figure 4.4. The balancing of the etching and passivation behaviour changes appreciably because the passivation behaviour is almost identical for a large range of  $C_4F_8$  flows/pressures [1]. This implies that the balancing of the etching and passivation can only be achieved by changing the pulse times. A thicker passivation layer is just achieved by a longer passivation pulse. Tuning the passivation pulse with the pulse time is more transparent than tuning with the magnitude of the  $C_4F_8$  flow/pressure, because the plasma conditions do not change this way.

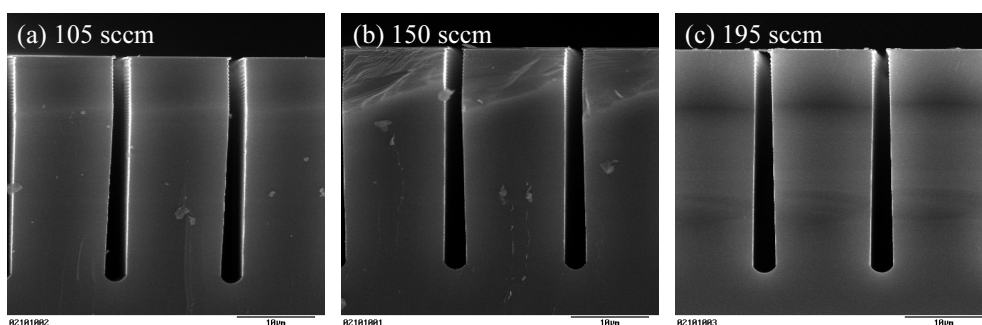


Figure 4.4 The sidewall taper of the trench profile is nearly independent of the  $C_4F_8$  flow. (a) 105 sccm, (b) 150 sccm and (c) 195 sccm.

### Improved sidewall passivation at lower substrate temperatures

Substrate temperature is an important factor for the deposition of the polymer passivation layer. Figure 4.5 shows SEM pictures of trenches etched at 25 °C and 0 °C with a passivation pulse time of 3 s and 2 s respectively. The trenches are nearly identical. Apparently, the adsorption probability of  $CF_x$  radicals is higher at lower temperatures because the sidewall erosion by ion bombardment is unaffected by the substrate temperature. The more effective passivation pulse at a lower temperature saves one third of the  $C_4F_8$  consumption and improves the duty cycle.

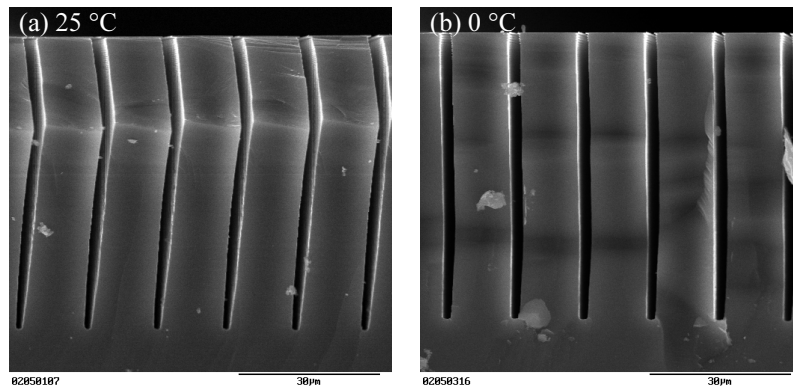


Figure 4.5 Comparison of trench profiles obtained with the Bosch process as a function of the substrate temperature. (a) 25 °C with a passivation pulse time of 3 s. (b) 0 °C with a passivation pulse time of 2 s.

### Sidewall ripples and polymer redeposition

The formation of sidewall ripples is inherent to the Bosch process and is the direct result of the alternation of etching and passivation pulses. For some applications, such as optical waveguides that need perfectly smooth surfaces, sidewall ripples are a severe problem. The sidewall ripples, which are visible in figure 4.6a, diminish deeper down the trench, because the fluorine radical flux decreases due to Knudsen transport. In addition, the ions that enter the trench with an off-normal angle of incidence are able to cause sidewall erosion deeper down the trench levelling off the sidewall corrugation. The passivation layer material on the sidewalls that has been removed by ion impact can also be redeposited, which is illustrated in figure 4.6b. In this experiment the anisotropic trenches were etched with the Bosch 1 process conditions. Subsequently, a polymer passivation layer was deposited for 2 min and an etching step of 4 min (corresponding to a duty cycle of 67 %) was performed. During the last step only a small lateral etch is found instead of an isotropic etch. This indicates that redeposition of the passivation layer from the upper sidewalls or the reactor walls plays a

role in the profile evolution during trench etching [2]. In literature, adjustments of the plasma conditions are given to minimise the sidewall ripples [3,4]. Decreasing the etching pulse time is the first option. Minimal sidewall ripples can also be achieved by pushing the etching to a more ion-induced regime with an increased polymer deposition. A new balance between etching and passivation must be found to obtain anisotropic profiles.

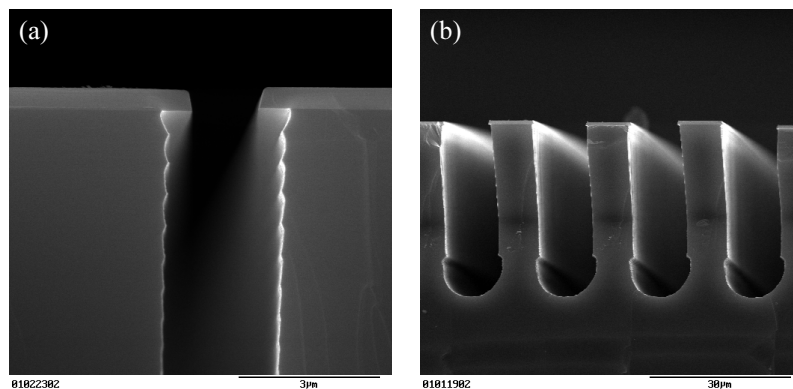


Figure 4.6 (a) Sidewall ripples are most pronounced at the top of the trench and diminish deeper down the trench. (b) Anisotropic trenches etched with the Bosch 1 process conditions are exposed to a continuous  $SF_6$  plasma for 4 min. Only a relative small lateral etch is observed near the bottom of the trench instead of isotropic etching.

#### 4.1.2 Optimising anisotropy by balancing the ion and radical flux

The ion and radical fluxes in the etching pulse play an important role in the balance between etching and passivation. To this aim the influence of the pressure on the trench profile was investigated. The gas flows were decreased while keeping all other plasma parameters constant. The  $SF_6$  and  $C_4F_8$  flow were 300 sccm and 115 sccm, 200 sccm and 77 sccm, 100 sccm and 38 sccm, and 50 sccm and 19 sccm respectively for figure 4.7a-d. The etching and passivation pulse time were 12 s and 6 s respectively. Two observations are made if the pressure decreases. First, the lateral etch directly below the mask decreases because of the lower fluorine radical flux. Second, the sidewall taper changes from positive to negative because the degree of ionisation increases. The balance between etching and passivation shifts towards etching for an increased ion-to-radical flux ratio. It is described in more detail for the etching of high aspect ratio trenches in section 4.2.



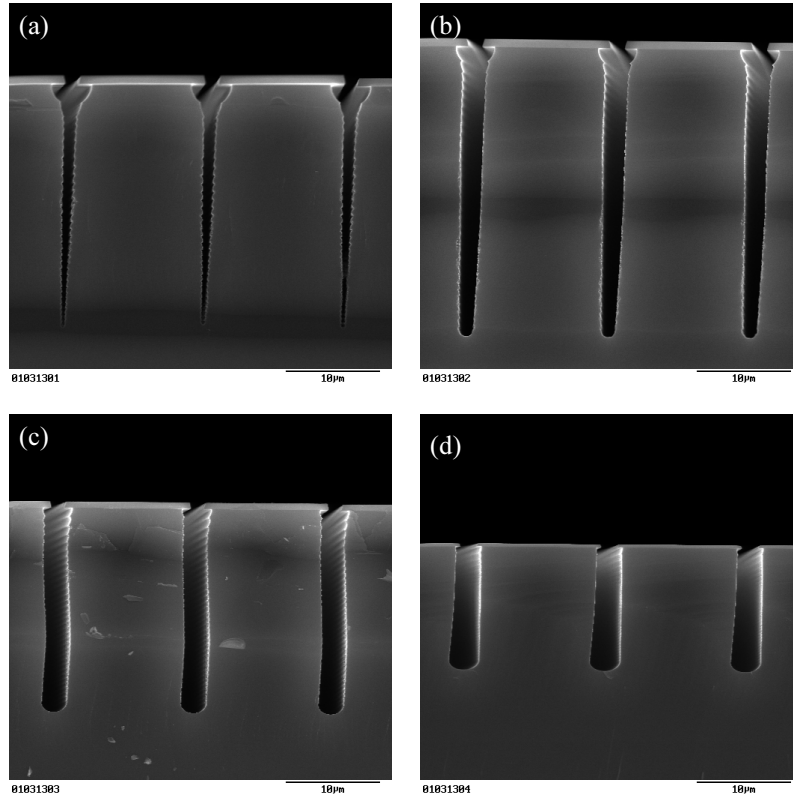


Figure 4.7 Effects of the pressure on the trench profile. The lateral etch decreases and the sidewall taper becomes more negative if the pressure decreases. The  $SF_6$  and  $C_4F_8$  flow are (a) 300 sccm and 115 sccm, (b) 200 sccm and 77 sccm, (c) 100 sccm and 38 sccm (the trench profile seems to zigzag, but this is caused by the imaging of a non-plane cross-section), and (d) 50 sccm and 19 sccm respectively.

## 4.2 The impact of the ion-to-radical flux ratio on the maximal obtainable aspect ratio

Aspect ratio dependent etching shows that there is a maximal obtainable aspect ratio, above which no trenches can be obtained for given plasma conditions. For this reason the influence of the ion-to-radical flux ratio is investigated to increase the maximal obtainable aspect ratio.

### 4.2.1 Aspect ratio dependent etching

The etching of anisotropic profiles was investigated to find the maximal obtainable aspect ratio. Trenches from 0.40  $\mu\text{m}$  to 20.0  $\mu\text{m}$  wide were etched for several time intervals with the Bosch 1 process conditions. The average etch rate is plotted as a function of aspect ratio in figure 4.8. The average etch rate is defined by the etch depth divided by the etch time and the aspect ratio is defined by the etch depth divided by the trench width. Mostly, the trench width varies with depth making it difficult to define the aspect ratio, so by definition, the trench width is measured in the middle of the trench giving the average trench width for a tapered profile. The results show ARDE for 5, 10 and 15 min etching including the turning point at an aspect ratio of 21. This turning point is clearly correlated with the bowing of the sidewalls beyond a certain aspect ratio. The corresponding SEM picture of trenches with a 1.5  $\mu\text{m}$  wide mask aperture is shown in figure 4.9. When the two sidewalls converge, the vertical etching is stopped and the average etch rate decreases quickly. Still, the slow lateral etching persists, which reduces the aspect ratio and thus causes the turning point of the curves in figure 4.8. For 1 and 2 min etching the decrease of the etch rate is steeper, thereafter the slope becomes less steep for longer etch times approaching an asymptotic value after 5 min. So, the etching is not only aspect ratio dependent, but apparently, also time-dependent.

The time-dependent effect can be explained by looking at the difference in etching for wide and narrow trenches transforming it to a shape-dependent effect. For narrow trenches the lateral etch is large compared to the mask aperture. The fluorine radical flux that enters the trench is distributed over an area that is much wider than the mask aperture reducing the fluorine radical flux to the silicon. Heafer's theorem relates the total vacuum conductance of a series of elements to the vacuum conductance of each element [5]. According to this theorem, this effect can easily reduce the etch rate by one third for low aspect ratio trenches. However, it also follows that the decrease of the etch rate is negligible for high aspect ratio trenches. In that case the fluorine transport is limited by sidewall collisions instead of the mask aperture. So, for narrow trenches the etch rate is lower than expected for short etch times, but the difference diminishes for long etch times in line with the observations. The polymer passivation can also reduce the etch rate for short etch times if the deposition rate is higher in shallow trenches. It has been shown in literature that a small sidewall taper does not influence the etch rate [6]. The modifications of the fluorine radical flux and the etched silicon area cancel out leading to a zero change of the etch rate.

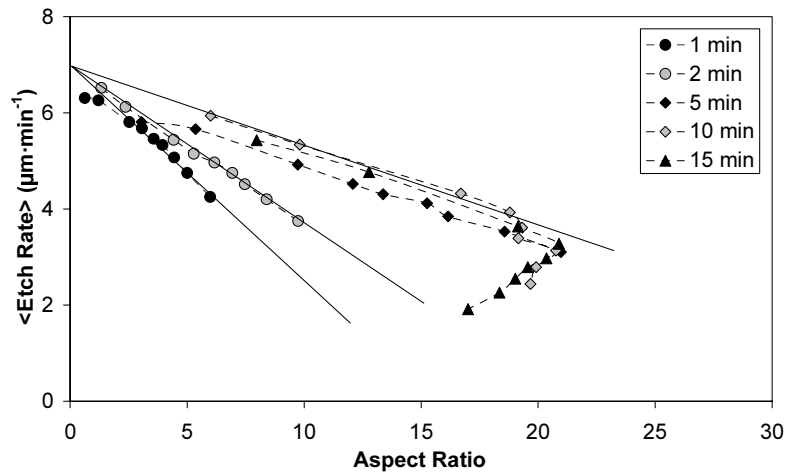


Figure 4.8 ARDE for the Bosch 1 process conditions. Except for 1 min and 2 min etching the curves more or less coincide including the turning point at an aspect ratio of 21.

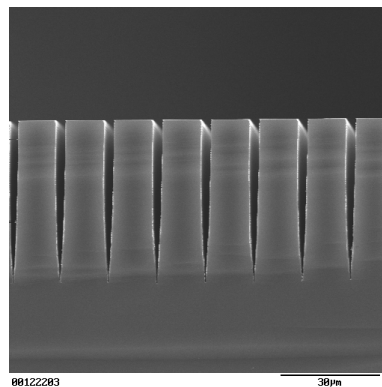


Figure 4.9 The profile of trenches with a 1.5 μm wide mask aperture that are etched with the Bosch 1 process conditions for 15 min. The maximal obtainable aspect ratio has been reached because the sidewalls have converged.

#### 4.2.2 Optimising the maximal obtainable aspect ratio by tuning the ion-to-radical flux ratio

The etching of structures with the highest possible aspect ratio is the ultimate goal and thus the point where the sidewalls coincide, should be delayed as long as possible. Presumably, high aspect ratio trench etching is limited by insufficient polymer removal from the trench

bottom. A higher or a more collimated ion flux improves the removal of the passivation layer especially in the corners of the trench where the ions are shadowed by the mask [6]. The ion bombardment is made stronger in three ways: (1) increasing the bias voltage: higher ion energy, (2) decreasing the substrate-to-source distance: higher ion flux, and (3) decreasing the pressure: higher ion flux and lower radical flux. The fluorine radical density is approximately proportional to the pressure, so it is nearly constant in the first two cases, but the ion-to-radical flux ratio is increased considerably in all three cases. ARDE results and a fit of the Knudsen transport model with a reaction probability of 0.5 are shown in figure 4.10, 4.11 and 4.12 respectively, which demonstrates that the maximal obtainable aspect ratio is increased for all three improved plasma conditions. The decay of the fluorine radical flux by is given in these three figures for comparison [7].

### Bias voltage

The DC bias voltage was increased from  $-90$  V to  $-150$  V, and the  $C_4F_8$  flow was increased from 115 sccm to 140 sccm to keep the sidewall taper constant. The samples were etched for 15 min. The increase of the  $C_4F_8$  flow indicates that the sidewall erosion is larger for a higher bias voltage giving the ions a higher energy. The results shown figure 4.10. The maximal obtainable aspect ratio is increased from 21 to 24.

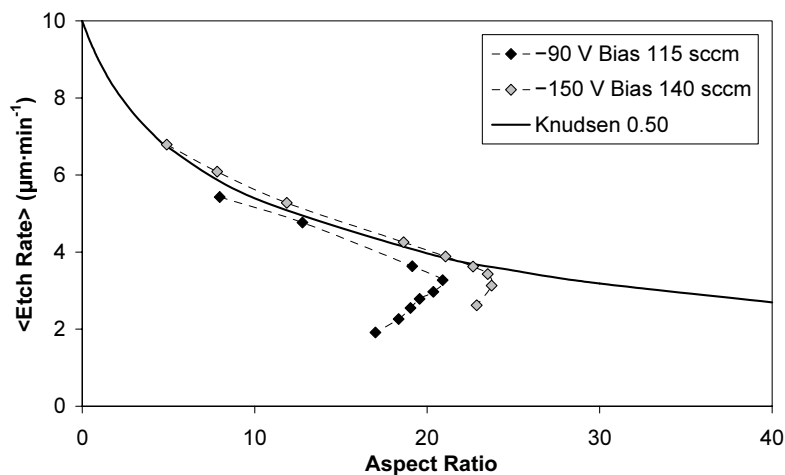


Figure 4.10 ARDE for an increased bias voltage shows that the turning point is shifted to a higher aspect ratio. The decay of the fluorine radical flux due to Knudsen transport with a reaction probability of 0.50 is given for comparison.

### Ion flux

By reducing the substrate-to-source distance the ion flux was increased by a factor of 6, whereas the fluorine radical flux remained approximately constant. The ion density was measured through the upper ( $2.57 \cdot 10^{10} \text{ cm}^{-3}$ ) and lower ( $4.93 \cdot 10^9 \text{ cm}^{-3}$ ) window of the reaction chamber a couple of centimetres above the substrate holder in a continuous  $\text{SF}_6$  plasma (250 sccm, 2100 W). Assuming exponential decay the ion density can be calculated in the upper and lower substrate holder position and for any position in between. The measured fluorine radical density showed a maximum variation of 20% between the upper and lower window. Etch experiments of 15 min were carried out in the lower substrate holder position, in an intermediate position with a factor of 3 increase of the ion flux and in the upper position with a factor of 6 increase of the ion flux. To obtain vertical sidewalls the  $\text{C}_4\text{F}_8$  flow was 115 sccm, 140 sccm and 160 sccm respectively. The results are shown in figure 4.11. The maximal obtainable aspect ratio is 21, 29 and more than 30 respectively. A drawback is that the mask erosion increases for higher ion fluxes.

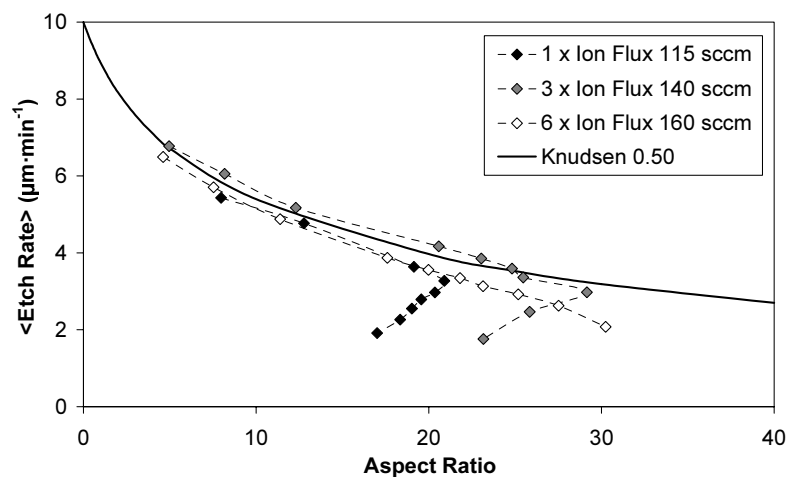


Figure 4.11 ARDE for an increased ion flux results in an increased maximal obtainable aspect ratio. The decay of the fluorine radical flux due to Knudsen transport with a reaction probability of 0.50 is given for comparison.

### Pressure

By setting the  $\text{SF}_6$  flow to 150 sccm and the  $\text{C}_4\text{F}_8$  flow to 55 sccm the pressure was decreased to 4.1 Pa and 1.2 Pa respectively. The etching pulse time was 12 s and the passivation pulse time was 6 s. The trench profile remains anisotropic with approximately half the pressure and doubled pulse times compared to the Bosch 1 process conditions. The

lateral etch also remains comparable, because the fluorine radical dose per pulse is approximately unchanged. The ion density in a continuous SF<sub>6</sub> plasma varies roughly inversely proportional with the square root of the pressure. The fluorine radical density is proportional to the pressure at high source power levels. Thus for a pressure decrease by a factor of 2, the ion-to-radical flux ratio increases approximately by a factor of 3. The results are shown in figure 4.12. The maximal obtainable aspect ratio is 24. Negative side effects of etching with a low pressure are the decrease of the selectivity due to the higher ion flux and the decrease of the etch rate due to the lower radical flux.

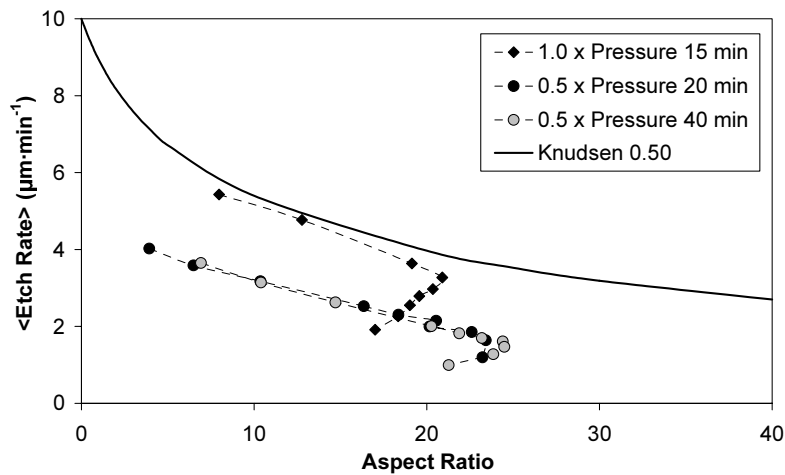


Figure 4.12 ARDE for a decreased pressure. The turning point is shifted to a higher aspect ratio. The decay of the fluorine radical flux due to Knudsen transport with a reaction probability of 0.50 is given for comparison.

### Trench profiles

The SEM pictures of trench profiles for a 1.5 μm wide mask aperture corresponding to etching with the high ion flux (15 min) and with the low pressure (40 min) are shown in figure 4.13a and 4.13b respectively. The anisotropy of high aspect ratio trenches is improved compared to the trenches shown in figure 4.9 that are obtained with the Bosch 1 process conditions. Although an increased ion-to-radical flux ratio leads to improved trench profiles and an increased maximal obtainable aspect ratio, the depassivation of the trench bottom remains the ultimate limiting factor. The depassivation is further refined with the triple pulse process, which is described in chapter 5. Methods that lead to a more polymer passivation layer deposition on the sidewalls than on the bottom of the trench could also

lead to further improvements. A systematic approach to achieve this is presented in chapter 6.

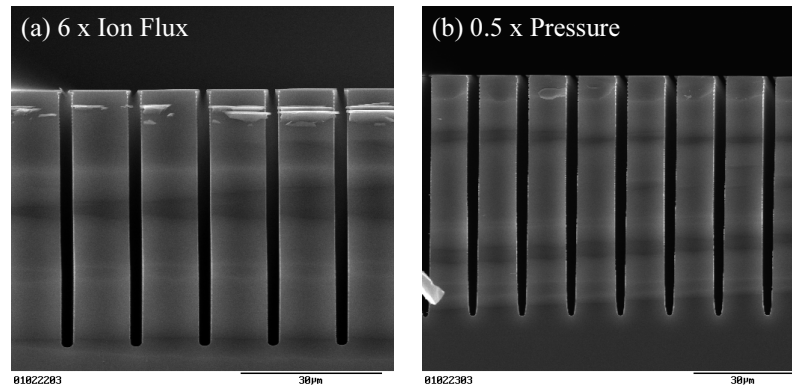


Figure 4.13 The profile of trenches with a  $1.5\ \mu\text{m}$  wide mask aperture. (a) Etching for 15 min with a factor of 6 increase of the ion flux. (b) Etching for 40 min with half the pressure. Anisotropy is much improved compared to the Bosch 1 process conditions.

### 4.3 Quantification of the ion transport in high aspect ratio trenches with the ion angular distribution

High aspect ratio trench etching is limited by the removal of the polymer passivation layer from the bottom of a trench. Increasing the ion-to-radical flux ratio leads to significant process improvements. In the Bosch process a large ion flux is essential for the profile evolution of deep trenches, because the polymer removal is strongly enhanced and the polymer deposition is reduced on bottom of the trench. In this section the transport of ions in high aspect ratio trenches is considered in more detail. The ions are directed perpendicular to the substrate after acceleration in the plasma sheath, but small deviations exist due to a small lateral thermal velocity. It is important to control the directionality of the ion beam, because it plays a crucial role in increasing the maximal obtainable aspect ratio.

#### 4.3.1 The influence of the average absolute ion angle on the ion transport

Divergence of the ion beam limits high aspect ratio trench etching, because only a fraction of the ions has a free path from the plasma to the bottom of the trench. The other ions collide with the sidewalls. Sidewall collisions cause erosion of the sidewall passivation layer and reduce the ion flux to the bottom of the trench. So divergence of the ion beam leads to a stronger lateral etch and less efficient depassivation. The shadowing of the ion

flux by the mask in a deep trench is schematically depicted in figure 4.14. The ion velocity is resolved in a radial (parallel to the substrate surface) and an axial (perpendicular to the substrate surface) component. The deviation of the ion velocity from the direction perpendicular to the substrate surface is given by the ion angle  $\theta$ . The frequency of occurrence of  $\theta$  is specified by the ion angular distribution (IAD).

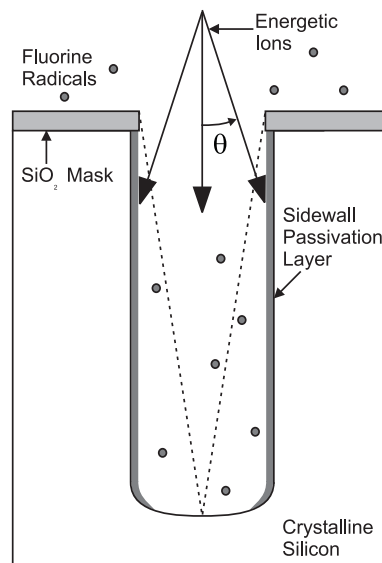


*Figure 4.14 Shadowing by the mask leads to a reduced ion flux in a deep trench because of the IAD. For example, only the ions that stay within the dotted sector have a free path to the middle of the bottom of the trench and are not lost by sidewall collisions.*

A part of the average radial thermal ion energy is intrinsic due to heating in the plasma source and cannot be avoided [8,9]. Besides, several mechanisms are identified that broaden the IAD: (1) ion-neutral collisions in the plasma pre-sheath and plasma sheath, (2) defocussing by the field curvature due to the surface topography, (3) bending by electrical fields due to the differential charging of insulating masks, and (4) the image force to the ions near the conducting silicon sidewalls. In the current etching plasmas, ion-neutral collisions provide the dominant contribution to the broadening of the IAD. The average radial thermal ion energy typically has values between 0.2 eV and 0.5 eV when the ions reach the substrate [10-13]. Field curvature, differential charging and image force have much smaller effects on the IAD. These effects are only noticed when the ions are in the trench. Field curvature scales with trench width, so that this mechanism could play a role in sidewall erosion of open structures [14]. Differential charging has considerable effects only if the insulating mask thickness is much larger than the mask aperture width [15-17]. The



image force has a range on the nanometre scale so this will not have a noticeable effect on trenches wider than 0.40  $\mu\text{m}$ .

It is assumed that the radial ion velocity is described by a two-dimensional Maxwell distribution. For an infinitely long trench only the lateral ion velocity component (perpendicular to the trench direction) needs to be considered. The two-dimensional Maxwell distribution is thus converted to a one-dimensional IAD shown in figure 4.15. The tangent of  $\theta$  is equal to the ratio of the lateral and the axial ion velocity component, and the tangent is approximately linear because  $\theta$  is small. The average absolute ion angle  $\theta_{\text{IAD}}$  is given by

$$\theta_{\text{IAD}} = \arctan\left(\sqrt{\frac{k \cdot T_i}{\pi \cdot E_i}}\right) \quad 4.1$$

where  $k \cdot T_i$  is the average radial thermal ion energy and  $E_i$  the axial ion energy. In good approximation,  $E_i$  is proportional to the DC bias voltage plus the plasma potential and  $E_i$  is much larger than  $k \cdot T_i$ .

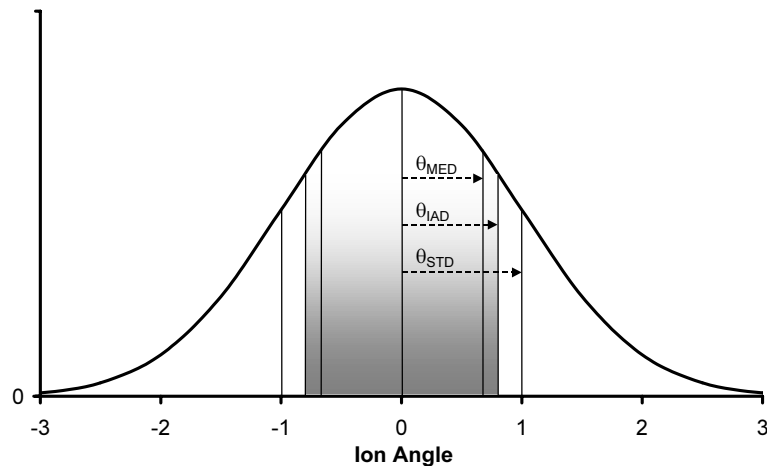


Figure 4.15 The one-dimensional ion angular distribution function. The ion angle is normalised by the standard deviation  $\theta_{\text{STD}}$ . The median and the average absolute ion angle are indicated by  $\theta_{\text{MED}}$  and  $\theta_{\text{IAD}}$  respectively. The shaded area between  $\pm\theta_{\text{IAD}}$  is a factor of 1.74 smaller than the area below the total curve.

Experiments show that a decrease of the ion flux by a factor of 3 or more while keeping all other plasma parameters constant leads to the formation of a severe positive sidewall taper. The similar reduction of the ion flux due to the IAD has comparable consequences for the

trench profile evolution. The aspect ratio where shadowing of the ions becomes substantial is quantified by the concept of a critical aspect ratio  $A_R^\theta$ . At the critical aspect ratio only ions with a sufficiently small angle ( $|\theta| \leq \theta_{IAD}$ ) have a direct path from the plasma to the middle of the bottom of the trench. The relation between  $\theta_{IAD}$  and  $A_R^\theta$  is given by

$$\theta_{IAD} = \arctan\left(\frac{1}{2 \cdot A_R^\theta}\right) \quad 4.2$$

The ion flux decreases by a factor of 1.74 at the critical aspect ratio for the one-dimensional IAD. In a typical situation,  $k \cdot T_i$  is 0.5 eV and  $E_i$  is 113 eV, so that  $\theta_{IAD}$  is  $2.1^\circ$  and  $A_R^\theta$  is 13. On the other hand, if  $k \cdot T_i$  is 0.2 eV, then  $\theta_{IAD}$  is  $1.4^\circ$  and  $A_R^\theta$  is 21. These numbers are consistent with the etching of real trenches. For the trench shown in figure 4.9 bowing sets in at an aspect ratio of about 14 leading to a maximal obtainable aspect ratio of 21. This shows that  $A_R^\theta$  is a reasonable measure for the maximal obtainable aspect ratio.

#### 4.3.2 Measurement of the average absolute ion angle

To verify the above analysis the average absolute ion angle was measured in real etching plasmas with a special overhang structure. A quantitative understanding of the reduction of the ion flux due to the IAD was obtained with this experiment because a precise comparison of the measured average absolute ion angle and the maximal obtainable aspect ratio was made. The overhang structure consisted of a membrane that blocks the ion flux. It was fabricated as follows. First, 750 nm low stress LPCVD  $Si_3N_4$  was deposited onto a silicon wafer, subsequently 5000 nm PECVD  $SiO_2$  and finally 250 nm low stress LPCVD  $Si_3N_4$ . The upper nitride layer was patterned with 100  $\mu m$  lines by RIE. After selective etching of the oxide layer in 13% BHF solution for 75 min a nitride membrane overhang of 5  $\mu m$  was obtained. A chromium layer was deposited by evaporation under an angle of  $45^\circ$ , so that there was a metal layer under the membrane. This was done to avoid charging of the lower nitride layer, which influences experiments where the ion energy plays a role. The membrane bends due to stress in the chromium layer. This can be avoided by using a membrane that is clamped at two sides forming a bridge.

The chromium layer has been etched in  $SF_6$  plasmas with  $-230$  V bias voltage. All four combinations of either 300 sccm  $SF_6$  or 150 sccm  $SF_6$  and either a low ion flux or a high ion flux are investigated to make a connection to the experiments of the previous section. In the open area the etch rate is maximal and under the membrane there is no etching, because it is a purely ion-induced etch process. Due to the IAD the etch rate will not stop abruptly under the membrane, but there is a transition region. Figure 4.16a gives the structure after etching and figure 4.16b is a close-up of the transition region directly below the edge of the membrane. The profile in the chromium layer depends on the form of the IAD, nevertheless a Maxwell distribution is assumed for further analysis.

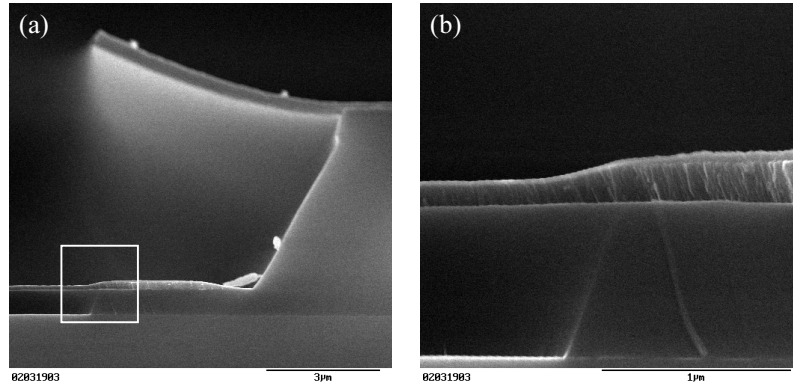


Figure 4.16 (a) The overhang structure used for the measurement of the average ion angle. Chromium was deposited on top of a silicon nitride membrane through a  $100\ \mu\text{m}$  wide window under an angle of  $45^\circ$ . Stress in the chromium layer bends the membrane. (b) Close-up of the transition region. The average absolute ion angle is calculated from the horizontal extent of the transition region.

Figure 4.17 shows the conceptual picture of figure 4.16. The median absolute ion angle  $\theta_{\text{MED}}$  is considered for further analysis because it is easily obtained from the profile in the chromium layer. By definition half of the ions has an absolute ion angle smaller than  $\theta_{\text{MED}}$ . For a Gaussian distribution  $\theta_{\text{MED}}$  is given by

$$\theta_{\text{MED}} = \arctan\left(\sqrt{\frac{k \cdot T_i}{4.45 \cdot E_i}}\right) \quad 4.3$$

The ratio  $k \cdot T_i$  over  $E_i$  is derived from this equation, so that  $\theta_{\text{IAD}}$  can be calculated. The median absolute ion angle is obtained in the following way. The etch depth exactly below the membrane edge is one half of the maximal value. The etch depth is one quarter and three quarters of the maximal value at the horizontal position where only ions with an ion angle larger than  $+\theta_{\text{MED}}$  and  $-\theta_{\text{MED}}$  hit the surface respectively. The tangent of  $\theta_{\text{MED}}$  is equal to the ratio of one half of the horizontal distance between these two positions and the height of the membrane edge above the chromium layer. The height is  $7\ \mu\text{m}$  due to bending of the membrane.

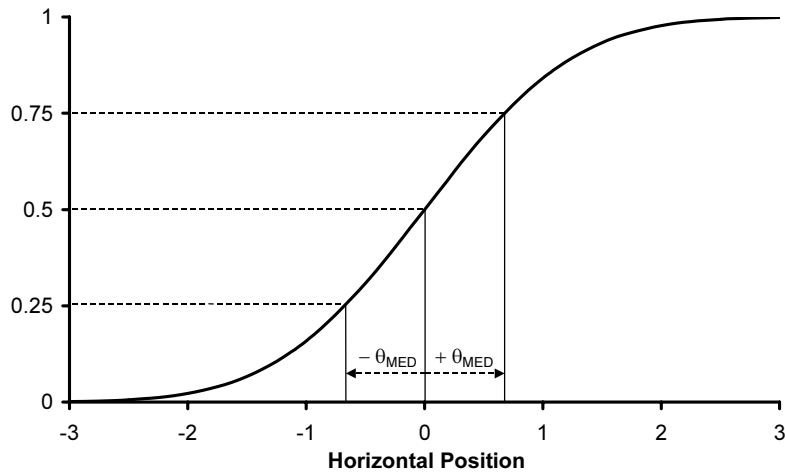


Figure 4.17 The layer profile in the transition region for a one-dimensional IAD as a function of the horizontal position below the membrane edge. The vertical scale is normalised by the maximal etch depth. The horizontal scale is normalised by the horizontal displacement of an ion that moves with an angle equal to  $\theta_{STD}$  from the membrane edge to the chromium layer. The etch depth is exactly 0.5 below the membrane edge. The etch depth decreases by  $\pm 0.25$  at the horizontal position that is equal to the horizontal displacement of an ion that moves with an angle equal to  $\pm \theta_{MED}$  from the membrane edge to the chromium layer.

The average absolute ion angle is given for the four combinations in table 4.1. The inaccuracy is due to the uncertainty in the measurement of the horizontal distance. Unfortunately, the membrane, which is curved due to stress in the chromium layer, bends back a little, because the chromium layer becomes thinner during etching. The membrane edge moves a little in the horizontal direction increasing the horizontal extent of transition region. The increase can be a significant fraction of the total horizontal extent. Because of this the values in table 4.1 are an upper limit. The chromium etch depth is approximately the same in the four circumstances, so that comparison among these values remains valid. Using equation 4.1  $\theta_{IAD}$  can be converted to  $k \cdot T_i$ . An average absolute ion angle of  $1.4 \pm 0.2^\circ$  corresponds to an average lateral thermal ion energy of  $0.49 \pm 0.14$  eV. This is consistent with values given in literature [10,16,18].

Table 4.1 The average absolute ion angle for a bias voltage of  $-230$  V. It is measured with the membrane overhang structure as a function of the  $SF_6$  flow and the ion flux.

Average Absolute Ion Angle	300 sccm $SF_6$	150 sccm $SF_6$
High Ion Flux	$1.1 \pm 0.2^\circ$	$1.4 \pm 0.2^\circ$
Low Ion Flux	$2.1 \pm 0.2^\circ$	$1.6 \pm 0.2^\circ$

Table 4.2 The critical aspect ratio for a bias voltage of  $-90$  V. It is calculated using the measured average absolute ion angle as a function of the  $SF_6$  flow and the ion flux.

Critical Aspect Ratio	300 sccm $SF_6$	150 sccm $SF_6$
High Ion Flux	$17.1 \pm 3.1$	$13.4 \pm 1.9$
Low Ion Flux	$8.9 \pm 0.8$	$11.7 \pm 1.5$

The critical aspect ratio is calculated with equation 4.2 to investigate the impact of the average absolute ion angle on the profile evolution. The average absolute ion angle measured for a bias voltage of  $-230$  V is extrapolated to a bias voltage of  $-90$  V to account for the lower ion energy in deep anisotropic trench etching according to equation 4.1. The critical aspect ratio values are given in table 4.2. In the next subsection these values are compared with the results of trench etching experiments under the same conditions.

In particular, the experiments for 300 sccm  $SF_6$  and a low ion flux are remarkable, because both for deep trench etching and ion angle measurement these conditions lead to a significantly lower maximal obtainable and critical aspect ratio respectively. This specific behaviour can be understood when the plasma sheath thickness and the mean free path are compared for the four different plasma conditions. The plasma sheath thickness is based on a bias voltage of  $-90$  V. The results are given in table 4.3. For 300 sccm  $SF_6$  and a low ion flux the plasma sheath thickness is much larger than the mean free path, so that the ions undergo the most ion-neutral collisions while traversing the plasma sheath and the broadening of the IAD is thus the largest. This shows once more, that a low  $SF_6$  flow/pressure and a high ion flux are favourable for the etching of high aspect ratio trenches.

Table 4.3 The plasma sheath thickness and the mean free path for a bias voltage of  $-90$  V. It is calculated as a function of the  $SF_6$  flow and the ion flux.

	300 sccm $SF_6$		150 sccm $SF_6$	
	Sheath Thickness (mm)	Mean Free Path (mm)	Sheath Thickness (mm)	Mean Free Path (mm)
High Ion Flux	2.76	1.63	2.03	2.83
Low Ion Flux	6.12	1.35	4.03	2.46

### 4.3.3 The impact of the ion angular distribution on the maximal obtainable aspect ratio

To verify the impact of the ion angular distribution on the maximal obtainable aspect ratio a new set of experiments was carried out. The plasma conditions of the etching pulse were identical to those used for the measurement of the average absolute ion angle except for the bias voltage. Two differences with the experiments in section 4.2 were introduced. First, the adverse  $SF_6$  buffer was closed, so that mixing of the gases was minimised. Second, a chromium mask was used instead of a  $SiO_2$  mask, so that it is possible to etch longer with high ion-to-radical flux ratios. The trench profile differences between a  $SiO_2$  and Cr mask are insignificant.

High aspect ratio trenches were etched for four different combinations of the plasma pressure and the ion flux. Table 4.4 gives the etching and passivation pulse times that resulted in anisotropic trench profiles for the four combinations of  $SF_6$  flow and ion flux. The  $C_4F_8$  flow was 150 sccm. The maximal obtainable aspect ratio that was achieved for each process is also given. The experimental inaccuracy in the maximal obtainable aspect ratio depends strongly on the aspect ratio of the trench and is about 10% in this range. The measurement of the trench width is the largest source of inaccuracy for these high aspect ratio trenches.

Table 4.4 The etching and passivation pulse time that results in anisotropic trench profiles and the maximal obtainable aspect ratio that has been achieved for four combinations of  $SF_6$  flow and ion flux.

		300 sccm $SF_6$	150 sccm $SF_6$
High Ion Flux	Pulse Time ( $SF_6 - C_4F_8$ )	6 s - 3 s	6 s - 3 s
	Maximal Obtainable Aspect Ratio	27±3	27±3
Low Ion Flux	Pulse Time ( $SF_6 - C_4F_8$ )	12 s - 3 s	12 s - 3 s
	Maximal Obtainable Aspect Ratio	22±2	28±3

The maximal obtainable aspect ratios given in table 4.4 show the same trend as the critical aspect ratios given in table 4.2, i.e. the maximal and critical aspect ratio obtained for 300 sccm  $SF_6$  and a low ion flux are significantly lower than the rest. So, the decrease of the ion flux due to the IAD strongly limits the depassivation in deep trenches. Especially in the corners of the trench the removal of the passivation layer becomes insufficient leading to a positive sidewall taper. This does not put aside the role that the radical fluxes play in the profile evolution, but it emphasises the prominent role of the ions in the etching mechanism.

#### 4.4 Conclusions

Deep anisotropic dry etching of silicon has been achieved in a wide range of plasma conditions by the tuning of the etching and passivation pulse in the time-multiplexed Bosch process. The etch rate in deep anisotropic trenches is a function of aspect ratio due to depletion of the fluorine radical flux and due to some polymer redeposition from the upper sidewalls. Anisotropic trench etching is limited to a certain aspect ratio where the sidewalls converge and the etch rate diminishes. Higher ion energy, higher ion flux and lower pressure push the process to higher aspect ratios. It has been demonstrated that deep anisotropic dry etching of trenches with an aspect ratio of more than 30 is feasible for high ion-to-radical flux ratios. Divergence of the ion beam leads to sidewall erosion and a reduction of the ion flux in deep trenches. The average absolute ion angle has been measured and compared quantitatively with trench etching experiments, which shows that a more directional ion flux leads to higher aspect ratios. The ion angular distribution is a fundamental limiting factor for high aspect ratio trench etching. The average absolute ion angle, which is increased by ion-neutral collisions in the plasma sheath, is minimised for higher ion flux and lower pressure.

## References

- [1] A.A. Ayón, R. Braff, C.C. Lin, H.H. Sawin and M.A. Schmidt, *J. Electrochem. Soc.* **146**, 339 (1999)
- [2] F. Lärmer, A. Schilp, K. Funk and M. Offenbergl, *Proceedings of the 12<sup>th</sup> IEEE International Conference on Microelectromechanical Systems*, 211 (1999)
- [3] B. Volland, F. Shi, P. Hudek, H. Heerlein and I.W. Rangelow, *J. Vac. Sci. Technol. B* **17**, 2768 (1999)
- [4] M. Chabloz, Y. Sakai, T. Matsuura and K. Tsutsumi, *Microsystem Technologies* **86-89**, 86 (2000)
- [5] J.F. O'Hanlon, *A User's Guide To Vacuum Technology 2<sup>nd</sup> edition*, 36 (Wiley, New York, USA, 1980)
- [6] J. Kiihamäki, *J. Vac. Sci. Technol. A* **18**, 1385 (2000)
- [7] J. W. Coburn, and H. F. Winters, *Appl. Phys. Lett.* **55**, 2730 (1989)
- [8] J.A. O'Neill, M.S. Barnes and J.H. Keller, *J. Appl. Phys.* **73**, 1621 (1993)
- [9] E.A. den Hartog, H. Persing and R. Claude Woods, *Appl. Phys. Lett.* **57**, 661 (1990)
- [10] J.R. Woodworth, M.E. Riley, D.C. Meister, B.P. Aragon, M.S. Le and H.H. Sawin, *J. Appl. Phys.* **80**, 1305 (1996)
- [11] J. Janes and C. Huth, *J. Vac. Sci. Technol. A* **10**, 3086 (1992)
- [12] G.S. Hwang and K.P. Giapis, *J. Vac. Sci. Technol. B* **15**, 70 (1997)
- [13] J. Zheng, R.P. Brinkmann and J.P. McVittie, *J. Vac. Sci. Technol. A* **13**, 859 (1995)
- [14] M. Ardehali, *Appl. Phys. Lett.* **64**, 169 (1994)
- [15] K.H.A. Bogart, F.P. Klemens, M.V. Malyshev, J.I. Colonell, V.M. Donnelly, J.T.C. Lee and J.M. Lane, *J. Vac. Sci. Technol. A* **18**, 197 (2000)
- [16] M.A. Vyvoda, M. Li and D.B. Graves, *J. Vac. Sci. Technol. A* **17**, 3293 (1999)
- [17] K.P. Giapis, G.S. Hwang and O. Joubert, *Microelectronic Engineering* **61-62**, 835 (2002)
- [18] E.S. Aydil, B.O.M. Quiniou, J.T.C. Lee, J.A. Gregus and R.A. Gottscho, *Materials Science in Semiconductor Processing* **1**, 75 (1998)



## Chapter 5

### Time-multiplexed directional depassivation with the triple pulse process

In chapter 4 it is shown that anisotropic silicon etching can be improved by increasing the ion-to-radical flux ratio. This is achieved by increasing the ion energy and the ion flux and by decreasing the pressure. As a result the directional depassivation, that is depassivation in the direction perpendicular to the substrate, is more efficient. However, the maximal obtainable aspect ratio is still limited. In this chapter new pulse sequences and new plasma chemistries are explored to push the performance of time-multiplexed etching beyond existing limits. In particular, the three essential sub-processes (silicon etching, surface passivation and directional depassivation) are independently optimised. The obvious way to achieve this goal is to perform the three sub-processes sequentially by introducing a third pulse after the passivation pulse.

The characteristics of the so-called triple pulse process are presented in section 5.1. Several oxygen-based depassivation chemistries ( $O_2$ ,  $CO_2$  and  $SO_2$ ) are explored. It is found that a low-pressure, high-density, oxygen-based plasma pulse removes the polymer passivation layer efficiently. The directionality of the ions is optimal for high aspect ratio trench etching because ion-neutral collisions are negligible. The performance of the triple pulse process regarding trench profile, etch rate and maximal obtainable aspect ratio is compared to the Bosch process in section 5.2.

#### 5.1 Optimisation of the depassivation pulse with a low-pressure, high-density, oxygen-based plasma

The Bosch process consists of a cycle of two plasma pulses, so that only silicon etching and surface passivation can be optimised independently. Directional depassivation on the bottom of the trench is performed in the first part of the etching pulse. Therefore, a process consisting of a repeated sequence of three pulses has been developed, so that directional depassivation can also be optimised independently [1]. The etching pulse is effectively longer, because silicon etching sets in directly when the etching pulse is switched on. However, the depassivation pulse also leads to increased erosion of the sidewall passivation layer, which is compensated by a longer passivation pulse. The effective duty cycle is reduced due to the depassivation pulse and the longer passivation pulse. In the following subsections several aspects of the so-called triple pulse process are further described. In subsection 5.1.1 and 5.1.2 it is shown that a depassivation pulse consisting of a reactive, low-pressure  $O_2$  plasma leads to anisotropic etching and removes the polymer passivation

layer very efficiently, respectively [2,3]. In subsection 5.1.3 the substantial sidewall taper range due to a controllable shift of the balance between sidewall deposition and erosion is described. In section 5.1.4 it is shown that the etch rate in deep trenches is limited by Knudsen transport of fluorine radicals in the room temperature triple pulse process. In subsection 5.1.5 the directional depassivation with O<sub>2</sub>, CO<sub>2</sub> and SO<sub>2</sub> is treated, which is aimed at a reduction of the lateral etch and an increase of the maximal obtainable aspect ratio.

### 5.1.1 Physical versus chemical depassivation

In this preliminary experiment the change from an inert to a reactive depassivation plasma was investigated for the triple pulse process. The third pulse consisted either of argon, nitrogen or oxygen. The triple pulse process was developed on the basis of the Bosch 2 process conditions given in appendix B. The directional depassivation chemistry varied and was 28.8 sccm Ar with 2 s depassivation pulse time for figure 5.1a, 30 sccm N<sub>2</sub> with 2 s depassivation pulse time in figure 5.1b, 30 sccm N<sub>2</sub> with 3 s depassivation pulse time in figure 5.1c and 30 sccm O<sub>2</sub> with 2 s depassivation pulse time in figure 5.1d. The pressure was 0.4 Pa, 0.5 Pa, 0.4 Pa and 0.6 Pa respectively.

With the more inert plasmas severe surface roughness was obtained, but the lateral etch was smaller. Increasing the depassivation pulse time for the N<sub>2</sub> plasma reduced the formation of surface roughness, but increased the lateral etch. Still, the profile shown in figure 5.1c is worse than the one obtained with the O<sub>2</sub> plasma because the shoulder, which is visible 15 μm below the mask, is due to excessive polymer growth that was not removed. So a low-pressure high-density O<sub>2</sub> plasma removes the polymer passivation layer most efficiently, but some sidewall passivation is also removed.

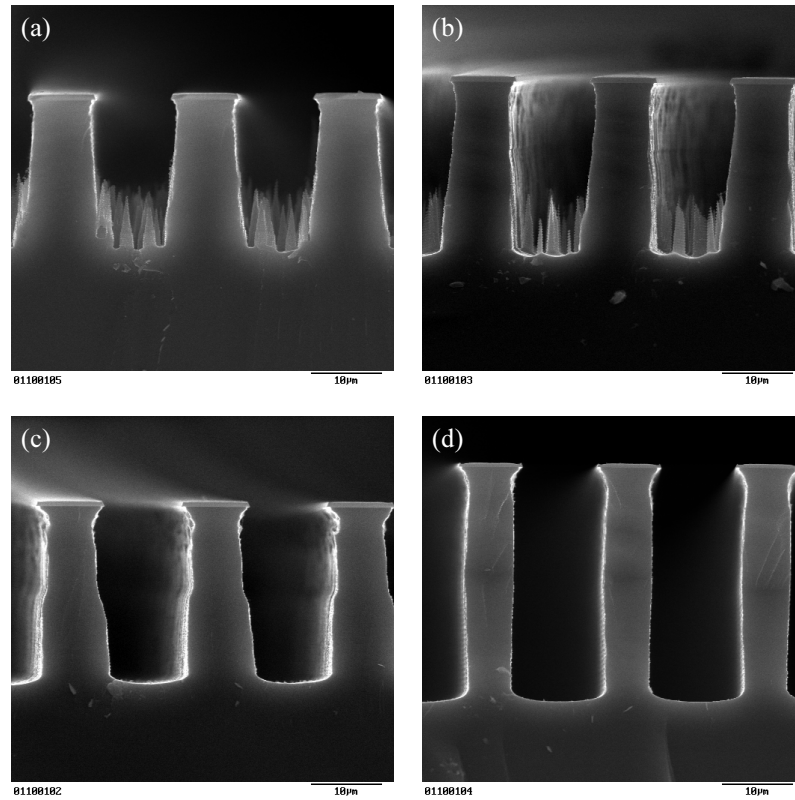


Figure 5.1 Trench profiles for inert and reactive depassivation pulse chemistries. (a) 2 s depassivation with an Ar plasma. (b) 2 s depassivation with an N<sub>2</sub> plasma. (c) 3 s depassivation an N<sub>2</sub> with plasma. (d) 2 s depassivation with an O<sub>2</sub> plasma.

### 5.1.2 Depassivation in SF<sub>6</sub> and O<sub>2</sub> plasmas monitored by *in situ* ellipsometry

In the actual Bosch process the polymer passivation layer is removed from the bottom of the trench before the silicon etching can proceed. For an efficient process the depassivation should be as fast as possible while keeping the sidewall passivation layer undamaged. In the following experiment, the etch rate of the polymer passivation layer in an SF<sub>6</sub> plasma, as used in the Bosch process, was compared to the etch rate in a low-pressure O<sub>2</sub> plasma, as used in the triple pulse process. The etch rate was measured as a function of the bias voltage by *in situ* ellipsometry. It is plotted as a function of ion energy using the measured plasma potential in figure 5.2. A source power of 1000 W, an SF<sub>6</sub> flow of 250 sccm and an O<sub>2</sub> flow of 100 sccm were used. The etch threshold is obtained by a linear extrapolation of the etch rate to zero. The polymer etch rate in a low-pressure O<sub>2</sub> plasma is much higher, which

indicates the potential advantages of the triple pulse process, although the etch threshold in an  $O_2$  plasma (18 eV) is slightly larger than in an  $SF_6$  plasma (10 eV).

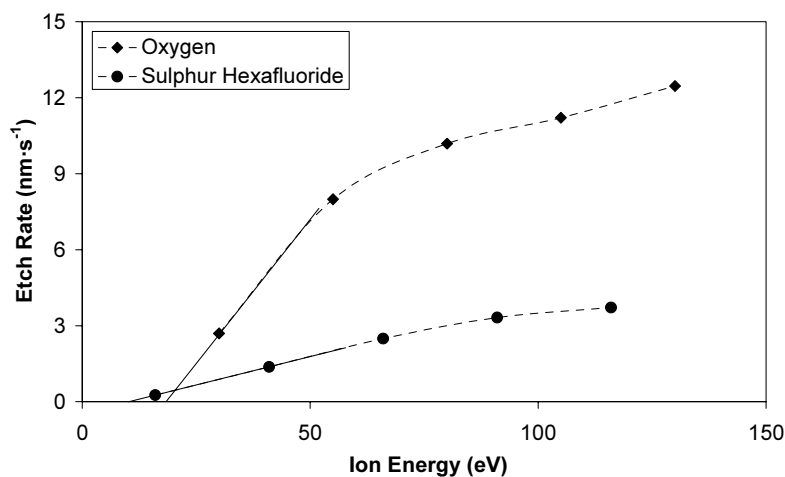


Figure 5.2 The polymer etch rate as a function of ion energy measured by *in situ* ellipsometry. Polymer etching is much more efficient in a low-pressure  $O_2$  plasma compared to an  $SF_6$  plasma despite the slightly higher etch threshold.

The polymer etch rate, the ion flux and the etch yield are given for frequently used plasma conditions in table 5.1. The  $SF_6$  flows were used for the actual etching experiments and a comparison is given of an  $SF_6$  and  $O_2$  plasma with identical flow rate. Other plasma conditions were 2000 W source power,  $-90$  V bias voltage,  $25$  °C substrate temperature. The polymer layer thickness was measured with the SEM before and after etching in the upper substrate holder position. The polymer deposition rate was  $340$  nm·min<sup>-1</sup> for a  $C_4F_8$  flow of 150 sccm and a bias voltage of  $-30$  V. The etch yield of the polymer layer is expressed as the number of  $CF_2$  units that is removed per ion impact. It is assumed that the polymer layer consists purely of  $(CF_2)_n$  (PTFE).

Table 5.1 The polymer etch rate, the ion flux and the etch yield for frequently used plasma conditions. It is assumed that the polymer layer consists of pure PTFE to calculate the etch yield.

Gas Flow (sccm)	Etch Rate Polymer (nm·min <sup>-1</sup> )	Ion Flux (mA·cm <sup>-2</sup> )	Etch Yield
300 sccm SF <sub>6</sub>	634	0.51	8.8
150 sccm SF <sub>6</sub>	837	0.75	7.9
100 sccm SF <sub>6</sub>	1014	0.92	7.8
100 sccm O <sub>2</sub>	1584	2.03	5.5
30 sccm O <sub>2</sub>	1522	2.65	4.1

The yield is higher for an SF<sub>6</sub> plasma compared to an O<sub>2</sub> plasma. Still the highest polymer etch rates are obtained for an O<sub>2</sub> plasma due to the much higher ion flux. The etch yield increases with pressure. This is explained by the involvement of the radicals presumably due to ion-neutral synergy, but there could also be a non-negligible spontaneous etching component. The silicon carbide etch yield given in chapter 7 is approximately a factor of 5 lower due to the strong silicon-carbon bonds.

### 5.1.3 Sidewall taper control

Due to increased erosion of the sidewall passivation layer the passivation pulse time has to be increased considerably for the triple pulse process. As a rule of thumb, each second of depassivation pulse time requires two seconds of passivation pulse time extra to maintain the same anisotropy, which reduces the net etch rate. The effect of the depassivation pulse time on the trench profile is given in figure 5.3. The Triple 1 process conditions given in appendix B were used for an etch time of 15 min. The depassivation pulse times were 2 s and 4 s for figure 5.3a and 5.3b respectively. If the depassivation plasma pulse time is increased from 2 s to 4 s, a strongly negative sidewall taper is obtained, which shows the substantial range of profile control for the triple pulse process. With the Bosch process it is difficult to obtain such a negative taper. The wider range of profile control for the triple pulse process could be advantageous for certain applications, e.g., a small negative taper could prevent the sticking of moving parts in inertial devices.

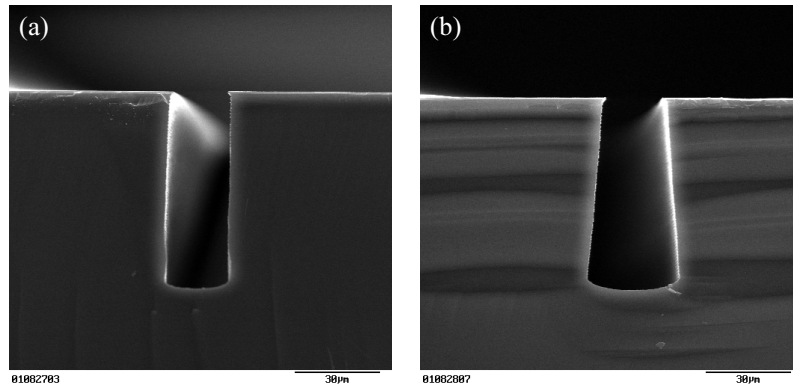


Figure 5.3 Profile control from fully anisotropic to a strongly negative sidewall taper. (a) 2 s depassivation with an  $O_2$  plasma. (b) 4 s depassivation with an  $O_2$  plasma.

Complex devices often consist of both closely and widely spaced structures. However, the sidewall taper is different for trenches and ridges that were etched with the Triple 1 process conditions for an etch time of 15 min. These conditions were the same as for the anisotropic trench profile shown in figure 5.3a, but a severely negative sidewall taper is observed for the ridge shown in figure 5.4a. This could be caused by bending of the ions by lateral electric fields, which arise when the plasma sheath is disturbed by the surface topography. For wider trenches the equipotential lines start to follow the substrate surface deflecting the path of the ions towards the sidewalls [4,5]. On the other hand, the better accessibility for fluorine radicals could also increase the negative sidewall taper of wider trenches due to a larger lateral etch. Figure 5.4b shows a structure consisting of two closely spaced ridges that is etched with a passivation pulse time of 9 s. Between the two ridges the etch rate is lower and the sidewall taper is less negative because of the limited access of fluorine radicals. The outer two sidewalls are less negatively tapered compared to figure 5.4a due to the longer passivation pulse time.

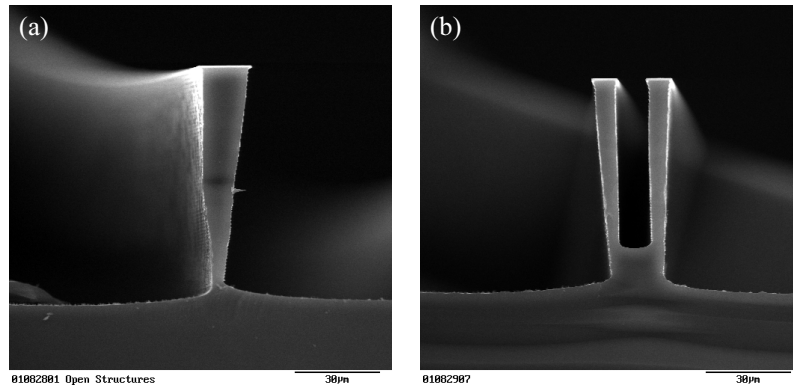


Figure 5.4 Severely negative sidewall taper of isolated ridges. (a) Single ridge etched with 6 s passivation pulse time. (b) Two closely spaced ridges etched with 9 s passivation pulse time.

#### 5.1.4 Sidewall corrugation and the transport of fluorine radicals

In general the sidewall ripples are sharper for the triple pulse process, which indicates that the etching pulse has a more isotropic character and redeposition of the polymer passivation layer has a smaller effect. This is often an undesirable property, but for some applications it may be useful, because such a controlled corrugation can avoid sticking of the parts in a micromechanical structure. The sidewall ripples can be reduced by tuning the etching pulse to a more ion-induced, anisotropic regime [6].

In the triple pulse process silicon etching sets in directly after the depassivation pulse on the entire bottom of the trench, so that the transport of fluorine radicals becomes a limiting factor in trenches. For a typical trench etching experiment the sidewall ripples shown in figure 5.5 are clearly visible from the top to the bottom. The distance between the sidewall ripples was used to calculate the instantaneous etch rate as a function of aspect ratio shown in figure 5.6, because the time of each etch cycle was constant (9 s silicon etching, 9 s surface passivation and 3 s directional depassivation). The data points in the plotted curve are the moving average of 5 consecutive ripples centered around a certain aspect ratio to reduce noise. The data were fitted with the Knudsen transport model using the least squares criterion, and a good fit was obtained for an initial etch rate of  $4.96 \mu\text{m}\cdot\text{min}^{-1}$  and a reaction probability of 0.50. This shows that the transport of fluorine radicals determines the etch rate in the triple pulse process. A fluorine radical partial pressure of 1.65 Pa was measured for a continuous  $\text{SF}_6$  plasma with the same conditions, and an initial etch rate of  $3.72 \mu\text{m}\cdot\text{min}^{-1}$  was calculated using the fitted reaction probability of 0.50. A duty cycle of 43% and thermal equilibrium between the plasma and the substrate were assumed. Two factors could explain the difference between the fitted and calculated

initial etch rate. First, the pressure fluctuates in the pulsed plasma, so that the average fluorine radical partial pressure is underestimated by the value measured in a continuous plasma, and second, mixing of gases leads to less well-defined pulse transitions, so that the duty cycle is underestimated.

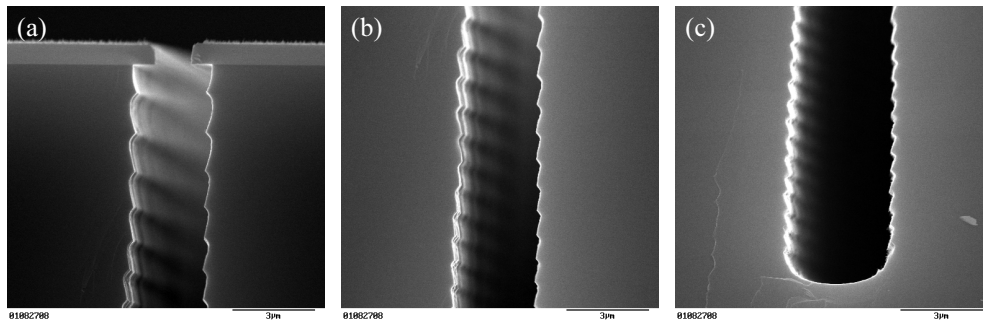


Figure 5.5 Close-up of the sidewall ripples in a trench with a  $1.5 \mu\text{m}$  wide mask aperture. (a) Top part. (b) Directly below the top part. (c) Bottom part.

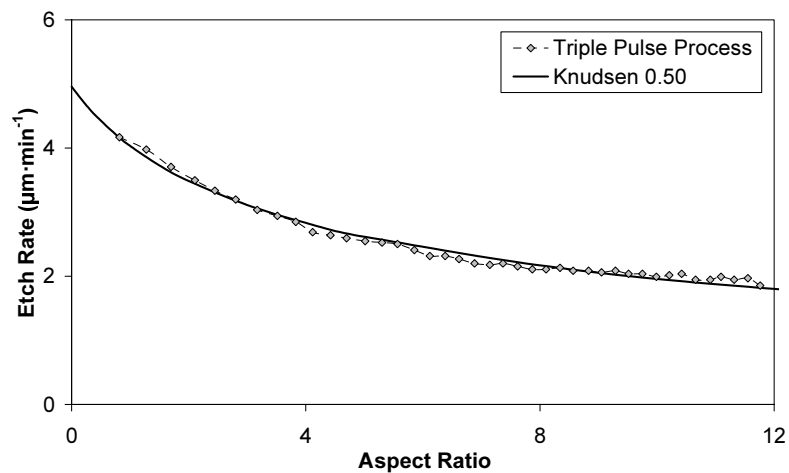


Figure 5.6 The instantaneous etch rate as a function of aspect ratio. The data are derived from the distance between the sidewall ripples of a trench with a  $1.5 \mu\text{m}$  wide mask aperture. The data are fitted with the Knudsen transport model.



### 5.1.5 Directional depassivation with CO<sub>2</sub> and SO<sub>2</sub> plasmas

In the triple pulse process the necessary increase of the passivation pulse time and the tendency to a negative sidewall taper are strong indications that the sidewall passivation layer is eroded during the O<sub>2</sub> depassivation plasma pulse. The maximal obtainable aspect ratio increases, if the lateral etch is reduced. Therefore, CO<sub>2</sub> and SO<sub>2</sub> are explored as alternative depassivation chemistries to improve the lateral etch control [7]. During depassivation carbon and sulphur species may form a thin film that inhibits the etching of the polymer sidewall passivation layer by the oxygen radicals. For SO<sub>2</sub> ECR plasma etching of polymers it has been shown, that sulphur species prevent lateral etching if the substrate is at or below room temperature [8].

Table 5.2 shows the ion flux measured for a 30 sccm O<sub>2</sub>, CO<sub>2</sub> and SO<sub>2</sub> plasma as well as for a low-pressure SF<sub>6</sub> and C<sub>4</sub>F<sub>8</sub> plasma. The ion flux is not highly dependent on the type of gas, certainly if one bears in mind that the ion flux of the SF<sub>6</sub> and C<sub>4</sub>F<sub>8</sub> plasma are comparatively lower due to the higher pressure. So, directional depassivation by physical sputtering in low-pressure oxygen-based plasmas is efficient irrespective of the type of gas.

Table 5.2 The pressure and the ion flux in a low-pressure high-density plasma for several gases.

Gas Flow (sccm)	Pressure (Pa)	Ion Flux (mA·cm <sup>-2</sup> )
30 sccm O <sub>2</sub>	0.29	2.79
30 sccm CO <sub>2</sub>	0.31	2.00
30 sccm SO <sub>2</sub>	0.29	2.06
50 sccm SF <sub>6</sub>	0.72	1.61
37.5 sccm C <sub>4</sub> F <sub>8</sub>	0.59	1.27

Etching was performed with the triple pulse process, and O<sub>2</sub> was replaced consecutively by either CO<sub>2</sub> or SO<sub>2</sub> for directional depassivation. All other plasma conditions were the same as the Triple 2 process conditions. SEM pictures of the trench profiles using O<sub>2</sub>, CO<sub>2</sub> and SO<sub>2</sub> for the depassivation pulse are shown in figure 5.7. The results for directional depassivation with either CO<sub>2</sub> or SO<sub>2</sub> do not show significant improvement. Presumably, carbon and sulphur species do not sufficiently protect the sidewall passivation layer against the attack of oxygen radicals. Furthermore, a SO<sub>2</sub> depassivation pulse using a lower ion flux does not lead to improved results, although the lower ion flux impairs the sidewall passivation layer less. An explanation for these results could be that the attack of the sidewall passivation layer is mainly due to ions instead of oxygen radicals.

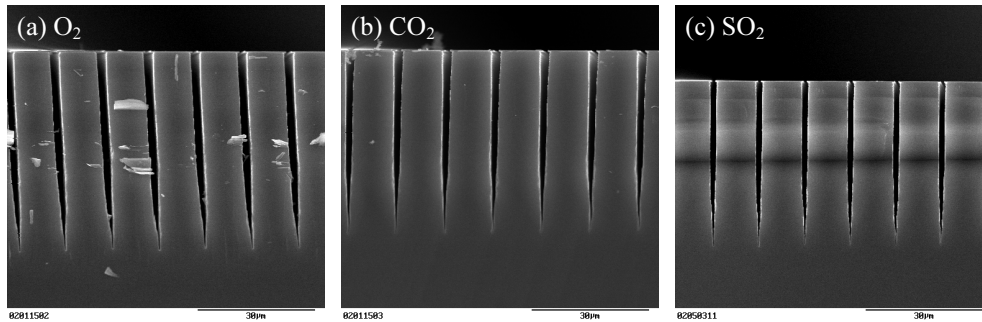


Figure 5.7 Comparison of the trench profiles obtained with the triple pulse process using  $O_2$ ,  $CO_2$  and  $SO_2$  for the depassivation pulse. (a)  $O_2$  for directional depassivation. (b)  $CO_2$  for directional depassivation. (c)  $SO_2$  for directional depassivation.

For directional depassivation with  $SO_2$ , experiments were also performed at a substrate temperature of 0 °C, because the protection of the sidewall passivation layer by sulphur species improves below room temperature [8]. However, no significant improvement in the profile evolution was observed for a  $SO_2$  depassivation pulse at 0 °C either. A benefit of a lower substrate temperature is the much more effective passivation pulse, which is discussed in chapter 4. Compared to etching at 25 °C the passivation pulse time is decreased by 2 s while keeping anisotropic profiles, which saves 40% of the  $C_4F_8$  consumption and improves the duty cycle.

## 5.2 Comparison of the triple pulse process and the Bosch process

The performance of the triple pulse process with regard to high aspect ratio trench etching is compared to the Bosch process to evaluate the presumed advantages. Experiments were performed with a low ion flux, an intermediate ion flux (a factor of 3 higher) and a high ion flux (a factor of 6 higher). Table 5.3 shows the plasma conditions, the average etch rate of a trench with a 1.5 µm wide mask aperture, the maximal obtainable aspect ratio and the selectivity to a silicon dioxide mask for an intermediate and a high ion flux. The etch time was 40 min for the triple pulse process and 30 min for the Bosch process. Other plasma conditions were 2000 W source power, -90 V bias voltage, 25 °C substrate temperature and open adverse  $SF_6$  buffer.

Table 5.3 Comparison of the Bosch process and the triple pulse process. The plasma conditions, the average etch rate of a trench with a 1.5  $\mu\text{m}$  wide mask aperture, the maximal obtainable aspect ratio and the selectivity to a silicon dioxide mask are given.

Process	Triple Pulse		Bosch	
	Intermediate	High	Intermediate	High
Silicon Etching ( $\text{SF}_6$ )	300 sccm 6.3 Pa 6 s	300 sccm 6.7 Pa 6 s	300 sccm 5.5 Pa 6 s	300 sccm 5.4 Pa 6 s
Surface Passivation ( $\text{C}_4\text{F}_8$ )	185 sccm 4.0 Pa 6 s	185 sccm 3.6 Pa 7 s	135 sccm 2.9 Pa 3 s	135 sccm 3.3 Pa 3 s
Directional Depassivation ( $\text{O}_2$ )	30 sccm 1.4 Pa 2 s	30 sccm 1.3 Pa 2 s	-	-
Average Etch Rate	2.12 $\mu\text{m}\cdot\text{min}^{-1}$	2.06 $\mu\text{m}\cdot\text{min}^{-1}$	2.88 $\mu\text{m}\cdot\text{min}^{-1}$	2.94 $\mu\text{m}\cdot\text{min}^{-1}$
Maximal Obtainable Aspect Ratio	24 $\pm$ 2	23 $\pm$ 2	22 $\pm$ 2	26 $\pm$ 3
Selectivity	146 $\pm$ 7	65 $\pm$ 3	139 $\pm$ 7	70 $\pm$ 4

The etch rate is lower for the triple pulse process due to the lower duty cycle, but it is higher than expected. The duty cycle changes by a factor of 0.64, whereas the etch rate only changes by a factor of 0.74 because silicon etching starts directly on the entire bottom of the trench when the etching pulse is switched on. Moreover, during the depassivation pulse all  $\text{C}_4\text{F}_8$  is depleted, so that there is no mixing with  $\text{SF}_6$  which reduces the etch rate for a moment.

SEM pictures of trenches with a 1.5  $\mu\text{m}$  wide mask aperture that are etched with the plasma conditions given in table 5.3 are shown in figure 5.8. Trenches etched with a low ion flux are also included, and in this case the maximal obtainable aspect ratio is 23 $\pm$ 2 and 21 $\pm$ 2 for the triple pulse process and the Bosch process respectively. The differences in the maximal obtainable aspect ratio are relatively small, because in the triple pulse process the small lateral etch counteracts the larger etch depth. Although, for the triple pulse process the maximal obtainable aspect ratio is almost constant, whereas for the Bosch process it decreases continuously when going from a high to a low ion flux. Even for dedicated depassivation in the low-pressure  $\text{O}_2$  plasma the intrinsic ion angular distribution remains probably an important limiting factor.

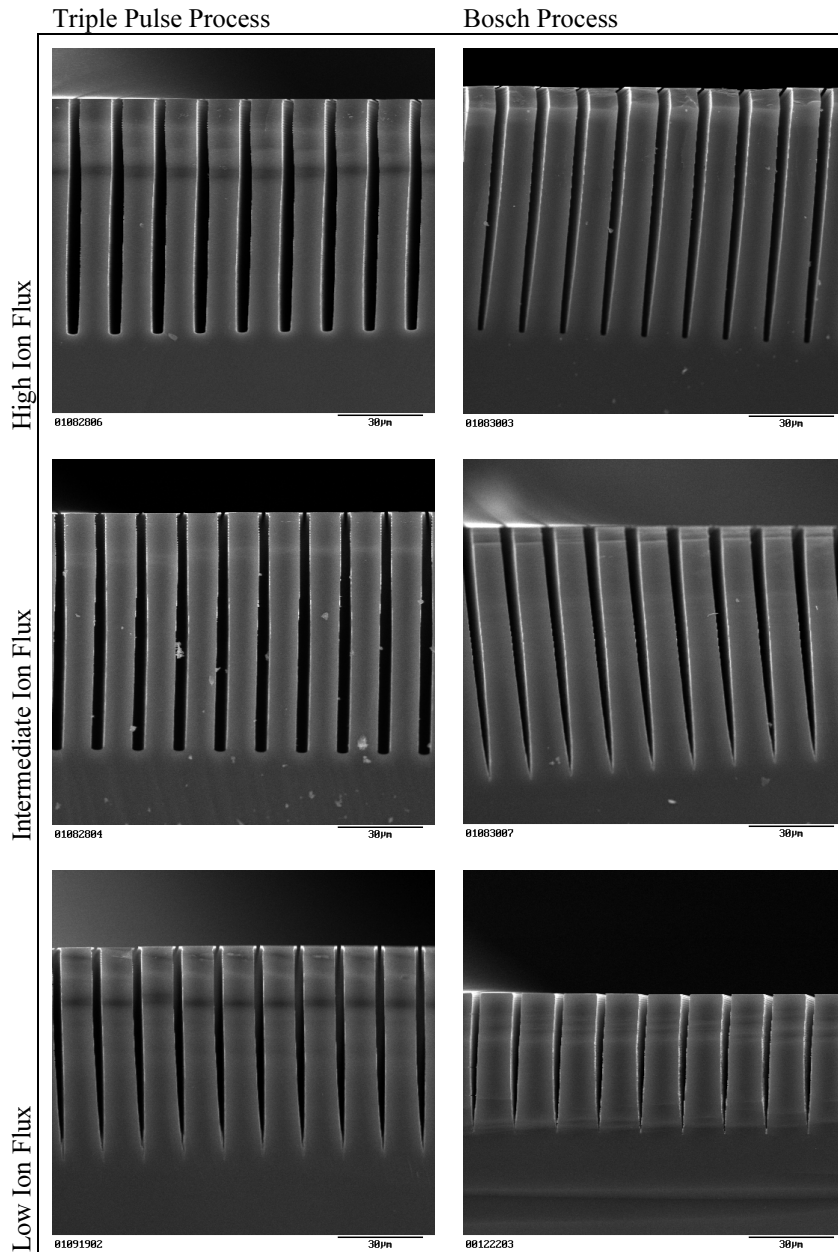


Figure 5.8 High aspect ratio trenches with a  $1.5\ \mu\text{m}$  wide mask aperture etched with the triple pulse process and the Bosch process for several ion fluxes.

The SEM pictures show that trenches etched with the triple pulse process tend to a slightly negative sidewall taper, whereas trenches etched with the Bosch process tend to a slightly positive sidewall taper. It demonstrates the efficient depassivation in the low-pressure O<sub>2</sub> plasma. The small lateral etch in the triple pulse process leads to improved profile control compared to the Bosch process. For the triple pulse process the sidewalls and the bottom of the trench remain straight with sharp corners down to a larger depth. Besides, the trench profile does not deteriorate when going from a high to an intermediate ion flux, while at the same time the selectivity increases from 65 to 146. This is an advantage of the triple pulse process because mask erosion is a limiting factor in the etching of deep structures. Only for the lowest ion flux the profile becomes worse, but it is still much better than for the Bosch process.

In the Bosch process a reduced pressure leads to better anisotropy due to the increased ion-to-radical flux ratio. A second set of data was acquired for the triple pulse process to investigate the influence of a reduced pressure in comparison with the Bosch process. The SF<sub>6</sub> flow was reduced by a factor of 2. In this case mixing of gases was minimal with the adverse SF<sub>6</sub> buffer closed and the SF<sub>6</sub> flow equal to the C<sub>4</sub>F<sub>8</sub> flow. Experiments were performed both with a low and a high ion flux. Table 5.4 shows the plasma conditions, the average etch rate of a trench with a 1.5 μm wide mask aperture, the maximal obtainable aspect ratio and the selectivity to a silicon dioxide mask. The etch time was 40 min both for the triple pulse process and the Bosch process.

Table 5.4 Comparison of the Bosch process and the triple pulse process for a decreased etching pulse pressure and closed SF<sub>6</sub> buffer. The plasma conditions, the average etch rate of a trench with a 1.5 μm wide mask aperture, the maximal obtainable aspect ratio and the selectivity to a silicon dioxide mask are given.

Process	Triple Pulse		Bosch	
	Low	High	Low	High
Silicon Etching (SF <sub>6</sub> )	150 sccm 3.0 Pa 6 s	150 sccm 2.8 Pa 6 s	150 sccm 2.8 Pa 12 s	150 sccm 2.7 Pa 6 s
Surface Passivation (C <sub>4</sub> F <sub>8</sub> )	150 sccm 3.2 Pa 4 s	150 sccm 2.7 Pa 5 s	150 sccm 3.1 Pa 3 s	150 sccm 2.8 Pa 3 s
Directional Depassivation (O <sub>2</sub> )	30 sccm 0.60 Pa 2 s	30 sccm 0.58 Pa 2 s	-	-
Average Etch Rate	1.24 μm·min <sup>-1</sup>	1.16 μm·min <sup>-1</sup>	1.76 μm·min <sup>-1</sup>	1.56 μm·min <sup>-1</sup>
Maximal Obtainable Aspect Ratio	26±3	25±3	28±3	27±3
Selectivity	83±4	21±1	160±8	41±2

Compared to the previous experiments the average etch rate was reduced because of the lower pressure during the etching pulse. The pressure during the depassivation pulse was also lower, which indicates substantial mixing of SF<sub>6</sub> and O<sub>2</sub> with the adverse SF<sub>6</sub> buffer open. So, the low pressure during the depassivation pulse rather than the type of reactive gas (SF<sub>6</sub> and O<sub>2</sub>) seems to determine the profile evolution. However, there is no significant improvement of the maximal obtainable aspect ratio for the triple pulse process. Probably, the polymer passivation layer is already completely removed in the previous experiments, so that an increased ion flux due to the lower pressure has no effect. The maximal obtainable aspect ratio of the triple pulse process and the Bosch process are very comparable in this case. The maximal obtainable aspect ratio is even a little higher for the Bosch process. It does not decrease for a low ion flux because the ion-to-radical flux ratio of the etching pulse is higher compared to the previous experiments. For the same reason the selectivity is reduced as well. A noticeable difference is the factor of 2 lower selectivity of the triple pulse process, whereas in the previous experiments it was approximately equal to the selectivity of the Bosch process. From this it is concluded that the mask is also etched during the depassivation pulse because the pressure during the depassivation pulse is also lower than in the previous experiments leading to a higher ion flux. Mask erosion is not necessarily due to physical sputtering by oxygen ions, but ion-induced chemical reactions

of the polymer passivation layer with the silicon dioxide mask could also occur. And, after the polymer passivation layer has been removed,  $CF_x$  radicals sputtered from the reactor walls could promote the etching of the silicon dioxide mask. In general the main difference of the triple pulse process is the slightly negative sidewall taper compared to the slightly positive sidewall taper for the Bosch process, which leads to improved profile control and square trench corners.

### 5.3 Conclusions

A novel time-multiplexed plasma etching process has been developed with separately tuneable etching, passivation and depassivation pulses. Low-pressure, high-density, oxygen-based plasmas ( $O_2$ ,  $CO_2$  and  $SO_2$ ) remove the polymer passivation layer efficiently from the bottom of a trench due to the high flux of reactive ions. However, the sidewall erosion is also stronger, and compared to the Bosch process, the passivation pulse time has to be increased significantly to obtain anisotropic profiles. A positive effect of the stronger sidewall erosion is that the range of profile control is larger: from fully anisotropic to a strongly negative sidewall taper. The main advantage of the so-called triple pulse process is that the sidewalls of high aspect ratio trenches remain straight down to a larger depth compared to the Bosch process. In addition, the anisotropy remains the same for a reduced ion flux in the triple pulse process while the selectivity is larger. The maximal obtainable aspect ratio for the triple pulse process is comparable to the Bosch process because the larger lateral etch cancels out the larger etch depth. The fairly constant maximal obtainable aspect ratio points to a common limiting factor: the limited access of the ion and radical fluxes to the bottom of high aspect ratio trenches.

### References

- [1] M. Puech and E. van der Drift, World Patent N° WO03060975 (2003)
- [2] J. Ohara, K. Kano, Y. Takeuchi, N. Ohya, Y. Otsuka, and S. Akita, *Proceedings of the 13<sup>th</sup> IEEE Annual International Conference on Microelectromechanical Systems*, 277 (IEEE, New York, US, 2000)
- [3] J. Ohara, K. Kano, Y. Takeuchi and Y. Otsuka, *Proceedings of the 14<sup>th</sup> IEEE Annual International Conference on Microelectromechanical Systems*, 76 (IEEE, New York, US, 2001)
- [4] J.R. Woodworth, P.A. Miller, R.J. Shul, I.C. Abraham, B.P. Aragon, T.W. Hamilton and C.G. Willison, *J. Appl. Phys.* **92**, 716 (2002)
- [5] M. Ardehali, *Appl. Phys. Lett* **64**, 169 (1994)
- [6] B. Volland, F. Shi, P. Hudek, H. Heerlein, and I.W. Rangelow, *J. Vac. Sci. Technol. B* **17**, 2768 (1999)

- [7] R.S. Hutton, C.H. Boyce and G.N. Taylor, *J. Vac. Sci. Technol. B* **13**, 2366 (1995)
- [8] M. Pons, J. Pelletier, and O. Joubert, *J. Appl. Phys.* **75**, 4709 (1994)



## Chapter 6

### Trench profile optimisation by adjusting the surface passivation

In chapter 4 it is shown that the etching of high aspect ratio trenches with the Bosch process is limited by insufficient de-passivation of the bottom of the trenches. Optimal results are obtained for a high ion-to-radical flux ratio. In chapter 5 it is described that the de-passivation is further improved by a high-density low-pressure O<sub>2</sub> plasma in the triple pulse process. In chapter 6 it is explained that the Bosch can be improved, if there is no polymer deposition on the bottom of the trench but on the trench sidewalls. In that case the surface passivation layer does not have to be removed by the ion bombardment at all.

This chapter is organised as follows. In section 6.1 it is shown that polymer deposition is a complex process with both a radical-induced and an ion-enhanced component [1]. The polymer deposition rate in a C<sub>4</sub>F<sub>8</sub> plasma is investigated with *in situ* ellipsometry and a model is developed to describe the polymer deposition mechanism as a function of the radical and ion fluxes. In addition, deposition on structures with an overhanging membrane was used to distinguish radical-induced component and the ion-enhanced component. The results show that plasma conditions exist without polymer deposition on a horizontal plane. In section 6.2 it is described that preferential sidewall deposition can be obtained by adjusting the ion flux and the ion energy. The investigation of the polymer deposition mechanism in deep trenches results in a better understanding of the impact of the passivation on the trench profile. In section 6.3 it is treated that independent variation of the bias voltage during etching and passivation can lead to optimised trench profiles. The profile can be controlled with the bias voltage. A higher bias voltage leads to a negative sidewall taper, but the mask erosion is stronger. Therefore, in section 6.4 the reduction of the mask erosion by ramping up the bias voltage during the process is discussed.

#### 6.1 The polymer passivation layer deposition mechanism

##### 6.1.1 The polymer deposition mechanism

The polymer deposition rate was deduced as a function of bias voltage, source power and C<sub>4</sub>F<sub>8</sub> flow from the ellipsometric measurement of the film thickness. All measurements were done in the low substrate holder position with a low ion flux. The C<sub>4</sub>F<sub>8</sub> flow was 66 sccm and the substrate temperature was 20 °C. Figure 6.1a shows the deposition rate as a function of the bias voltage for several source power settings. In the low power regime (500 W) the deposition rate is relatively independent of the bias voltage, because the ion density

in the  $C_4F_8$  plasma is low and the deposition mechanism is thus largely radical-induced. In the high power regime (2000 W) the deposition rate is initially higher due to the highly dissociated and ionised plasma. However, it decreases quickly if the bias voltage increases, because the ions begin to sputter the polymer passivation layer. Increasing the bias voltage from 0 V to  $-25$  V for a source power of 1500 W leads to a slight increase of the deposition rate indicating that there is an ion-induced component in the deposition mechanism [1].

A change in the plasma pressure due to variation of the  $C_4F_8$  flow had a similar effect on the deposition rate as a change in the source power. This is shown in figure 6.1b. The source power was constant at 1500 W. The low-pressure plasma for a  $C_4F_8$  flow of 33 sccm leads to a high degree of dissociation and ionisation. So the high initial deposition rate and the quick decrease as a function of the bias voltage can be understood. On the contrary in the high pressure plasma for a  $C_4F_8$  flow of 133 sccm the ion density is much lower and the  $CF_x$  radical density is high. An increase of the deposition rate is observed for lower bias voltages, because all reactive sites created by ion impact are used by the excessive amount of radicals that form bonds with the underlying polymer layer. A higher ion energy leads to more reactive sites and the deposition rate goes up, but when the ion energy is too high sputtering starts to dominate and the deposition rate decreases.

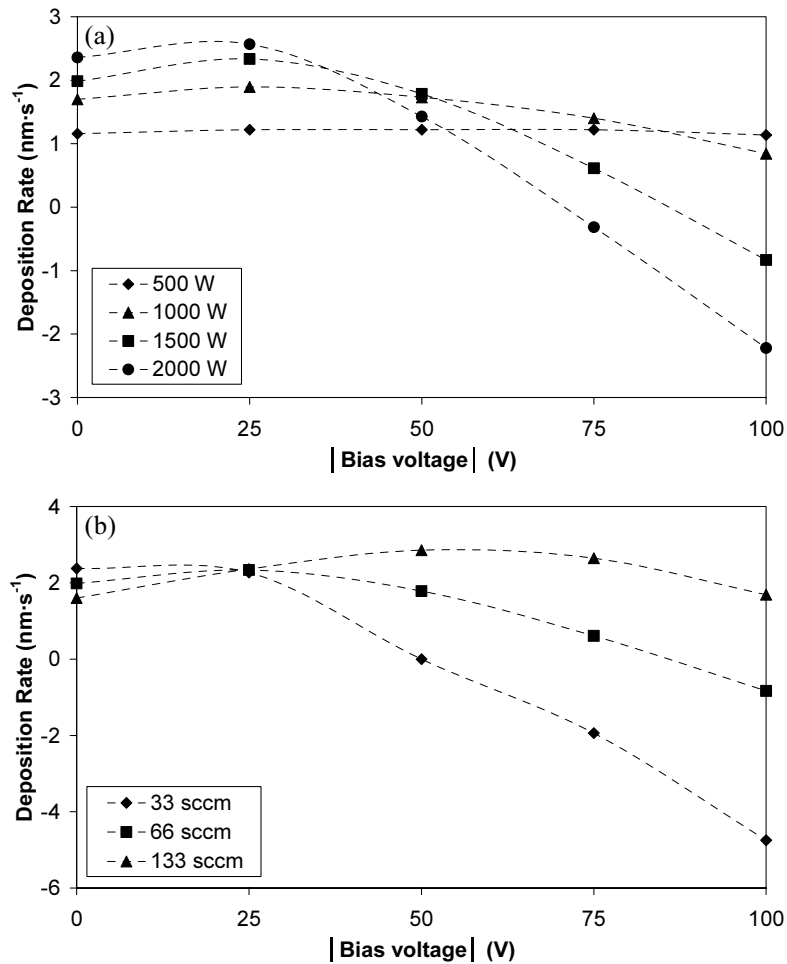


Figure 6.1 The polymer deposition rate as a function of bias voltage measured by *in situ* ellipsometry. (a) The deposition rate is low and nearly constant for a low source power, whereas it is high and decreases quickly for a high source power. (b) The deposition rate is nearly independent of C<sub>4</sub>F<sub>8</sub> flow at a low bias voltage. At higher bias voltages it decreases quickly for a low C<sub>4</sub>F<sub>8</sub> flow, whereas it shows a maximum for a high C<sub>4</sub>F<sub>8</sub> flow.

The impact of the ion flux was investigated in the following experiment. The polymer deposition was performed in the lower and the upper substrate holder position, i.e., at a low and a high ion flux respectively. It was physically impossible to do *in situ* ellipsometry in the upper substrate holder position, but to circumvent this the polymer passivation layer thickness was measured after deposition when the substrate holder was brought back in the lower position for *in situ* ellipsometry. Passivation layers were deposited for all

combinations of 500 W and 2000 W source power, -25 V and -75 V bias voltage, and a low and a high ion flux. The  $C_4F_8$  flow was 66 sccm. The results are given in table 4.1. In the case of 500 W source power the deposition rate increases by approximately a factor of 2 for both -25 V and -75 V going from a low to a high ion flux. In the case of 2000 W source power the deposition rate increases only slightly for -25 V while it decreases by a factor of 2 for -75 V. This confirms that the ion flux creates sites that are reactive to  $CF_x$  radicals leading to an enhanced deposition rate. However, sputtering prevails if the ion bombardment becomes too strong. For anisotropic trench etching it would be advantageous to have no deposition on the bottom of the trench while there still is deposition on the trench sidewalls due to the much lower ion flux.

Table 6.1 The polymer deposition rate for several combinations of ion flux, source power and bias voltage.

Polymer Deposition Rate ( $nm \cdot min^{-1}$ )	Source Power 500 W		Source Power 2000 W	
	Bias Voltage -25 V	Bias Voltage -75 V	Bias Voltage -25 V	Bias Voltage -75 V
High Ion Flux	139	144	296	74
Low Ion Flux	67	88	241	153

The polymer deposition process is the net result of a radical-induced, an ion-enhanced and a sputtering component. In literature, it has been shown that the deposition rate at floating potential mainly depends on the  $CF$  density, the  $CF_2$  density and the ion flux [1]. However, at floating potential the ion energy is too low for sputtering. A model for the polymer deposition mechanism including sputtering has been derived in appendix C. In this model the deposition rate  $R_D$  is expressed by

$$R_D = \frac{M_{CF_2}}{\rho_{PTFE} \cdot N_A} \cdot \left( \kappa_{CF_x} \cdot \varphi_{CF_x} + \frac{\gamma^* \cdot \varphi_i}{1 + \frac{\gamma^* \cdot \varphi_i}{\kappa_{CF_x} \cdot \varphi_{CF_x}}} - Y_{CF_2} \cdot \varphi_i \right) \quad 6.1$$

where the three terms indicate the radical-induced component, ion-enhanced component and sputtering component respectively. It is assumed that the polymer layer consists of polytetrafluoroethylene (PTFE). The symbols in equation 6.1 are  $M_{CF_2}$  the molar mass of the  $CF_2$  units in PTFE,  $\rho_{PTFE}$  the density of PTFE,  $N_A$  the Avogadro number,  $\kappa_{CF_x}$  the adsorption probability,  $\varphi_{CF_x}$  the  $CF_x$  radical flux,  $\gamma^*$  is the surface site activation coefficient,

$\phi_i$  the ion flux,  $\kappa_{CF_x}^*$  is the adsorption probability on the activated surface sites and  $Y_{CF_2}$  the sputter yield of the polymer layer.

The polymer deposition model given by equation 6.1 is fitted to the experimental results shown in figure 6.1 using the measured radical and ion fluxes. Only the  $CF_2$  radical flux could be measured qualitatively. It is assumed that the  $CF_x$  radical flux is proportional to the  $CF_2$  radical flux and that the ratio of the different  $CF_x$  radicals is constant irrespective of the plasma conditions. The best fit is obtained if the ion energy dependence of  $\gamma^*$  and  $Y_{CF_2}$  is given by  $\gamma^* = \gamma_0^* \cdot (\sqrt{E_i} - \sqrt{E_T^*})$  and  $Y_{CF_2} = Y_{CF_2}^0 \cdot (E_i - E_T^*)$ , respectively. The parameters  $\gamma_0^*$  and  $Y_{CF_2}^0$  are prefactors, and  $E_T^*$  and  $E_T$  are energy thresholds for surface site activation and sputtering, respectively. The linear dependence of  $Y_{CF_2}$  is necessary to explain the strong decrease of the deposition rate with higher bias voltages, for example in the case of 1500 W and 66 sccm. The fitted curves are shown in figure 6.2 and the fit parameter values are given in table 6.2.

Qualitative agreement is obtained for the general trends in the experimental results, but quantitative agreement cannot be obtained with a single set of fit parameters. However, it is a simple model that only includes the main effects of many possible surface reactions. The deviations can be caused by the coarse approximation of the different  $CF_x$  radicals that play a role in the polymer deposition process. Only a single  $CF_x$  radical flux, which is based on the measured  $CF_2$  radical flux, is used in the model. The parameters  $\kappa_{CF_x}$  and  $\kappa_{CF_x}^*$  are the weighted average for the different  $CF_x$  radicals in the  $CF_x$  radical flux. The model fails if the ratio of the CF and  $CF_2$  radical flux varies for different plasma conditions. The CF radicals are mainly responsible for the radical-induced component whereas  $CF_2$  radicals are mainly responsible for the ion-enhanced component. Besides,  $C_xF_y$  fragments with a larger mass ( $x > 1$ ) also exist in fluorocarbon plasmas, which can lead to a higher deposition rate for a given radical flux [2].

The deviations are larger for higher bias voltages, which suggests that the ion energy is important in the explanation of the experimental results. Several causes can explain the misfit. The polymer deposition model depends on the measured ion energy. The number of ion-neutral collisions in the plasma sheath increases with pressure, which leads to a decrease of the ion energy that is not reckoned in. The inaccuracy of the measured plasma potential can also lead to a mistaken ion energy. Besides, the distribution of the different types of ions that exist in the plasma depends on the plasma conditions. As a result the impact of the ion bombardment can vary.

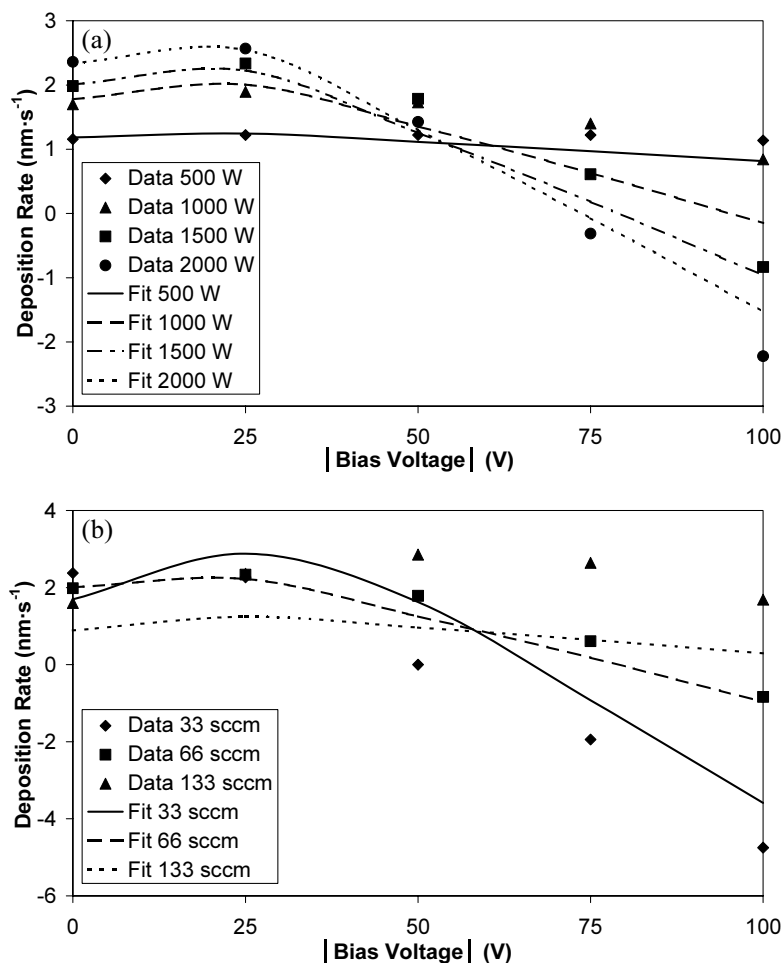


Figure 6.2 The polymer deposition model fitted to the experimental data as a function of bias voltage. (a) Fitted curves for several source powers. (b) Fitted curves for several C<sub>4</sub>F<sub>8</sub> flows. Qualitative agreement is obtained for the general trends, but quantitative agreement cannot be obtained using a single set of fit parameters.

The CF<sub>x</sub> radical reaction probability for the radical-induced component is equal to the fitted  $\kappa_{\text{CF}_x}$  value of 0.00058. It is much smaller than the CF radical reaction probability of 0.83 that is found in literature [1]. It indicates that the CF radical flux is only a small fraction of the total CF<sub>x</sub> radical flux. The CF<sub>x</sub> radical reaction probability for the ion-enhanced component is equal to the product of the fitted  $\kappa_{\text{CF}_x}^*$  value and the fraction of activated surface sites. It is 0.0036 at a bias voltage of 0 V in the case of 1500 W and 66 sccm. On the other hand a value of 0.0042 is found in literature for an ion current density of 0.31

$\text{mA}\cdot\text{cm}^{-2}$ . This is close to the observed value. The low energy threshold for surface site activation of 9.0 eV is consistent with the results given in literature where ion-enhanced deposition has been observed at floating potential. The fitted sputter energy threshold of 58 eV is fairly large. Possibly, the  $\text{CF}_x^+$  ions also add mass to the polymer passivation layer. As a consequence more than one  $\text{CF}_2$  unit has to be sputtered per  $\text{CF}_x^+$  ion before the net removal is larger than zero.

Table 6.2 The fit parameters of the polymer deposition model for deposition in a  $\text{C}_4\text{F}_8$  plasma.

$\kappa_{\text{CF}_x}$	$\kappa_{\text{CF}_x}^*$	$\gamma_0^*$	$E_T^*$ (eV)	$Y_{\text{CF}_2}^0$	$E_T$ (eV)
0.00058	0.060	0.76	9.0	0.086	58

### 6.1.2 Radical-induced and ion-enhanced polymer deposition

To distinguish the radical-induced and ion-enhanced components the polymer was deposited on structures with an overhanging membrane that blocks the directional ion flux. These structures were similar to those that were used to measure the ion angular distribution in chapter 4. The radical-induced deposition rate under the membrane and the ion-enhanced polymer deposition rate beside the membrane were measured simultaneously. A chromium layer was deposited under the membrane by evaporation to avoid charging of the lower nitride layer, which is important for experiments where the ion energy plays a role. The membrane bends due to stress in the chromium layer, but this is not detrimental for this experiment.

The polymer was deposited with conditions that were identical to the Bosch 3 process conditions given in appendix B. However, the  $\text{C}_4\text{F}_8$  flow, the ion flux and the bias voltage were varied. Experiments were performed with a  $\text{C}_4\text{F}_8$  flow of either 150 sccm or 75 sccm, a bias voltage of either  $-30$  V and  $-90$  V and an either low or high ion flux. The low and high ion flux were obtained in the lower and upper substrate holder position respectively. Figure 6.3 shows the structure after deposition with 150 sccm  $\text{C}_4\text{F}_8$ , a high ion flux and  $-90$  V bias voltage. An interesting detail is the small bump in the polymer layer directly below the edge of the membrane. In this region the ion flux decreases quickly, and apparently, the ion-enhanced deposition is most effective for an intermediate ion flux.

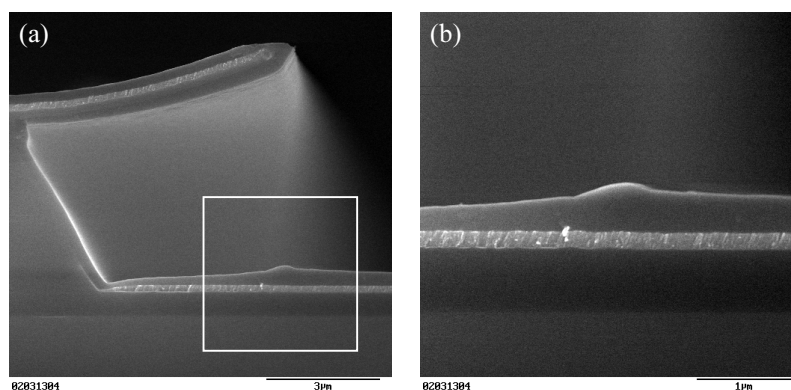


Figure 6.3 Polymer deposition on the structure with an overhanging membrane. (a) Under the membrane the deposition is radical-induced, in the open area the deposition is ion-enhanced. (b) Close-up of the region under the edge of the membrane.

The radical-induced and ion-enhanced deposition rate were measured 2  $\mu\text{m}$  from the edge under and beside the membrane respectively. The radical-induced component and ion-enhanced component are given for all eight different plasma conditions in table 6.3. The ion-enhanced component is equal to the ion-enhanced deposition rate minus the radical-induced deposition rate.

Table 6.3 The radical-induced component and ion-enhanced component measured with the overhanging membrane structure for eight combinations of  $\text{C}_4\text{F}_8$  flow, bias voltage and ion flux.

Polymer	Deposition Rate ( $\text{nm}\cdot\text{min}^{-1}$ )	Low Ion Flux		High Ion Flux	
		Radical-Induced Component	Ion-Enhanced Component	Radical-Induced Component	Ion-Enhanced Component
75 sccm	-30 V	17 $\pm$ 2	110 $\pm$ 3	33 $\pm$ 2	176 $\pm$ 3
	-90 V	14 $\pm$ 2	26 $\pm$ 3	24 $\pm$ 2	33 $\pm$ 3
150 sccm	-30 V	40 $\pm$ 2	107 $\pm$ 3	48 $\pm$ 2	199 $\pm$ 3
	-90 V	36 $\pm$ 2	105 $\pm$ 3	52 $\pm$ 2	26 $\pm$ 3

The polymer deposition rates are used to validate the polymer deposition model using the relevant radical and ion fluxes. The  $\text{CF}_2$  radical partial pressure, the low ion flux and the high ion flux are given as a function of the  $\text{C}_4\text{F}_8$  flow in table 6.4. The  $\text{CF}_2$  radical partial pressure increases and the ion flux decreases as a function of  $\text{C}_4\text{F}_8$  flow/pressure. The ratio of the high and the low ion flux is smaller for a lower  $\text{C}_4\text{F}_8$  flow/pressure because the electron temperature is higher for lower pressure, so that the excitation rate is higher in the



downstream region. Moreover, the diffusion length is larger for lower pressure, so that the ion density gradient is smaller.

Table 6.4 The  $CF_2$  radical partial pressure, the low ion flux and the high ion flux for several  $C_4F_8$  flows.

$C_4F_8$ Flow (sccm)	$CF_2$ Actinometry (a.u.)	Low Ion Flux ( $mA \cdot cm^{-2}$ )	High Ion flux ( $mA \cdot cm^{-2}$ )
37.5	0.16±0.02	1.02±0.02	1.27±0.02
75	0.59±0.06	0.38±0.01	0.62±0.01
100	1.07±0.11	0.27±0.01	0.56±0.01
150	1.38±0.14	0.14±0.01	0.45±0.01

The measured polymer deposition rates given in table 6.3 are fitted with the polymer deposition model. The calculated radical-induced and ion-enhanced components are given in table 6.5. The fit parameters for this experiment are given in table 6.6. To a certain extent they are comparable to the fit parameters given in table 6.2. In general, the model is qualitatively consistent with the measured polymer deposition rates, which is illustrated in the following three paragraphs.

Table 6.5 The radical-induced component and the ion-enhanced component calculated with the polymer deposition model for eight combinations of  $C_4F_8$  flow, bias voltage and ion flux.

Polymer Deposition Rate ( $nm \cdot min^{-1}$ )		Low Ion Flux		High Ion Flux	
		Radical-Induced Component	Ion-Enhanced Component	Radical-Induced Component	Ion-Enhanced Component
75 sccm	−30 V	26	112	26	197
	−90 V	26	6	26	20
150 sccm	−30 V	61	49	61	165
	−90 V	61	17	61	62

Table 6.6 The fit parameters for the polymer deposition on the overhanging membrane structure.

$\kappa_{CFx}$	$\kappa_{CFx}^*$	$\gamma_0^*$	$E_T^*$ (eV)	$Y_{CF_2}^0$	$E_T$ (eV)
0.00090	0.078	0.62	9.0	0.058	54

The measured radical-induced component is roughly proportional to the measured  $\text{CF}_2$  radical flux in agreement with the polymer deposition model. In the lower substrate holder position the radical-induced component is smaller probably because of recombination of  $\text{CF}_x$  radicals. For example, in the downstream region the  $\text{CF}_2$  radical density decreases due to recombination of  $\text{CF}_2$  and F to  $\text{CF}_3$ . A decrease of 30% has been calculated using the residence time in the reactor and the known recombination rate, which is close to the observed decrease [3].

The measured ion-enhanced component increases with a higher ion flux at a bias voltage of  $-30$  V. The ion-enhanced component calculated with equation 6.1 is nearly proportional to the ion flux because an excessive amount of  $\text{CF}_x$  radicals is available. For 75 sccm the measured ion-enhanced component is also proportional to the ion flux. However, for 150 sccm the increase of the ion-enhanced component is lower than the threefold increase of the ion flux. Besides, the ion-enhanced component for 150 sccm is nearly equal to the ion-enhanced component for 75 sccm despite the smaller ion flux. It indicates that the ion-enhanced component for 150 sccm is stronger than accounted for by the model. Possibly, this is due to a different plasma composition at a higher pressure.

The measured ion-enhanced component is strongly reduced at a bias voltage of  $-90$  V compared to a bias voltage of  $-30$  V. With the exception that the ion-enhanced component is nearly constant for 150 sccm and a low ion flux. However, the ion-enhanced component calculated with equation 6.1 decreases strongly in all cases due to the sputtering component. In the previous paragraph it was explained that the ion-enhanced component for 150 sccm is stronger than accounted for by the model. As a consequence the ion-enhanced component could still dominate for 150 sccm and a low ion flux. Besides, the plasma sheath thickness is comparable to the ion mean free path for these plasma conditions. For example, the plasma sheath thickness and the ion mean free path are 1.9 mm and 1.8 mm respectively for 150 sccm. Ion-neutral collisions occur more frequently at a higher pressure, so that the average ion energy and the sputtering component are reduced. Only for a high ion flux the ion-enhanced component decreases strongly due to the sputtering component.

## 6.2 The polymer deposition mechanism in trenches

In this section the polymer deposition in high aspect ratio structures is described. The ultimate aim is to obtain predominant polymer deposition on the trench sidewalls. The influence of the ion flux and ion energy on the polymer deposition on the bottom and sidewalls is investigated. In section 6.1 it was shown that the polymer deposition rate on a plane perpendicular to the ion flux is reduced for higher ion fluxes and higher ion energies. This result is used to adjust the surface passivation to preferential sidewall deposition in view of the more than one order of magnitude smaller ion flux to the sidewalls.

A trench, which had been etched with the Bosch process, was exposed to a continuous  $\text{C}_4\text{F}_8$  plasma for 5 min. A large increase of the polymer passivation layer is observed on the trench sidewalls at about  $15 \mu\text{m}$  below the mask as shown in figure 6.4a [4]. This increase

is presumably due to ion-enhanced deposition because the ions with a narrow IAD can reach the sidewall below a certain depth under the mask despite the lateral etch. Above this depth the mask shadows the ion beam. Deeper down the trench the polymer deposition becomes gradually smaller again. On the one hand this is due to the limited transport of  $CF_x$  radicals deeper into the trench, but on the other hand the thick sidewall passivation layer itself starts to shadow the ion beam [4]. When the polymer passivation layer was exposed for 5 min to a continuous  $SF_6$  plasma most of the sidewall erosion is observed around the same depth as the largest sidewall deposition as shown in figure 6.4b. This confirms that the ions can only reach the sidewall below a certain depth under the mask. The asymmetry of the sidewall erosion is possibly due to a local asymmetry in the plasma exposure leading to a deflection of the ion beam. Fortunately, the position of the largest sidewall erosion and the largest sidewall deposition coincide keeping a good balance between etching and passivation.

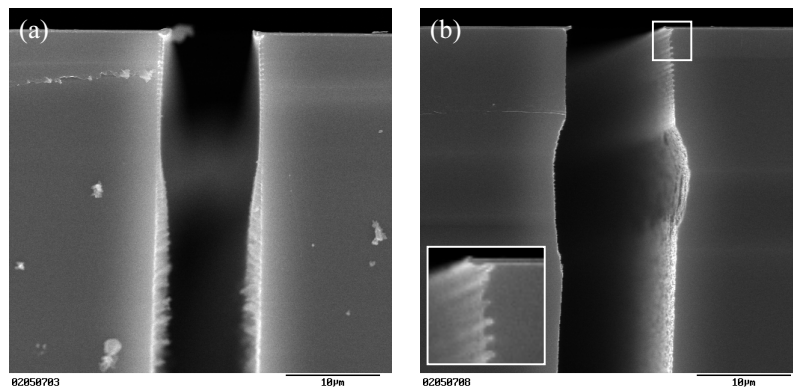
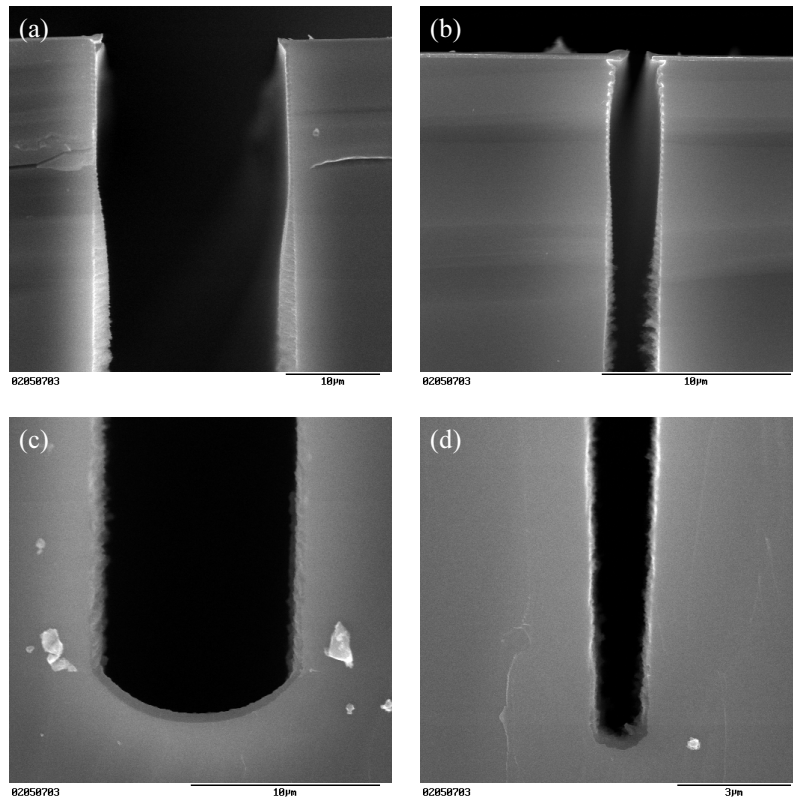


Figure 6.4 (a) Large sidewall deposition is visible about  $15\ \mu\text{m}$  below the mask. (b) The largest sidewall erosion is visible around the same depth after exposure to a continuous  $SF_6$  plasma. The inset shows a close-up of the mask region where the lateral etch is visible.

Close-ups of the top of a trench with a  $20\ \mu\text{m}$  and a  $2\ \mu\text{m}$  wide mask aperture are given in figure 6.5a and 6.5b respectively. The polymer sidewall deposition is much more pronounced in the wide trench due to the broad access of  $CF_x$  radicals. Close-ups of the bottom of a trench with a  $10\ \mu\text{m}$  and  $1.5\ \mu\text{m}$  wide mask aperture are given in figure 6.5c and 6.5d respectively. Substantial deposition is even visible on the bottom of the smallest trench, although it is a factor of 2 thinner than on the bottom of the largest trench possibly due to the reduced  $CF_x$  radical and ion flux.

The polymer layer on the bottom of the trench is denser than on the sidewalls. The difference in morphology is ascribed to the influence of the ions on the deposition mechanism. It indicates that the radical-induced component and the ion-enhanced component are not independent as is assumed in the deposition model. In consequence, the

model could deviate from the experimental especially for higher ion fluxes and ion energies in accordance with the experiments.



*Figure 6.5 (a) Polymer deposition on the sidewall of a trench with a 20  $\mu\text{m}$  wide mask aperture. (b) A trench with a 2  $\mu\text{m}$  wide mask aperture. (c) Polymer deposition on the bottom of a trench with a 10  $\mu\text{m}$  wide mask aperture. (d) A trench with a 1.5  $\mu\text{m}$  wide mask aperture.*

### **Ion flux variation**

The polymer deposition in trenches is compared to the polymer deposition on the structures with the overhanging membrane as a function of the ion flux and the pressure. The polymer deposition rate was measured on the sidewalls about 15  $\mu\text{m}$  below the mask and on the bottom of a trench with a 10  $\mu\text{m}$  wide mask aperture and an aspect ratio of 8. The results for all four combinations of either 150 sccm or 75 sccm  $\text{C}_4\text{F}_8$  and either a low or a high ion flux are given in table 6.7. Other plasma conditions were identical to the Bosch 3 process

conditions. For comparison the radical-induced deposition rate and ion-enhanced deposition rate on an open area taken from table 6.3 are given in parentheses.

*Table 6.7 The polymer deposition rate on the sidewalls about 15  $\mu\text{m}$  below the mask and on the bottom of a trench with a 10  $\mu\text{m}$  wide mask aperture for different  $\text{C}_4\text{F}_8$  flows and ion fluxes. For comparison the radical-induced and ion-enhanced deposition rate taken from table 6.3 are given in parentheses.*

Deposition Rate ( $\text{nm}\cdot\text{min}^{-1}$ )			Low Ion Flux		High Ion Flux	
75 sccm	Sidewalls	(Radical-Induced)	107 $\pm$ 8	(14 $\pm$ 2)	236 $\pm$ 8	(24 $\pm$ 2)
	Bottom	(Ion-Enhanced)	52 $\pm$ 8	(40 $\pm$ 2)	73 $\pm$ 8	(57 $\pm$ 2)
150 sccm	Sidewalls	(Radical-Induced)	57 $\pm$ 8	(36 $\pm$ 2)	257 $\pm$ 8	(52 $\pm$ 2)
	Bottom	(Ion-Enhanced)	56 $\pm$ 8	(141 $\pm$ 2)	98 $\pm$ 8	(78 $\pm$ 2)

The sidewall deposition rate is larger than the radical-induced deposition rate, which indicates that the polymer deposition is ion-enhanced. Moreover, the sidewall deposition rate is also larger than the ion-enhanced polymer deposition rate on an open area except for the case of 150 sccm  $\text{C}_4\text{F}_8$  and a low ion flux. Such a large ion-enhanced the sidewall deposition is unexpected because the ion flux to the sidewalls is much smaller (approximately a factor of 30 smaller for an average absolute ion angle of  $2^\circ$ ). However, ions with a grazing angle of incidence lose their energy over a large area and near the surface, so that they can create more activated surface sites on the trench sidewalls. Sputtering is reduced for a grazing angle of incidence. An angle-dependent surface site activation coefficient and an angle-dependent sputter yield are necessary to understand the thick polymer deposition on the trench sidewalls.

Despite the narrow trench the deposition rate on the bottom is slightly larger than the ion-enhanced deposition rate on an open area except for the case of 150 sccm  $\text{C}_4\text{F}_8$  and a low ion flux. Polymer redeposition from the sidewalls possibly increases the deposition rate in deep trenches [5]. The polymer deposition rate on the sidewalls is larger than on the bottom, which is advantageous for the etching of high aspect ratio trenches. The ratio is the largest for the case of 75 sccm  $\text{C}_4\text{F}_8$  and a high ion flux, which is consistent with the results given in chapter 4 where the maximal obtainable aspect ratio is higher for a lower pressure and a higher ion flux. However, there is still substantial polymer deposition on the bottom.

### **Ion energy variation**

An increase of the ion energy can lead to predominant sidewall deposition in deep trenches because it leads to a decrease of the polymer deposition rate on an open area. The better directionality of the ions is an additional advantage. The twin ridge structure, which is visible in figure 6.6, was used to investigate influence of the bias voltage on the polymer

sidewall deposition. In the narrow trench between the two ridges the polymer deposition is comparable to the previous experiments. In the wide trenches beside the two ridges the sidewall deposition extends along the whole structure due to unlimited access of  $CF_x$  radicals. Besides, the ions hit the sidewall deeper down the trench due to the more negative sidewall taper shifting the ion-enhanced deposition down.

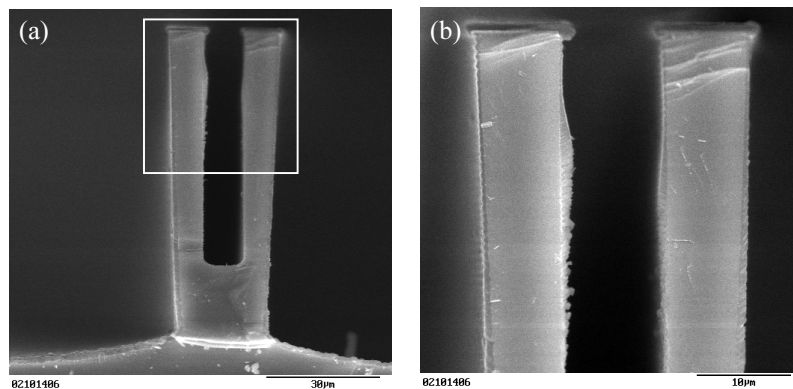


Figure 6.6 (a) Polymer deposition on a twin ridge structure. (b) The sidewall deposition extends along the whole sidewall of the wide trench (left), whereas it is localised near the top of the narrow trench (middle).

The polymer deposition in a deep trench was investigated for several  $C_4F_8$  flows/pressures as a function of the bias voltage. Other plasma conditions were identical to the Bosch 3 process conditions. In high-density plasmas the ion flux does not depend on the bias voltage and is thus constant for given plasma conditions. Trenches with a mask aperture of  $10\ \mu\text{m}$  were etched to a depth of  $65\ \mu\text{m}$  and were subsequently exposed to the continuous  $C_4F_8$  plasma. The deposition rate was measured on the bottom in the middle of the trench and on the trench sidewall  $5\ \mu\text{m}$  above the bottom. The sidewall deposition was measured near the bottom instead of near the mask because the anisotropic etching process is limited by excessive passivation deep down the trench. The results are shown in figure 6.7a and 6.7b respectively, and the ratio of the deposition rate on the bottom and on the sidewall is plotted in figure 6.7c.

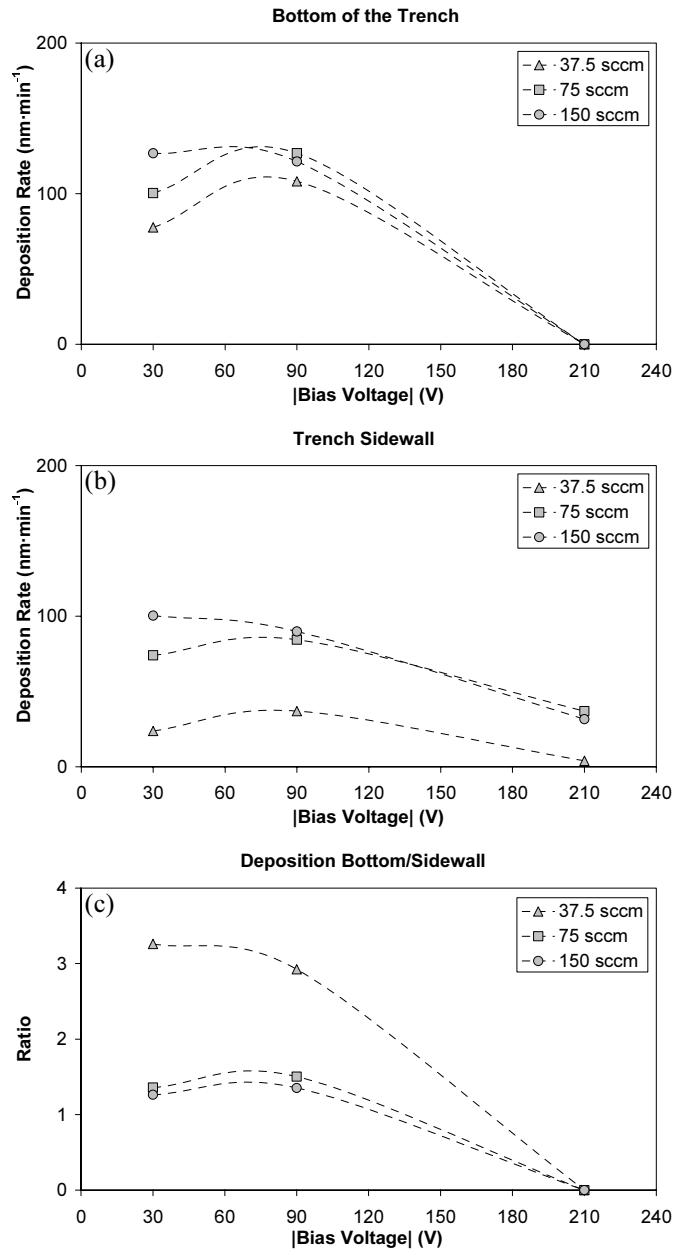


Figure 6.7 (a) The deposition rate on the bottom of the trench. (b) The deposition rate on the trench sidewall. (c) The ratio of the deposition rate on the bottom and the sidewall.

The deposition rate on the bottom of the trench has a weak dependence on the  $C_4F_8$  flow and at a bias voltage of  $-90$  V it is comparable to the values given in table 6.7. For  $-210$  V bias voltage there was no deposition on the bottom, whereas there was still polymer deposition on the sidewalls. For 37.5 sccm  $C_4F_8$  the sidewall deposition rate was much smaller presumably due to the high ion flux and the low  $CF_x$  radical flux. So a low  $C_4F_8$  flow/pressure does not enhance the ratio of the deposition rate on the bottom and the sidewall. On the contrary, the lowest ratio was obtained for 75 sccm and 150 sccm  $C_4F_8$ , and the ratio was zero for a bias voltage of  $-210$  V. Preferential sidewall deposition is thus obtained by an increase of the bias voltage from  $-90$  V to  $-210$  V.

### 6.3 Trench profile optimisation by controlling the ion energy

The preferential sidewall deposition found for higher bias voltages was used to optimise the trench profiles. The optimal bias voltage for etching and passivation can be different. Therefore, the bias voltage was pulsed along with the gases. The independent control of the ion energy during etching and passivation was used to obtain a more profound understanding of the passivation and depassivation mechanisms in deep trenches. In this section three experiments, where the influence of the bias voltage on the trench profile was investigated, are described. First, the bias voltage during the passivation pulse was varied, second, the bias voltage during the etching pulse was varied, and third, the bias voltage during the passivation and etching pulse were varied simultaneously. The passivation and etching pulse time were necessarily adjusted to obtain anisotropic profiles. The plasma conditions were based on the Bosch 4 process conditions given in appendix B, but the varied bias voltage and the adjusted pulse time settings are summarised in table 6.8.

*Table 6.8 The bias voltage and the pulse time settings for etching and passivation (Etch. = Etching, Pass. = Passivation) that are used in anisotropic trench etching experiments. The bias voltage during etching and passivation are varied, and for each experiment the passivation pulse time is adjusted so that anisotropic profiles are obtained. The etching pulse time has to be increased for a bias voltage of  $-30$  V because the passivation pulse time cannot be reduced below 2 s due to hardware constraints.*

Passivation Bias Voltage Variation				Etching Bias Voltage Variation				Simultaneous Bias Voltage Variation			
Bias Voltage (V)		Pulse Time (s)		Bias Voltage (V)		Pulse Time (s)		Bias Voltage (V)		Pulse Time (s)	
Etch.	Pass.	Etch.	Pass.	Etch.	Pass.	Etch.	Pass.	Etch.	Pass.	Etch.	Pass.
$-90$	$-30$	6	3	$-30$	$-90$	7	2	$-30$	$-30$	8	2
$-90$	$-90$	6	4	$-90$	$-90$	6	4	$-90$	$-90$	6	4
$-90$	$-210$	6	7	$-210$	$-90$	6	6	$-210$	$-210$	6	10



### Bias voltage variation during passivation

In the first experiment the bias voltage during passivation was varied while the bias voltage during etching is kept constant at  $-90$  V. The necessary increase of the passivation pulse time for a bias voltage of  $-210$  V is caused by the lower sidewall deposition rate already shown in figure 6.7b. SEM pictures of trenches with a mask aperture of  $1\ \mu\text{m}$  are shown in figure 6.8. The maximal obtainable aspect ratio of 25 does not increase significantly, but the sidewall taper is slightly negative for a bias voltage of  $-210$  V. There is no polymer deposition on the bottom of the trench due to the energetic ion flux for a bias voltage of  $-210$  V. As a result silicon etching starts immediately after the etching pulse is switched on. The width of the etched silicon area increases gradually with depth because the ion beam is slightly diverging, which explains the slightly negative sidewall taper. The trench profile cannot be improved substantially by increasing the passivation pulse time. Apparently, the polymer deposition in the corners of the trench is zero, so that the etched silicon area does not become narrower.

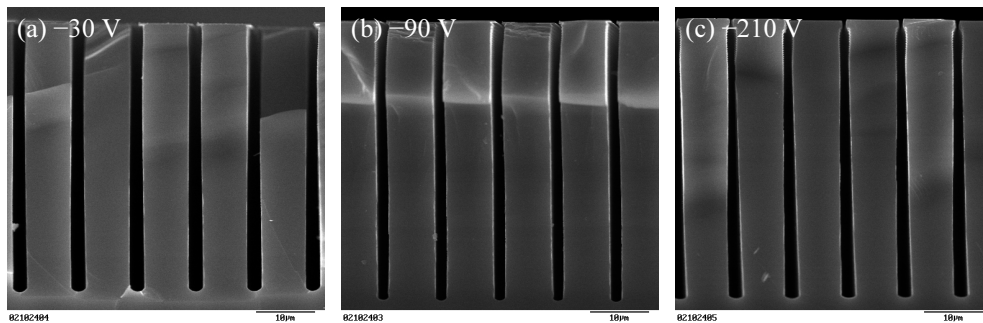
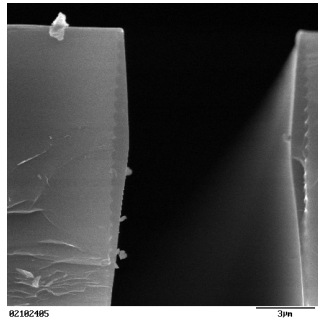


Figure 6.8 The influence of the bias voltage during passivation on the trench profile. The bias voltage during etching is  $-90$  V. The bias is voltage during passivation (a)  $-30$  V, (b)  $-90$  V, and (c)  $-210$  V. The sidewall taper is slightly negative for a bias voltage of  $-210$  V.

The long passivation pulse time for a bias voltage of  $-210$  V during passivation leads to a thick polymer layer near the top of the trench, which is shown in figure 6.9. Compared to figure 6.4 the polymer deposition is located much closer to the mask indicating that it has a radical-induced origin and the structure is more compact. Below this region, the sidewall taper is slightly negative because the erosion is slightly stronger than the deposition due to the divergent, energetic ion flux.



*Figure 6.9 Radical-induced polymer deposition near the top of the trench leads to a thick passivation layer due to the long passivation pulse time for a bias voltage of  $-210$  V.*

#### **Bias voltage variation during etching**

In the second experiment the bias voltage during etching was varied while the bias voltage during passivation was kept constant at  $-90$  V. The SEM pictures of the trench profiles are shown in figure 6.10. Compared to the passivation experiment in figure 6.8, the sidewall taper depends strongly on the bias voltage during etching. An increase of the bias voltage from  $-30$  V to  $-90$  V leads to a strong decrease of the positive sidewall taper and a strong increase of the maximal obtainable aspect ratio from 14 to 28. This shows once more that the divergence of the ions during the etching pulse, which is larger for a bias voltage of  $-30$  V, is an important limiting factor in the profile evolution. For a bias voltage of  $-210$  V the sidewall taper is negative and the maximal obtainable aspect ratio is 29. So the divergence of the ions is not limiting anymore, but the maximal obtainable aspect ratio does not increase significantly because of the larger lateral etch due to sidewall erosion by the energetic ions. The advantage is that the depth of trenches is not limited by convergence of the sidewalls.

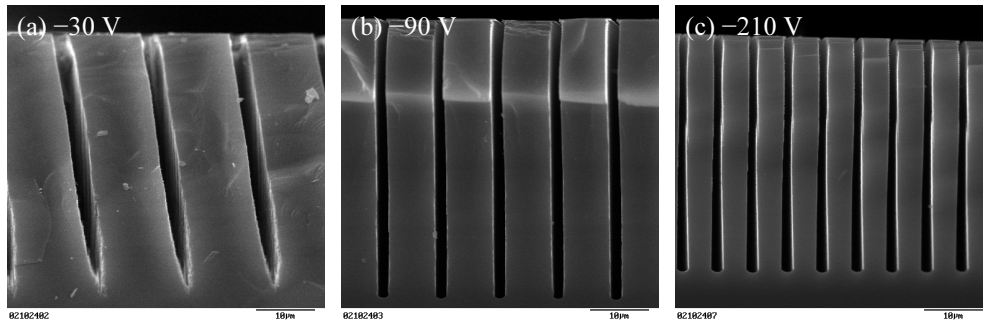


Figure 6.10 The influence of bias voltage during etching on the trench profile. The bias voltage during passivation is  $-90\text{ V}$ . The bias voltage during etching is (a)  $-30\text{ V}$ , (b)  $-90\text{ V}$ , and (c)  $-210\text{ V}$ . An increase of the bias voltage leads to a negative sidewall taper.

#### Simultaneous bias voltage variation

An increase of the bias voltage improves the trench profile both during passivation and etching. The largest improvement of the trench profile can thus be obtained for a simultaneous increase of the bias voltage during passivation and etching. So bias voltage pulsing appears to be unnecessary.

In the third experiment the bias voltage during passivation and etching were varied simultaneously and were kept equal. The SEM pictures of the trench profiles are shown in figure 6.11. A transition from a severe positive sidewall taper for  $-30\text{ V}$  bias voltage to a severe negative sidewall taper for  $-210\text{ V}$  bias voltage is visible. For a bias voltage of  $-120\text{ V}$  the sidewalls were nearly vertical, the bottom of the trench was flat and the maximal obtainable aspect ratio was 33. So, the optimal trench profile for the current plasma conditions was obtained by tuning the bias voltage.

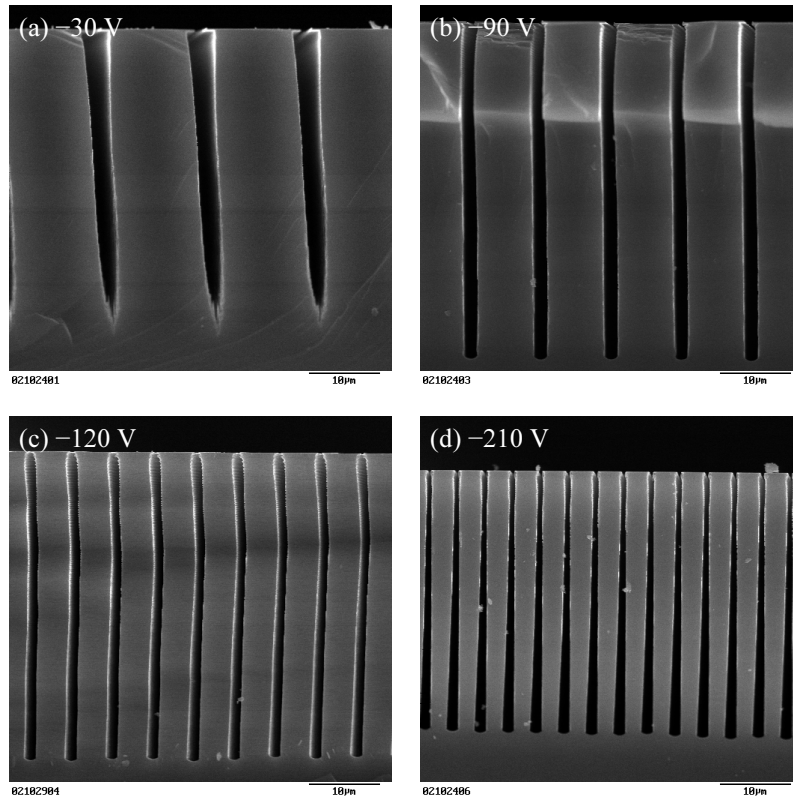


Figure 6.11 Transition from a severe positive sidewall taper to a severe negative sidewall taper as a function of bias voltage. The bias voltage is (a)  $-30$  V, (b)  $-90$  V, (c)  $-120$  V, and (d)  $-210$  V. The optimal anisotropy is obtained at a bias voltage of  $-120$  V.

Depletion of  $\text{CF}_x$  radicals and ions play an important role in trench etching and can explain the transition from a positive sidewall taper to a negative sidewall taper. The depletion of ions decreases with increasing bias voltage because of the decreasing average absolute ion angle. The depletion of  $\text{CF}_x$  radicals does not depend on the bias voltage. As a result, for higher bias voltages ( $-210$  V) the passivation decreases with depth faster than the etching, so that the etched silicon area increases with depth leading to a negative sidewall taper. The opposite is true for lower bias voltages ( $-30$  V). In the optimal case ( $-120$  V) the passivation and etching decrease equally fast with depth leading to perfectly anisotropic profiles.

## 6.4 Bias voltage ramping

The optimal bias voltage obtained in the previous section is quite high leading to strong mask erosion and low etch selectivity. To reduce this effect a lower bias voltage can be used in the beginning of the process because the magnitude of the bias voltage is only critical for high aspect ratio trenches. Subsequently, the bias voltage is ramped up to influence dynamically the balance between passivation and depassivation. Pressure ramping can also be used to arrive at a higher ion-to-radical flux ratio [6].

In this experiment the bias voltage was ramped up from  $-50$  V to  $-125$  V in 5 successive steps of  $-15$  V. The other plasma conditions were identical to the Bosch 4 plasma conditions, but the  $C_4F_8$  flow was 105 sccm. The passivation pulse time was set for an intermediate value, so that there was a transition from overpassivation in the beginning to underpassivation at the end. This way the lateral etch and the sidewall ripples were reduced at the top of the trench [7,8]. The trenches with a mask aperture of  $0.6\ \mu\text{m}$  were perfectly anisotropic, but had a uniform lateral etch of  $0.9\ \mu\text{m}$ . Wider trenches had a more negative sidewall taper. The SEM pictures of these trenches are given in figure 6.12. The bias voltage ramping is only optimal for a certain trench width, because sidewall bowing is aspect ratio dependent and not time dependent. The maximal obtainable aspect ratio was 30. It seems that at this aspect ratio the vertical etch rate is outweighed by a small lateral etch, so that the aspect ratio does not increase anymore. An improvement could be to ramp up the passivation pulse time along with the bias voltage, so that the lateral etch is reduced. The plasma conditions from the previous section are a good starting point, because the bottom of high aspect ratio trenches is flat for higher bias voltages.

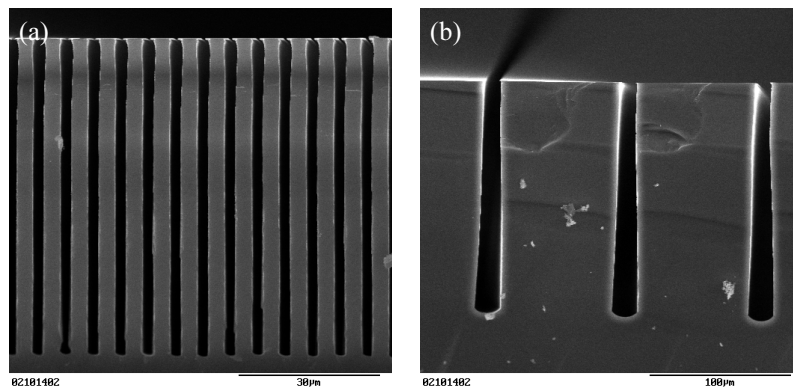


Figure 6.12 Bias voltage ramping is only optimal for a certain trench width. (a) Perfectly anisotropic trenches with a mask aperture of  $0.6\ \mu\text{m}$ . (b) Wider trenches have a negative sidewall taper.

## 6.5 Conclusions

The polymer deposition rate in a  $C_4F_8$  plasma is strongly ion-enhanced for ion energies below the sputter energy threshold. For higher ion energies the deposition rate is reduced by the sputtering component. A model has been developed that qualitatively describes the polymer deposition as a function of the radical and ion fluxes. Predominant sidewall deposition has been obtained for higher ion energies because the ion flux to the sidewalls is much lower than the ion flux to the bottom of the trench. The bias voltage during passivation and etching have been optimised independently with bias voltage pulsing. A higher bias voltage during passivation leads to a flat bottom of the trench and a slightly negative sidewall taper because no polymer passivation layer has to be removed from the bottom of the trench due to the predominant sidewall deposition. A higher bias voltage during etching leads to the same improvements because the divergence of the ion flux is smaller. However, the largest improvements have been achieved for a simultaneous increase of the bias voltage during passivation and etching. It demonstrates that bias voltage pulsing is unnecessary afterwards. The trench profile has been optimised by adjusting the ion energy. As a result the sidewall taper is minimal and the maximal obtainable aspect ratio is 33 for the optimal plasma conditions. The maximal obtainable aspect ratio is only limited by the small lateral etch rate, which outweighs the vertical etch rate for longer etch times.

## References

- [1] M.J. Sowa, M.E. Littau, V. Pohray, and J.L. Cecchi, *J. Vac. Sci. Technol. A* **18**, 2122 (2000)
- [2] W. Schwarzenbach, G. Cunge and J.P. Booth, *J. Appl. Phys.* **85**, 7562 (1999)
- [3] G. Cunge, P. Chabert and J.P. Booth, *J. Appl. Phys.* **89**, 7750 (2001)
- [4] Y. Horiike, K. Kubota, H. Shindo and T. Fukasawa, *J. Vac. Sci. Technol. A* **13**, 801 (1995)
- [5] T. Ono, R. Hamasaki and T. Mizutani, *Jpn. J. Appl. Phys.* **35**, 2468 (1996)
- [6] J. Hopkins, H. Ashraf, J.K. Bhardwaj, A.M. Hynes, I. Johnston and J.N. Shepherd, *Proceedings of the Materials Research Society Fall Meeting*, 1 (Boston, USA, 1998)
- [7] A.M. Hynes, H. Ashraf, J.K. Bhardwaj, J. Hopkins, I. Johnston and J.N. Shepherd, *Sensors and Actuators* **74**, 13 (1999)
- [8] M. Chabloz, Y. Sakai, T. Matsuura and K. Tsutsumi, *Microsystem Technologies* **6**, 86 (2000)

## Chapter 7

# Plasma-material interactions in ion-induced etching of silicon carbide and silicon

Fluorine-based plasma etching of silicon can be explained well by the transport of the fluorine radicals. However, the transport of the ions cannot be illustrated clearly because the ion-induced features are smoothed by the spontaneous chemical reactions. A better understanding of the transport of the ions in deep anisotropic trenches can help to clarify the crucial role of the ions in the depassivation mechanism. Therefore, the role of the ions is investigated more explicitly by using plasma-material combinations for which the spontaneous chemical reaction is absent. In this chapter silicon carbide etching in an SF<sub>6</sub>-O<sub>2</sub> plasma and silicon etching in a Cl<sub>2</sub> plasma are treated as examples of ion-induced etching.

The outline of this chapter is as follows. In section 7.1 ion-induced silicon carbide etching in an SF<sub>6</sub>-O<sub>2</sub> plasma is described. The plasma-material interactions are unravelled by the combination of etch rate investigation and plasma characterisation. Fluorine-limited and ion-limited etching regimes are identified. In this respect the etching mechanism influences both the trench profile and the etch rate. Aspect ratio dependent etching (ARDE) is investigated for trenches aimed at aspect ratios much larger than 1. In the ion-limited regime the etching is aspect ratio independent. In the fluorine-limited regime the etch rate decreases with aspect ratio because the fluorine radical flux is reduced by Knudsen transport due to the high reaction probability. In section 7.2 ion-induced silicon etching in a Cl<sub>2</sub> plasma is described. A quantitative analysis of the surface kinetics shows that the etching mechanism is described by the ion-neutral synergy model and that the reaction probability is much lower than 1. The low reaction probability leads to aspect ratio independent etching (ARIE).

### 7.1 Fluorine-based high-density plasma etching of high aspect ratio silicon carbide structures

Silicon carbide is an excellent substrate material for many special applications. However, the chemical inertness due to the strong silicon-carbon bond (4.25 eV) makes wet chemical processing difficult. Ion-assisted dry etching in both fluorine-based and chlorine-based high-density plasmas is the obvious method to fabricate silicon carbide devices [1-3]. For an SF<sub>6</sub>-O<sub>2</sub> plasma it has been shown that the ions break the silicon-carbide bonds near the surface, so that the silicon atoms can react with the fluorine radicals forming volatile SiF<sub>4</sub> and the carbon atoms can form a thin fluorocarbon layer. Sputtering of the fluorocarbon layer is the rate limiting reaction step and the major reaction products are CF and CF<sub>2</sub> [4,5].

Etch rates up to  $1.35 \mu\text{m}\cdot\text{min}^{-1}$  have been obtained due to the ion-neutral synergy. The silicon carbide etching mechanism in an  $\text{SF}_6\text{-O}_2$  plasma is treated in more detail in subsection 7.1.1.

Silicon carbide etching in an  $\text{SF}_6\text{-O}_2$  plasma is suitable for the fabrication of anisotropic structures. Etch depths of hundreds of microns have been achieved, but most fabricated structures have fairly large lateral dimensions. As a result the transport of fluorine radicals and ions is not hindered by sidewall collisions and the etch rate is constant throughout the process [4]. The influence of the plasma-material interactions on the profile of trenches and ridges is treated in subsection 7.1.2.

For higher integration densities and for nanoelectromechanical systems the lateral dimensions will be smaller. It can safely be assumed that the aspect ratios will be much higher than 1 for devices with supreme performance. As a result the transport of fluorine radicals is significantly hindered. The transport of ions is hindered much less because the ions move almost perpendicular to the substrate. The etching of high aspect ratio silicon carbide structures is described in subsection 7.1.3.

### **Specific applications of silicon carbide**

Power electronics and microelectromechanical systems (MEMS) are specific applications of silicon carbide. The high breakdown electric field strength, the high band gap and the high thermal conductivity make it an extremely attractive material for power electronics. The high Young's modulus, the high mechanical strength and the chemical inertness are important properties for high-quality MEMS devices. Sensors operating in chemically harsh environments are an example of the application of silicon carbide in MEMS [6]. Silicon carbide is also a suitable material for smaller dimensions due to its stability, so that the fabrication of nanoelectromechanical systems (NEMS) becomes feasible [7].

### **Experimental conditions**

Samples were cut from different types of 2" silicon carbide wafers depending on availability. For the etch rate investigation, 4H-SiC samples were patterned with NUV lithography. For the profile investigation, trenches and ridges in the range of  $0.40 \mu\text{m}$  to  $10.0 \mu\text{m}$  were defined with electron beam lithography on nitrogen doped,  $0.051 \Omega\cdot\text{cm}$ , n-type 6H-SiC samples. The patterns were transferred with metal evaporation and lift-off. Chromium and nickel were used as mask material with a thickness from ranging  $200 \text{ nm}$  to  $500 \text{ nm}$  because with these metals an etch selectivity up to 35 was achieved. Adhesion of the nickel layer to the substrate was improved with a  $20 \text{ nm}$  thick titanium layer.

Samples were etched in the Alcatel ICP reactor. The substrate holder was fixed in the position where the ion flux was maximal. The ion flux and plasma potential were measured with the Langmuir probe system and the fluorine radical partial pressure was measured by actinometry.



### **7.1.1 SiC etching kinetics: etch rate investigation and plasma characterisation**

Plasma characterisation and etch rate investigation were combined to investigate the plasma-material interactions. The measurement of the fluorine radical partial pressure and the ion flux were performed under conditions that are identical to those during the etch rate experiments. The surface kinetics were quantified by the etch yield (defined by the number of SiC molecules removed per ion) and the reaction probability of fluorine radicals. In the calculation of the reaction probability it was assumed that SiF<sub>4</sub> and CF<sub>2</sub> are the reaction products of the etching process [4]. The initial plasma parameters were 40.0 sccm SF<sub>6</sub>, 10.0 sccm O<sub>2</sub>, 0.68 Pa pressure, 2000 W source power, -300 V bias voltage and 25 °C substrate temperature. In literature it is found that the addition of 20% oxygen improves the process, because it prevents the deposition of material on the reactor walls [4]. In all experiments the plasma sheath thickness was smaller than the mean free path, so that ion-neutral collisions played a minor role.

At first the bias voltage was varied. The etch rate was nearly proportional to the etch yield, because the ion flux variations were smaller than 6%. The fluorine radical-to-ion flux ratio, the flux ratio for short, was nearly constant for the same reason. The etch yield is plotted as a function of ion energy in figure 7.1. The ion energy is proportional to the plasma potential minus the bias voltage. The etch yield increases strongly over a large range of the ion energy, which is indicative of an ion-induced process, but two points deviate significantly from this trend. At the lowest ion energy (a bias voltage of 0 V) significant etching takes place, which cannot be explained by sputtering alone, so at this point chemical reaction with fluorine radicals adds to the etch yield. On the other hand at the highest ion energy (a bias voltage of -450 V) the etch yield levels off because the supply of fluorine radicals is probably rate limiting.

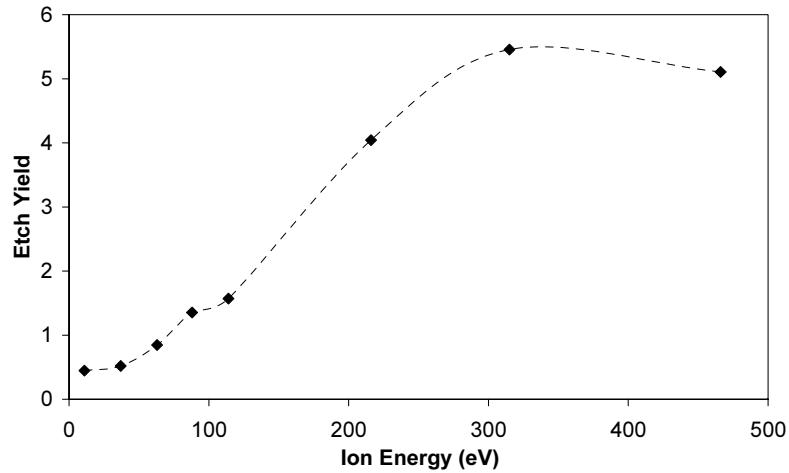


Figure 7.1 The etch yield increases strongly as a function of the ion energy, but for the lowest and highest ion energy the etch yield deviates from this trend.

Subsequently the pressure and the source power were varied. The pressure rise was achieved by an increase of the gas flow from 25.0 sccm to 100.0 sccm with increments of 25.0 sccm and keeping the oxygen fraction constant. A typical etch rate of  $0.69 \mu\text{m}\cdot\text{min}^{-1}$  was obtained for a pressure of 0.68 Pa. The etch yield and the flux ratio are plotted as a function of pressure and power in figure 7.2 and 7.3 respectively. The etch yield increases for an increase of the pressure from 0.38 Pa to 0.68 Pa and is constant for pressures of 0.68 Pa and above, which indicates that the etching is fluorine-limited for a pressure of 0.38 Pa and ion-limited for pressures of 0.68 Pa and above. The flux ratio increases quickly as a function of pressure both due to an increased fluorine radical partial pressure and a decreased ion flux.

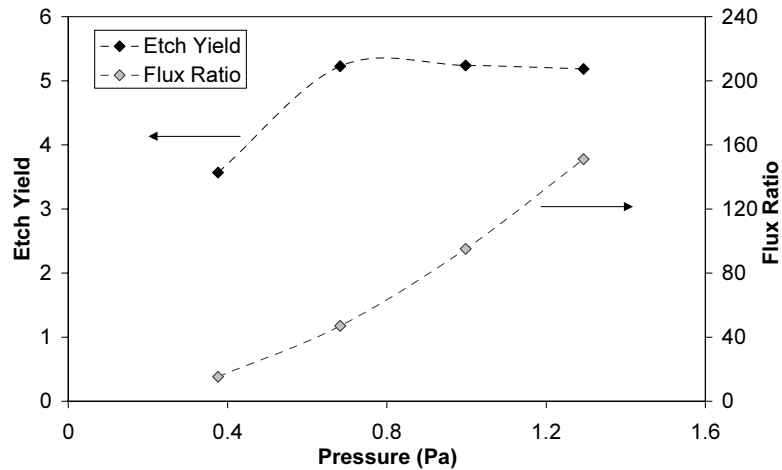


Figure 7.2 The etch yield and the flux ratio as a function of pressure. The etch yield decreases below a certain radical-to-ion flux ratio.

The etch yield was nearly constant in the investigated range of source power. The pressure was kept constant at 0.68 Pa. The flux ratio shows a decreasing trend, which is mainly caused by the increase of the ion flux, but the flux ratio is larger than 43. The etching is thus ion-limited, because an increase of the ion flux leads to a proportionally higher etch rate. In general the etch yield is constant as a function of both pressure and source power for flux ratios larger than about 40. This means that the etching mechanism changes from fluorine-limited to ion-limited around a flux ratio of 40, which is consistent with the results shown in figure 7.2 [8-10].

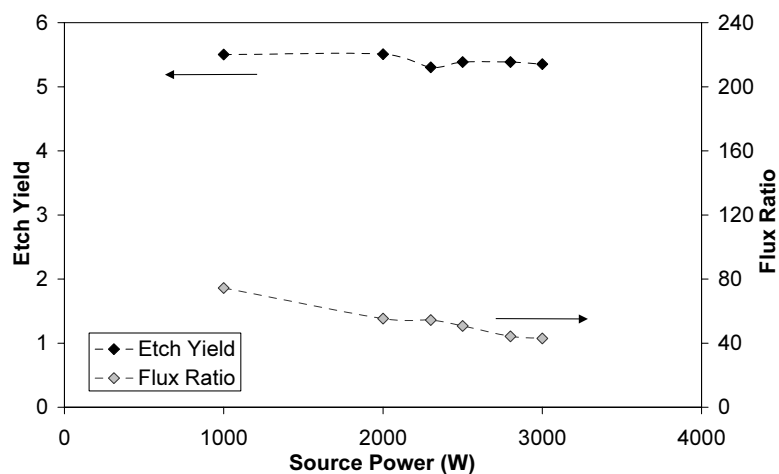


Figure 7.3 The etch yield and the flux ratio as a function of source power. The radical-to-ion flux ratio decreases due to a decrease of the ion flux.

The reaction probability was calculated using the ratio of the etch rate and the fluorine radical flux. The flux ratio and the calculated reaction probability are given as a function of pressure and source power in table 7.1. The observed trends are that it decreases for higher flux ratios and that it is nearly 1 for lower flux ratios. A transition from ion-limited to fluorine-limited etching simply must have occurred for lower flux ratios since all available fluorine radicals are consumed. Surprisingly, the calculated reaction probability is larger than 1 for the lowest pressure. The reason for this non-physical result could be that the reaction products contain less fluorine than assumed due to the lack of fluorine radicals, so that the reaction probability is overestimated. Moreover, the sputtering of a fluorocarbon layer resulting in reaction products such as CF and C in stead of CF<sub>2</sub> is more difficult, which is in line with the reduced etch yield for the lowest pressure. The experiments thus show that the etching mechanism depends on the flux ratio, which can be influenced by the plasma conditions.

Table 7.1 The flux ratio and the reaction probability as a function of pressure and source power.

Pressure (Pa)	Flux Ratio	Reaction Probability	Source Power (W)	Flux Ratio	Reaction Probability
0.38	15	1.41	1000	74	0.44
0.68	47	0.67	2000	55	0.60
1.00	95	0.33	3000	43	0.75
1.29	151	0.21	-	-	-

### 7.1.2 Profile evolution for ion-induced SiC etching

In the previous subsection it is shown that the plasma conditions strongly influence the silicon carbide etching mechanism. The profile of trenches and ridges is mainly determined by the etching mechanism for given radical and ion fluxes. Accurate profile control is necessary if the lateral dimensions are small compared to the depth. Therefore, the influence of the plasma conditions on the profile is described in this subsection. Profile investigations were performed with similar plasma conditions as in the previous subsection, but the bias voltage of  $-250$  V was slightly lower. The profiles of  $5.0$   $\mu\text{m}$  wide trenches etched for 20 min with a source power of 2000 W and a pressure of 0.39, 0.72 and 1.30 Pa are shown in figure 7.4a, 7.4b and 7.4c respectively. Figure 7.4d shows a  $5.0$   $\mu\text{m}$  wide ridge etched with a pressure of 0.39 Pa. Three aspects of the profile are of importance for further consideration: sidewall tapering, sidewall bowing and microtrenching.

#### Sidewall tapering

In all cases the profile has a positive sidewall taper, that is the mask aperture is larger than the width at the base of the structure. For the highest pressure the most severe positive sidewall taper is visible and surface roughness becomes problematic. The production and the consumption of the fluorocarbon layer have to be well balanced with the ion flux similar to the Bosch process to obtain anisotropic profiles. However, the lowest ion flux was measured for the highest pressure, so that the removal of the fluorocarbon layer was a strongly limiting factor. Redeposition of  $\text{CF}_x$  radicals most likely played a role, because it increases the sidewall taper [11].

#### Sidewall bowing

Distinct sidewall bowing was observed for the lowest pressure, which was superimposed on the sidewall tapering. Due to the ion angular distribution (IAD) the ions are able to hit the sidewall, but the IAD is not broadened by ion-neutral collisions in the plasma sheath for

these low-pressure high-density plasma conditions. Despite the narrow IAD the largest sidewall etching was observed for the lowest pressure because the ion flux was the highest. Backscattered ions from the trench bottom could also contribute to the sidewall etching. Sidewall bowing was observed for both trenches and ridges, which demonstrates that ion scattering from an opposite mask sidewall does not play a role.

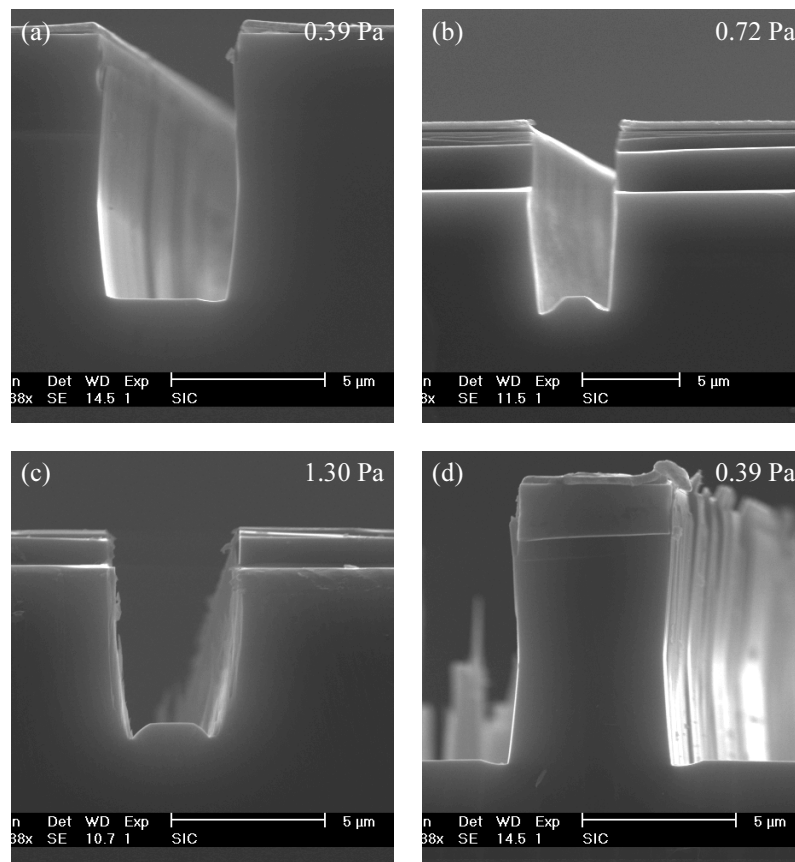


Figure 7.4 Anisotropic profiles for SiC etching in an  $SF_6-O_2$  plasma with a source power of 2000 W. A 5.0 μm wide trench after etching with a pressure of (a) 0.39 Pa, (b) 0.72 Pa and (c) 1.30 Pa. (d) A 5.0 μm wide ridge after etching with a pressure of 0.39 Pa.

### Microtrenching

The small depressions near the base of the sidewalls are the so-called microtrenches. They are caused by the focussing of ions into the corners of a trench by either sidewall collisions or electrostatic deflection [12-14]. However, electrostatic charging did not play a role in this

experiment because of the conducting metal mask. Microtrenching was nearly suppressed for the lowest pressure, which can be observed in figure 7.4a and 7.4d. In the previous subsection it was shown that etching is fluorine-limited for comparable plasma conditions. In a fluorine-limited regime there is no enhancement of the etch rate due to an increased ion flux, so that microtrenching is suppressed in agreement with the observations. Conversely, the microtrenches are the deepest in an ion-limited regime.

The same effects are observed for an increase of the source power. The profiles of 1.5  $\mu\text{m}$  wide ridges etched for 10 min etching with a pressure of approximately 0.72 Pa and a source power of 1000 W, 2000 W and 3000 W are shown in figure 7.5a, 7.5b and 7.5c respectively. The depth of the microtrenches relative to the height of the ridge decreases for increasing source power. The explanation is that the flux ratio decreases, so that a fluorine-limited regime is approached. The sidewall bowing increases for increasing source power because the ion flux increases.

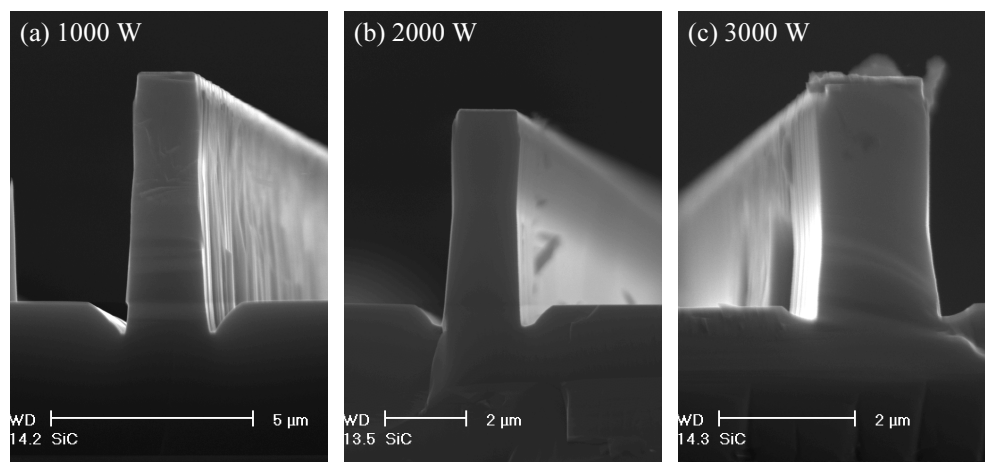


Figure 7.5 Anisotropic profiles of 1.5  $\mu\text{m}$  wide ridges etched with a pressure of approximately 0.72 Pa. (a) 1000 W source power. (b) 2000 W source power. (c) 3000 W source power.

### 7.1.3 High aspect ratio structures and aspect ratio dependent etching

In narrow trenches the transport of radicals and ions is restricted, which can lead to aspect ratio dependent etching. The transport of radicals is hindered by sidewall collisions and due to the high reaction probability the fluorine radical flux decreases as a function of aspect ratio [15,16]. Trenches were etched with the same plasma conditions as in the previous subsection to investigate aspect ratio dependent etching. The average etch rate of trenches in the range of 0.40  $\mu\text{m}$  to 10.0  $\mu\text{m}$  is shown as a function of aspect ratio for several

pressures in figure 7.6 and for several source powers in figure 7.7. The aspect ratio is defined by the ratio of the depth and width in the middle of the trench. This representation can result in a reciprocating curve for high aspect ratios because the dimensions of high aspect ratio trenches are not well-defined due to the positive sidewall taper.

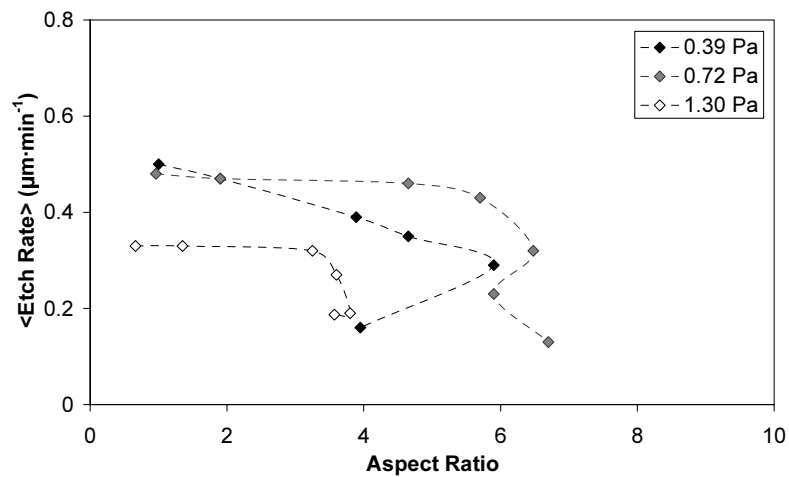


Figure 7.6 The average etch rate as a function of the aspect ratio for several pressures. It shows a steady decrease of the etch rate for the lowest pressure.



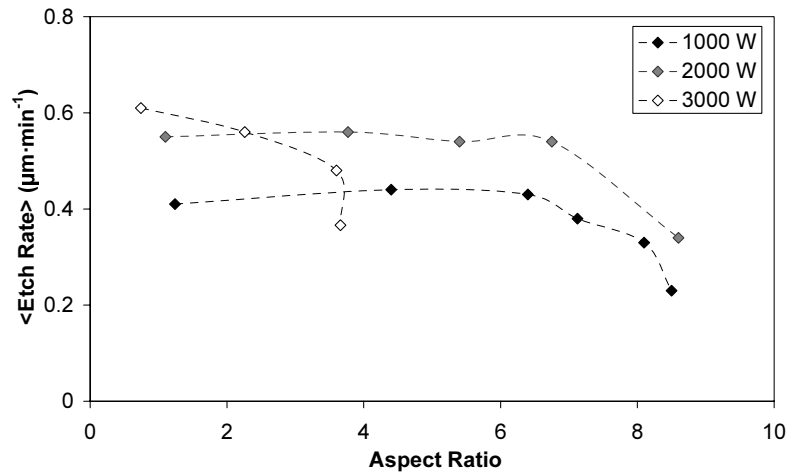


Figure 7.7 The average etch rate as a function of the aspect ratio for several source powers. It shows a steady decrease of the etch rate for the highest source power.

Two observations are important. First, the etch rate is nearly constant for low aspect ratios, except for the lowest pressure in figure 7.6 and for the highest source power in figure 7.7. For low pressure and high source power the flux ratio is low and the etching is fluorine-limited. The etch rate decreases as a function of aspect ratio because the reaction probability is high for these plasma conditions, by which Knudsen transport leads to depletion of the fluorine radical flux. Second, in all cases the etch rate drops drastically at a certain aspect ratio. The fluorocarbon layer is insufficiently removed in the corners of the trenches by the ion bombardment, so that the sidewalls converge and the average etch rate goes down.

A low pressure and a high source power are favourable for a good profile evolution resulting in a small sidewall taper and shallow microtrenches. However a too low pressure and a too high source power lead to aspect ratio dependent etching. A medium pressure and a medium source power are a good compromise, because the etch rate is optimal and aspect ratio independent. For this process a 1.5 μm wide trench with an aspect ratio of 3.8 etched for 10 min is shown in figure 7.8a. The stricture directly below the mask aperture is ascribed to mask erosion that increases the mask aperture and some sidewall bowing is also observed. The microtrenches are much smaller because they overlap partly. A trench and a ridge with a nominal width of 0.40 μm are shown in figure 7.8b and 7.8c respectively. The aspect ratio of these narrow structures is about 11, but the definition of the width is poor due to the positive sidewall taper. The etching of structures with aspect ratios higher than 10 is difficult, because for trenches the etching stops and for ridges the lateral dimension increases.

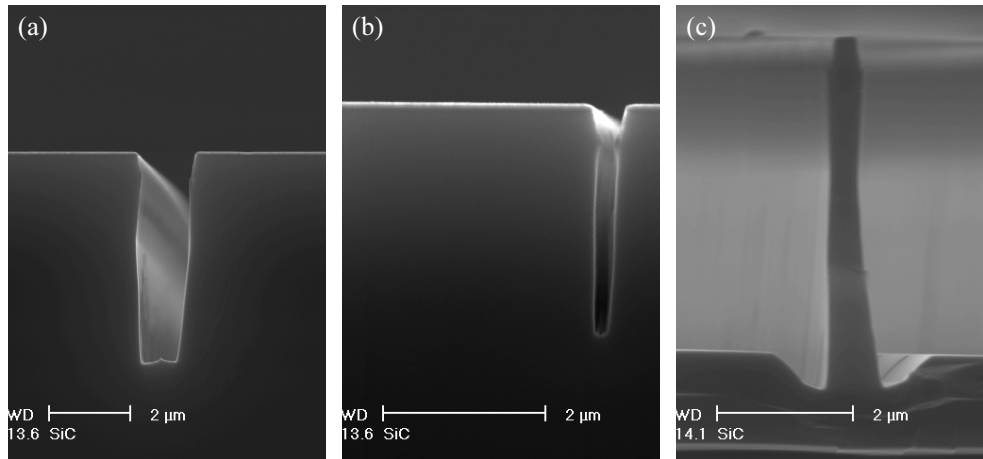


Figure 7.8 Profiles after etching with 0.72 Pa pressure and 2000 W source power. (a) 1.5  $\mu\text{m}$  wide trench. (b) 0.4  $\mu\text{m}$  wide trench. (c) 0.4  $\mu\text{m}$  wide ridge.

The analogy of SiC etching and the Bosch process is that the removal of a fluorocarbon layer by ion bombardment is an essential factor in the profile evolution and ultimately limits the etching of high aspect ratio trenches. However, in the Bosch process the fluorocarbon layer is deposited, and in SiC etching it is a reaction product. In the Bosch process the maximal obtainable aspect ratio of about 30 is much larger due to the chemical component in the etching mechanism.

In summary, the silicon carbide etching mechanism in an  $\text{SF}_6\text{-O}_2$  plasma ranges from fluorine-limited to ion-limited with increasing radical-to-ion flux ratio because of the ion neutral synergy. The profile of trenches and ridges depends on the details of the ion angular distribution and the angle dependent etch yield. Aspect ratio dependent etching is obtained because the reaction probability of the fluorine radicals is nearly one in a fluorine-limited regime.

## 7.2 Anisotropic silicon etching in $\text{Cl}_2$ plasmas

The etching of silicon in a  $\text{Cl}_2$  plasma is a well-known ion-induced process, so that it can be used as a good reference for silicon carbide etching. Samples with a silicon dioxide mask were etched in an ICP reactor dedicated to chlorine etching and of which the design is identical to the ICP reactor that was used in fluorine etching. Three different  $\text{Cl}_2$  flows were used: 20.0 sccm, 50.0 sccm and 100.0 sccm with a pressure of 0.10 Pa, 0.24 Pa and 0.43 Pa, respectively. Other plasma conditions were 500 W source power,  $-150$  V bias voltage and  $25^\circ\text{C}$  substrate temperature. In the following the impact of the ion bombardment on the etch yield, the trench profile and ARDE is investigated and compared to the etching of

silicon carbide in an SF<sub>6</sub>-O<sub>2</sub> plasma. Studying the differences and similarities helps to understand the reaction mechanism of both processes.

### **7.2.1 Ion-neutral synergy**

The silicon etch yield is plotted as a function of the flux ratio in figure 7.9a and compared to the silicon carbide etch yield shown in figure 7.9b. Plasma diagnostics are necessary to determine the etch yield and the flux ratio. The measured ion flux was approximately inverse proportional to the square root of the pressure ( $J_i \propto p^{-0.5}$ ) in a Cl<sub>2</sub> plasma. This power law was used to interpolate the ion flux at pressures where the etching experiments were actually performed. The chlorine radical partial pressure could only be measured qualitatively with actinometry, which showed that the chlorine radical partial pressure was approximately proportional to the pressure. More detailed studies have shown that Cl<sub>2</sub> is almost entirely dissociated for comparable plasma conditions [17]. This justifies the assumption that the chlorine radical partial pressure is equal the plasma pressure in the calculation of the flux ratio. The measured etch rate is almost independent of pressure. On the basis of these observations it is concluded that the silicon etch yield increases but that the chlorine radical reaction probability decreases with higher pressures. The increase of the silicon etch yield indicates that the experiments are performed in the transition from chlorine-limited to ion-limited etching.

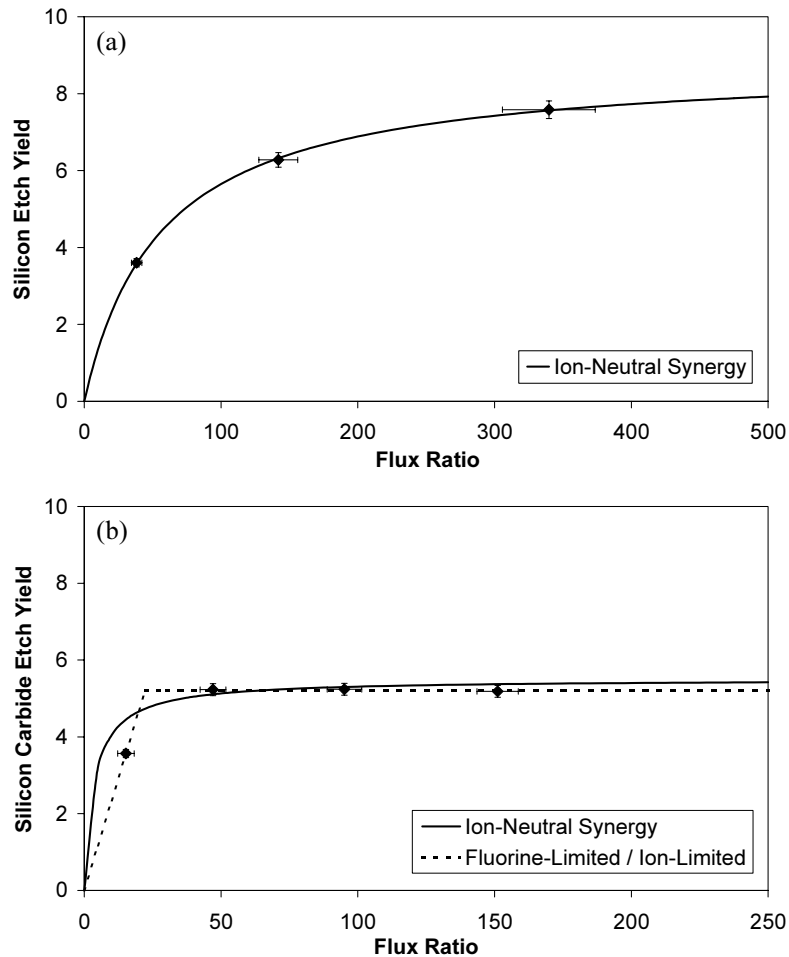


Figure 7.9 The etch yield as a function of the flux ratio. (a) Silicon etched in a  $\text{Cl}_2$  plasma. (b) Silicon carbide etched in an  $\text{SF}_6\text{-O}_2$  plasma. The silicon etch yield is fitted well by the ion-neutral synergy model. Silicon carbide etching is characterised by a more abrupt transition between fluorine-limited and ion-limited etching for lower flux ratios. The dotted line represents purely fluorine-limited and ion-limited etching.

The etch yield is fitted by the ion-neutral synergy model given in appendix A using the least squares method and the best fit is shown by the solid curve [9,18]. The experimental accuracy of the plotted quantities is given for a significant comparison of the data and the model. The experimental accuracy of the etch yield depends mainly on the ion flux measurement, which is accurate within 2%. The estimate of the chlorine flux ratio is accurate within 10% because the degree of dissociation of  $\text{Cl}_2$  is higher than 90%, and the

accuracy of the fluorine flux ratio is mainly determined by the accuracy of the Ar pressure measurement. The silicon etch yield is fitted well by the ion-neutral synergy model, but the silicon carbide etch yield cannot be fitted with this model for lower flux ratios, although it is only one point that deviates significantly from the ion-neutral synergy model. Nevertheless, the measured etch yield for a flux ratio of 15 lies well below the curve of the ion-neutral synergy model, which indicates that the transition between fluorine-limited (linear increase of the etch yield) and ion-limited etching (constant etch yield) is more abrupt. Purely fluorine-limited and ion-limited etching are represented by the dashed line for comparison. The distinct plasma-surface interactions are the most likely cause of the difference.

In silicon etching the ions are responsible for the sputtering of adsorbed reaction products [19]. The  $\text{SiCl}_x$  ( $x=1,2,3$ ) surface coverage increases progressively as the chlorine radical flux increases leading to a gradual increase of the etch yield. In silicon carbide etching the relatively abrupt transition between fluorine-limited and ion-limited etching is presumably caused by the different reaction mechanisms for silicon and carbon atoms. For high flux ratios (an excess of fluorine radicals) the breaking of the strong atomic bonds and the sputtering of the fluorocarbon layer are the rate limiting steps [4]. The etch yield and thus the fluorocarbon layer thickness is virtually independent of the ion flux, because there has to be a balance between the number of broken bonds and the number of sputtered  $\text{CF}_2$  radicals. Silicon atoms react spontaneously to  $\text{SiF}_4$  and disappear quickly from the surface not hindering the impact of the ions. Due to the abundant amount of fluorine radicals the  $\text{SiF}_x$  ( $x=0,1,2,3$ ) surface coverage is presumably below one monolayer and negligible in comparison with the fluorocarbon layer. However, below a certain flux ratio all fluorine radicals are consumed and unsaturated silicon reaction products accumulate on the surface reducing the etch yield. At this point sputtering of unsaturated  $\text{SiF}_x$  species starts to play a role. XPS analysis could give further details of the surface composition both for fluorine-limited and ion-limited etching [20,21].

### 7.2.2 Profile evolution: tapering, bowing and microtrenching

Sidewall tapering, sidewall bowing and microtrenching were investigated for silicon etching in a  $\text{Cl}_2$  plasma, so that the trench profiles can be compared to silicon carbide etching. The profiles of 5.0  $\mu\text{m}$  wide trenches etched for 10 min with a pressure of 0.10 Pa and 0.43 Pa are shown in figure 7.10a and 7.10b, respectively. Sidewall tapering is clearly visible and decreases considerably for a higher pressure in contrast to silicon carbide etching. Sidewall bowing is not visible in these figures, but it appears with narrower trenches. Microtrenching occurs in both cases, but the microtrenches are obviously narrower and deeper for a higher pressure. The depth of the microtrenches is qualitatively consistent with the etch yield shown in figure 7.9a.

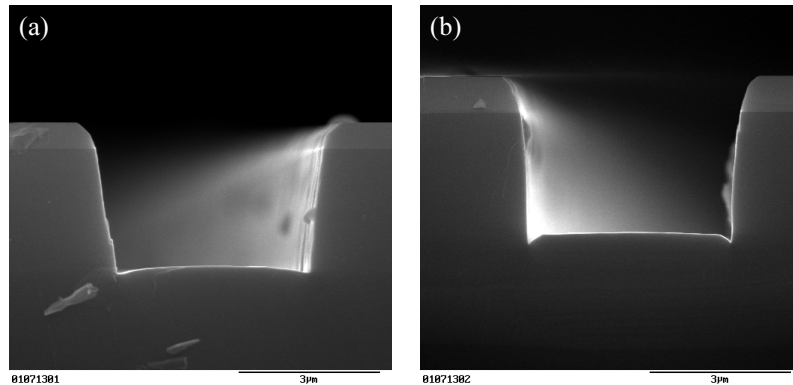


Figure 7.10 Anisotropic profiles of  $5.0\ \mu\text{m}$  wide trenches for silicon etching in a  $\text{Cl}_2$  plasma with several pressures. (a)  $0.10\ \text{Pa}$ . (b)  $0.43\ \text{Pa}$ .

### Sidewall Tapering

Mask erosion leads to a positive sidewall taper if the mask sidewalls are sloped, because the taper of the mask aperture is transferred to the substrate. The positive sidewall taper is inversely proportional to the selectivity of silicon etching in relation to the silicon dioxide mask, which is 8 at a pressure of  $0.24\ \text{Pa}$ . The selectivity decreases for a lower pressure because the mask erosion increases due to a higher ion flux consistent with the observed positive sidewall taper [22].

### Sidewall bowing

For a  $0.80\ \mu\text{m}$  wide trench etched at pressure of  $0.24\ \text{Pa}$  sidewall bowing is visible below the silicon dioxide mask in figure 7.11a. This is ascribed to ions that are reflected on the opposite mask sidewall, because for a  $10.0\ \mu\text{m}$  wide trench no sidewall bowing is visible in figure 7.11b. Ions that are reflected on a sloped mask sidewall can cause erosion further down the trench on the opposite trench sidewall, which has been illustrated in literature with Monte Carlo profile simulations [23]. In silicon carbide etching the proximity of another sidewall is not necessary to obtain sidewall bowing, which is explained by sidewall erosion as a result of obliquely incident ions. Differential charging of the mask, which deflects the ions to the sidewalls, could also be a cause [14,24,25]. However, no significant differences were observed between an insulating silicon dioxide and a conducting chromium mask, which demonstrates that differential charging did not play a role.

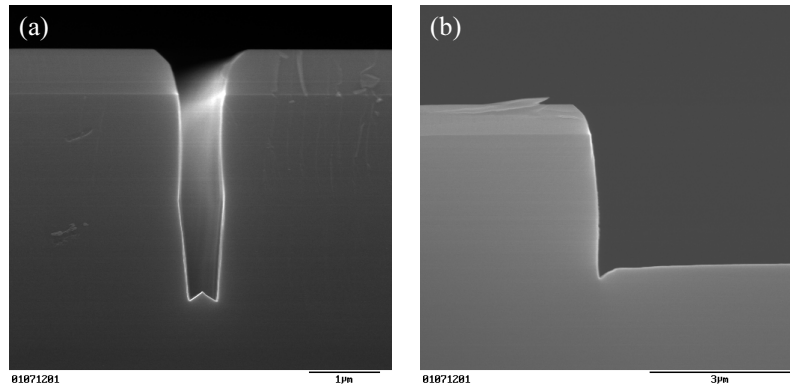


Figure 7.11 Trenches etched in a  $\text{Cl}_2$  plasma. (a) Sidewall bowing for a  $0.80 \mu\text{m}$  wide trench with an aspect ratio of 4.4. (b) The left part of a  $10.0 \mu\text{m}$  wide trench without sidewall bowing.

### Microtrenching

The microtrenches that are visible in figure 7.10 are obviously narrower and deeper for higher pressure. The width of the microtrenches is mainly determined by the sidewall taper, because the ions hit the sidewalls with a grazing angle of incidence and are specularly reflected [26-29]. The less positive sidewall taper for higher pressures leads to narrower microtrenches, because the focus of the reflected ions near the base of the sidewalls is narrower.

The depth of the microtrenches is primarily determined by the ion-neutral synergy. In contrast to silicon carbide etching the depth of the microtrenches is not entirely suppressed for a lower pressure, which is qualitatively in agreement with the more gradual transition from radical-limited to ion-limited etching.

### 7.2.3 Aspect ratio independent etching

The average etch rate of trenches is plotted as a function of aspect ratio for the three different pressures in figure 7.12, which shows that the average etch rate is approximately aspect ratio independent. The small increase of the average etch rate for the lowest aspect ratios with a pressure of 0.10 Pa is explained by the broad microtrenches that overlap for higher aspect ratios enlarging the depth in the middle of the trench. For the highest aspect ratios the average etch rate is only slightly reduced, but the etching of high aspect ratio trenches in a  $\text{Cl}_2$  plasma is ultimately limited by the positive sidewall taper. The average etch rate is nearly independent of pressure due to the increase of the etch yield shown in figure 7.9. Owing to the ion-neutral synergy the decrease of the ion flux is compensated by an increase of the chlorine radical flux for higher pressures.

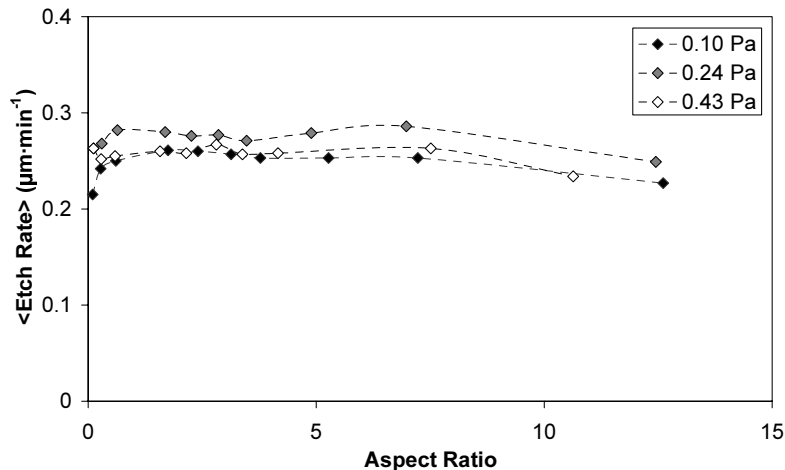


Figure 7.12 The average etch rate as a function of the aspect ratio for silicon etching in a  $\text{Cl}_2$  plasma with several pressures.

The major cause for the aspect ratio independent etching of silicon in a  $\text{Cl}_2$  plasma is the low chlorine radical reaction probability even for the lowest pressure. The chlorine radical reaction probability can easily be a factor of 5 lower than the fluorine radical reaction probability, so that the chlorine radical flux decreases more gradually due to the Knudsen transport than the fluorine radical flux for silicon carbide etching. Three aspects of the etching mechanism are given that make this assertion plausible. First, the etch rate was about a factor of 2 lower, so that the radical consumption is reduced. Second, the stoichiometry of the reaction products is different. The most likely reaction products are  $\text{SiCl}$  and  $\text{SiCl}_2$  compared to  $\text{SiF}_4 + \text{CF}_2$ , which also reduces the radical consumption [30,31]. Third, although the lowest pressure during silicon etching (0.10 Pa) was lower than the lowest pressure during silicon carbide etching (0.38 Pa) the radical partial pressures were comparable due to the high degree of dissociation in a  $\text{Cl}_2$  plasma [17]. In this experiment it led to a chlorine radical partial pressure of nearly 0.10 Pa. In comparison the measured fluorine radical partial pressure was 0.069 Pa.

The ion-neutral synergy helps to explain the aspect ratio independent etching because even for the lowest pressure the etching was not purely chlorine-limited. As a consequence, a possible small decrease of the chlorine radical flux in high aspect ratio trenches does not result in an appreciable decrease of etch rate. In chapter 4 it is shown that the ion flux is almost constant for aspect ratios smaller than 10 due to the narrow angular distribution of the ions in low-pressure plasmas, and consequently, the role of the ions can be disregarded. Redeposition of silicon dioxide, which is released by the sputtering of the silicon dioxide mask, reduces the etch rate [18]. The mask erosion is especially substantial for a lower pressure due to the higher ion flux. If the reaction probability for oxygen radicals is larger



than for chlorine radicals the decrease of the etch rate as a function of aspect ratio could be less severe in a manner comparable to the aspect ratio independent etching of silicon in an SF<sub>6</sub>-O<sub>2</sub> plasma at low temperatures.

### 7.3 Conclusions

Ion-induced silicon carbide etching in an SF<sub>6</sub>-O<sub>2</sub> plasma and ion-induced silicon etching in a Cl<sub>2</sub> plasma have been investigated to understand better the role of the ions in the etching mechanism. For silicon carbide the transition from fluorine-limited to ion-limited etching with increasing flux ratio is relatively abrupt. The plasma-surface interactions have a strong impact on the profile evolution and ARDE. The sidewall taper is more positive in an ion-limited etching regime, because the removal of the fluorocarbon reaction layer is limited due to the low ion flux. Microtrenching is suppressed in a fluorine-limited regime because a larger ion flux near the base of the sidewalls does not increase the etch rate. The fluorine radical flux decreases in trenches because of the high reaction probability, but in spite of this, the etch rate is constant in an ion-limited regime. On the contrary, in a fluorine-limited regime the fluorine reaction probability is nearly 1, so that the etch rate decreases considerably. The etching of high aspect ratio structures is ultimately limited by the positive sidewall taper. For silicon the plasma-surface interactions are noticeably different. The transition between chlorine-limited and ion-limited etching is more gradual and in accordance with the ion-neutral synergy model. The observed sidewall taper was less positive for a higher pressure because the erosion rate of the silicon dioxide mask was lower. The microtrenches were narrower and deeper for a higher pressure due to the less positive sidewall taper and the more ion-limited etching. ARDE was not observed, because silicon etching is not purely chlorine-limited, and more importantly, the chlorine reaction probability is much lower than 1.

### References

- [1] P. Chabert, N. Proust, J. Perrin and R.W. Boswell, *Appl. Phys. Lett.* **76**, 2310 (2000)
- [2] J.J. Wang, E.S. Lambers, S.J. Pearton, M. Ostling, C.M. Zetterling, J.M. Grow and F. Ren, *Solid State Electronics* **42**, 743 (1998)
- [3] F.A. Khan, B. Roof, L. Zhou and I. Adesida, *Journal of Electronic Materials* **30**, 212 (2001)
- [4] P. Chabert, *J. Vac. Sci. Technol. B* **19**, 1339 (2001)
- [5] P. Chabert, G. Cunge, J.P. Booth and J. Perrin, *Appl. Phys. Lett.* **79**, 916 (2001)
- [6] P.M. Sarro, *Sensors and Actuators A* **82**, 210 (2000)

- 
- [7] X.M.H. Huang, C.A. Zorman, M. Mehregany and M.L. Roukes, *Nature* **421**, 496 (2003)
- [8] J.P. Chang, A.P. Mahorowala and H.H. Sawin, *J. Vac. Sci. Technol. A* **16**, 217 (1998)
- [9] T. Lagarde, J. Pelletier and Y. Arnal, *J. Vac. Sci. Technol. B* **17**, 118 (1999)
- [10] T.M. Mayer and R.A. Barker, *J. Vac. Sci. Technol.* **21**, 757 (1982)
- [11] S. Hamaguchi and M. Dalvie, *J. Electrochem. Soc.* **141**, 1964 (1994)
- [12] M.A. Vyvoda, H. Lee, M.V. Malyshev, F.P. Klemens, M. Cerullo, V.M. Donnelly, D.B. Graves, A. Kornblit and J.T.C. Lee, *J. Vac. Sci. Technol. A* **16**, 3247 (1998)
- [13] K.H.A. Bogart, F.P. Klemens, M.V. Malyshev, J.I. Colonell, V.M. Donnelly, J.T.C. Lee and J.M. Lane, *J. Vac. Sci. Technol. A* **18**, 197 (2000)
- [14] M.A. Vyvoda, M. Li and D.B. Graves, *J. Vac. Sci. Technol. A* **17**, 3293 (1999)
- [15] R.A. Gottscho, C.W. Jurgensen and D.J. Vitkavage, *J. Vac. Sci. Technol. B* **10**, 2133 (1992)
- [16] J.W. Coburn and H.F. Winters, *Appl. Phys. Lett.* **55**, 2730 (1989)
- [17] M.V. Malyshev and V.M. Donnelly, *J. Appl. Phys.* **88**, 6207 (2000)
- [18] A.D. Bailey III, M.C.M. van de Sanden, J.A. Gregus and R.A. Gottscho, *J. Vac. Sci. Technol. B* **13**, 92 (1995)
- [19] K.H.A. Bogart and V.M. Donnelly, *J. Appl. Phys.* **86**, 1822 (1999)
- [20] L. Jiang, R. Cheung, R. Brown and A Mount, *J. Appl. Phys.* **93**, 1376 (2003)
- [21] D.J. Morrison, A.J. Pidduck, V. Moore, P.J. Wilding, K.P. Hilton, M.J. Uren and C.M. Johnson, *Materials Science Forum* **338-342**, 1199 (2000)
- [22] J.P. Chang and H.H. Sawin, *J. Vac. Sci. Technol. B* **19**, 1319 (2001)
- [23] G. Marcos, A. Rhallabi and P. Ranson, *J. Vac. Sci. Technol. A* **21**, 1 (2003)
- [24] G.S. Hwang and K.P. Giapis, *J. Appl. Phys.* **82**, 566 (1997)
- [25] K.P. Giapis, G.S. Hwang and O. Joubert, *Microelectronic Engineering* **61-62**, 835 (2002)
- [26] B.A. Helmer and D.B. Graves, *J. Vac. Sci. Technol. A* **16**, 3502 (1998)
- [27] S. Abdollahi-Alibeik, J.P. McVittie, K.C. Saraswat, V. Sukharev and P. Schoenborn, *J. Vac. Sci. Technol. A* **17**, 2485 (1999)
- [28] R.J. Hoekstra, M.J. Kushner, V. Sukharev and P. Schoenborn, *J. Vac. Sci. Technol. B* **16**, 2102 (1998)
- [29] A.P. Mahorowala and H.H. Sawin, *J. Vac. Sci. Technol. B* **20**, 1064 (2002)
- [30] D. Dane and T.D. Mantei, *Appl. Phys. Lett.* **65**, 478 (1994)

- [31] F.M. Sanders, A.W. Kolfchoten, J. Dieleman, R.A. Haring, A. Haring and A.E. de Vries, *J. Vac. Sci. Technol. A* **2**, 487 (1984)



---

## Chapter 8

### Conclusions and recommendations

#### 8.1 Conclusions

Deep anisotropic silicon etching has been investigated with high-density fluorine-based plasmas. The etching and passivation mechanisms have been clarified for both the cryo-process and the Bosch process. Besides, the influence of the transport of the ions and radicals on the etch rate and the trench profile has been explained.

The *cryo-process* is characterised by oxygen passivation that is described by ion-neutral synergy. It has been shown with surface analysis that the reaction layer thickness is reduced with an increased ion bombardment. The fluorine reaction probability increases up to a maximum of approximately 0.5. A high reaction probability leads to ARDE due to Knudsen transport of fluorine radicals. For a decreased ion bombardment ARIE is obtained because the etching is controlled by the surface kinetics and the reaction probability is low. It shows the trade-off between a high etch rate and ARIE. The chemically enhanced ion-neutral synergy model, which includes the interactions between fluorine radicals, oxygen radicals and ions, describes the etching mechanism well.

The cryo-process is especially suitable for the fabrication of inertial sensors based on capacity measurement because large arrays of high aspect ratio trenches can be etched controllably. Moreover, optical structures such as waveguides and photonic crystals can be made because the cryo-process results in smooth sidewall surfaces. However, the simultaneous etching of trenches, ridges and more complex structures is more difficult because the oxygen passivation is different for each structure. Besides, crystal orientation dependent etching can lead to badly defined structures if they are not aligned along the crystal planes.

Perfect anisotropy is obtained in the *Bosch process* by balancing the etching and polymer passivation. The etching of high aspect ratio trenches is limited because the sidewalls converge. It has been shown that an increased ion-to-radical flux ratio improves the trench profiles and increases the maximal obtainable aspect ratio significantly. However, the ion angular distribution remains the limiting factor. It results in a decrease of the ion flux to the bottom of the trench due to sidewall collisions leading to a decrease of the polymer depassivation rate.

In contrast to the cryo-process, the applications of the Bosch process can consist of complex structures because no crystal orientation dependent etching has been observed. For high aspect ratio trenches the polymer passivation has to be strongly removed. As a result

the fluorine reaction probability is high and ARDE is obtained. Simultaneous etching of trenches and ridges is also more difficult for the Bosch process.

The polymer depassivation has been improved with a low-pressure, high-density, O<sub>2</sub> plasma in the *triple pulse process*. The major advantage of the triple pulse process is the larger depth that can be obtained with a flat bottom of the trench. The maximal obtainable aspect ratio is comparable to the Bosch process because of the larger sidewall erosion. The process offers better profile control because the controlled sidewall erosion can lead to negatively tapered sidewalls.

The polymer deposition is the net result of a radical-induced, an ion-enhanced deposition and a sputtering component. The mechanism has been modelled qualitatively. No polymer passivation has been obtained on the bottom of the trench for higher bias voltages because sputtering prevails. The sidewall passivation is still sufficient due to the lower ion flux to the trench sidewalls. The sidewalls do not converge for higher bias voltages because the passivation decreases with depth faster than the depassivation.

Ion-induced etching of silicon carbide in an SF<sub>6</sub>-O<sub>2</sub> plasma and of Si in a Cl<sub>2</sub> plasma have been investigated to demonstrate the role of the ions in the etching mechanism. The etching mechanisms have been characterised with plasma diagnostics. Silicon carbide etching is strongly ion-induced for most plasma conditions resulting in microtrenching and ARIE. Although the reaction probability is high compared to silicon etching. Silicon etching is described well by the ion-neutral synergy model. All silicon carbide trenches have a positive sidewall taper and the maximal obtainable aspect ratio is lower than 10. In the Bosch process the maximal obtainable aspect ratio is approximately 30 because the chemical component enhances the etch rate and counteracts the positive sidewall taper.

## **8.2 Recommendations**

The etching processes have been optimised to obtain high aspect ratio trenches, but this process could be non-optimal for other structures. The etching of ridges and trenches simultaneously could be investigated to optimise the etching processes for more complex structures. In the cryo-process, ramping of the oxygen flow could lead to improved trench profiles. A negative sidewall taper is often obtained for low temperatures, which could be reduced by an increase of oxygen flow. In the Bosch process, simultaneous ramping of the bias voltage and the passivation pulse time could lead to an improvement of the selectivity and the maximal obtainable aspect ratio. The lateral etch is reduced due to the exact balance of the sidewall passivation and erosion.

The quantitative approach combining the etch results and plasma diagnostics has been successful to explain the silicon etching mechanism. However, the concentration gradients of the plasma species have to be known to predict the etching uniformity on a whole wafer. Actinometry only gives an average value. Modelling of the plasma generation and the gas flow could give further insight in the distribution of the plasma species and the concentration gradients. The fluorine radical flux to the substrate depends on the plasma temperature. Modelling could also give information about temperature gradients. Besides, plasma temperature measurement by using the rotational states in the optical emission spectrum of  $N_2$  could give experimental support.

The polymer deposition model has only been compared qualitatively with the experimental results. An accurate measurement of the CF,  $CF_2$  and ion fluxes could verify the polymer deposition model quantitatively. It could also clarify the specific role of the CF and  $CF_2$  fluxes.





## Appendix A

### Modelling of the surface kinetics and evaluation of the etch rate in deep structures

#### A.1 The ion-neutral synergy model

Synergy means that the etch rate with ions and neutrals together is higher than with ions or neutrals alone. The surface is the intermediary through which the ions and neutrals interact. Neutrals adsorb on empty surface sites and the filled surface sites are removed by ion bombardment corresponding to ion-induced etching. The etch rate  $R_E$  in the ion-neutral synergy model is expressed by

$$R_E = \frac{1}{\rho} \cdot Y_X \cdot \varphi_i \cdot \theta_X = \frac{1}{\rho} \cdot \frac{Y_X \cdot \varphi_i}{1 + \frac{\gamma_X \cdot \varphi_i}{\kappa_X \cdot \varphi_X}} \quad \text{A.1}$$

where  $\rho$  is the atomic density of the substrate and  $Y_X$  the sputter yield of saturated substrate atoms. This equation is derived from the surface site balance of the neutral species  $X$  given by

$$\sigma \cdot \frac{d\theta_X}{dt} = \varphi_X \cdot \kappa_X \cdot (1 - \theta_X) - \gamma_X \cdot \varphi_i \cdot \theta_X \quad \text{A.2}$$

where  $\sigma$  is the surface site area density,  $\theta_X$  the surface coverage,  $\varphi_X$  the neutral flux,  $\varphi_i$  the ion flux,  $\kappa_X$  the adsorption probability,  $\gamma_X$  the ion-induced desorption coefficient. This mechanism is typically applicable to the etching of silicon with chlorine where  $X = \text{Cl}$  [1,2]. In the situations, where  $\varphi_i$  or  $\varphi_X$  is negligible, the etch rate goes to zero. The optimal condition is defined by  $\gamma_X \cdot \varphi_i = \kappa_X \cdot \varphi_X$ , so that the neutrals and the ions are perfectly balanced. In this equation spontaneous chemical reactions are not taken into account. A detailed derivation of a similar equation including spontaneous etching is given in section A.3. In that case two types of neutrals are considered, that is, fluorine and oxygen compete for the available surface sites.

## A.2 Knudsen transport of radicals

The reaction of the radicals results in a flow from the plasma to the substrate. It leads to a depletion of the radical flux in deep anisotropic cavities due to the finite flow conductance. For HDP etching the flow is in the Knudsen regime because the mean free path is much larger than the dimensions of the microstructures. As a result the sidewall collisions dominate the transport of radicals. It is assumed that the radicals have a thermal isotropic velocity distribution and that the reflection from the sidewalls is diffusive. The Knudsen transport is described by the probability that a random particle entering the cavity at one side is transmitted to the other side where it disappears. For trenches and circular vias these probabilities, the so-called Clausing factors, can be found as a function of aspect ratio in vacuum technology handbooks [3,4].

In real etching processes the radicals do not disappear when they hit the bottom of the cavity, but they react with the substrate. The incoming radicals that do not react are reflected back into the cavity. However, only a fraction of the reflected radicals is able to escape from the cavity and the rest is returned to the bottom of the cavity. The radical flux to the bottom of the cavity is increased due to the repeated backward and forward scattering [5]. The radical flux is described by

$$\varphi_X = \varphi_X^0 \cdot \frac{K^{AR}}{K^{AR} + S_X - K^{AR} \cdot S_X} \quad A.3$$

where  $\varphi_X^0$  is the radical flux entering the cavity,  $K^{AR}$  the Clausing factor for a certain aspect ratio and  $S_X$  the reaction probability. For spontaneous silicon etching in a fluorine-based plasma, the etch rate is proportional to the fluorine radical flux and the reaction probability. The etch rate in deep anisotropic cavities is determined by the Knudsen transport model given by

$$R_E = \frac{S_F \cdot \varphi_F^0}{4 \cdot \rho} \cdot \frac{K^{AR}}{K^{AR} + S_F - K^{AR} \cdot S_F} \quad A.4$$

which is derived from equation A.3 where  $X = F$ . If the Knudsen transport model is used to fit etch rate data the reaction probability  $S_F$  and the initial etch rate  $S_F \cdot \varphi_F^0 / 4 \cdot \rho$  are varied. It is assumed that the reaction probability does not depend on the fluorine radical flux.

An important observation is that Knudsen transport leads to aspect ratio dependent etching. The average etch rate that has been calculated up to an aspect ratio of 60 is plotted in figure A.1. The reaction probability is varied from 0.1 to 1.0 in 0.1 steps to illustrate how the reaction probability influences the etch rate in high aspect ratio trenches. The fluorine flux at zero aspect ratio is constant and has a value that leads to a maximum etch rate of 1.0

$\mu\text{m}\cdot\text{min}^{-1}$ . The average etch rate is high but decreases relatively fast for a high reaction probability, whereas the etch rate is low and smooth for a low reaction probability.

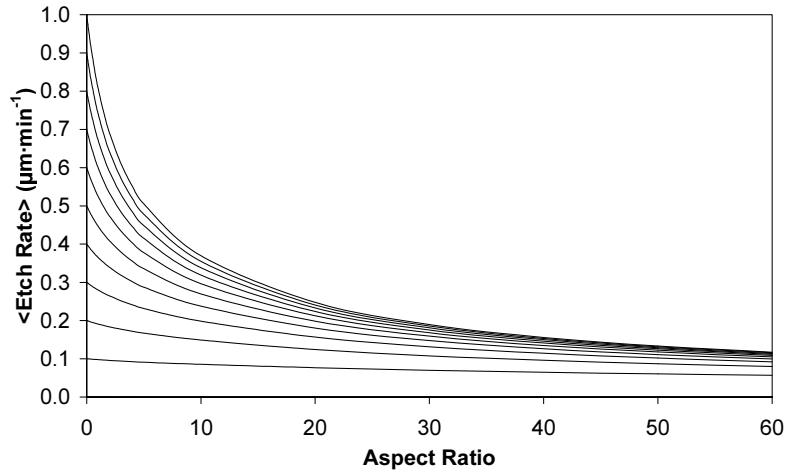


Figure A.1 The average etch rate in trenches as a function of aspect ratio for a reaction probability between 0.1 and 1.0. The etch rate is normalised to a maximum value of  $1.0 \mu\text{m}\cdot\text{min}^{-1}$  and decreases due to depletion of radicals

### A.3 The chemically enhanced ion-neutral synergy model

In the cryogenic etching process the silicon etch rate is evaluated with the chemically enhanced ion-neutral synergy model. It takes into account the surface passivation by oxygen. This model is obtained by considering the surface site balance for both fluorine and oxygen radicals given by equation A.5.

$$\sigma \cdot \frac{d\theta_F}{dt} = \varphi_F \cdot \kappa_F \cdot (1 - \theta_O - \theta_F) - \sigma \cdot \varepsilon_F \cdot \theta_F - \gamma_F \cdot \varphi_i \cdot \theta_F \quad \text{A.5a}$$

$$\sigma \cdot \frac{d\theta_O}{dt} = \varphi_O \cdot \kappa_O \cdot (1 - \theta_O - \theta_F) - \gamma_O \cdot \varphi_i \cdot \theta_O \quad \text{A.5b}$$

The symbols in this equation are  $\sigma$  the surface site area density,  $\theta_F$  the surface coverage of fluorine,  $\theta_O$  the surface coverage of oxygen,  $\varphi_F$  the fluorine flux,  $\varphi_O$  the oxygen flux,  $\varphi_i$  the ion flux,  $\kappa_F$  the adsorption probability for fluorine,  $\kappa_O$  the adsorption probability for oxygen,

$\varepsilon_F$  the spontaneous reaction rate for fluorine,  $\gamma_F$  the ion-induced desorption coefficient for fluorine and  $\gamma_O$  the ion-induced desorption coefficient for oxygen. For quasi steady state the derivatives are negligible and the set of linear equations can be solved for  $\theta_F$  and  $\theta_O$ . The etch rate is obtained by substituting these quantities in equation A.6.

$$R_E = \frac{1}{\rho} \cdot \left( \frac{\sigma \cdot \varepsilon_F \cdot \theta_F}{4} + Y_F \cdot \varphi_i \cdot \theta_F + Y_O \cdot \varphi_i \cdot \theta_O \right) \quad \text{A.6}$$

The spontaneous reaction term is responsible for chemical etching of silicon with volatile  $\text{SiF}_4$  as the reaction product. In this equation  $Y_F$  and  $Y_O$  are the sputter yields for silicon fluorides and silicon oxides respectively and  $\rho$  is the silicon atom density. When one silicon atom is sputtered, four surface sites are cleared ( $\gamma_F = 4 \cdot Y_F$  and  $\gamma_O = 4 \cdot Y_O$ ). Equation 6 is very comparable to the equation for ion-induced etching including an etch inhibitor, but the important difference is the incorporation of the spontaneous reaction term [1,2,6]. In high-density plasmas the ion flux is much lower than the radical flux. If it is assumed that the spontaneous reaction is much faster than the ion-induced desorption of fluorine ( $\sigma \cdot \varepsilon_F \gg \gamma_F \cdot \varphi_i$ ) the etch rate is given by equation A.7.

$$R_E = \frac{1}{\rho} \cdot \frac{\left( \frac{\kappa_F \cdot \varphi_F}{4 \cdot \kappa_O \cdot \varphi_O} + \frac{Y_O}{\gamma_O} \right) \cdot \gamma_O \cdot \varphi_i}{1 + \left( \frac{\kappa_F \cdot \varphi_F}{\sigma \cdot \varepsilon_F} + 1 \right) \cdot \frac{\gamma_O \cdot \varphi_i}{\kappa_O \cdot \varphi_O}} \quad \text{A.7}$$

In cryogenic ICP etching the fluorine flux is typically much higher than the oxygen flux ( $\kappa_F \cdot \varphi_F \gg \kappa_O \cdot \varphi_O$ ). Actinometry confirms this. It can also be assumed that the spontaneous reaction is much faster than the supply of fluorine ( $\sigma \cdot \varepsilon_F \gg \kappa_F \cdot \varphi_F$ ) because the silicon etch rate is proportional to the fluorine radical partial pressure. Therefore, the fluorine surface coverage is negligible compared to the oxygen surface coverage. Nevertheless, in literature some saturation has been observed above a pressure of 0.55 Pa, but this has been ascribed to surface oxidation [7]. With these assumptions equation A.7 can be simplified to equation A.8.

$$R_E = \frac{1}{\rho} \cdot \frac{\left( \frac{\kappa_F \cdot \varphi_F}{4 \cdot \kappa_O \cdot \varphi_O} \right) \cdot \gamma_O \cdot \varphi_i}{1 + \frac{\gamma_O \cdot \varphi_i}{\kappa_O \cdot \varphi_O}} \quad \text{A.8}$$

The oxygen passivation mechanism is described by ion-neutral synergy similar to equation A.1. The etch rate is strongly enhanced by the spontaneous chemical reaction of fluorine with silicon, which is expressed by the factor  $\kappa_F \cdot \varphi_F$  over  $\kappa_O \cdot \varphi_O$ . With this amplification the extremely high etch yield in the order of 1000 that has been observed for cryogenic silicon etching can be understood better [8]. Alternatively written the etch rate is given by equation A.9.

$$R_E = \frac{\kappa_F \cdot \varphi_F}{4 \cdot \rho} \cdot (1 - \theta_O) \quad \text{A.9a}$$

where

$$\theta_O = \frac{1}{1 + \frac{\gamma_O \cdot \varphi_i}{\kappa_O \cdot \varphi_O}} \quad \text{A.9b}$$

The etch rate is thus proportional to the fluorine radical flux. The reaction probability is equal to the product of the fluorine adsorption probability and the fraction of uncovered surface sites. When equation A.8 is used for the etch rate evaluation in trenches, the decrease of the radical fluxes  $\varphi_F$  and  $\varphi_O$  with depth should be taken into account [5]. For this purpose  $\varphi_F$  and  $\varphi_O$  are expressed as a constant flux at zero aspect ratio times an aspect ratio dependent factor similar to equation A.3. These functions are defined in equation A.10 where  $X = F, O$ .

$$\varphi_X = \varphi_X^0 \cdot \varphi_X^{AR} \quad \text{A.10a}$$

where

$$\varphi_X^{AR} = \frac{K^{AR}}{K^{AR} + \kappa_X \cdot (1 - \theta_O) - K^{AR} \cdot \kappa_X \cdot (1 - \theta_O)} \quad \text{A.10b}$$

The four unknown parameters  $\varphi_F^0$ ,  $\gamma_O \cdot \varphi_i / \varphi_O^0$ ,  $\kappa_F$  and  $\kappa_O$  can be determined by fitting the model to experimental data. However, the result is inaccurate if the parameters are dependent. The number of parameters is reduced by setting  $\kappa_F$  to 0.5 and  $\kappa_O$  to 0.7 to avoid this problem. For fluorine the value of 0.5 has been determined for the etching of horizontal lines at room temperature. For oxygen it has been shown in literature that the adsorption probability is near unity on bare silicon and that it is reduced for the subsequent monolayers [9]. In the model four adsorption sites are available per silicon atom and the value of 0.7 is a

good approximation of the average oxygen adsorption probability. The etch rate given by equation A.9 is transformed to an expression with the two fit parameters  $a$  and  $b$  by substitution of equation A.10. The expression is given by equation A.11.

$$R_E = \varphi_F^{AR} \cdot a \cdot (1 - \theta_O) \quad A.11a$$

where

$$\theta_O = \frac{1}{1 + \frac{b}{\varphi_O^{AR}}} \quad A.11b$$

The fit parameters are given by equation A.12.

$$a = \frac{\kappa_F \cdot \varphi_F^0}{4 \cdot \rho} \quad A.12a$$

$$b = \frac{\gamma_O \cdot \varphi_i}{\kappa_O \cdot \varphi_O^0} \quad A.12b$$

The oxygen flux in equation A.10b and the oxygen surface coverage in equation A.11b are interdependent. By substituting equation A.10b in A.11b a quadratic expression for  $\theta_O$  is obtained. This gives a solution for  $\theta_O$  as a function of  $K^{AR}$ ,  $\kappa_O$  and  $b$ . The solution is substituted in function A.11a. By varying  $a$  and  $b$  in this final expression the least squares fit is obtained. In the limit of zero oxygen surface coverage ( $b \gg 1$ ), the chemically enhanced ion-neutral synergy model is identical to the Knudsen transport model with a reaction probability of 0.5.

The average etch rate is often measured instead of the instantaneous etch rate. The etch time is calculated by integrating the inverse of the etch rate over the depth. The average etch rate is obtained by dividing the depth by the etch time.

The solution has been obtained for a steady state process, but it is also interesting to look at time dependent processes. An interesting case is the etching of a clean silicon substrate in the absence of an ion bombardment. The etch rate decays exponentially due to saturation of the oxygen surface coverage with the time constant  $\tau$  given in equation A.13.

$$\tau = \frac{\sigma}{\kappa_{\text{O}} \cdot \varphi_{\text{O}}} \quad \text{A.13}$$

The total etch depth is equal to  $\tau \kappa_{\text{F}} \varphi_{\text{F}} / 4 \cdot \rho$  and can be taken as an estimate of the lateral etch depth. For typical conditions in the ECR system this depth is in the order of 10-20 nm. It indicates that the cryogenic etching process should not be used for the etching of structures with lateral dimensions smaller than 40 nm. A process without spontaneous reactions should be chosen instead. In experiments the lateral etch is usually much larger than this value, which suggests that some oxygen radicals desorb without ion impact. For example, compounds like  $\text{Si}_2\text{OF}_6$  could be slightly volatile. For MEMS the critical dimensions are much larger and the small lateral etch does not raise problems.

## References

- [1] R.A. Gottscho, C.W. Jurgensen and D.J. Vitkavage, *J. Vac. Sci. Technol. B* **10**, 2133 (1992)
- [2] A.D. Bailey III, M.C.M. van de Sanden, J.A. Gregus and R.A. Gottscho, *J. Vac. Sci. Technol. B* **13**, 92 (1995)
- [3] S. Dushman and J.M. Lafferty, *Scientific Foundations of Vacuum Technique* 2<sup>nd</sup> edition, 94 (Wiley, New York US, 1962)
- [4] J.F. O'Hanlon, *A User's Guide to Vacuum Technology* 2<sup>nd</sup> edition, 36 (Wiley, New York US, 1989)
- [5] J. W. Coburn and H. F. Winters, *Appl. Phys. Lett.* **55**, 2730 (1989)
- [6] V. F. Lukichev, *Microelectronic Engineering* **41/42**, 423 (1998)
- [7] K. Ninomiya, K. Suzuki, S. Nishimatsu and O. Okada, *J. Appl. Phys.* **58**, 1177 (1985)
- [8] M. A. Blauw, T. Zijlstra, R. A. Bakker and E. van der Drift, *J. Vac. Sci. Technol. B* **18**, 3453 (2000)
- [9] T. Engel, *Surface Science Reports* **18**, 91 (1993)





## Appendix B

### Plasma conditions of the etching experiments

In the following tables the plasma conditions are given for the etching experiments presented in chapter 3 to 7. The order of these tables is roughly equal to the order in the text.

#### B.1 The cryogenic etching process

##### ECR reactor

	Cryo 1	Cryo 2	Cryo 3	Cryo 4	Cryo 5	Cryo 6
SF <sub>6</sub> Flow (sccm)	30.0	32.5	20.0	20.0	10 to 40	20.0
O <sub>2</sub> Flow (sccm)	1.1 and 3.3	3.6	1.6 to 3.2	2.0	1.0 to 4.0	2.6
Ar Flow (sccm)	0	1.0	1.0	1.0	1.0	1.0
Pressure (Pa)	0.23	0.30	0.20	0.40	0.10 to 0.40	0.20 to 0.40
ECR Source Power (W)	400	400	400	400	400	400
Bias Voltage (V)	-13	-20	-20	-20	-20	-20
Substrate Temperature (°C)	-20 to -120	-65 to -95	-80	-80	-80	-80
Etching Time (min)	5	20	20	20	20	20

	Cryo 7	Cryo 8	Cryo 9	Cryo 10	Cryo 11
SF <sub>6</sub> Flow (sccm)	32.5	22.3	20.0	40.0	20.0
O <sub>2</sub> Flow (sccm)	3.6	3.1	2.6	4.4	2.2
Ar Flow (sccm)	1.0	0	0	0	0
Pressure (Pa)	0.30	0.20	0.18	0.32	0.17
ECR Source Power (W)	400	400	400	400	400
Bias Voltage (V)	0 to -100	0 to -20	-20	-13	-20
Substrate Temperature (°C)	-80	-95	-90	-100	-80
Etching Time (min)	20		20	40	40

**ICP reactor**

	Cryo 12	Cryo 13	Cryo 14	Cryo 15	Cryo 16
SF <sub>6</sub> Flow (sccm)	400	500	300	300	300
O <sub>2</sub> Flow (sccm)	36	25	0	0	0
Ar Flow (sccm)	0	0	0	0	0
Pressure (Pa)	4.31	5.77	3.81	3.4	3.6
ICP Source Power (W)	1050	2200	2000	2000	2000
Bias Voltage (V)	-40	0 to -25	-25	-50	0 to -50
Substrate Temperature (°C)	-125	-115	-80	-80	-80
Substrate Position (cm)	9	15	6 to 15	6	6
Etching Time (min)	10	5	5	6	6

	Cryo 17	Cryo 18	Cryo 19	Cryo 20	Cryo 21
SF <sub>6</sub> Flow (sccm)	300	240	300	500	300
O <sub>2</sub> Flow (sccm)	0	0	0	0	5.5
Ar Flow (sccm)	0	10	0	0	0
Pressure (Pa)	3.46	2.5	3.82	5.8	3.4
ICP Source Power (W)	2000	1500 to 2000	2200	2200	2500
Bias Voltage (V)	0	0	-25	-25	-25
Substrate Temperature (°C)	-80	+25	-115 to +25	+25	-120
Substrate Position (cm)	6		15	6	7.5
Etching Time (min)	5	10	6	0.5 to 20	

## B.2 The Bosch process

		Bosch 1	Bosch 2	Bosch 3	Bosch 4
Etching pulse	SF <sub>6</sub> Flow (sccm)	300	150	300	150
	Time (s)	6	6	6	6
	Pressure (Pa)	6.4	2.7	4.5	2.4
Passivation Pulse	C <sub>4</sub> F <sub>8</sub> Flow (sccm)	115	150	150	75
	Time (s)	3	3	3	4
	Pressure (Pa)	2.6	2.8	2.7	1.1
ICP Source Power (W)		2000	2000	2000	2000
Bias Voltage (V)		-90	-90	-90	-90
Substrate Temperature (°C)		+25	+25	+25	+25
Substrate Position* (cm)		6.0	15.0	15.0	15.0
Etch Time (min)		10	40	25	44

\*A higher substrate position corresponds to a lower substrate-to-source distance and thus to a higher ion flux. A low ion flux corresponds to a substrate position of 6.0 cm, an intermediate ion flux to 11.5 cm and a high ion flux to 15.0 cm.

### B.3 The triple pulse process

		Triple 1	Triple 2
Etching pulse	SF <sub>6</sub> Flow (sccm)	300	150
	Time (s)	6	6
	Pressure (Pa)	6.3	2.8
Passivation Pulse	C <sub>4</sub> F <sub>8</sub> Flow (sccm)	185	150
	Time (s)	6	5
	Pressure (Pa)	4.0	2.7
Depassivation Pulse	O <sub>2</sub> Flow (sccm)	30	30
	Time (s)	2	2
	Pressure (Pa)	1.4	0.58
ICP Source Power (W)		2000	2000
Bias Voltage (V)		-90	-90
Substrate Temperature (°C)		+25	+25
Substrate Position (cm)		11.5	15.0
Etch Time (min)		40	40

**B.4 The silicon carbide etching process**

	SiC 1	SiC 2
SF <sub>6</sub> Flow (sccm)	40.0	40.0
O <sub>2</sub> Flow (sccm)	10.0	10.0
Pressure (Pa)	0.68	0.72
ICP Source Power (W)	2000	2000
Bias Voltage (V)	-300	-250
Substrate Temperature (°C)	+25	+25
Substrate Position (cm)	15.0	15.0
Etching Time (min)	10	10





## Appendix C

### Modelling of the polymer passivation layer deposition mechanism

The deposition of a fluorocarbon polymer passivation layer is applied in the deep anisotropic dry etching of silicon. A  $C_4F_8$  plasma is often used in the Bosch process because  $CF_2$  radicals, which are the precursors for polytetrafluoroethylene (PTFE), are easily formed. A theoretical description of the polymer passivation layer deposition mechanism, which explains the experimental results, is given as a function of the  $CF_x$  ( $x = 1,2$ ) radical flux and the ion flux. The deposition mechanism is composed of three components: radical-induced deposition due to the chemical reaction of the radicals, ion-enhanced deposition due to the creation of activated surface sites, and sputtering. If sputtering dominates, the net result is not deposition but etching.

In literature it has been shown that CF radicals are responsible for radical-induced deposition, whereas  $CF_2$  radicals are involved in ion-enhanced deposition [1]. The  $CF_2$  radical flux has been measured with actinometry. However, only the relative changes of the  $CF_2$  radical flux can be measured because the calibration factor is not known. The peaks of the CF radicals have not been observed in the optical emission spectrum. In literature it has been shown that the  $CF_2$  radical density is one order of magnitude larger than the CF radical density. The  $CF_2$  and CF radical densities decrease with increasing source power because they are intermediate dissociation products [2-4]. In the following, no distinction is made between CF and  $CF_2$  radicals and it is assumed that the ratio of the CF and  $CF_2$  radical densities is fixed. The measured  $CF_2$  radical flux is used to predict the total  $CF_x$  radical flux. The introduced adsorption probabilities are thus as the weighted average for all  $CF_x$  radicals, and besides, they incorporate the unknown factor that relates the relative  $CF_2$  radical flux to the total  $CF_x$  radical flux. The deposition rate  $R_D$  is written as

$$R_D = R_D^r + R_D^i + R_D^s \quad C.1$$

where  $R_D^r$  is the radical-induced deposition component,  $R_D^i$  the ion-enhanced deposition component and  $R_D^s$  the sputtering component. The radical-induced deposition component is proportional to the  $CF_x$  radical flux  $\phi_{CF_x}$  and is given by

$$R_D^r = \frac{M_{CF_2}}{\rho_{PTFE} \cdot N_A} \cdot K_{CF_x} \cdot \phi_{CF_x} \quad C.2$$

where  $M_{CF_2}$  is the molar mass of the  $CF_2$  units in PTFE,  $\rho_{PTFE}$  the density of PTFE,  $N_A$  the Avogadro number and  $\kappa_{CF_x}$  the adsorption probability. The ion-enhanced deposition component is proportional to the fraction of activated surface sites  $\theta^*$  and is written as

$$R_D^i = \frac{M_{CF_2}}{\rho_{PTFE} \cdot N_A} \cdot \kappa_{CF_x}^* \cdot \varphi_{CF_x} \cdot \theta^* \quad C.3$$

where  $\kappa_{CF_x}^*$  is the adsorption probability for the activated surface sites. The fraction of activated surface sites  $\theta^*$  can be found by solving the following surface site balance for steady state conditions.

$$\sigma^* \cdot \frac{d\theta^*}{dt} = \gamma^* \cdot \varphi_i \cdot (1 - \theta^*) - \kappa_{CF_x}^* \cdot \varphi_{CF_x} \cdot \theta^* - \frac{\sigma^* \cdot \theta^*}{\tau^*} \quad C.4$$

where  $\sigma^*$  is the activation surface site area density,  $\gamma^*$  is the ion-induced activation coefficient,  $\varphi_i$  the ion flux and  $\tau^*$  the lifetime of activated surface sites. If  $\theta^*$  is substituted in equation C.3, the ion-enhanced deposition component becomes

$$R_D^i = \frac{M_{CF_2}}{\rho_{PTFE} \cdot N_A} \cdot \frac{\gamma^* \cdot \varphi_i}{\gamma^* \cdot \varphi_i + \frac{\sigma^*}{\tau^*}} \cdot \frac{1}{1 + \frac{\kappa_{CF_x}^* \cdot \varphi_{CF_x}}{\sigma^*}} \quad C.5$$

The ion-induced activation coefficient depends on the ion energy and follows a square root relation given by

$$\gamma^* = \gamma_0^* \cdot (\sqrt{E_i} - \sqrt{E_T^*}) \quad C.6$$

where  $\gamma_0^*$  is the square root of energy normalised ion-induced activation coefficient,  $E_i$  the ion energy and  $E_T^*$  the energy threshold for surface site activation. A square root dependence is characteristic for physical processes such as the breaking of molecular bonds [5]. The sputtering component is given by

$$R_D^s = -\frac{M_{CF_2}}{\rho_{PTFE} \cdot N_A} \cdot Y_{CF_2} \cdot \varphi_i \quad C.7$$

where  $Y_{CF_2}$  is the sputter yield of the polymer layer, which is expressed by

$$Y_{CF_2} = Y_{CF_2}^0 \cdot (E_i - E_T) \quad C.8$$

where  $Y_{CF_2}^0$  is the energy normalised sputter yield and  $E_T$  the sputter energy threshold. A linear dependence has been assumed because a linear trend has been observed in the reactive ion etching of polymers in an  $O_2$  plasma [6]. Moreover, a linear dependence is obviously better adapted to the experimental results. When all components are combined the deposition rate is formulated as

$$R_D = \frac{M_{CF_2}}{\rho_{PTEF} \cdot N_A} \cdot \left( \kappa_{CF_x} \cdot \Phi_{CF_x} + \frac{\gamma^* \cdot \Phi_i}{1 + \frac{\gamma^* \cdot \Phi_i}{\kappa_{CF_x} \cdot \Phi_{CF_x}}} - Y_{CF_2} \cdot \Phi_i \right) \quad C.9$$

It is assumed that  $\tau^*$  is infinitely long ( $\sigma^*/\tau^* \ll \gamma^* \cdot \Phi_i$ ), because  $\gamma^* \cdot \Phi_i$  is large as a result of the high ion energies and ion fluxes that are used in the experiments. The equation given in literature is obtained if  $\tau^*$  is short ( $\sigma^*/\tau^* \gg \gamma^* \cdot \Phi_i$ ) and sputtering is not included [1]. It has been derived for deposition with the substrate at floating potential, so that the ion energies are low and sputtering is unlikely. Equation C.9 has been used to fit the experimental deposition rate as a function of the measured  $CF_x$  radical flux and the measured ion flux with the fit parameters  $\kappa_{CF_x}$ ,  $\kappa_{CF_x}^*$ ,  $\gamma_0^*$ ,  $E_T^*$ ,  $Y_{CF_2}^0$  and  $E_T$ .

## References

- [1] M.J. Sowa, M.E. Littau, V. Pohray, and J.L. Cecchi, J. Vac. Sci. Technol. A **18**, 2122 (2000)
- [2] S. Samukawa, T. Mukai and K. Tsuda, J. Vac. Sci. Technol. A **17**, 2551 (1999)
- [3] H.H. Doh, J.H. Kim, K.W. Whang and S.H. Lee, J. Vac. Sci. Technol. A **14**, 1088 (1996)
- [4] K. Miyata, M. Hori and T. Goto, J. Vac. Sci. Technol. A **14**, 2343 (1996)
- [5] C. Steinbrüchel, Appl. Phys. Lett. **55**, 1960 (1989)
- [6] J.A.G. Baggerman, R.J. Visser and E.J.H. Collart, J. Appl. Phys. **75**, 758 (1994)



---

## Summary

This thesis deals with the dry etching of deep anisotropic microstructures in monocrystalline silicon by high-density plasmas. High aspect ratio trenches are necessary in the fabrication of sensitive inertial devices such as accelerometers and gyroscopes. The etching of silicon in fluorine-based plasmas is isotropic. To obtain anisotropy the addition of sidewall passivation is necessary. This is achieved with both oxygen passivation at low temperatures and fluorocarbon passivation at room temperature. A quantitative approach was pursued to explain the etching mechanism. The etch results were analysed using the measured plasma species fluxes and the surface composition. Moreover, the transport of the plasma species in narrow anisotropic structures is a fundamental factor determining the etch rate and the profile evolution. The experimental methods such as the etching equipment, plasma diagnostics, surface analysis and sample preparation are described in chapter 2. Three etching processes were investigated: the cryogenic etching process with oxygen passivation at low temperatures, the Bosch process with fluorocarbon passivation at room temperature and the novel triple pulse process that was developed in our laboratory. The polymer deposition mechanism and the characteristic role of the ions are also explained.

The *cryogenic etching process* is discussed in chapter 3. Fluorine radicals, oxygen radicals and ion bombardment are responsible for the three main sub-processes, that is, etching, sidewall passivation and depassivation of the trench bottom, respectively. Etching experiments with an extremely low ion-to-radical flux ratio were used to reveal the etching mechanism. Crystal orientation dependent etching leading to Si(111) crystal facets is observed in a surface kinetics controlled regime. By varying the plasma conditions it is possible to adjust the etching mechanism from fluorine-limited to ion-limited. Controlled etching is obtained because the etching is tuned from *aspect ratio dependent* in the fluorine-limited domain to *aspect ratio independent* in the ion-limited domain. The transport of radicals in high aspect ratio trenches is an important limiting factor and was investigated with special structures. The etch results are described by an analytic model that is based on the surface site balance of fluorine and oxygen radicals. The results are further explained with a Monte Carlo simulation model.

The *Bosch process* is clarified in chapter 4. The anisotropy of the etched structures is controlled by balancing the etching and passivation pulse. However, the maximal obtainable aspect ratio is limited by convergence of the trench sidewalls due to excessive passivation. The maximal obtainable aspect ratio increases if the ion-to-radical flux ratio increases. The transport of ions is an important limiting factor in the depassivation of the bottom of the trench. Divergence of the ion beam leads to a reduction of the ion flux, so that the fluorocarbon passivation is insufficiently removed near the base of the sidewalls. The average ion angle was measured and correlated to the maximal obtainable aspect ratio. The

Bosch process was improved at the *depassivation* side with the triple pulse process and at the *passivation* side with preferential sidewall deposition.

The triple pulse process that is described in chapter 5 has the aim to improve the depassivation in deep trenches. The three main sub-processes are decoupled using a separate depassivation pulse directly after the etching and passivation pulses. The fluorocarbon passivation is efficiently removed with low-pressure, high-density, oxygen-based plasmas. The investigated plasma chemistries include O<sub>2</sub>, CO<sub>2</sub> and SO<sub>2</sub>. The triple pulse process leads to better profile control with a straight trench bottom. However, the maximal obtainable aspect ratio is comparable to the Bosch process because a larger etch depth and a small lateral etch cancel out.

The polymer deposition mechanism is treated in chapter 6 with the aim to understand the fluorocarbon passivation in deep trenches. The deposition on plane surfaces and on special structures was investigated to distinguish between the radical-induced and ion-enhanced components. A simple analytical model, which explains the main deposition characteristics, was developed. Preferential sidewall deposition is obtained for higher ion fluxes and higher bias voltages where sputtering plays an important role. In this case no fluorocarbon passivation has to be removed from the bottom of the trench. The trench profile was optimised in the Bosch process by tuning the bias voltage during etching and passivation independently. It resulted in perfectly anisotropic trenches but the maximal obtainable aspect ratio was still limited by a small lateral etch.

The characteristic role of the ions in the etching mechanism is explained in chapter 7. Ion-induced etching of both SiC in a SF<sub>6</sub>-O<sub>2</sub> plasma and Si in a Cl<sub>2</sub> plasma were investigated. The impact of the ions on the profile evolution can be examined more explicitly because spontaneous chemical reactions are absent for these plasma-material systems. The etching mechanism varies from fluorine-limited to ion-limited depending on the radical-to-ion flux ratio. Microtrenches are observed for an ion-limited etching mechanism. Fluorine-limited SiC etching is aspect ratio dependent in contrast to ion-limited SiC etching, which is aspect ratio independent. The etching of high aspect ratio SiC structures is limited by the positive sidewall taper. This is presumably caused by insufficient removal of the thin fluorocarbon layer on the surface. Si etching in a Cl<sub>2</sub> plasma is always aspect ratio independent in contrast to SiC etching because of the low reaction probability. The conclusions and recommendations of this thesis are given in chapter 8.

## Samenvatting

Dit proefschrift behandelt het drooetsen van diepe anisotrope microstructuren in monokristallijn silicium door middel van hoge-dichtheidsplasma's. Trenches met een hoge aspectverhouding zijn noodzakelijk voor de fabricage van gevoelige bewegingssensoren zoals versnellingsmeters en gyroscopen. Het etsen van silicium in fluor-gebaseerde plasma's is isotroop. Zijwandpassivatie is nodig om een anisotroop etsproces te verkrijgen. Dit wordt bereikt door het toevoegen van zuurstof bij lage temperaturen of door het toevoegen van een fluorkoolwaterstof bij kamertemperatuur. Voor het verklaren van het etsmechanisme is een kwantitatieve benadering gevolgd. De etsresultaten zijn geanalyseerd door gebruik te maken van de gemeten fluxen van plasmadeeltjes en de oppervlaktesamenstelling. Daarnaast is het transport van de plasmadeeltjes in smalle anisotrope structuren een fundamentele factor die de etssnelheid en de profielontwikkeling bepaalt. De gebruikte experimentele methoden zoals etsapparatuur, plasmadiagnostiek, oppervlakteanalyse en preparaatvoorbereiding worden beschreven in hoofdstuk 2. Drie etsprocessen zijn onderzocht: het cryogene etsproces met zuurstofpassivatie bij lage temperaturen, het Bosch-proces met fluorkoolwaterstofpassivatie bij kamertemperatuur en het nieuwe drie-pulsenproces dat in ons laboratorium is ontwikkeld. Het polymeerdepositiemechanisme en de karakteristieke rol van de ionen in het etsmechanisme worden eveneens verklaard.

Het *cryogene etsproces* wordt besproken in hoofdstuk 3. Fluorradicalen, zuurstofradicalen en het ionenbombardement zijn verantwoordelijk voor de drie belangrijkste subprocessen, respectievelijk etsen, zijwandpassivatie en depassivatie van de bodem van de trench. Etsexperimenten met een extreem lage verhouding van ionen ten opzichte van radicalen zijn gebruikt om het etsmechanisme te onderzoeken. Kristalorientatie-afhankelijk etsen dat tot Si(111)-kristalfacetten leidt wordt waargenomen in een regime dat gedomineerd wordt door de oppervlaktekinetiek. Door de plasmacondities te variëren is het mogelijk om het etsmechanisme te verschuiven van fluor-gelimiteerd naar ionen-gelimiteerd. Gecontroleerd etsen wordt daarbij verkregen omdat het etsgedrag verandert van *aspectverhouding-afhankelijk* in het fluor-gelimiteerde gebied naar *aspectverhouding-onafhankelijk* in het ionen-gelimiteerde gebied. Het transport van radicalen in trenches met een hoge aspectverhouding is een belangrijke beperkende factor en is onderzocht met speciale structuren. De etsresultaten worden beschreven door een analytisch model dat is gebaseerd op de oppervlaktebalans van fluor- en zuurstofradicalen. De resultaten worden nader verklaard met een Monte-Carlo-simulatiemodel.

In hoofdstuk 4 wordt het *Bosch-proces* verhelderd. De anisotropie van de geëtste structuren wordt beheerst door de ets- en passivatiepuls met elkaar in evenwicht te brengen. De maximaal haalbare aspectverhouding wordt beperkt door de naar elkaar toelopende zijwanden als gevolg van een overmatige passivatie. De maximaal haalbare

aspectverhouding neemt toe als de verhouding van ionen ten opzichte van radicalen groter wordt. Het transport van de ionen is een belangrijke beperkende factor in de depassivatie van de bodem van de trench. Divergentie van de ionenbundel leidt tot een vermindering van de ionenflux nabij de voet van de zijwanden. De gemiddelde ionenhoek is gemeten en in verband gebracht met de maximaal haalbare aspect ratio. Het Bosch-proces is verbeterd aan de *depassivatiezijde* met het drie-pulsenproces en aan de *passivatiezijde* met preferentiële zijwanddepositie.

Het drie-pulsenproces dat wordt beschreven in hoofdstuk 5 heeft het doel om de depassivatie in diepe trenches te verbeteren. De drie belangrijkste subprocessen zijn ontkoppeld door gebruik te maken van een afzonderlijke depassivatiepuls direct na de ets- en de passivatiepuls. De fluorkoolwaterstofpassivatie wordt efficiënt verwijderd met lage-druk, hoge-dichtheid, zuurstof-gebaseerde plasma's. De onderzochte plasmachemie omvat  $O_2$ ,  $CO_2$  en  $SO_2$ . Het proces leidt tot betere beheersing van het profiel met een rechte bodem van de trench. De maximaal haalbare aspectverhouding is echter vergelijkbaar met het Bosch-proces omdat de grotere etsdiepte en de kleine laterale ets tegen elkaar wegvallen.

Het polymeerdepositie-mechanisme wordt behandeld in hoofdstuk 6 met het doel om de fluorkoolwaterstofpassivatie in diepe trenches beter te begrijpen. Een eenvoudig analytisch model, dat de belangrijkste karakteristieken verklaart, is ontwikkeld. De depositie op vlakke substraten en op speciale structuren is onderzocht om onderscheid te maken tussen de radicaal-geïnduceerde en ionen-versterkte componenten. Preferentiële zijwanddepositie wordt verkregen bij hogere ionenfluxen en hogere biasspanningen waar sputteren een grote rol speelt. De fluorkoolwaterstofpassivatie hoeft in dit geval niet van de bodem van de trench verwijderd te worden. Het trenchprofiel is geoptimaliseerd in het Bosch-proces door de biasspanning tijdens het etsen en het passiveren onafhankelijk van elkaar in te stellen. Dit resulteerde in zeer anisotrope trenches, maar de maximaal haalbare aspectverhouding is nog steeds beperkt door een kleine laterale ets.

De karakteristieke rol van de ionen in het etsmechanisme wordt toegelicht in hoofdstuk 7. Ionen-geïnduceerd etsen van SiC in een  $SF_6-O_2$  plasma en ionen-geïnduceerd etsen van Si in een  $Cl_2$  plasma zijn onderzocht. De impact van de ionen op de ontwikkeling van het profiel kan explicieter onderzocht worden, omdat spontane, chemische reacties afwezig zijn in deze plasma-materiaalsystemen. Het etsmechanisme varieert van fluor-gelimiteerd tot ionen-gelimiteerd afhankelijk van de verhouding van radicalen ten opzichte van ionen. Microtrenches worden waargenomen voor een ionen-gelimiteerd etsmechanisme. Fluor-gelimiteerd SiC etsen is aspectverhouding-afhankelijk in tegenstelling tot ionen-gelimiteerd SiC etsen, dat aspectverhouding-onafhankelijk is. Het etsen van SiC structuren met een hoge aspectverhouding wordt beperkt door de positieve zijwandhoek. Dit wordt waarschijnlijk veroorzaakt door onvoldoende verwijdering van de dunne fluorkoolwaterstoflaag aan het oppervlak. Si etsen in een  $Cl_2$  plasma is altijd aspectverhouding-onafhankelijk in tegenstelling tot SiC etsen vanwege de lage reactiewaarschijnlijkheid. De conclusies en aanbevelingen van dit proefschrift worden gegeven in hoofdstuk 8.



---

## List of abbreviations

AFM	Atomic force microscopy
AR	Aspect ratio
ARDE	Aspect ratio dependent etching
ARIE	Aspect ratio independent etching
DECR	Distributed electron cyclotron resonance
ECR	Electron cyclotron resonance
HDP	High-density plasma
IAD	Ion angular distribution
ICP	Inductively coupled plasma
LIF	Laser induced fluorescence
MEMS	Microelectromechanical system
OES	Optical emission spectroscopy
PLC	Programmable logic control
PMMA	Polymethylmethacrylate
PTFE	Polytetrafluoroethylene
RF	Radio frequency
RIE	Reactive ion etching
RMS	Root mean square
SCREAM	Single crystal reactive etching and metallisation
SEM	Scanning electron microscopy
SNR	Silicon-based negative resist
SOI	Silicon on insulator
TCP	Transformer coupled plasma
TEM	Transmission electron microscopy
VLSI	Very large scale integration
XPS	X-ray photoelectron spectroscopy



## List of symbols

$a$	Fit parameter
$A$	Square root of energy normalised sputter yield
$A_R^\theta$	Critical aspect ratio
$b$	Fit parameter
$B$	Magnetic field strength
$B_X$	Branching ratio
$D$	Effective plasma diameter
$D$	Trench diameter
$d_s$	Plasma sheath thickness
$d_{SiO_2}$	Silicon dioxide layer thickness
$d_X$	Diameter of the plasma species
$E$	Electric field strength
$e$	Elementary charge
$e$	Natural exponential base
$E_i$	Ion energy
$E_T$	Sputter energy threshold
$E_T^*$	Energy threshold for surface site activation
$f$	Electron energy distribution function
$h$	Planck constant
$I_A$	Line intensity of the actinometer gas
$I_{Si}$	Photoelectron intensity of the Si peak
$I_{Si}^\infty$	Photoelectron intensity of the Si peak on a clean substrate
$I_{SiO_2}$	Photoelectron intensity of the SiO <sub>2</sub> peak
$I_{SiO_2}^\infty$	Photoelectron intensity of the SiO <sub>2</sub> peak on an infinitely thick silicon dioxide layer
$I_X$	Line intensity of the plasma species
$J_i$	Ion current density
$k$	Boltzmann constant
$K^{AR}$	Clausen factor
$Kn$	Knudsen number
$M_{CF_2}$	Molar mass of the CF <sub>2</sub> units in PTFE
$m_i$	Ion mass
$M_S$	Molar mass of the substrate atoms
$m_X$	Mass of the plasma species
$N_A$	Avogadro number
$n_A$	Density of the actinometer gas
$n_e$	Electron density
$n_i$	Positive ion density

$n_X$	Density of the plasma species
$n_{X^*}$	Density of the excited species
$p$	Pressure
$p_X$	Pressure of the plasma species
$R_D$	Deposition rate
$R_D^i$	Ion-enhanced deposition component
$R_D^r$	Radical-induced deposition component
$R_D^s$	Sputtering component
$R_E$	Etch rate
$r_F$	Stoichiometric ratio of fluorine and substrate atoms in the reaction product
$S_F$	Fluorine reaction probability
$S_X$	Reaction probability of the plasma species
$T$	Plasma temperature
$t$	Time
$T_e$	Electron temperature
$T_i$	Ion temperature
$t_{\text{pulse}}$	Pulse time
$v$	Electron velocity
$V$	Potential difference between the plasma and the substrate
$V_b$	Bias voltage
$V_f$	Floating potential
$V_p$	Plasma potential
$x$	Space coordinate
$y$	Space coordinate
$Y$	Sputter yield
$Y_{\text{CF}_2}$	Sputter yield of the $\text{CF}_2$ units in PTFE
$Y_{\text{CF}_2}^0$	Energy normalised sputter yield of the $\text{CF}_2$ units in PTFE
$Y_F$	Sputter yield of saturated silicon fluoride
$Y_O$	Sputter yield of saturated silicon oxide
$Y_X$	Sputter yield of substrate atoms saturated with the plasma species
$Y_{x,y}$	$\text{SiO}_x\text{F}_y$ sputter yield
$\alpha$	Proportionality constant of actinometry
$\alpha_{x,y}$	Modulation factor of the $\text{SiO}_x\text{F}_y$ sputter yield
$\gamma^*$	Ion-induced activation coefficient
$\gamma_0$	Square root of energy normalised ion-induced activation coefficient
$\gamma_F$	Ion-induced desorption coefficient of fluorine
$\gamma_O$	Ion-induced desorption coefficient of oxygen
$\gamma_X$	Ion-induced desorption coefficient of the plasma species
$\varepsilon$	Electron energy
$\varepsilon_0$	Permittivity of vacuum
$\varepsilon_F$	Spontaneous reaction rate of fluorine

---

$\varepsilon_X$	Radiative lifetime of the plasma species
$\theta$	Photoelectron angle, ion angle
$\theta^*$	Fraction of activated surface sites
$\theta_F$	Surface coverage of fluorine
$\theta_{IAD}$	Average absolute ion angle
$\theta_{MED}$	Median absolute ion angle
$\theta_O$	Surface coverage of oxygen
$\theta_{STD}$	Standard deviation of the ion angle
$\theta_X$	Surface coverage of the plasma species
$\kappa_{CF_x}$	Adsorption probability of $CF_x$ radicals
$\kappa_{CF_x}^*$	Adsorption probability of $CF_x$ radicals on activated surface sites
$\kappa_F$	Adsorption probability of fluorine
$\kappa_O$	Adsorption probability of oxygen
$\kappa_X$	Adsorption probability of the plasma species
$\lambda_c$	Ion mean free path
$\lambda_D$	Debye length
$\lambda_e$	Inelastic mean free path of the photoelectrons in $SiO_2$
$\nu$	Frequency
$\rho$	Atomic density of the substrate
$\rho_{PTFE}$	Density of PTFE
$\rho_S$	Density of the substrate
$\sigma$	Surface site area density
$\sigma^*$	Activation surface site area density
$\sigma_c$	Collision cross-section
$\sigma_X$	Excitation cross-section of the plasma species
$\tau$	Time constant of the oxygen surface coverage formation
$\tau^*$	Lifetime of activated surface sites
$\varphi_{CF_x}$	$CF_x$ radical flux
$\varphi_F$	Fluorine radical flux
$\varphi_i$	Ion flux
$\varphi_O$	Oxygen radical flux
$\varphi_X$	Plasma species flux
$\varphi_X^0$	Plasma species flux towards a structure
$\varphi_X^{AR}$	Aspect ratio dependent factor of the plasma species flux



---

## List of publications

### Journal publications

M.A. Blauw, E. van der Drift, G. Marcos and A. Rhallabi, "*Modeling of fluorine-based high-density plasma etching of anisotropic silicon trenches with oxygen sidewall passivation*", J. Appl. Phys. **94**, 6311 (2003)

M.A. Blauw, G. Craciun, W.G. Sloof, P.J. French and E. van der Drift, "*Advanced time-multiplexed plasma etching of high aspect ratio silicon structures*", J. Vac. Sci. Technol. B **20**, 3106 (2002)

M.A. Blauw, T. Zijlstra and E. van der Drift, "*Balancing the etching and passivation in time-multiplexed deep dry etching of silicon*", J. Vac. Sci. Technol. B **19**, 2930 (2001)

M.A. Blauw, T. Zijlstra, R.A. Bakker and E. van der Drift, "*Kinetics and crystal orientation dependence in high aspect ratio silicon dry etching*", J. Vac. Sci. Technol. B **18**, 3453 (2000)

### Contributions to journal publications

N.O.V. Plank, M.A. Blauw, E. van der Drift and R. Cheung, "*The etching of silicon carbide in inductively coupled SF<sub>6</sub>-O<sub>2</sub> plasma*", J. Phys. D **36**, 482 (2003)

G. Craciun, M.A. Blauw E. van der Drift, P. M. Sarro and P.J. French, "*Temperature influence on etching deep holes with SF<sub>6</sub>-O<sub>2</sub> cryogenic plasma*", Journal of Micromechanics and Microengineering **12**, 390 (2002)

**Conference publications**

M.A. Blauw, G. Craciun, E. van der Drift and P.J. French, "*Limitations and complementary value of cryogenic SF<sub>6</sub>-O<sub>2</sub> and Bosch plasma etch process for silicon micromachining*", Proceedings of the 4<sup>th</sup> National Dutch Sensor Conference, 89 (Enschede NL, 2001)

M.A. Blauw, T. Zijlstra and E. van der Drift, "*Radical transport in deep silicon structures during dry etching*", Proceedings of the 1<sup>st</sup> Dutch Workshop on Semiconductor Sensor and Actuator Technology, 617 (Veldhoven NL, 2000)

**Contributions to conference publications**

G. Craciun, H. Yang, H.W. van Zeijl, L. Pakula, M.A. Blauw, E. van der Drift and P.J. French, "*Single step cryogenic SF<sub>6</sub>-O<sub>2</sub> plasma etching process for the development of inertial devices*", Proceedings of the 3<sup>rd</sup> Dutch Workshop on Semiconductor Sensor and Actuator Technology, 612 (Veldhoven NL, 2002)

G. Craciun, M.A. Blauw E. van der Drift and P.J. French, "*Aspect ratio and crystallographic orientation dependence in deep dry silicon etching at cryogenic temperatures*", Proceedings of the 11<sup>th</sup> International Conference on Solid State Sensors and Actuators, 612 (München DE, 2001)

G. Craciun, M.A. Blauw, E. van der Drift and P.J. French, "*High aspect ratio cryogenic etching of silicon with SF<sub>6</sub>-O<sub>2</sub> plasma*", Proceedings of the 2<sup>nd</sup> Dutch Workshop on Semiconductor Sensor and Actuator Technology, 783 (Veldhoven NL, 2001)



---

## Curriculum Vitae

Michiel Alexander BLAUW

Born on December 5, 1974, in Alkmaar, The Netherlands

- 1987 – 1993            Secondary school (VWO) at OSG Huygenwaard in Heerhugowaard.
- 1993 – 1998            M.Sc. in Applied Physics *cum laude* at the Delft University of Technology. Undergraduate research in the group Nanotechnology under supervision of prof. dr. ir. S. Radelaar. *“Solution phase molecular layer deposition: Growth characterization and scanning tunneling spectroscopy”*
- 1998 – 2003            Ph.D. research at the Delft University of Technology in the group Nanophysics under supervision of prof. dr. ir. S. Radelaar, prof. dr. P.J. French and dr. E. van der Drift. The research was performed at the Delft Institute of Microelectronics and Submicron Technology. *“Deep anisotropic dry etching of silicon microstructures by high-density plasmas”*



---

## Acknowledgements

Plasma etching is an indispensable technology in semiconductor processing and it is successfully applied to the fabrication of many different devices. Nevertheless, plasmas are a complex medium and in many cases they are considered as a black box. Since many years research is performed at the Delft Institute of Microelectronics and Submicron Technology (DIMES) to obtain a better understanding of the practical plasma processes. The black box becomes gradually more transparent because of this effort. The research described in this thesis is a part of it. I would like to express my gratitude to everyone who has contributed to the realisation of this thesis.

First, I would like to thank my supervisors who provided me with the necessary support to complete this research. Prof. dr. ir. Sieb Radelaar analysed the experimental results sharply, which contributed much to the content of this thesis. Thanks to his expertise in the field of semiconductor processing the research was placed in the right framework. Prof. dr. Paddy French had a positive influence on the design of the experiments due to his practical approach. His enthusiasm for the research helped a lot to put the deep anisotropic dry etching into practice. I would like to thank dr. Emile van der Drift for his continuous encouragement of the followed approach in this research. We spent many hours discussing the significance of the experimental results. I admire the inexhaustible way by which he always came up with new ideas that pushed the research in the right direction.

The technical support of the DIMES-crew was essential for the research in the cleanroom. I would like to mention Gilles Gobr eau, Bert de Groot, Marco van der Krogt, Anja van Langen-Suurling, Roel Mattern, Bernard Rousseeuw, Arnold van Run, Tony Zijlstra, Marc Zuiddam and Arjan van Zuuk. I highly appreciate the flexible way by which Gilles Gobr eau solved technical problems if the etching equipment was out of order. In the beginning Tony Zijlstra provided much practical knowledge of plasma etching leading to a quick start of this project.

At the department of Materials Science and Technology I would like to thank dr. ir. Wim Sloof and Cees Borsboom for discussing and performing the XPS measurements. I would like to acknowledge prof. dr. Henny Zandbergen (Delft University of Technology) for the TEM analysis and prof. dr. ir. Gerrit Kroesen (Eindhoven University of Technology) for the discussion of the ellipsometry results.

It was a pleasure to attend the meetings of the EXSTC-project led by dr. Fred Roozeboom of Philips Research, which were a great opportunity to show the first achievements. Afterwards, the user committee meetings of the Technology Foundation STW became an important platform to discuss the results.

The plasma etching physicists who were permanently or temporarily placed in DIMES brought the understanding of plasma etching to a higher level: Mischa Andriesse, Bifeng Rong, Liudi Jiang, Natalie Plank and Jérôme Thiault. It is legitimate to speak of a “plasma etching school” because of the many people that used the expertise gathered by this team. In particular, I would like to mention Gabriel Craciun of the Electronic Instrumentation Laboratory who investigated deep anisotropic dry etching for application to inertial devices.

Occasionally, I travelled to France during my research. The French connection contributed a lot to the development of the etching kinetics model: Pierre Ranson and Rémi Dussart from Université d’Orléans, and, Ahmed Rhallabi and Grégory Marcos from Université de Nantes. I would like to acknowledge our cooperation especially during my stay in Nantes for one month. The use of the Monte Carlo simulation model written by Grégory Marcos greatly helped to understand the etching mechanism. Besides, I would like to mention the pleasant collaboration with Michel Puech and Peter Dijkstra of Alcatel Vacuum Technology France. They provided a lot of input and encouragement for this research.

To end, I would like to thank my family and friends for their interest in my research. Although, in the past years it may not always have been clear what I was doing in the building on the other side of the street. Nevertheless, I could always count on their support! The activities with members of the athletics club De Delters kept me in the right condition, physically and mentally. In particular, I would like to thank my parents, Henk and Sofie, who always stood behind me with good advice. My sister, Marjon, who put the difficulties that I was confronted with into perspective. And first of all, Diana, who showed much understanding each time I had almost, but not quite yet, finished a part of this thesis. You showed me that together we can face up to any challenge.